DUAL-PHASE MATERIALS IN THE MEDIUM AND HIGH ENTROPY ALLOY SYSTEMS Al-Cr-Fe-Ni AND Al-Co-Cr-Fe-Ni

EDITED BY: Ulrike Hecht, Mark L. Weaver and Sheng Guo
PUBLISHED IN: Frontiers in Materials

frontiers Research Topics

frontiers

ISSN 1664-8714
ISBN 978-2-88971-225-0
DOI 10.3389/978-2-88971-225-0

About Frontiers

Frontiers is more than just an open-access publisher of scholarly articles: it is a pioneering approach to the world of academia, radically improving the way scholarly research is managed. The grand vision of Frontiers is a world where all people have an equal opportunity to seek, share and generate knowledge. Frontiers provides immediate and permanent online open access to all its publications, but this alone is not enough to realize our grand goals.

Frontiers Journal Series

The Frontiers Journal Series is a multi-tier and interdisciplinary set of open-access, online journals, promising a paradigm shift from the current review, selection and dissemination processes in academic publishing. All Frontiers journals are driven by researchers for researchers; therefore, they constitute a service to the scholarly community. At the same time, the Frontiers Journal Series operates on a revolutionary invention, the tiered publishing system, initially addressing specific communities of scholars, and gradually climbing up to broader public understanding, thus serving the interests of the lay society, too.

Dedication to Quality

Each Frontiers article is a landmark of the highest quality, thanks to genuinely collaborative interactions between authors and review editors, who include some of the world's best academicians. Research must be certified by peers before entering a stream of knowledge that may eventually reach the public - and shape society; therefore, Frontiers only applies the most rigorous and unbiased reviews.
Frontiers revolutionizes research publishing by freely delivering the most outstanding research, evaluated with no bias from both the academic and social point of view. By applying the most advanced information technologies, Frontiers is catapulting scholarly publishing into a new generation.

What are Frontiers Research Topics?

Frontiers Research Topics are very popular trademarks of the Frontiers Journals Series: they are collections of at least ten articles, all centered on a particular subject. With their unique mix of varied contributions from Original Research to Review Articles, Frontiers Research Topics unify the most influential researchers, the latest key findings and historical advances in a hot research area! Find out more on how to host your own Frontiers Research Topic or contribute to one as an author by contacting the Frontiers Editorial Office: frontiersin.org/about/contact

DUAL-PHASE MATERIALS IN THE MEDIUM AND HIGH ENTROPY ALLOY SYSTEMS Al-Cr-Fe-Ni AND Al-Co-Cr-Fe-Ni

Topic Editors:
Ulrike Hecht, Access e.V., Germany
Mark L. Weaver, University of Alabama, United States
Sheng Guo, Chalmers University of Technology, Sweden

Citation: Hecht, U., Weaver, M. L., Guo, S., eds. (2021). Dual-phase Materials in the Medium and High Entropy Alloy Systems Al-Cr-Fe-Ni and Al-Co-Cr-Fe-Ni. Lausanne: Frontiers Media SA. doi: 10.3389/978-2-88971-225-0

Table of Contents

frontiers in Materials

EDITORIAL
published: 24 June 2021
doi: 10.3389/fmats.2021.718788

Editorial: Dual-Phase Materials in the Medium and High Entropy Alloy Systems Al-Cr-Fe-Ni and Al-Co-Cr-Fe-Ni

Ulrike Hecht[1]*, *Sheng Guo*[2] and *Mark L. Weaver*[3]

[1]Access e.V., Aachen, Germany, [2]Industrial and Materials Science, Chalmers University of Technology, Gothenburg, Sweden, [3]Department of Metallurgical and Materials Engineering, The University of Alabama, Tuscaloosa, AL, United States

Keywords: high entropy alloys, medium entropy alloys, processing, microstructure evolution, structural and functional properties

Editorial on the Research Topic

Dual-Phase Materials in the Medium and High Entropy Alloy Systems Al-Cr-Fe-Ni and Al-Co-Cr-Fe-Ni

The pioneering work of Yeh et al. (2004) and Cantor et al. (2004) initiated an expansive research activity on high entropy alloys (HEAs), aiming at discovering novel materials in the newly opened compositional spaces. The original concept of entropically stabilized solid solution phases around equimolar alloy compositions with not less than 5 elements has driven the quest for single phase high entropy alloys, as described in a critical update (Streuer, 2020). Recent review articles provide critical assessments of the HEA concept while trying to structure and condense the ample and diverse research results and also provide guidance for future research (Miracle and Senkov, 2017; George et al., 2019; George et al., 2020; Li et al., 2021). Besides continuous research on "*ad litteram*" HEAs which closely follows the original definition, the scope was soon extended as to accommodate multicomponent alloys with lower configurational entropy of mixing, so-called medium entropy alloys, MEAs (i.e., Zhou et al., 2018). Special interest was further focused on alloys that provide pathways to dual-phase or multi-phase microstructures (these alloys are sometimes categorized as compositional complex alloys, CCAs, to differentiate with single phase HEAs/MEAs), thus enabling more options for microstructure engineering.

The alloy systems Al-Cr-Fe-Ni and Al-Co-Cr-Fe-Ni are most attractive in this respect. Both systems host compositional ranges for the design of dual-phase materials composed of a face centered cubic (FCC-A1) and a body centered cubic (BCC-B2) phase following distinct phase transformation pathways. Examples are the alloys $Al_{0.7}CoCrFeNi$ and $AlCrFe_2Ni_2$ (Dong et al., 2016; DeJeer et al., 2017) which pass through a BCC-B2→FCC-A1 solid state phase transformation and the alloys $AlCoCrFeNi_{2.1}$, $Al_{0.9}CrFeNi_{2.1}$ which display eutectic growth following Liquid → BCC-B2+FCC-A1 (Lu et al., 2014; Jin et al., 2019). Importantly, in both alloy systems the Al-rich BCC-B2 phase is prone to spinodal decomposition, which may impact on the overall phase transformation cascade and certainly affect the mechanical properties.

This "Research Topic" was initiated with main focus on dual-phase HEAs and MEAs from the above alloy systems, calling for contributions on a wide range of open issues, including phase transformation pathways, alloy processing by conventional and additive technologies, mechanical and functional properties, i.e., corrosion behavior, and other more. From the perspective of future applications knowledge on all these aspects is required in equal measure. For dual-phase MEAs

Edited and reviewed by:
John L. Provis,
The University of Sheffield,
United Kingdom

***Correspondence:**
Ulrike Hecht
u.hecht@access-technology.de

Specialty section:
This article was submitted to Structural Materials, a section of the journal Frontiers in Materials

Received: *01 June 2021*
Accepted: *14 June 2021*
Published: *24 June 2021*

Citation:
Hecht U, Guo S and Weaver ML (2021) Editorial: Dual-Phase Materials in the Medium and High Entropy Alloy Systems Al-Cr-Fe-Ni and Al-Co-Cr-Fe-Ni. Front. Mater. 8:718788. doi: 10.3389/fmats.2021.718788

around the composition $AlCrFe_2Ni_2$ this special issue draws on contributions from several partners of the joint European project "NADEA" funded by national agencies in the frame of the M-era. Net program. In fact 7 out of 11 papers relate to this project and capture the progress toward objectives at mid-term. NADEA aims at targeted MEA developments for applications which require a good balance between strength and ductility or toughness along with wear and corrosion resistance in areas commonly served by duplex and superduplex steels. In the following we briefly introduce the individual contributions:

Stryzhyboroda et al. presented key experiments and results from current CALPHAD modeling efforts for the alloy systems Al-(Co)-Cr-Fe-Ni. CALPHAD databases and thermodynamic codes are valuable digital tools for alloy design and ICME modeling, if phase equilibria as well as segregation trends are well described. Currently this is not the case (Gorsse and Senkov, 2018) and more work is required for database modeling and validation specifically also re-assessing entire sub-systems. Kuczyk et al. showed how additive manufacturing by laser metal deposition can provide a fast track to valuable data about phase equilibria, i.e., for validation of CALPHAD databases, using compositionally graded samples. One single sample designed to screen through a selected section plane can be used to accurately measure phase equilibria along one or more isotherms after correspondingly selected annealing treatments. Data were provided for Al_xCoCrFeNi with x = 0.2 to1.5 (5–30 at. % Al) at T = 1350 K.

Hecht et al. discussed phase transformations in the dual-phase alloy $AlCrFe_2Ni_2$ which are similar to $Al_{0.8}$AlCoCrFeNi and which depend on the cooling rate applied during the BCC-B2→FCC-A1 solid state phase transformation. Apart from the classical Widmanstätten structure obtained upon slow cooling, an ultrafine vermicular microstructure, previously termed noodle-like or worm-like (Dong et al., 2016), was identified for higher cooling rates and associated to a characteristic "duplex spinodal" phase transformation pathway. The related crystal orientation relationship (OR) between FCC and BCC was analyzed in detail, being distinct and different from all well-known ORs established between BCC and FCC phases. Gein et al. further investigated the ultrafine vermicular microstructure in alloys based on $AlCrFe_2Ni_2$ however with minor additions of molybdenum ranging from 1 to 3 at.%. The alloys were prepared by arc melting of large (300 g) buttons and subjected to annealing treatments. For 2 at.% Mo a well-balanced microstructure with promising mechanical properties was reported after annealing at 1,100°C for 1 h with subsequent water quenching. The flexural stress/strain behavior favorably compares to the reference superduplex steel EN 1.4517.

Vogiatzief et al. and Roccio Molina et al. explored additive manufacturing (AM) of an alloy with composition close to $AlCrFe_2Ni_2$, but with 17.5 rather than 16.7 at.% aluminum, using laser powder bed fusion (L-PBF) and laser metal deposition/direct energy deposition (LMD/DED), respectively. Alloy processing required substrate preheating to at least 450°C (LMD/DED) and 700°C (L-PBF), respectively. The applied preheating effectively reduced thermal gradients but also allowed some amount of FCC-A1 to form during the build operation thus mitigating the cracking susceptibility of the spinodally decomposing BCC-B2. The full amount of FCC-A1 was only achieved by post build annealing heat treatments and the annealing temperature and duration was used to tailor microstructure and properties, e.g., the flexural stress/strain behavior. Comparison to a reference superduplex steel EN 1.4517 showed that the target MEA is a promising material with good chances to compete with duplex steels. However, both alloy composition and processing parameters must be further optimized in order to establish a robust AM manufacturing route.

Eshed et al. investigated a casting route for alloy $AlCrFe_2Ni_2$ with main emphasis on microstructure and phase analysis after selected homogenization and annealing treatments. Transmission electron microscope (TEM) and high resolution TEM provided detailed insight into phase constitution. An unexpected carbide phase was observed, which raises questions as to the origin and role of impurities, a subject which calls for further and systematic investigation.

Zollinger and Fleury provided a brief report on the effect of casting texture on the elastoplastic behavior of $Al_{0.8}CrCuFeNi_2$ during uniaxial compression tests. The alloy solidified with a primary FCC-A1 phase and interdendritic BCC-B2 in a hybrid mould with alumina walls and a copper base, thus displaying a morphological transition from a columnar (textured) to an equiaxed (untextured) FCC-A1 phase. When tested under uniaxial compression with the loading axis parallel to the direction of solidification, the columnar microstructure, with a preferred orientation of the fcc phase toward the <100> direction showed remarkably higher yield strength than the equiaxed microstructure. The improved macroscopic behavior of the <100> textured sample was related to confinement of the activated slip system(s) to FCC-A1 dendrites separated from one another by the BCC-B2 envelop. Wang et al. and Godlewska et al. investigated the corrosion behavior of selected Al-(Co)-Cr-Fe-Ni alloys using, among others, potentiodynamic polarization tests and electrochemical impedance spectroscopy.

Wang et al. focused on the alloy $Al_{0.1}$CoCrFeNi and its behavior in NaCl-containing aqueous solutions of various concentration, while Godlewska et al. probed several alloys around the baseline composition $AlCrFe_2Ni_2$ in a 3.5 wt.% NaCl aqueous solution including for reference three Al_xCoCrFeNi alloys as well as the superduplex steel EN 1. 4517. At room temperature the pitting corrosion resistance and passivation capability of EN 1.4517 are outstanding and unrivaled by $AlCrFe_2Ni_2$-based alloys, irrespective of small Mo-additions. This behavior is due to the Cr-depletion of the BCC phase. The performance in potentiodynamic tests is judged rather similar to lean duplex steels (Siow et al., 2001). The nearly fully FCC alloy tested by Wang and independently confirmed by Godlewska for an alloy with similar composition is the most resistant to pitting corrosion and closely matches the superduplex steel behavior.

Finally, Röhrens et al. addressed dual-phase eutectic alloys prepared by suction casting from ternary, quaternary and quinary eutectic alloys, i.e., $Ni_{48}Fe_{34}Al_{18}$, $Ni_{44}Fe_{20}Cr_{20}Al_{16}$

and $Ni_{34.4}Fe_{16.4}Co_{16.4}Cr_{16.4}Al_{16.4}$. The special merit of the investigation relates to the fact that it incorporates the ternary alloy, originally investigated 20 years ago (Misra and Gibala, 1997; Misra and Gibala, 1999) in an attempt to ductilize the NiAl-B2 intermetallic alloy. This family of alloys could indeed serve as a very good reference for future research on HEA and MEA eutectics for the Al-Co-Cr-Fe-Ni alloy system.

We hope that the reader will find this collection of articles interesting and useful as reference for future research endeavors in this emerging field of alloy design, processing and materials characterization.

AUTHOR CONTRIBUTIONS

UH and SG wrote the editorial article, while UH, SG, and MW served as editors for this Frontier's research topic.

FUNDING

The corresponding author would like the acknowledge funding through the German Federal Ministry for Education and Research (BMBF) under grant number 03XP0163A in the frame of the M-era.Net Joint Call 2017, Project NADEA (no. 5129).

REFERENCES

Cantor, B., Chang, I. T. H., Knight, P., and Vincent, A. J. B. (2004). Microstructural Development in Equiatomic Multicomponent Alloys. *Mater. Sci. Eng. A* 375-377, 213–218. doi:10.1016/j.msea.2003.10.257

De Jeer, L. T. H., Ocelík, V., and De Hosson, J. T. M. (2017). Orientation Relationships in Al0.7CoCrFeNi High-Entropy Alloy. *Microsc. Microanal.* 23, 905–915. doi:10.1017/S1431927617012442Yeh

Dong, Y., Gao, X., Lu, Y., Wang, T., and Li, T. (2016). A Multi-Component AlCrFe2Ni2 alloy with Excellent Mechanical Properties. *Mater. Lett.* 169, 62–64. doi:10.1016/j.matlet.2016.01.096

George, E. P., Curtin, W. A., and Tasan, C. C. (2020). High Entropy Alloys: A Focused Review of Mechanical Properties and Deformation Mechanisms. *Acta Materialia* 188, 435–474. doi:10.1016/j.actamat.2019.12.015

George, E. P., Raabe, D., and Ritchie, R. O. (2019). High-entropy Alloys. *Nat. Rev. Mater.* 4, 515–534. doi:10.1038/s41578-019-0121-4

Gorsse, S., and Senkov, O. (2018). About the Reliability of CALPHAD Predictions in Multicomponent Systems. *Entropy* 20, 899. doi:10.3390/e20120899

Jin, X., Bi, J., Zhang, L., Zhou, Y., Du, X., Liang, Y., et al. (2019). A New CrFeNi2Al Eutectic High Entropy alloy System with Excellent Mechanical Properties. *J. Alloys Compounds* 770, 655–661. doi:10.1016/j.jallcom.2018.08.176

Li, W., Xie, D., Li, D., Zhang, Y., Gao, Y., and Liaw, P. K. (2021). Mechanical Behavior of High-Entropy Alloys. *Prog. Mater. Sci.* 118, 100777. doi:10.1016/j.pmatsci.2021.100777

Lu, Y., Dong, Y., Guo, S., Jiang, L., Kang, H., Wang, T., et al. (2014). A Promising New Class of High-Temperature Alloys: Eutectic High-Entropy Alloys. *Sci. Rep.* 4, 6200. doi:10.1038/srep06200

Miracle, D. B., and Senkov, O. N. (2017). A Critical Review of High Entropy Alloys and Related Concepts. *Acta Materialia* 122, 448–511. doi:10.1016/J.ACTAMAT.2016.08.081

Misra, A., and Gibala, R. (1997). Room-temperature Deformation Behavior of Directionally Solidified Multiphase Ni-Fe-Al Alloys. *Metall. Mat Trans. A.* 28, 795–807. doi:10.1007/s11661-997-0066-x

Misra, A., and Gibala, R. (1999). Slip Transfer and Dislocation Nucleation Processes in Multiphase Ordered Ni-Fe-Al Alloys. *Metall. Mat Trans. A.* 30, 991–1001. doi:10.1007/s11661-999-0152-3

Siow, K. S., Song, T. Y., and Qiu, J. H. (2001). Pitting Corrosion of Duplex Stainless Steels. *Anti-Corrosion Meth Mater.* 48 (No. 1), 31–37. doi:10.1108/00035590110365309

Steurer, W. (2020). Single-phase High-Entropy Alloys - A Critical Update. *Mater. Characterization* 162, 110179. doi:10.1016/j.matchar.2020.110179

Yeh, J. W., Chen, S. K., Lin, S. J., Gan, J. Y., Chin, T. S., Shun, T. T., et al. (2004). Nanostructured High-Entropy Alloys with Multiple Principal Elements: Novel alloy Design Concepts and Outcomes. *Adv. Eng.Mater.* 6, 299–303. doi:10.1002/adem.200300567

Zhou, Y., Zhou, D., Jin, X., Zhang, L., Du, X., and Li, B. (2018). Design of Non-equiatomic Medium-Entropy Alloys. *Sci. Rep.* 8 (1), 1–9. doi:10.1038/s41598-018-19449-0

Conflict of Interest: The authors declare that the research was conducted in the absence of any commercial or financial relationships that could be construed as a potential conflict of interest.

frontiers in Materials

ORIGINAL RESEARCH
published: 28 July 2020
doi: 10.3389/fmats.2020.00248

Laser Powder Bed Fusion and Heat Treatment of an $AlCrFe_2Ni_2$ High Entropy Alloy

Dimitrios Vogiatzief[1], Alper Evirgen[1], Sergej Gein[2], Veronica Rocio Molina[3], Andreas Weisheit[3] and Mikkel Pedersen[1]*

[1] Oerlikon AM GmbH, Feldkirchen, Germany, [2] Access e.V., Aachen, Germany, [3] Fraunhofer-Institut für Lasertechnik ILT, Aachen, Germany

Recent research in the Al-Co-Cr-Fe-Ni and Al-Cr-Fe-Ni systems has shown that novel duplex materials composed of FCC and BCC phases can be obtained. Among them, alloys with a composition close to $AlCrFe_2Ni_2$ retain their structural properties while being Co-free. Their strength and ductility can be tailored by adjusting the phase fractions of FCC and BCC phases, while the latter is undergoing a spinodal decomposition into ordered and disordered BCC phases. Further improvement of the properties is expected with the use of novel processing techniques such as laser powder bed fusion. This process stands out due to high geometric complexity capabilities, a wide range of accessible processing parameters, and high cooling rates that support microstructure refinement. Within the frame of the present study, alloy powder around the composition $AlCrFe_2Ni_2$ was produced and coupons for material characterization were built with laser powder bed fusion. In this paper, the following will be presented: (i) prealloyed powder properties, (ii) laser powder bed fusion processing of the material, (iii) heat treatments and their subsequent effect on microstructure, and (iv) mechanical properties obtained by three-point bending and microhardness tests. A highlight of this study is the novel pathway to obtain an ultrafine duplex microstructure, which forms upon heat treatment from a metastable as-built microstructure. A spinodally decomposed BCC microstructure, retained due to solidification under high cooling rates, is used to nucleate and grow FCC micro-platelets during a subsequent heat treatment step. This ultrafine duplex material cannot be obtained under conventional processing; thus, it can be considered a unique additive manufacturing material. In the context of the heat treatment study carried out in the present work, the influence of heat treatment parameters on the phase fraction of FCC platelets and the resulting hardness and flexural properties will be discussed. Finally, the current challenges concerning the processing of the alloy and the possible optimization paths for best material performance will be discussed.

Keywords: laser powder bed fusion, high entropy alloy, $AlCrFe_2Ni_2$, baseplate preheating, heat treatment, duplex microstructure, BCC, FCC

OPEN ACCESS

Edited by:
Sheng Guo, Chalmers University of Technology, Sweden

Reviewed by:
Zhang Hui, Anhui University of Technology, China
Igor Moravcik, Brno University of Technology, Czechia

****Correspondence:***
Dimitrios Vogiatzief
dimitrios.vogiatzief@oerlikon.com

Specialty section:
This article was submitted to Structural Materials, a section of the journal Frontiers in Materials

Received: *28 May 2020*
Accepted: *07 July 2020*
Published: *28 July 2020*

Citation:
Vogiatzief D, Evirgen A, Gein S, Molina VR, Weisheit A and Pedersen M (2020) Laser Powder Bed Fusion and Heat Treatment of an $AlCrFe_2Ni_2$ High Entropy Alloy. Front. Mater. 7:248. doi: 10.3389/fmats.2020.00248

INTRODUCTION

Over the past two decades, research on High Entropy Alloys (HEAs) has intensified. The term HEA is widely used in the literature to describe alloys with unusual compositions consisting of multiple principle elements. The origin of the naming comes from the high configurational entropy that these alloys exhibit when the concentration of their constituting elements is near-equimolar according to the Boltzmann's hypothesis (Yeh et al., 2004; Yeh, 2006). Multiple systems have been investigated, with some of them exhibiting excellent compression properties (Zhou et al., 2007), high hardness (Kao et al., 2009), wear and corrosion resistance (Poletti et al., 2017; Nair et al., 2018). Based on their properties, HEAs have been characterized as interesting candidates for numerous applications. HEAs consisting of 3d transition metals showed mechanical properties comparable to Ni alloys and various grades of stainless steels, e.g., austenitic or duplex stainless steels (Miracle and Senkov, 2017), making them promising for structural applications. One of the most studied HEA systems is Al-Co-Cr-Fe-Ni. Alloys within this system consist of solid solution phases, e.g., Body-Centered Cubic (BCC), Face-Centered Cubic (FCC), or both, depending on the Al concentration or Al/Ni ratio (Kao et al., 2009; Sistla et al., 2015). The other constituents are similarly influencing phase formation such as stabilizing the BCC phase, e.g., Cr (Zhang et al., 2016), or the FCC phase, e.g., Co (Qin et al., 2018). A great number of studies on Al-Co-Cr-Fe-Ni based HEAs showed that mechanical properties, such as hardness (Kao et al., 2009; Wang et al., 2012), tensile and compression strength (Joseph et al., 2017) can be altered by controlling the microstructure through alloying or heat treatment. Furthermore, the corrosion resistance of these alloys can be similar to stainless steel grades such as the austenitic steels (Kuwabara et al., 2018), suggesting the suitability of the alloys for a greater range of applications that require durability in corrosive environments. Such applications can be found in the marine and offshore industry (Nair et al., 2018).

Commonly, in applications where high strength and corrosion resistance are needed, the austenitic, ferritic, and austenitic-ferritic (duplex) steels are used (Nilsson, 1992; Charles, 2008; Aribo et al., 2013; Chai and Kangas, 2017). When compared to stainless steel, HEAs usually contain a large weight percentage of relatively expensive elements such as Co, Cr, and Ni. This certainly is a challenge for the industrialization of these novel alloys and the development of their applications (Yin et al., 2019), and greater focus is needed on the development of cost-effective compositions. While Al-Co-Cr-Fe-Ni based HEAs have been gathering much attention, the Co-free Al-Cr-Fe-Ni system may have comparable properties and a theoretical lower cost. The reported phases, e.g., FCC, BCC, and BCC-B2 and their volume fractions, can be altered by modifying the concentrations of Al and Ni. The mechanical properties can also be modified since they are influenced by the volume fractions of the prescribed phases (Zeng et al., 2018). Jiang et al. showed on an equiatomic cast AlCrFeNi HEA that exhibits mechanical properties such as yield strength higher than 1000 MPa and failure strain greater than 40% (Jiang et al., 2019). Moreover, an excellent combination of fracture strength and ductility was reported for an as-cast $AlCrFe_2Ni_2$ HEA, owing to the combination and morphology of the BCC and FCC phases in the microstructure (Dong et al., 2016). To be precise, the Co-free alloys are rather medium entropy alloys, since their ideal entropy of mixing $\Delta S_{\mathrm{mix}} = -R\sum_{i=1}^{n}\left(x_i \ln x_i\right)$ ranges from 1R to 1.5R, e.g., 1.33R for $AlCrFe_2Ni_2$. Nevertheless, the distinction is somewhat arbitrary and the HEA concept itself has considerable limitations.

Recently, innovative manufacturing techniques such as Additive Manufacturing (AM) have been utilized for novel alloy processing (Azizi et al., 2018; Li W.et al., 2018; Pozdniakov et al., 2018). Many studies have been focused on the processing of HEAs with AM techniques (Brif et al., 2015; Li R.et al., 2018; Zhang et al., 2019). AM processes offer flexibility in the production of chemically homogenous mixtures from metal powders (Joseph et al., 2015). Laser Powder Bed Fusion (LPBF) is an AM process that offers more advantages related to the final product, such as design freedom and optimized complex shaped parts. Moreover, there are advantages related to the obtained material after processing (as-built material). Microstructures of LPBF processed materials are finer due to fast cooling and exhibit enhanced mechanical properties (Yap et al., 2015).

The current study aimed to process the $AlCrFe_2Ni_2$ alloy with LPBF and investigate the influence of the microstructure on the mechanical properties through subsequent heat treatment. The prescribed composition was selected due to its remarkably well-balanced mechanical properties in the as-cast condition and the fact that it is Co-free and therefore a cost-effective solution for structural applications. It was expected that the LPBF processing would further increase the performance of the alloy by obtaining a finer microstructure compared to casting. The heat treatment was used to control the ratio of the formed phases and investigate their impact in the mechanical response of the novel AM material.

MATERIALS AND METHODS

In the context of the present study, prealloyed powder with composition $Al_{17.8}Cr_{16.4}Fe_{33.2}Ni_{32.7}$ close to $AlCrFe_2Ni_2$ ($Al_{16.7}Cr_{16.7}Fe_{33.3}Ni_{33.3}$), was produced with gas atomization by Oerlikon Metco. The powder was characterized in terms of chemical composition, particle size distribution (PSD), and morphology. The chemical composition of the powder was measured by Energy Dispersive X-ray Spectroscopy (EDS) using a Zeiss Merlin scanning electron microscope (SEM). Multiple EDS measurements were performed on individual particles and the results were averaged to calculate the powder composition.

TABLE 1 | LPBF process parameters used for coupon production.

Laser power (W)	Scanning speed (mm/s)	Laser spot size (μm)	Hatch space (μm)	Layer height (μm)
175	1700	80	60	30

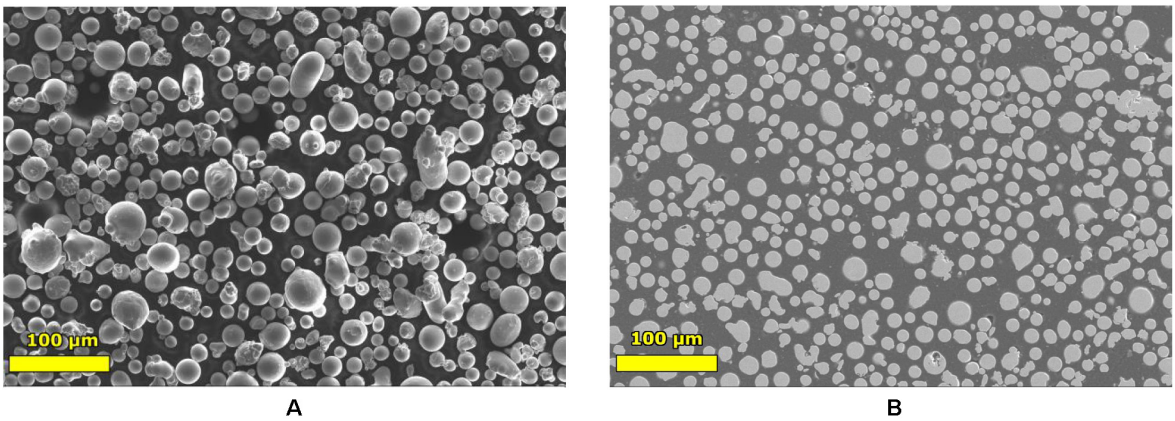

FIGURE 1 | SEM micrographs of **(A)** the $AlCrFe_2Ni_2$ prealloyed powder particles and **(B)** cross-section of powder particles.

The powder PSD and morphology were investigated via optical method using a Malvern Morphologi four equipment. For this purpose, powder was sampled from the atomized powder batch and dispersed on a glass plate. Individual optical micrographs of 10000 particles were captured to estimate the PSD based on their diameter. The particle circularity distribution was also estimated as an indication of the sphericity of the powder particles. The circularity of each particle was calculated by the equipment using the following formula:

$$\text{Circularity} = \frac{2 \times \sqrt{\pi \times \text{Area}}}{\text{Perimeter}}$$

The LPBF coupons were built in an Aconity3D MINI machine with a baseplate preheating feature to reduce thermal stresses during the process (Kempen et al., 2014; Mertens et al., 2018). Initial screening builds without baseplate preheating resulted in cracked coupons irrespective of the process parameters. However, process parameters for minimum porosity were developed during the screening builds but will not be discussed further in the current study. Increasing the preheating up to 700°C was needed to obtain bulk material suitable for characterization. The selected process parameters for the build presented in the current study are listed in **Table 1**. A typical meander scanning strategy (Koutny et al., 2018) with a scan vector rotation of 90° per layer was applied. The preheating of the baseplate was kept constant at 700°C during the build and was switched off after the end of the process. The process chamber was filled with argon, while the oxygen content was controlled by the machine and stabilized below 100 ppm. The selected geometry of the coupons was 10 mm × 10 mm × 35 mm blocks. After LPBF processing, the chamber was cooled down to room temperature and the baseplate with the coupons was removed from the printer. The coupons were cut from the baseplate using Wire Electro Discharge Machining (WEDM).

Five coupons were used for post-build annealing heat treatments at 750, 800, 850°C for 3 h and 900, 950°C for 6 h to test the higher temperature and longer treatment time effects on the microstructure. The coupons were heat treated in a Carbolite Gero CWF 11/13 furnace with a heating rate at 1.1°C/s, under a protective argon atmosphere. After heat treatment, they were left to cool down to room temperature inside the furnace (cooling rate around 0.5°C/s). Thin plate three-point bending specimens with dimensions of 30 mm × 5 mm × 1.6 mm were extracted from the heat treated coupons with WEDM with their length being aligned to the build direction Before the three-point bending test, the specimens were gently polished to remove surface anomalies. The applied strain rate of the bending test was 0.2 mm/min and the strain limit of the device was 21%. The bending span of the device was 17.2 mm. The microhardness measurements were performed using a Struers DuraScan Microhardness testing equipment with an applied load of 1 kgf.

The porosity levels in the as-built condition were studied using a Zeiss Smartzoom optical microscope by investigating cross-section (perpendicular to build direction) and longitudinal (parallel to build direction) specimens extracted from the coupons. The SEM and Electron Backscatter Diffraction (EBSD) measurements were performed in a Zeiss Merlin and a Zeiss Gemini field emission microscope equipped with backscattered electron detectors.

Postprocessing of the EBSD data was conducted in Matlab® MTEX toolbox for texture and crystallography analysis (Bachmann et al., 2010) and in the Aztec software from Oxford Instruments. Sample preparation for optical microscopy, SEM and EBSD included mechanical grinding down to 4000 µm and subsequent polishing using a diamond paste (1 µm) and a colloidal silica suspension (0.02 µm).

TABLE 2 | Chemical composition of the powder measured by EDS.

Element	Average (wt.%)	Average (at.%)
Al	9.4 ± 0.2	17.8 ± 0.4
Cr	16.7 ± 0.2	16.4 ± 0.2
Fe	36.3 ± 0.7	33.2 ± 0.6
Ni	37.6 ± 0.7	32.7 ± 0.7

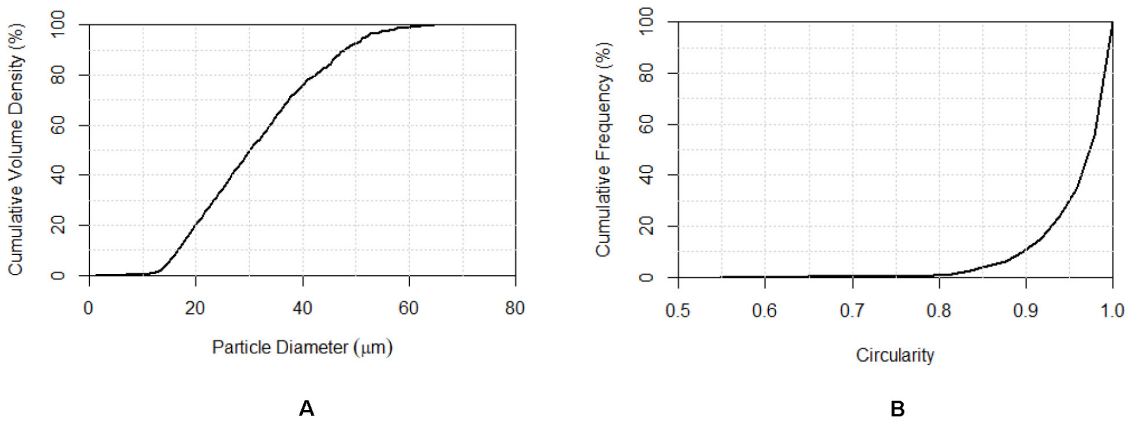

FIGURE 2 | Cumulative distribution graphs of the **(A)** $AlCrFe_2Ni_2$ prealloyed powder particle diameter and **(B)** circularity, based on optical analysis of 10000 particles.

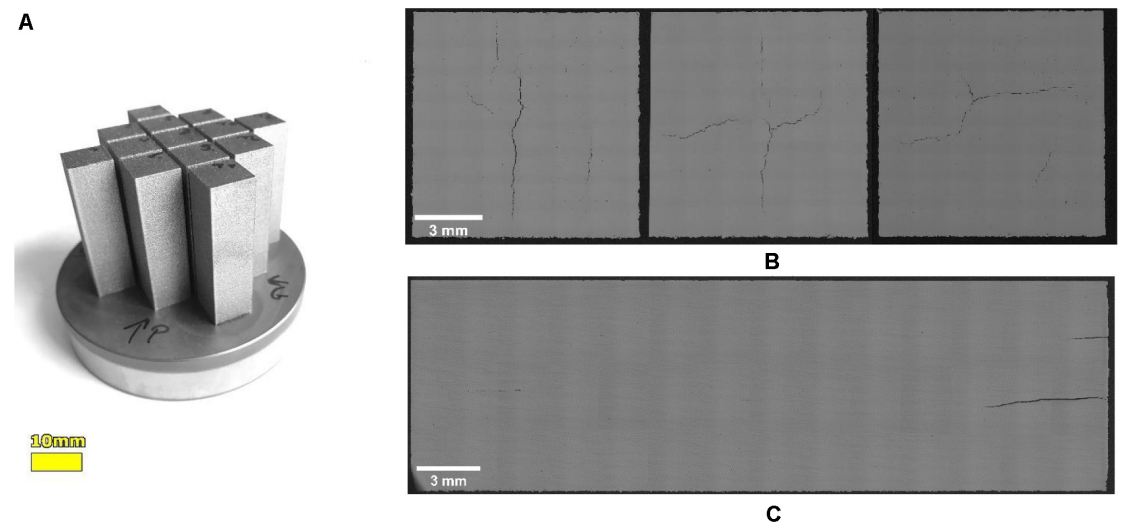

FIGURE 3 | (A) $AlCrFe_2Ni_2$ LPBF coupons on the baseplate after the build and **(B,C)** optical microscopy micrographs in cross-section and longitudinal section of the coupons, respectively.

RESULTS AND DISCUSSION

The overall morphology of the gas atomized $AlCrFe_2Ni_2$ powder is shown in **Figure 1A**. As seen, highly spherical particles were observed and few satellites were visible on larger particles. Generally, highly spherical particles are preferred for better powder flow and spreading during the LPBF process. A cross-section SEM micrograph of the particles is shown in **Figure 1B**. No internal defects or inclusions were found in the particles. The chemical composition of the powder measured by EDS on cross-sections of the particles is summarized in **Table 2**. The composition of the powder was found to be matching the nominal composition of the alloy, being slightly higher in Al content and slightly lower in Ni content compared to the baseline $AlCrFe_2Ni_2$. The overall morphology of the powder was further studied via optical imaging. The cumulative frequency distribution of the powder particle diameter can be seen in **Figure 2A**. From the values that correspond to the 10th (D10) and 90th (D90) percentile, it was estimated that the particle size was ranging between 17 and 48 μm. The presence of fine particles (diameter < 15 μm) did not affect the flowability of the powder during processing. The cumulative distribution graph obtained by optical measurement confirmed that the majority of the particles were highly circular (circularity ≥ 0.9) as seen in **Figure 2B**.

TABLE 3 | Chemical composition of the LPBF coupons measured by EDS.

Element	Average (wt.%)	Average (at.%)
Al	9.5 ± 0.1	18.2 ± 0.2
Cr	16.9 ± 0.1	16.5 ± 0.1
Fe	36.4 ± 0.1	33.2 ± 0.2
Ni	37.1 ± 0.2	32.2 ± 0.2

An image of the coupons on the baseplate after LPBF processing can be seen in **Figure 3A**. All coupons were built successfully without noticeable irregularities on the side and top surfaces. Three of them were selected randomly and cross-section specimens were extracted. The specimens were studied using the optical microscope to ensure that they were equivalent in terms of the as-built condition. The corresponding optical microscopy micrographs can be seen in **Figure 3B**. The coupons showed low porosity but exhibited internal cracks. A micrograph taken on a longitudinal specimen can be seen in **Figure 3C**. The cracks were seen to run parallel to the build direction, but no other notable defects were observed. The chemical composition of the specimens was also analyzed. The aim was to ensure that there was no significant deviation from the baseline powder composition due to potential elemental loss from evaporation during LPBF. The results of the chemical analysis by EDS can be seen in **Table 3**. Based on the given table, and unlike expected, no significant elemental losses were found taking into account the standard error of the EDS measurement.

Microstructural Analysis of the LPBF As-Built $AlCrFe_2Ni_2$

The SEM micrographs obtained from longitudinal sections of as-built blocks can be seen in **Figure 4**. The cracks that were observed under the optical microscope were found to form at intergranular locations, initiating as micro-voids at the grain boundaries as seen in **Figure 4A**. For phase identification,

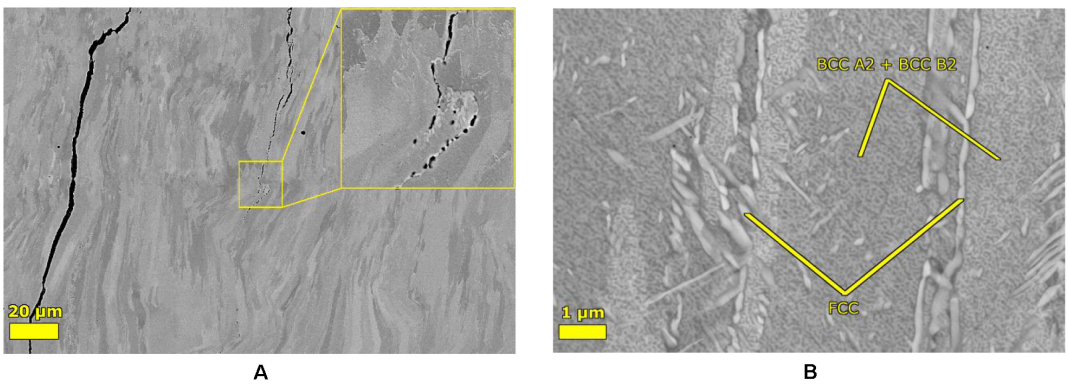

FIGURE 4 | SEM micrographs on a longitudinal section of the $AlCrFe_2Ni_2$ as-built LPBF coupons; **(A)** columnar grains and crack formation along the grain boundaries and **(B)** observed phases in high magnification.

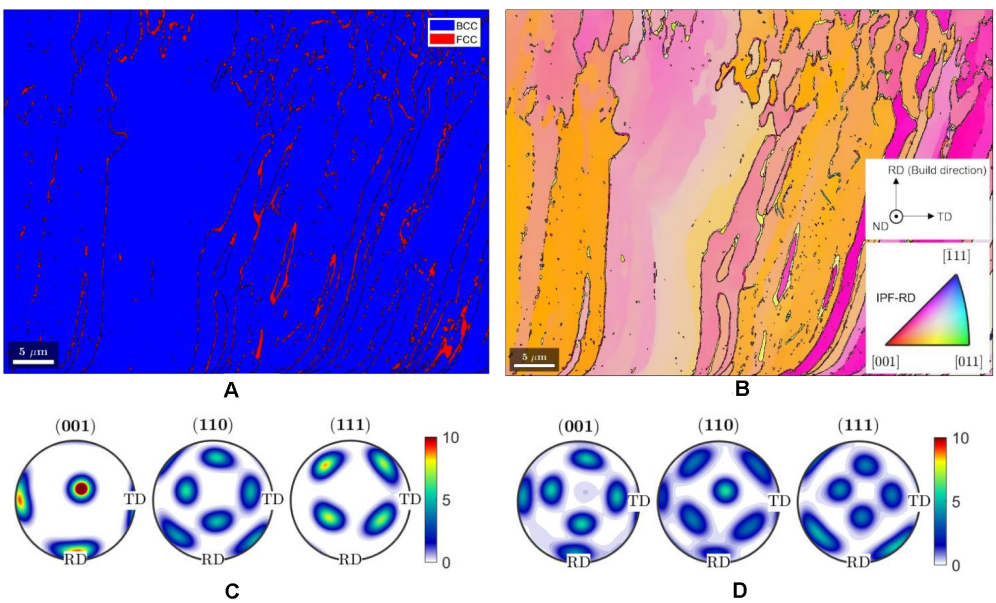

FIGURE 5 | The **(A)** phase map and **(B)** IPF-RD map of the $AlCrFe_2Ni_2$ LPBF coupon in the as-built condition, obtained by EBSD on a longitudinal section. Build direction is the Rolling Direction (RD). The pole figures with orientation density distribution for the BCC and FCC phase are also included in **(C,D)**, respectively.

EBSD was utilized. The diffraction patterns of the columnar grains matched with the iron ferrite phase, while those of the precipitates seen in **Figure 4B** matched with the iron gamma phase, indicating a BCC and an FCC phase, respectively. Most of the secondary phase precipitation was observed mainly in the grain boundaries and only a few intergranular precipitates were present. Apart from the FCC precipitates, at high magnification, a spinodal decomposition (Porter et al., 2009) structure inside the BCC grains was also revealed and can be seen in **Figure 4B**. Similar to previous studies in as-cast $AlCrFe_2Ni_2$ (Dong et al., 2016), the brighter precipitate-like features in the spinodal decomposed BCC matrix are disordered, Fe-, Cr-rich A2, while the inter-precipitates seen with gray contrast are ordered B2. Compared to the as-cast $AlCrFe_2Ni_2$, in the as-built LPBF microstructure the FCC phase was absent in the volume of the grains. The transformation path of the current HEA is considered similar to that of highly alloyed steels, such as duplex steels (Knyazeva and Pohl, 2013), where initially a ferrite solidification is promoted and on further cooling a diffusion-controlled ferrite to austenite transformation is taking place. However, due to the significantly high cooling rates of the LPBF process (Hooper, 2018; Zhang et al., 2018) the FCC formation is suppressed and limited in the grain boundaries of the parent BCC grains. Thus, the microstructure of the LPBF as-built $AlCrFe_2Ni_2$ is

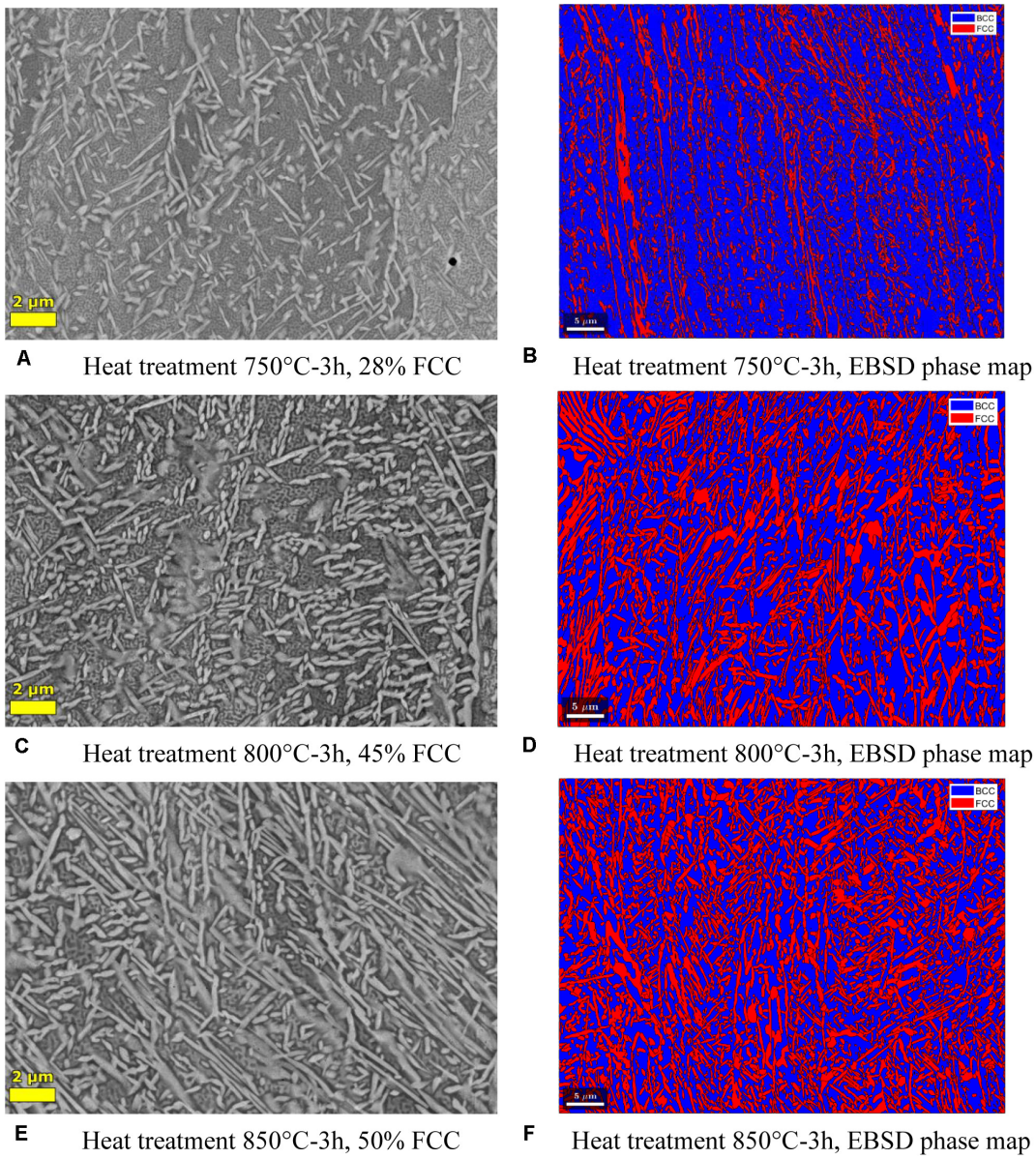

FIGURE 6 | SEM micrographs and EBSD phase maps of the $AlCrFe_2Ni_2$ microstructures after heat treatment at **(A,B)** 750°C, **(C,D)** 800°C, and **(E,F)** 850°C for 3 h. The percentage of the FCC phase is also included in the labels for each heat treatment condition.

in a metastable state. Secondary phase suppression has been observed in LPBF of other alloys before, e.g., the suppression of austenite in LPBF of duplex steels (Davidson and Singamneni, 2016; Hengsbach et al., 2017) and similar cases of FCC or BCC suppression in LPBF of HEAs such as Al0.5CoCrFeNi (Zhou et al., 2019), AlCoCrFeNi (Niu et al., 2019) and AlCoCuFeNi (Zhang et al., 2019).

The phase map of the LPBF as-built condition obtained by EBSD can be seen in **Figure 5A**. Based on the EBSD results, the as-built microstructure consisted of mainly the BCC phase (95%) with a pronounced growth texture. Elongated FCC structures were observed mainly along the parent BCC grain boundaries. The texture of the BCC grains was influenced by the directional heat transfer during the LPBF process. The parent grains grew along the build direction following near <001>orientations as seen in the build direction inverse pole figure (IPF) map in **Figure 5B**. The strong cube texture of the BCC grains can be also seen in the pole figures of the BCC phase, where the highest pole density was found near the <001> orientation, as seen in **Figure 5C**. The FCC pole figures in the as-built condition showed more orientations with higher pole density, as seen in the FCC pole figures of **Figure 5D**. The latter observation indicates the presence of an Orientation Relationship (OR) between the BCC and the FCC phase.

As mentioned earlier, cracks formed at the grain boundaries. Since the microstructure consisted mainly of columnar grains parallel to the build direction, the prolonged grain boundaries could enhance the crack growth. However, with BCC being the high-temperature phase, it is challenging to avoid the columnar grain growth during solidification in LPBF. The epitaxial columnar grain growth along the build direction is common during LPBF and favorable for BCC and FCC metals (Yan et al., 2017). Numerous studies on other BCC and FCC solidifying alloys such as AlCoCrFeNi, AlCoCuFeNi, Inconel 718, and Invar have described the formation of columnar grains parallel to the build direction with LPBF processing (Amato et al., 2012; Qiu et al., 2016; Ni et al., 2017; Niu et al., 2019; Zhang et al., 2019). The cube texture is certainly related to the hatching strategy (90° scan vector rotation per layer) applied during the build. Alternative rotations such as 67°could avoid the cube texture formation but certainly not the <001>orientation of the parent grains.

Microstructural Analysis of the Heat Treated $AlCrFe_2Ni_2$

The purpose of the annealing heat treatments was to investigate the evolution of the FCC phase concerning its phase fraction, morphology, crystal OR, and variant selection as well as precipitate size. The spinodally decomposed parent BCC structure obtained by LPBF was expected to greatly increase the nucleation site density for FCC formation during these heat treatments, given the elastic strain energy (coherency stresses) associated with the spinodal interfaces.

The SEM micrographs and EBSD phase maps, given in **Figure 6**, show the microstructure evolution for three heat treatment conditions. After 750°C-3 h heat treatment, FCC precipitates were found to grow at grain boundaries but also inside the spinodally decomposed BCC matrix as seen in **Figures 6A,B**. The FCC fraction increased from 5% (as-built) to 28%. Therefore, it can be concluded that the temperature of the coupons during LPBF did not exceed 750°C for extended periods even with the combined effect of the baseplate preheating and the laser exposure. At higher heat treatment temperatures such as 800°C and 850°C, the FCC phase fraction reached 45 and 50%, respectively. The FCC precipitates were ultrafine platelets, termed microplatelets, as displayed in **Figures 6C–F**. The parent BCC phase retained the spinodal nanostructure, which slightly coarsened.

Heat treatment for longer periods and at higher temperatures revealed slightly different microstructures as displayed in **Figures 7A,B**. The FCC percentage increased to 56 and 63% at 900°C-6 h and 950°C-6 h, respectively. The microplatelets were larger and more homogeneously dispersed in the matrix, while the A2 and B2 spinodal structures of the parent BCC phase were very coarse. In fact, the A2 phase almost vanished after

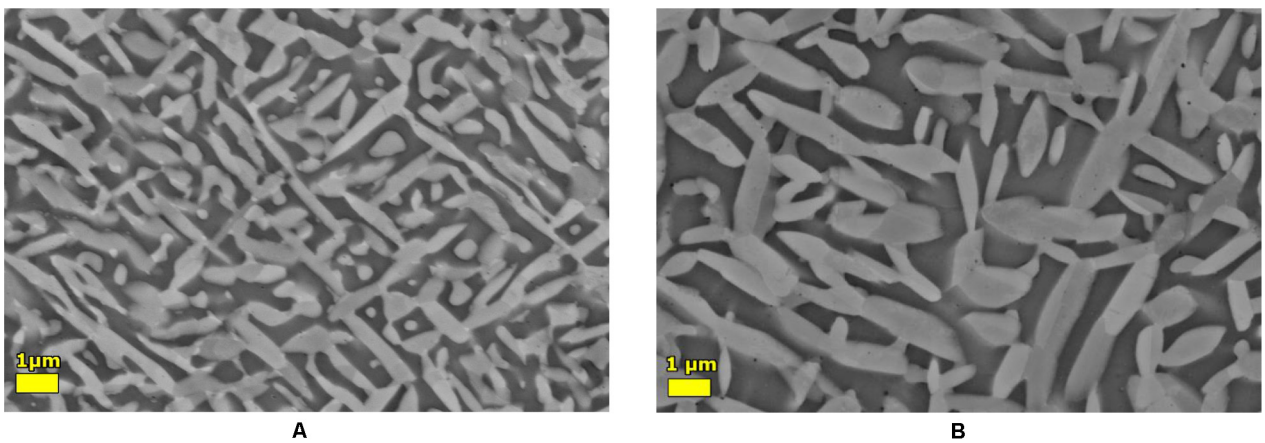

FIGURE 7 | SEM micrographs of the $AlCrFe_2Ni_2$ microstructures after heat treatment at 900°C-6 h **(A)** and 950°C-6 h **(B)**, respectively.

950°C-6 h treatment. To investigate the OR between the parent BCC phase and the FCC microplatelets, an EBSD analysis was performed inside a single BCC grain of the 950°C-6 h heat treated coupon. The Euler color map in the region of interest is shown in **Figures 8A,B** for the BCC and FCC phases, respectively. The FCC microplatelets were present in many crystal orientations, which were variants of the crystallographic OR. The variants were homogeneously distributed and no colony formation was observed. From the selected pole figures displayed in **Figure 8C**, it can be concluded that the Nishiyama–Wasserman (N–W) OR

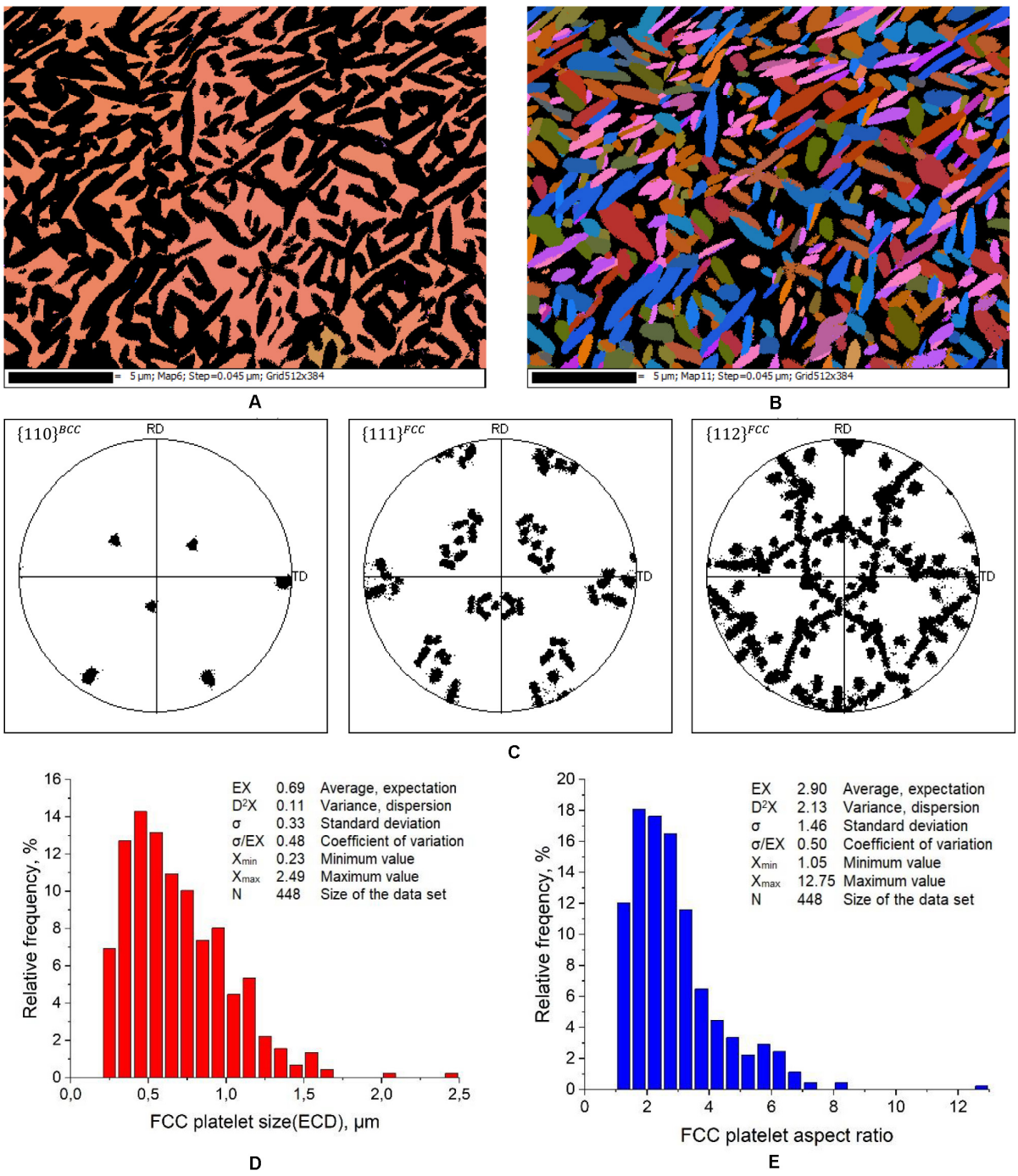

FIGURE 8 | OR in the $AlCrFe_2Ni_2$ 950°C-6 h heat treated coupon. Euler maps of the **(A)** BCC phase and **(B)** FCC phase showing the varied orientations of the FCC microplatelets. **(C)** The {110} BCC, {111}, and {112} FCC pole figures with the obtained N–W variants. **(D)** The FCC microplatelet size, and **(E)** aspect ratio distributions.

applies and that certainly all of its 12 variants are present. The family of common planes and directions of the N–W OR are:

$$\{111\}^{FCC}$$

$$\langle 11\bar{2}\rangle^{FCC}$$

The full symmetry of the {111} and {112} pole figures is a fingerprint of the fact that all variants are present. This result is remarkable, showing that colony formation and variant selection can be avoided along this transformation pathway, even if FCC is present along grain boundaries in the parent, metastable BCC (as-built). This strongly supports the idea that the spinodal interfaces provide a high number of nucleation sites with a low energy barrier for FCC nucleation. The microplatelet size distribution based on the equivalent circle diameter (ECD), as well as the aspect ratio distribution, can be seen in **Figures 8D,E** for the 950°C-6 h heat treated coupon. The FCC platelets were in the submicron scale and together with the BCC matrix, they formed an ultrafine duplex microstructure. It should be noted that similar pole figures were obtained in the EBSD analysis of a single grain of the 850°C-3 h heat treated coupon, suggesting the presence of all N–W variants already at lower heat treatment temperatures.

The heat treatment study showed that the LPBF process provides unique means to obtain ultrafine or even nanoscale duplex microstructures after heat treatment below 950°C thanks to the formation of FCC platelets from metastable BCC parent grains that have undergone a spinodal decomposition. Prolonged heat treatment at 900°C or higher resulted in significant coarsening of the spinodal structure and partial dissolution of the A2 phase from within the spinodal BCC matrix. The use of a metastable AM microstructure to control the secondary precipitation through subsequent heat treatment is a unique processing path for the $AlCrFe_2Ni_2$ HEA.

Mechanical Properties of the Heat Treated $AlCrFe_2Ni_2$

The mechanical response of the heat treated specimens (30 mm × 5 mm × 1.6 mm) was studied via three-point bending tests. Given the small thickness required for the test specimens crack-free material was extracted by WEDM. The extracted specimens were visually inspected before testing to ensure the absence of cracks. The obtained flexural stress-strain curves are presented in **Figure 9A**. The presented curves are averages from at least three tests. The HEA was not tested in the as-built condition, due to early brittle failure. A super duplex steel (EN 1.4517) was tested as reference material. The curves presented an elastic region followed by plastic deformation with significant work hardening. Compared to the reference material, the heat treated HEA specimens showed significant strain hardening ability and higher flexural strength. However, the super duplex steel showed slightly greater flexural proof stress (1031 MPa) compared to the 900°C-6 h (985 MPa) and 950°C-6 h (851 MPa) heat treated HEA specimens. The 750°C-3 h and 800°C-3 h heat treated specimens showed flexural strength as high as ∼3000 and 2800 MPa but failed relatively early during the test, at fracture strains of 10–16%. The 850°C-3 h heat treated specimen retained high flexural strength at 2805 MPa and exhibited greater fracture strain at 18.9%. However, the fracture strain was much lower than the reference material which did not fail and reached the strain limit of the testing device (21%). The 900°C-6 h heat treated specimens exhibited the best combination of flexural strength and strain among all tested conditions. The calculated flexural strength was 2051 MPa and the specimen reached the strain limit of the device without failing, while the super duplex steel specimen showed significantly lower flexural strength at 1632 MPa without failing. Therefore, it can be said that the 900°C-6 h annealing heat treatment led to the $AlCrFe_2Ni_2$ outperforming the reference material in terms of flexural strength in the three-point bending test. However, since those specimens did not fail during the test and exceeded the strain limit of the device, their ductility cannot be directly compared. As of the 950°C-6 h heat treated specimen, a significant decrease in flexural strength was observed compared to the 900°C-6 h. The specimen did not fail during the test but did not exceed the flexural strength of the reference material considerably. The decrease in strength observed in the 950°C-6 h heat treated specimen could be attributed to the coarsening of the microstructure, specifically the coarsening of the spinodal structure inside the BCC matrix along with a partial dissolution of the A2 phase which was described in section "Microstructural Analysis of the Heat Treated $AlCrFe_2Ni_2$".

Based on the obtained curves from all conditions and the phase fractions obtained by EBSD for the HEA specimens, it was seen that the increase of the FCC phase fraction in the microstructure also increased the ductility while decreasing the flexural strength. The specimens that were heat treated at lower temperatures and less time (750, 800, and 850°C-3 h) retained the spinodal decomposition of the BCC phase in their microstructure and exhibited remarkably high flexural strength. However, they underwent early failure in the test. Longer annealing times at higher temperatures led to microstructures with excessively coarse spinodal structure and the Fe-, Cr- rich A2 phase being partially dissolved. Optimum parameters for an annealing heat treatment thus range from 850 to 900°C for durations from 3 to 6 h, followed by air cooling or furnace cooling. Without being shown here in detail it is important to remark that ideally specimens should be introduced into the preheated furnace or heated up as rapidly as possible to the nominal annealing temperature. These procedures ensure that all nucleation sites are exploited at best and with an equal driving force, which leads to a homogeneous microstructure.

The heat treated specimens were also tested for microhardness. The microhardness values and the FCC percentage in the microstructure of each specimen can be seen in **Figure 9B**. Increased FCC percentage in the microstructure resulted in a decrease in the hardness. However, the hardness of the $AlCrFe_2Ni_2$ was higher compared to the reference material for all tested conditions. From the $AlCrFe_2Ni_2$ measurements, the 950°C-6 h specimen exhibited the lowest hardness at 303 HV and the highest FCC percentage at 63% in the microstructure. A detailed overview of the flexural and hardness properties obtained from the tests and the respective phase fractions in the microstructures measured by EBSD is presented in **Table 4**.

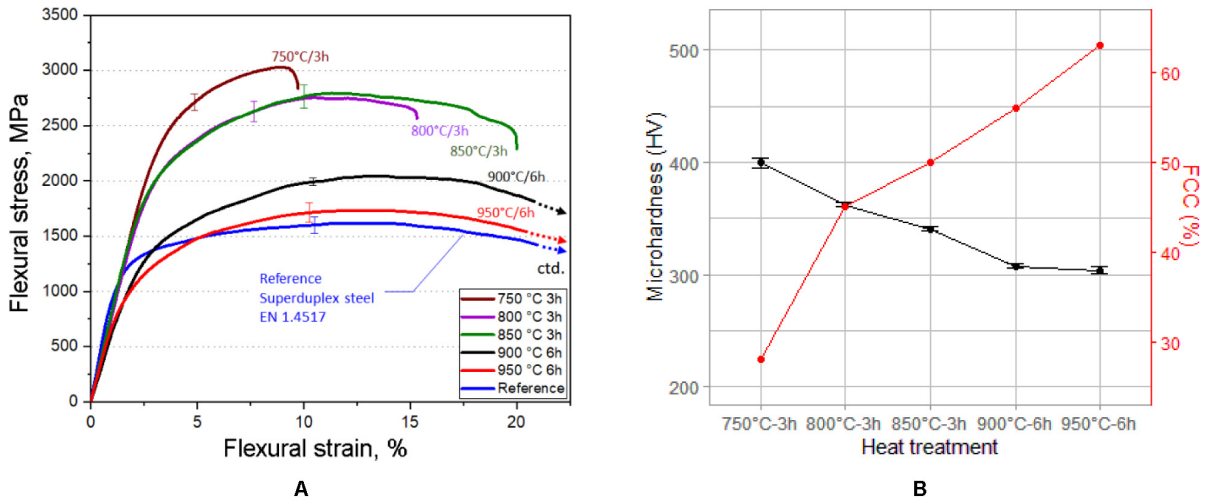

FIGURE 9 | (A) Flexural stress-strain curves, **(B)** microhardness and FCC percentage of the $AlCrFe_2Ni_2$ after heat treatment.

TABLE 4 | Mechanical properties based on three-point bending and microhardness tests, including phase percentages in the microstructure measured by EBSD.

Coupon	BCC%	FCC%	Proof stress Rp.02 (MPa)	Flexural strength (MPa)	Flexural strain (%)	Hardness (HV1)
As-built	95	5				483 ± 8
750°C 3 h	72	28	2108 ± 141	3046 ± 99	10.9 ± 1.2	399 ± 5
800°C 3 h	55	45	1785 ± 22	2760 ± 82	16.5 ± 1.3	362 ± 2
850°C 3 h	50	50	1691 ± 47	2805 ± 94	18.9 ± 1.1	341 ± 2
900°C 6 h	44	56	985 ± 47	2051 ± 24	>21	307 ± 2
950°C 6 h	37	63	851 ± 52	1735 ± 73	>21	304 ± 3
EN 1.4517	38	62	1031 ± 70	1633 ± 76	>21	276 ± 2

CONCLUSION

In this study, a Co-free alloy with a composition close to $AlCrFe_2Ni_2$ was prepared by LPBF for the first time to the best of the authors' knowledge. A major issue in the LPBF processing of $AlCrFe_2Ni_2$ was cracking that was observed in intergranular sites. However, dense specimens suitable for mechanical testing such as three-point bending and microhardness were successfully obtained with baseplate preheating to mitigate thermo-mechanical stresses. The alloy retained a metastable structure in the as-built condition, mainly consisting of a spinodally decomposed BCC phase. Distinct heat treatment conditions were applied to investigate the precipitation of the FCC phase from the parent BCC and its influence on mechanical properties. The following conclusions are presented:

(i) Prealloyed HEA powder can be atomized based on the $AlCrFe_2Ni_2$ composition with spherical particles and PSD suitable for LPBF processing.
(ii) Processing the $AlCrFe_2Ni_2$ with LPBF requires high preheating of the baseplate to obtain bulk material suitable for mechanical testing.
(iii) The microstructure of the as-built $AlCrFe_2Ni_2$ is metastable. It consists of columnar BCC grains with nanoscale spinodal decomposition B2 and A2 structures and grains that are parallel to the build direction with near <001>texture. For the applied hatching strategy and build parameters, a cube texture is expected.
(iv) Based on the observations from the heat treatment studies, increasing the treatment temperature and time allows reaching equilibrium values (i.e., 63% FCC), while FCC fractions remain below the equilibrium values if temperature and/or time are too low. Notably, the FCC phase is precipitating as microplatelets, thus leading to an ultrafine and homogeneous duplex microstructure. Furthermore, the FCC microplatelets display all crystal orientations compatible with the N–W OR. All crystallographic variants are present and randomly distributed, such that the overall texture is mitigated. Colony formation is suppressed because the spinodal structure of the parent BCC provides a high density of nucleation sites.
(v) The optimum annealing heat treatment parameters range from 850 to 900°C for 3 to 6 h. In these conditions, the HEA's strength is superior to the super-duplex steel EN 1.4517, while a good balance between strength and ductility is achieved. Further mechanical and corrosion tests are due to characterize the property profile and envisage application cases.

DATA AVAILABILITY STATEMENT

The raw data supporting the conclusions of this article will be made available by the authors, without undue reservation.

AUTHOR CONTRIBUTIONS

DV designed the experiments, analyzed the powder, the bulk material, and the results obtained from all measurements and tests presented in this manuscript. AE carried out EBSD measurements and took part in the SEM investigation. MP contributed to the planning of the work and supervision of the actions. SG carried out the three-point bending tests. VM and AW carried out screening builds toward baseplate preheating temperature selection. All authors contributed to the article and approved the submitted version.

FUNDING

This research was supported by the German Federal Ministry for Education and Research (BMBF) under grant number 03XP0163D in the frame of the M-era.Net Joint Call 2017, Project NADEA (no. 5129).

ACKNOWLEDGMENTS

The authors kindly thank Otto Junker GmbH for providing the super-duplex steel EN 1.4517 (ASTM A890 Grade 1C) in the cast and fully heat treated condition to serve as reference material.

REFERENCES

Amato, K. N., Gaytan, S. M., Murr, L. E., Martinez, E., Shindo, P. W., Hernandez, J., et al. (2012). Microstructures and mechanical behavior of Inconel 718 fabricated by selective laser melting. *Acta Mater.* 60, 2229–2239. doi: 10.1016/j.actamat.2011.12.032

Aribo, S., Barker, R., Hu, X., and Neville, A. (2013). Erosion-corrosion behaviour of lean duplex stainless steels in 3.5% NaCl solution. *Wear* 302, 1602–1608. doi: 10.1016/j.wear.2012.12.007

Azizi, H., Zurob, H., Bose, B., Reza Ghiaasiaan, S., Wang, X., Coulson, S., et al. (2018). Additive manufacturing of a novel Ti-Al-V-Fe alloy using selective laser melting. *Addit. Manuf.* 21, 529–535. doi: 10.1016/j.addma.2018.04.006

Bachmann, F., Hielscher, R., and Schaeben, H. (2010). Texture analysis with MTEX- Free and open source software toolbox. *Solid State Phenom.* 160, 63–68. doi: 10.4028/www.scientific.net/ssp.160.63

Brif, Y., Thomas, M., and Todd, I. (2015). The use of high-entropy alloys in additive manufacturing. *Scr. Mater.* 99, 93–96. doi: 10.1016/j.scriptamat.2014.11.037

Chai, G., and Kangas, P. (2017). Recent developments of advanced austenitic and duplex stainless steels for oil and gas industry. *Energy Mater.* 2014, 703–709. doi: 10.1007/978-3-319-48765-6_85

Charles, J. (2008). Duplex stainless steels, a review after DSS'07 in Grado. *Rev. Métallurgie* 105, 155–171. doi: 10.1051/metal:2008028

Davidson, K., and Singamneni, S. (2016). Selective laser melting of duplex stainless steel powders: an investigation. *Mater. Manuf. Process.* 31, 1543–1555 doi: 10.1080/10426914.2015.1090605

Dong, Y., Gao, X., Lu, Y., Wang, T., and Li, T. (2016). A multi-component AlCrFe2Ni2 alloy with excellent mechanical properties. *Mater. Lett.* 169, 62–64. doi: 10.1016/j.matlet.2016.01.096

Hengsbach, F., Koppa, P., Duschik, K., Holzweissig, M. J., Burns, M., Nellesen, J., et al. (2017). Duplex stainless steel fabricated by selective laser melting - Microstructural and mechanical properties. *Mater. Des.* 133, 136–142. doi: 10.1016/j.matdes.2017.07.046

Hooper, P. A. (2018). Melt pool temperature and cooling rates in laser powder bed fusion. *Addit. Manuf.* 22, 548–559. doi: 10.1016/j.addma.2018.05.032

Jiang, Z., Chen, W., Xia, Z., Xiong, W., and Fu, Z. (2019). Influence of synthesis method on microstructure and mechanical behavior of Co-free AlCrFeNi medium-entropy alloy. *Intermetallics* 108, 45–54. doi: 10.1016/j.intermet.2019.02.006

Joseph, J., Jarvis, T., Wu, X., Stanford, N., Hodgson, P., and Fabijanic, D. M. (2015). Comparative study of the microstructures and mechanical properties of direct laser fabricated and arc-melted AlxCoCrFeNi high entropy alloys. *Mater. Sci. Eng. A* 633, 184–193. doi: 10.1016/j.msea.2015.02.072

Joseph, J., Stanford, N., Hodgson, P., and Fabijanic, D. M. (2017). Understanding the mechanical behaviour and the large strength/ductility differences between FCC and BCC AlxCoCrFeNi high entropy alloys. *J. Alloys Compd.* 726, 885–895. doi: 10.1016/j.jallcom.2017.08.067

Kao, Y.-F., Chen, T.-J., Chen, S.-K., and Yeh, J.-W. (2009). Microstructure and mechanical property of as-cast, -homogenized, and -deformed AlxCoCrFeNi (0=x=2) high-entropy alloys. *J. Alloys Compd.* 488, 57–64. doi: 10.1016/j.jallcom.2009.08.090

Kempen, K., Vrancken, B., Buls, S., Thijs, L., Van Humbeeck, J., and Kruth, J.-P. (2014). Selective laser melting of crack-free high density M2 high speed steel parts by baseplate preheating. *J. Manuf. Sci. Eng.* 136:061026. doi: 10.1115/1.4028513

Knyazeva, M., and Pohl, M. (2013). Duplex steels: part i: genesis, formation, structure. *Metallogr. Microstruct. Anal.* 2, 113–121. doi: 10.1007/s13632-013-0066-8

Koutny, D., Palousek, D., Pantelejev, L., Hoeller, C., Pichler, R., Tesicky, L., et al. (2018). Influence of scanning strategies on processing of aluminum alloy EN AW 2618 using selective laser melting. *Materials* 11:298. doi: 10.3390/ma11020298

Kuwabara, K., Shiratori, H., Fujieda, T., Yamanaka, K., Koizumi, Y., and Chiba, A. (2018). Mechanical and corrosion properties of AlCoCrFeNi high-entropy alloy fabricated with selective electron beam melting. *Addit. Manuf.* 23, 264–271. doi: 10.1016/j.addma.2018.06.006

Li, R., Niu, P., Yuan, T., Cao, P., Chen, C., and Zhou, K. (2018). Selective laser melting of an equiatomic CoCrFeMnNi high-entropy alloy: processability, non-equilibrium microstructure and mechanical property. *J. Alloys Compd.* 746, 125–134. doi: 10.1016/j.jallcom.2018.02.298

Li, W., Chen, X., Yan, L., Zhang, J., Zhang, X., and Liou, F. (2018). Additive manufacturing of a new Fe-Cr-Ni alloy with gradually changing compositions with elemental powder mixes and thermodynamic calculation. *Int. J. Adv. Manuf. Technol.* 95, 1013–1023. doi: 10.1007/s00170-017-1302-1

Mertens, R., Dadbakhsh, S., Van Humbeeck, J., and Kruth, J. P. (2018). Application of base plate preheating during selective laser melting. *Proc. CIRP* 74, 5–11. doi: 10.1016/j.procir.2018.08.002

Miracle, D. B., and Senkov, O. N. (2017). A critical review of high entropy alloys and related concepts. *Acta Mater.* 122, 448–511. doi: 10.1016/j.actamat.2016.08.081

Nair, R. B., Arora, H. S., Mukherjee, S., Singh, S., Singh, H., and Grewal, H. S. (2018). Exceptionally high cavitation erosion and corrosion resistance of a high entropy alloy. *Ultrason. Sonochem.* 41, 252–260. doi: 10.1016/j.ultsonch.2017.09.044

Ni, M., Chen, C., Wang, X., Wang, P., Li, R., Zhang, X., et al. (2017). Anisotropic tensile behavior of in situ precipitation strengthened Inconel 718 fabricated by additive manufacturing. *Mater. Sci. Eng. A* 701, 344–351. doi: 10.1016/j.msea.2017.06.098

Nilsson, J.-O. (1992). Super duplex stainless steels. *Mater. Sci. Technol.* 8, 685–700. doi: 10.1179/mst.1992.8.8.685

Niu, P. D., Li, R. D., Yuan, T. C., Zhu, S. Y., Chen, C., Wang, M. B., et al. (2019). Microstructures and properties of an equimolar AlCoCrFeNi high entropy alloy printed by selective laser melting. *Intermetallics* 104, 24–32. doi: 10.1016/j.intermet.2018.10.018

Poletti, M. G., Fiore, G., Gili, F., Mangherini, D., and Battezzati, L. (2017). Development of a new high entropy alloy for wear resistance: FeCoCrNiW0.3 and FeCoCrNiW0.3 + 5 at.% of C. *Mater. Des.* 115, 247–254. doi: 10.1016/j.matdes.2016.11.027

Porter, D. A., Easterling, K. E., and Sherif, M. Y. (2009). *Phase Transformations in Metals and Alloys, Third Edition*. Cheltenham: Nelson Thornes Ltd.

Pozdniakov, A. V., Churyumov, A. Y., Loginova, I. S., Daubarayte, D. K., Ryabov, D. K., and Korolev, V. A. (2018). Microstructure and properties of novel AlSi11CuMn alloy manufactured by selective laser melting. *Mater. Lett.* 225, 33–36. doi: 10.1016/j.matlet.2018.04.077

Qin, G., Xue, W., Fan, C., Chen, R., Wang, L., Su, Y., et al. (2018). Effect of Co content on phase formation and mechanical properties of (AlCoCrFeNi)100-xCox high-entropy alloys. *Mater. Sci. Eng. A* 710, 200–205. doi: 10.1016/j.msea.2017.10.088

Qiu, C., Adkins, N. J. E., and Attallah, M. M. (2016). Selective laser melting of Invar 36: microstructure and properties. *Acta Mater.* 103, 382–395. doi: 10.1016/j.actamat.2015.10.020

Sistla, H. R., Newkirk, J. W., and Frank Liou, F. (2015). Effect of Al/Ni ratio, heat treatment on phase transformations and microstructure of Al<inf>*x*</inf>FeCoCrNi<inf>*2-x*</inf> (x=0.3, 1) high entropy alloys. *Mater. Des.* 81, 113–121. doi: 10.1016/j.matdes.2015.05.027

Wang, W. R., Wang, W. L., Wang, S. C., Tsai, Y. C., Lai, C. H., and Yeh, J. W. (2012). Effects of Al addition on the microstructure and mechanical property of Al xCoCrFeNi high-entropy alloys. *Intermetallics* 26, 44–51. doi: 10.1016/j.intermet.2012.03.005

Yan, F., Xiong, W., and Faierson, E. J. (2017). Grain structure control of additively manufactured metallic materials. *Materials* 10:1260. doi: 10.3390/ma10111260

Yap, C. Y., Chua, C. K., Dong, Z. L., Liu, Z. H., Zhang, D. Q., Loh, L. E., et al. (2015). Review of selective laser melting: materials and applications. *Appl. Phys. Rev.* 2:041101. doi: 10.1063/1.4935926

Yeh, J.-W. (2006). Recent progress in high-entropy alloys. *Ann. Chim. Sci. des Matériaux* 31, 633–648. doi: 10.3166/acsm.31.633-648

Yeh, J. W., Chen, S. K., Lin, S. J., Gan, J. Y., Chin, T. S., Shun, T. T., et al. (2004). Nanostructured high-entropy alloys with multiple principal elements: novel alloy design concepts and outcomes. *Adv. Eng. Mater.* 6, 299–303. doi: 10.1002/adem.200300567

Yin, Y., Zhang, J., Tan, Q., Zhuang, W., Mo, N., Bermingham, M., et al. (2019). Novel cost-effective Fe-based high entropy alloys with balanced strength and ductility. *Mater. Des.* 162, 24–33. doi: 10.1016/j.matdes.2018.11.033

Zeng, J., Wu, C., Peng, H., Liu, Y., Wang, J., and Su, X. (2018). Microstructure and microhardness of as-cast and 800°C annealed AlxCr0.2*Fe*0.2Ni0.6-x and Al0.2Cr0.2FeyNi0.6-y alloys. *Vacuum* 152, 214–221. doi: 10.1016/j.vacuum.2018.03.035

Zhang, C., Zhang, F., Diao, H., Gao, M. C., Tang, Z., Poplawsky, J. D., et al. (2016). Understanding phase stability of Al-Co-Cr-Fe-Ni high entropy alloys. *Mater. Des.* 109, 425–433. doi: 10.1016/j.matdes.2016.07.073

Zhang, D., Feng, Z., Wang, C., Wang, W., Liu, Z., and Niu, W. (2018). Comparison of microstructures and mechanical properties of Inconel 718 alloy processed by selective laser melting and casting. *Mater. Sci. Eng. A* 724, 357–367. doi: 10.1016/j.msea.2018.03.073

Zhang, M., Zhou, X., Wang, D., Zhu, W., Li, J., and Zhao, Y. F. (2019). AlCoCuFeNi high-entropy alloy with tailored microstructure and outstanding compressive properties fabricated via selective laser melting with heat treatment. *Mater. Sci. Eng. A* 743, 773–784. doi: 10.1016/j.msea.2018.11.118

Zhou, P. F., Xiao, D. H., Wu, Z., and Ou, X. Q. (2019). $Al_{0.5}$FeCoCrNi high entropy alloy prepared by selective laser melting with gas-atomized pre-alloy powders. *Mater. Sci. Eng. A* 739, 86–89. doi: 10.1016/j.msea.2018.10.035

Zhou, Y. J., Zhang, Y., Wang, Y. L., and Chen, G. L. (2007). Microstructure and compressive properties of multicomponent Alx(TiVCrMnFeCoNiCu)100-x high-entropy alloys. *Mater. Sci. Eng. A* 454–455, 260–265. doi: 10.1016/j.msea.2006.11.049

Conflict of Interest: DV, AE, and MP were employed by the company Oerlikon AM GmbH.

The remaining authors declare that the research was conducted in the absence of any commercial or financial relationships that could be construed as a potential conflict of interest.

frontiers in Materials

PERSPECTIVE
published: 30 July 2020
doi: 10.3389/fmats.2020.00238

Influence of Solidification Microstructure on Mechanical Properties of $Al_{0.8}CrCuFeNi_2$ High Entropy Alloy

Julien Zollinger[1,2]* *and Eric Fleury*[2,3]

[1] Department of Metallurgy & Materials Science and Engineering, Institut Jean Lamour, Université de Lorraine, Nancy, France,
[2] Laboratory of Excellence on Design of Alloy Metals for low-mAss Structures (DAMAS), Université de Lorraine, Metz, France,
[3] Université de Lorraine, CNRS, Arts et Métiers ParisTech, LEM3, Metz, France

The solidification microstructure of $Al_{0.8}CrCuFeNi_2$ high entropy alloy consists of primary fcc dendrites decorated with interdendritic bcc and B2 phases. In this work the mechanical properties obtained for columnar oriented growth and equiaxed microstructures are compared. Highest properties are obtained for columnar structures when loading is parallel to the growth direction due to confinement of the deformation inside the columnar dendrite trunks.

Keywords: solidification, high entropy alloys, mechanical properties, microstructure, multi-phase alloys

OPEN ACCESS

Edited by:
Sheng Guo,
Chalmers University of Technology, Sweden

Reviewed by:
Yiping Lu,
Dalian University of Technology, China
Guillaume Reinhart,
Aix-Marseille Université, France

***Correspondence:**
Julien Zollinger
julien.zollinger@univ-lorraine.fr

Specialty section:
This article was submitted to Structural Materials, a section of the journal Frontiers in Materials

Received: *29 May 2020*
Accepted: *29 June 2020*
Published: *30 July 2020*

Citation:
Zollinger J and Fleury E (2020) Influence of Solidification Microstructure on Mechanical Properties of $Al_{0.8}CrCuFeNi_2$ High Entropy Alloy. Front. Mater. 7:238. doi: 10.3389/fmats.2020.00238

1. INTRODUCTION

High Entropy Alloys (HEAs) are equiatomic multicomponent alloys that form simple solid solutions without embrittling intermetallics compounds. Since the development of the HEAs concept (Cantor et al., 2004; Yeh et al., 2004), the probably most studied has been the CoCrFeMnNi alloy that exhibits a simple fcc crystal structure but very high mechanical properties down to cryogenic temperatures (Gludovatz et al., 2014). Many alloys are derived from it, replacing the problematic manganese and cobalt with other elements, such as copper, or increasing Ni of Fe content. Interestingly, alluminium additions allows to modify and tune the crystal structure from fcc to bcc (Tang et al., 2013). An increasing Al content in the alloy will change the fcc structure to a mixture of fcc and bcc, to a single bcc structure for higher additions, even in the as-cast state (Guo et al., 2013). Two-phase alloys are generally the most interesting owing to their superior mechanical properties that can be optimized by adjusting the volume fraction, size of dispersion of both phases.

In this work, a two-phases $Al_{0.8}CrCuFeNi_2$ alloy is investigated. This alloy starts to solidify with a fcc crystal structure, and due to microsegregation of alloying elements a bcc phase appears during solidification (Choudhuri et al., 2017). Under the usual casting conditions, the primary phase solidifies in the form of dendrites whose arms grow with the <100> directions parallel to the thermal gradient. When the thermal gradient is low enough, free growth can occur and lead to an equiaxed microstructure. The different mechanical properties resulting from these two types of microstructure is well-known since a long time in the field of Nickel-based superalloys (Versnyder and Shank, 1970) but has never been studied for HEAs. This paper shows the first results obtained for $Al_{0.8}CrCuFeNi_2$ alloy and with an emphasis on the effect of solidification microstructure anisotropy on the obtained microstructure and properties.

2. EXPERIMENTAL DETAILS

$Al_{0.8}CrCuFeNi_2$ alloys were prepared using a cold crucible induction melting furnace from commercial purity elements (>99.8%). Samples were cast using an Inducast tilt-caster into a cylindrical mold (20 mm diameter, 50 mm height) with alumina wall and a copper base, in order to achieve a directional solidification. With this set-up, the first 2 cm of alloy in contact with the copper shows a columnar zone while the top zone is fully equiaxed (see section 3). Three samples were prepared and cast, from which were machined $10 \times 10 \times 4$ mm^3 specimens for compression tests in both columnar and equiaxed zones. After standard metallographic preparation with colloidal silica finishing, SEM BSE images and EDS analyses were performed on a FEI Quanta 600 F FEG-SEM equipped with a Brücker Si-drift Quantax EDS detector. Samples were also examined by optical microscopy. Compression specimens were polished on one side prior to loading in order to observe the microstructure after deformation. Compression tests were made on a 50 kN MTS mechanical test system with a compression rate of 20 mm/min.

3. RESULTS AND DISCUSSION

Figure 1 shows the microstructure of the alloy at different locations and different magnifications. The columnar microstructure can be observed in **Figure 1a**, where the growth direction, parallel to the thermal gradient is indicated by the vertical arrow. It can be seen that the fcc phase primary arms, growing following the <100> direction in cubic metals are aligned with the thermal gradient. Dendrites are decorated with interdendritic secondary phases whose details are given in **Figure 1c**. While a single bcc phase was expected, some precipitates, visible in light gray on the BSE image and with typical size < 100 nm are also observed. This microstructure is similar to those observed by Guo et al. (2017) where the precipitates are identified as a Fe and Cr rich bcc phase while the interdendritic matrix consists of an Al and Ni rich B2 ordered structure. **Figure 1b** presents the microstructure observed in the equiaxed region, where the typical grain size is around 40 μm. Except for its morphology, the phases are the same as in the columnar zone, with fcc equiaxed grains decorated with a mixture of bcc and B2 phases as shown in **Figure 1d**. It is interesting to note that the primary arms spacing in the columnar zone and the grain size of the equiaxed region take very similar values. Since primary arm spacing depends on thermal gradient and interface velocity, and equiaxed grain size varies mainly with undercooling and number of potent nucleants, this is rather fortuitous but result in microstructures having similar characteristic lengths as well as secondary phases size and distribution. Moreover, the fraction of secondary

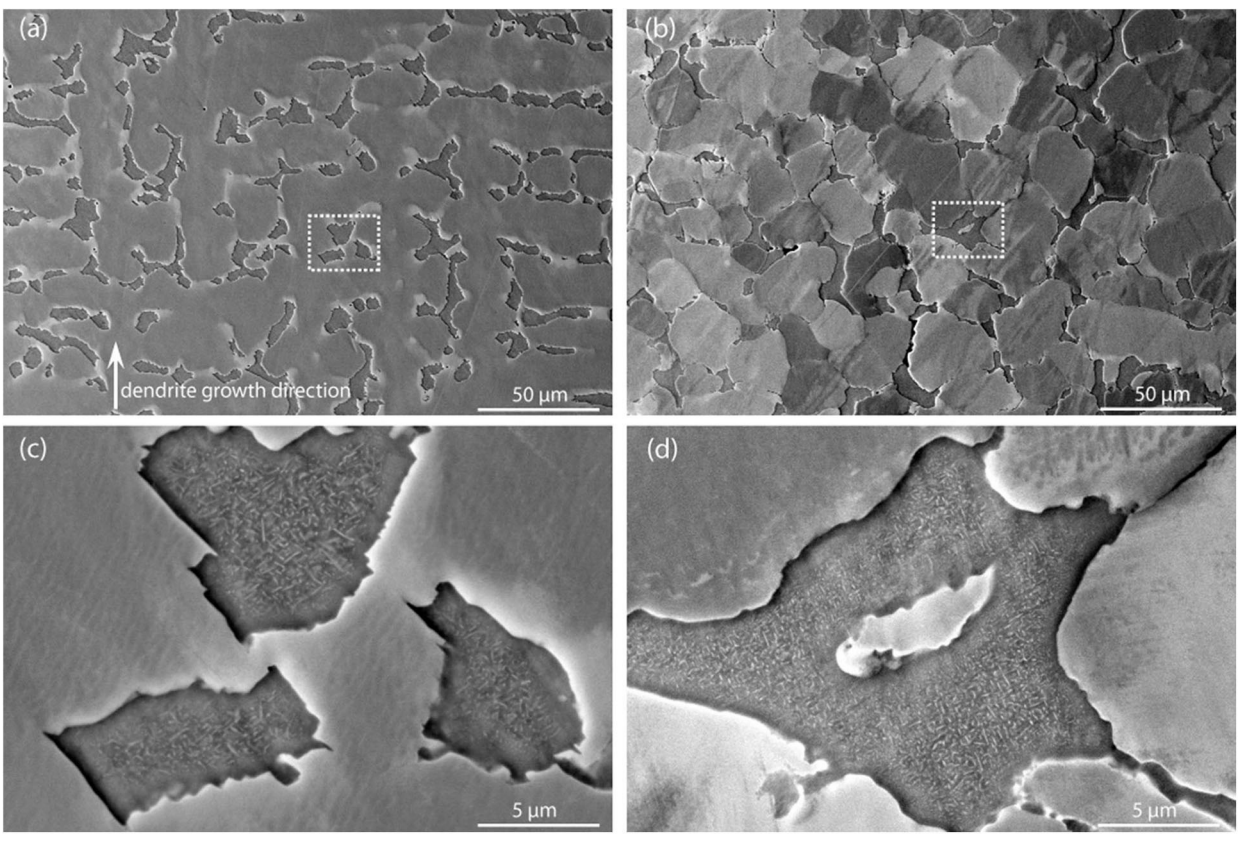

FIGURE 1 | As cast microstructures: **(a)** columnar zone and **(b)** equiaxed zone of the ingot. **(c,d)** shows higher magnification images of the interdendritic regions corresponding to the dashed rectangles in **(a,b)**, respectively.

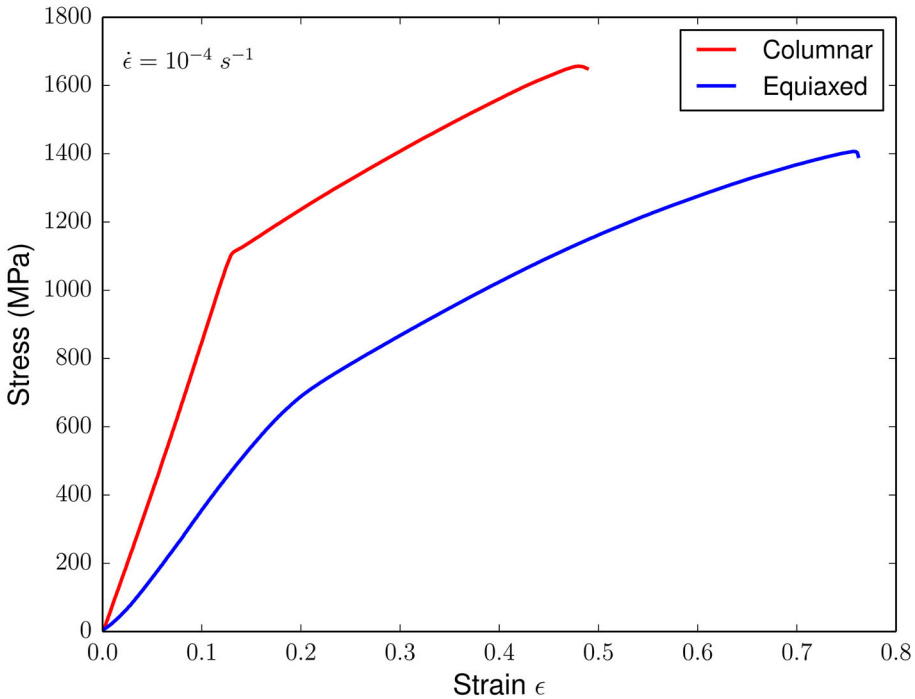

FIGURE 2 | Typical strain-stress curves obtained for the columnar and equiaxed structures. For columnar samples, the loading direction is parallel to the growth direction.

TABLE 1 | Average values obtained from the compression and hardness tests (S.D., standard deviation deduced from the three specimens tested for each type of microstructure).

Microsctructure	Young Modulus E (GPa)	Y_s (MPa)	$R_{p0.2}$ (MPa)	R_m (Mpa)	Hardness (HV_{30})
Equiaxed	132	650	832	1,406	345
(S.D.)	(2)	(42)	(81)	(145)	(5)
Columnar	292	1,050	1,350	1,656	341
(S.D.)	(20)	(70)	(140)	(155)	(5)

phases, determined by image analysis and supplemented by microsegregation analyzes is also very close in the two types of microstructures, and are 20.7 ± 1.1 and 18.6 ± 0.8% for the columnar and equiaxed zone, respectively.

The uniaxial compression properties obtained for both columnar and equiaxed structures are presented in **Figure 2**, and values of the mechanical properties have been summarized in **Table 1**. For this two-phase alloy, the directionally solidified structure displayed superior mechanical properties in terms of Young's modulus, yield strength, and maximum compression strength in comparison to the equiaxed structure. In contrast the total plastic deformation accommodated by the alloy with directionally solidified structure is slightly reduced, while the work-hardening are found to be similar. The hardness takes similar values for both microstructure, and has been measured perpendicularly to the growth direction in the columnar sample. The crystallographic texture is less pronounced in this direction since directionally solidified alloys usually have a fiber type texture. This result shows that intrinsic phases properties between the two types of microstructure are similar. For nickel-based superalloy, Versnyder and Shank (1970) reported superior values of the room temperature strength for directionally solidified structure in comparison to equiaxed structure. However, in comparison to nickel-based superalloy that are composed of two phases having similar lattice parameters and identical crystallographic orientation, the microstructure obtained in this directionally solidified alloy is more complex since the interdendritic region is misoriented in comparison to the dendrites. Indeed, the fcc and bcc/B2 phases formed during solidification are related through Kurdjumov-Sachs orientation relationships, as shown by Borkar et al. (2016). These differences in crystallographic orientation can induce additional local internal stresses that can play a role in strengthening properties and explain the properties obtained in this study.

Figures 3a,b shows the microstructure after loading in the columnar and equiaxed regions, respectively. The corresponding inserts show OM micrographs obtained at low magnification.

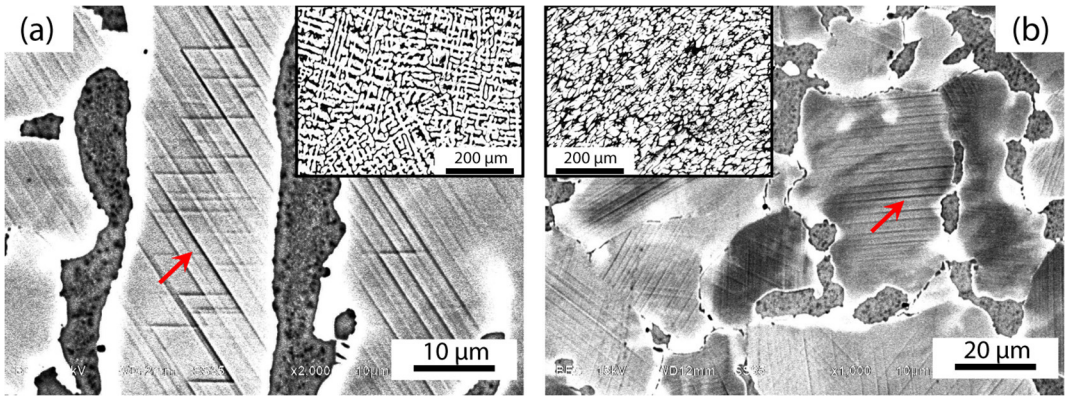

FIGURE 3 | Post-loading microstructures in **(a)** columnar and **(b)** equiaxed regions where sliding planes (some are indicated with a red arrow) are clearly visible. The small inserts show OM micrographs of the samples after loading tests.

Two observations can be made from this figure. The first one concerns the slipping planes that can be observed in both figures but in the fcc phase only. It means that most of the strain is solely accommodated by the fcc phase. A second observation is related to the orientation anisotropy inherent to columnar dendritic structures: the sliding planes in **Figure 3a** all have the same orientation, because all the dendrites arms are oriented along the <100> direction. The number of slip systems is thus limited in this type of microstructure, but also constrained by the interdendritic bcc/B2 phases. This lead to this "stair-like" slipping plane visible in the figure. In **Figure 3b**, the equiaxed grains which have a random orientation show, per grain, one, sometimes two sliding planes of different crystallographic orientation. The observable slip planes thus have a different orientation in each grain. The macroscopic consequence of the difference between columnar and equiaxed zone can be seen in the inserts in **Figures 3a,b**: while the columnar zone does not seem very different from the initial one, the equiaxed microstructure is visibly deformed after the compression test. For the samples with directionally solidified structure tested along the <001> crystallographic orientation, eight slip systems can theoretically be activated if the uniaxial applied stress is larger than CRSS/m, CRSS being the critical resolved shear stress and m the Schmid factor, which is about 0.40 in this case. This large number of activated system is expected to lead to a strong hardening and a limited plastic deformation (Meyers and Chawla, 2008). On the other hand in the samples with an equiaxed structure, each grain with a random orientation will tend to deform plastically according the same relation CRSS/m. However the number of activated slip system is more likely to be limited to 1 (ex: grain oriented along the <123> direction or <153> direction), 2 (ex: grain oriented along <112> direction), 4 (ex: grain oriented along <101> direction), etc., with values of the Schmid factor larger than 0.4. The important number of randomly oriented equiaxed grains (6.4 10^7 grains/cm^3 for a grain size of 25 μm) is favorable for the plastic deformation through activation of single slip system compared to the columnar microstructure. The highest strength and lowest ductility of directionally solidified samples thus comes from the interaction between different slip systems in the fcc phase compared to samples with an equiaxed structure. It is remarkable that no slip system can be observed in the B2 phases suggesting that this phase play the role of reinforcement in this alloy. Further analyses should be carry on to study thoroughly the interaction between both face-centered, disordered and ordered body-centered cubic phases.

4. CONCLUSIONS

The influence of the solidification microstructure on mechanical response of $Al_{0.8}CrCuFeNi_2$ alloy containing fcc and bcc/B2 phases was investigated. Both microstructures contain the same amount of bcc/B2 phases in the interdendritic region. The following conclusions can be drawn:

- When tested under uniaxial compression mode with the loading axis parallel to the direction of solidification, the columnar microstructure, with a preferred orientation of the fcc phase toward the <100> direction exhibits higher mechanical properties than the equiaxed microstructures with fcc grains randomly oriented.
- From the current observation slip is visible in the fcc phase only, and the superior mechanical properties measured for the oriented microstructure are due to a limited number of slipping plane constrained by the interdendritic bcc/B2 region.

DATA AVAILABILITY STATEMENT

The raw data supporting the conclusions of this article will be made available by the authors, without undue reservation.

AUTHOR CONTRIBUTIONS

JZ contributed conception, design of the study, and wrote the first draft of the manuscript. JZ and EF wrote sections of the

manuscript. All authors contributed to manuscript revision, read and approved the submitted version.

FUNDING

This work was also supported by the French State through the program Investment in the future operated by the National Research Agency (ANR) and referenced by ANR-11-LABX-0008-01 (LabEx DAMAS).

ACKNOWLEDGMENTS

JZ would like to thank A. Richy, E. Aguinaco, C. Begouin, C. Bernillon, E. Coma Prieto, and A. Dyja for their technical support.

REFERENCES

Borkar, T., Gwalani, B., Choudhuri, D., Mikler, C., Yannetta, C., Chen, X., et al. (2016). A combinatorial assessment of $Al_xCrCuFeNi_2$ ($0< x <1.5$) complex concentrated alloys: microstructure, microhardness, and magnetic properties. *Acta Mater.* 116, 63–76. doi: 10.1016/j.actamat.2016.06.025

Cantor, B., Chang, I., Knight, P., and Vincent, A. (2004). Microstructural development in equiatomic multicomponent alloys. *Mater. Sci. Eng. A* 375, 213–218. doi: 10.1016/j.msea.2003.10.257

Choudhuri, D., Gwalani, B., Gorsse, S., Mikler, C., Ramanujan, R., Gibson, M., et al. (2017). Change in the primary solidification phase from fcc to bcc-based b2 in high entropy or complex concentrated alloys. *Scripta Mater.* 127, 186–190. doi: 10.1016/j.scriptamat.2016.09.023

Gludovatz, B., Hohenwarter, A., Catoor, D., Chang, E. H., George, E. P., and Ritchie, R. O. (2014). A fracture-resistant high-entropy alloy for cryogenic applications. *Science* 345, 1153–1158. doi: 10.1126/science.1254581

Guo, L., Wu, W., Ni, S., Wang, Z., and Song, M. (2017). Effects of annealing on the microstructural evolution and phase transition in an $AlCrCuFeNi_2$ high-entropy alloy. *Micron* 101, 69–77. doi: 10.1016/j.micron.2017.06.007

Guo, S., Ng, C., and Liu, C. T. (2013). Anomalous solidification microstructures in Co-free $Al_xCrCuFeNi_2$ high-entropy alloys. *J. Alloys Compd.* 557, 77–81. doi: 10.1016/j.jallcom.2013.01.007

Meyers, M. A., and Chawla, K. K. (2008). *Mechanical Behavior of Materials*. Cambridge, UK: Cambridge University Press.

Tang, Z., Gao, M. C., Diao, H., Yang, T., Liu, J., Zuo, T., et al. (2013). Aluminum alloying effects on lattice types, microstructures, and mechanical behavior of high-entropy alloys systems. *JOM* 65, 1848–1858. doi: 10.1007/s11837-013-0776-z

Versnyder, F. I., and Shank, M. (1970). The development of columnar grain and single crystal high temperature materials through directional solidification. *Mater. Sci. Eng.* 6, 213–247. doi: 10.1016/0025-5416(70)90050-9

Yeh, J.-W., Chen, S.-K., Lin, S.-J., Gan, J.-Y., Chin, T.-S., Shun, T.-T., et al. (2004). Nanostructured high-entropy alloys with multiple principal elements: novel alloy design concepts and outcomes. *Adv. Eng. Mater.* 6, 299–303. doi: 10.1002/adem.200300567

Conflict of Interest: The authors declare that the research was conducted in the absence of any commercial or financial relationships that could be construed as a potential conflict of interest.

frontiers in Materials

ORIGINAL RESEARCH
published: 31 July 2020
doi: 10.3389/fmats.2020.00242

Alloy Design and Microstructure Evolution in the $Al_xCoCrFeNi$ Alloy System Synthesized by Laser Metal Deposition

Martin Kuczyk[1,2], Liliana Kotte[1], Jörg Kaspar[1], Martina Zimmermann[1,2] and Christoph Leyens[1,2]*

[1] Fraunhofer Institute for Material and Beam Technology IWS, Dresden, Germany, [2] Institute of Materials Science, Technische Universität Dresden, Dresden, Germany

In this contribution the $Al_xCoCrFeNi$ alloy system is explored thoroughly over a wide compositional range of $x = 0.2$ to 1.5 (5 to 30 at% Al). For this alloy system compositional gradient structures were produced by laser metal deposition of pre-alloyed CoCrFeNi and elemental Al powders using an in-house developed coaxial cladding system COAXpowerline. The evolution of the microstructure with increasing Al content was analyzed in the as built as well as the homogenized condition (1350 K for 20 h). Metallographic cross sections were prepared and thoroughly analyzed by means of scanning electron microscopy, energy dispersive X-ray spectroscopy, and electron backscattered diffraction. Additionally, the evolution of the sample hardness with increasing Al contents was determined for both sample conditions. In the $Al_xCoCrFeNi$ alloy system the lattice structure as well as the sample hardness can easily be adjusted by the variation of Al. With increasing Al content a phase transition from a solid solution fcc phase toward a multiphase bcc microstructure consisting of a Fe and Cr rich solid solution bcc phase and an ordered Al and Ni rich bcc B2 phase can be observed. This is combined with an increase in sample hardness from around 200 HV up to around 500 HV in the as built condition. The compositional regions of the phase transitions for both sample conditions were compared to ab initio thermodynamic calculations done using a CALPHAD approach. For the as built condition a strong deviation from the calculated transition regime could be observed. After homogenization the experimental and calculated data are in good agreement.

Keywords: additive manufacturing, laser metal deposition, high entropy alloys, high throughput screening, microstructure

OPEN ACCESS

Edited by:
Mark L. Weaver, The University of Alabama, United States

Reviewed by:
Sung Bo Lee, Seoul National University, South Korea
Liang-Yu Chen, Jiangsu University of Science and Technology, China

****Correspondence:***
Martin Kuczyk
martin.kuczyk@iws.fraunhofer.de

Specialty section:
This article was submitted to Structural Materials, a section of the journal Frontiers in Materials

Received: *29 April 2020*
Accepted: *01 July 2020*
Published: *31 July 2020*

Citation:
Kuczyk M, Kotte L, Kaspar J, Zimmermann M and Leyens C (2020) Alloy Design and Microstructure Evolution in the $Al_xCoCrFeNi$ Alloy System Synthesized by Laser Metal Deposition. Front. Mater. 7:242. doi: 10.3389/fmats.2020.00242

INTRODUCTION

In 2004 Yeh et al. (2004) and Cantor et al. (2004) suggested a new group of alloys, the so called high entropy alloys (HEA). Those alloys are usually comprized of five or more metals in near equimolar ratio to each other which maximizes their configurational entropy, hence the name high entropy alloy. The microstructure of those alloys usually consists of simple solid solution fcc (e.g., Cantor alloy and its derivates) or bcc phases (Senkov alloys and derivates). Numerous

works showed that HEA demonstrate promising mechanical as well as functional properties (Miracle and Senkov, 2017).

With the introduction of HEAs and in the further sense the introduction of compositionally complex alloys (CCAs)—which are derived by softening the condition of near equal ratio of the alloyed metals—a shear infinite space of possible interesting sample compositions open up. To explore this vast space of sample compositions, the development and use of effective high throughput screening strategies becomes more and more important (Marshal et al., 2017; Li et al., 2018). Amongst those methods additive manufacturing of samples by laser metal deposition (LMD) appears very promising. The fabrication by LMD is a very suitable manufacturing process for this group of alloys. It has already been established in several industrial branches with the purpose of coating, part refurbishment, but also for the manufacturing of functional 3D components (Leino et al., 2016). LMD is suitable for a broad spectrum of metals (e.g., Fe, Ni, Ti, or Co based alloys). By combining several powder feeders a variation of the composition within the manufactured structure is feasible and therefore well suited for the exploration and development of new material systems (Brueckner et al., 2018; Gwalani et al., 2019). Moreover the typically high cooling rates (10^3–10^5 Ks^{-1}) achieved during LMD are advantageous for a significant non-equilibrium solute trapping effect which prevents the segregation of components with differing melting points and counteracts the limitations associated with low solubility (Xiang et al., 2019). In addition, the deposition by LMD can be guided by ab initio thermodynamic calculations which help identifying interesting compositional regions (Haase et al., 2017).

The vast compositional space of HEAs and CCAs, which cannot be dealt with here, has been classified into seven alloy families (Miracle and Senkov, 2017). The group of 3d transition metals has been by far the most widely studied alloy family. Within this alloy family the $Al_xCoCrFeNi$ alloy system has been of particular interest over the past years. These alloys are thought to possess considerable potential for high-temperature structural applications because of their high strength and excellent corrosion resistance (Lim et al., 2017; Mohanty et al., 2019). Usually $Al_xCoCrFeNi$ alloys are manufactured by the conventional melting and casting route and the microstructure can easily be adjusted by the variation of the overall Al content. With the addition of Al the lattice structure transforms from a solid solution fcc phase to a dual phase bcc microstructure consisting of a Fe and Cr rich solid solution bcc (A2) and an Al and Ni rich ordered bcc B2 phase (Kao et al., 2009; Wang et al., 2012). The formation of the dual A2 + B2 bcc phases has been attributed to a spinodal decomposition process (Manzoni et al., 2013). In the as cast condition this transition takes place in the compositional range from $0.4 \leq x \leq 1.0$ (8–20 at% Al). With the addition of Al ($0 \leq x \leq 1.2$) and alongside the transition from fcc to bcc microstructure, the hardness of the alloy increases from about 120 HV to about 500 HV (Kao et al., 2009). Different studies indicate that the as cast microstructures of the Al-rich ($x \geq 1$) alloys are not stable at elevated temperatures (Wang et al., 2014; Munitz et al., 2016; Meshi et al., 2019). At temperatures above 923 K the dual A2 + B2 bcc structure decomposes into B2 + fcc + σ phase. Above 1250 K the σ phase dissolves leading to a mixture of A2 + B2 + fcc phases.

In 2015, for the first time additive manufacturing of AlCoCrFeNi was demonstrated by selective electron beam melting (SEBM; Fujieda et al., 2015) and laser engineered net shaping (LENS; Kunce et al., 2015). Since then other additive manufacturing methods like LMD (Wang et al., 2017), selective laser melting (SLM; Niu et al., 2019), and binder jetting (Karlsson et al., 2019a) have been utilized to fabricate the equimolar AlCoCrFeNi alloy. Generally, within the $Al_xCoCrFeNi$ alloy system the work on additive manufacturing mainly concentrates on the equimolar AlCoCrFeNi composition. Similarly to conventionally cast samples additively manufactured AlCoCrFeNi mostly consists of a fine modulated structure of A2 + B2 bcc phases (Kunce et al., 2015; Wang et al., 2017). Only the SEBM fabricated AlCoCrFeNi samples additionally showed some minor amount of fcc phase, which was attributed to the process induced preheating (Fujieda et al., 2015). The dissimilar temperature regimes of the fabrication methods also led to different hardness values ranging from about 400 HV for SEBM samples (Shiratori et al., 2016) to about 600 HV in SLM samples (Niu et al., 2019).

Very recently it was demonstrated that LMD provides a suitable methodology for the production of compositionally graded $Al_xCoCrFeNi$ alloys (Gwalani et al., 2019) and for the high throughput screening of different alloy compositions (Li et al., 2018). The aim of the present study is to combine these two approaches and develop LMD as an effective tool for the high throughput screening of HEAs/CCAs using the $Al_xCoCrFeNi$ alloy system as an example. It will be shown that by utilizing LMD for the deposition of gradient structures the composition can be controlled sufficiently well in order to generate samples exhibiting a wide range of compositions while being deposited in one single built process. With the use of large area energy dispersive X-ray spectroscopy (EDS) and hardness line profiles over the full build height the transitional region can be characterized both sufficiently as well as efficiently. Furthermore, the microstructures within the transitional region will be analyzed in detail using scanning electron microscopy (SEM), EDS, and electron backscattered diffraction (EBSD).

AB INITIO THERMODYNAMIC CALCULATIONS

Ab initio thermodynamic calculations were done to estimate interesting compositional regions and compare the experimental results with the current understanding of the analyzed alloy system by means of the CALPHAD (CAlculation of PHase Diagrams) method. The calculations were based on databases derived from data of lower ordered systems such as binary and ternary phase diagrams as well as experimental data derived from X-ray diffraction (XRD), transmission electron microscopy (TEM), calorimetric measurements, and others. In this study the calculations were executed using ThermoCalc and the TCNi7 database. This database was optimized for calculations on Ni based alloys. However, it will be shown that the database can also

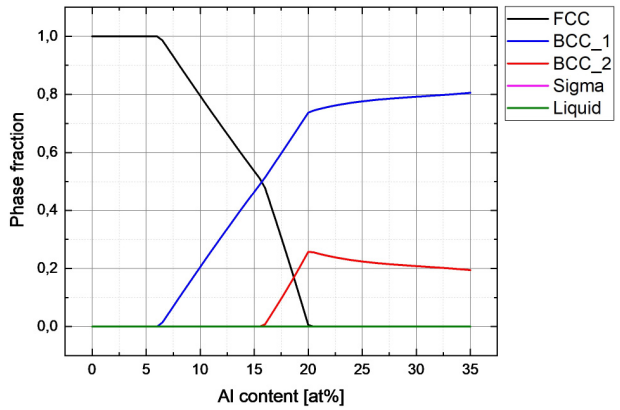

FIGURE 1 | CALPHAD calculation of the expected phase composition in the $Al_xCoCrFeNi$ alloy system at 1350 K in dependence on the Al content.

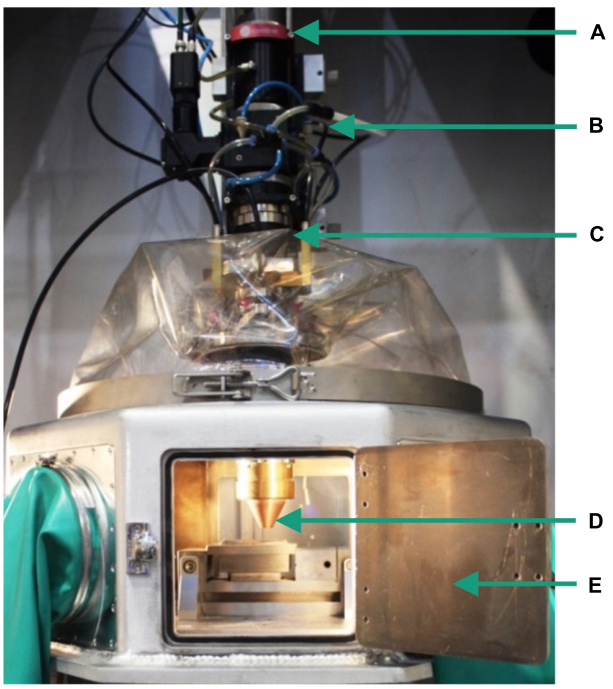

FIGURE 2 | Laser Metal Deposition (LMD) test assembly: **(A)** fiber plug; Laser LDM4000-100, Laserline GmbH; **(B)** Powder inlets; **(C)** OTS-2-optic with laser-focus of 3.8 mm; **(D)** Powder-nozzle COAXpowerline with powder-focus of 1.9–2.2 mm; and **(E)** Shielding gas chamber with Ar (O_2 < 20 ppm).

be used for the HEA material system and allows a reasonable estimation on the desired phase system.

Figure 1 summarizes the results of the CALPHAD calculations. The diagram shows the phase composition as a function of the Al content in at% near the solidification temperature at 1350 K. With increasing Al content a change in phase composition was observed. Up to an overall Al content of 5 at% the microstructure only consisted of the solid solution fcc phase. Exceeding 5 at% Al content a second phase with bcc structure denoted bcc1 appeared. Above 15 at% Al content a second bcc phase, denoted as bcc2, evolved. With increasing Al content the phase fraction of the fcc phase decreases in favor of the two bcc phases. Exceeding an Al content of 20 at% the solid solution fcc phase completely vanishes leading to a structure of mainly bcc1 and minor bcc2. Based on these calculations the interesting compositional range for the LMD experiments was set to the range from 5 to 30 at% Al content. In this region the phase transformation behavior of the LMD samples was thoroughly studied.

EXPERIMENTAL DETAILS

Two powders were used for the deposition of the gradient structures: a pre-alloyed and atomized CoCrFeNi powder with particle sizes between 45 and 90 μm (produced by Nanoval GmbH, Germany) and pure Al powder with particle sizes between 63 and 150 μm (produced by Ecka Granules, Austria). Samples of the two powders were analyzed by SEM and EDS.

The LMD experiments were carried out using the cladding nozzle COAXpowerline developed at Fraunhofer IWS. This nozzle is designed as a coaxial ring with a powder focus diameter of 1.9 to 2.2 mm. The size of the powder focus diameter was determined by the powder feed rate and its carrier gas volume flow. LMD took place in an Ar atmosphere at a working distance (distance between substrate and nozzle tip) of 13 mm. The argon atmosphere was generated in an in-house developed shielding gas chamber, having a slight overpressure of 200 mbar and a residual oxygen content of 20 ppm. A laser spot diameter of 3.81 mm being significantly larger than the diameter of the powder spot was applied for optimum powder utilization. The powder was introduced into the nozzle by four evenly distributed powder inlets. A powder distributor was positioned in front of the powder inlets in which the two base powders are fed and evenly mixed. A 4 kW diode laser from Laserline GmbH was utilized in the LMD process. The applied laser equipment is shown in **Figure 2**. In order to build up gradual compositional changes with respect to the Al content, a methodology similar to the one described by Gwalani et al. (2019) was deployed. However, in our double powder feeder arrangement, instead of $Al_{0.3}CoCrFeNi$ and $Al_{0.7}CoCrFeNi$ we used Al in one hopper and pre-alloyed CoCrFeNi in the second hopper. This development allowed to control the flow rate of both powders with high accuracy

TABLE 1 | Powder feed rate of the two powders for the three cladded gradient structures.

	Powder feed rate in g/min		Powder feed rate in g/min		Powder feed rate in g/min	
Layers	**CoCrFeNi**	**Al**	**CoCrFeNi**	**Al**	**CoCrFeNi**	**Al**
1.–3.	19.5	0.5	19.5	0.5	19.0	1.0
4.–6.	19.0	1.0	18.4	1.6	17.8	2.2
7.–9.	18.4	1.5	17.3	2.7	16.6	3.4
System	5/10/15 at% Al		5/15/25 at% Al		10/20/30 at% Al	

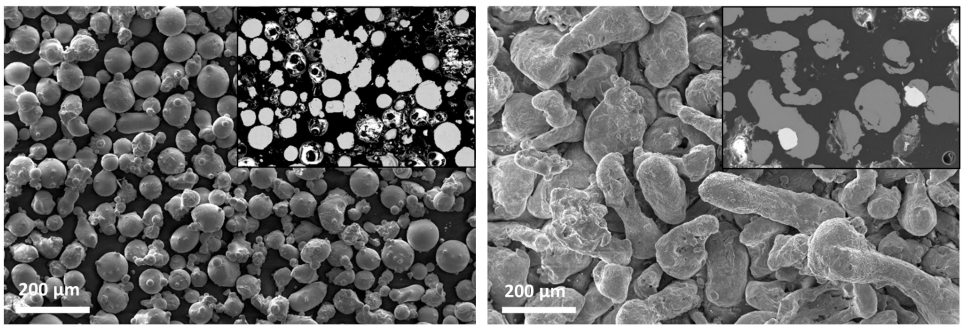

FIGURE 3 | SEM images of the used powders and powder cross sections; CoCrFeNi powder (left); Al powder (right).

TABLE 2 | Chemical composition (EDS measurements) of the used powders in at%.

	Co	Cr	Fe	Ni
CoCrFeNi	25.2	26.1	25.4	23.3
	Al	**O**		
Al	98.8	1.2		

and moreover to evenly mix the two powders in the powder distributor. Utilizing this a smooth compositional gradient was realized and the Al content was varied over a large range from 0 to 30 at% in only one gradient structure.

The cladded gradient structures were composed of nine individual unidirectional welded layers. Stainless steel 1.4301 plates of 10 mm thickness were used as substrate material. The powder feed rates of the CoCrFeNi and Al powders were varied as described in **Table 1** to produce three different gradient structures. The total powder feed rate was kept at a constant level of 20 g/min for all three samples. All samples were welded with a laser power of 1700 W and a process velocity of 600 mm/min. The gradient structures produced that way are hereby referred to as the as built sample condition.

To study the phase composition at near thermal equilibrium the laser cladded samples were subjected to a homogenization heat treatment. The samples were homogenized for 20 h at 1350 K under Ar atmosphere followed by cooling in the oven back to room temperature. The temperature range and duration were chosen on the basis of work on the same material system found in literature (Kao et al., 2009; Karlsson et al., 2019a). Those samples are hereby referred to as the heat treated or homogenized sample condition.

For the microstructural investigations the cladded samples were cut and mounted using a cold mounting epoxy resin. The samples were ground with SiC abrasive paper, wet-polished using a diamond polishing suspension, and finally vibratory polished for multiple hours using Al and Si oxide polishing suspensions. For light microscopic investigations the samples were etched using a V2A etching solution consisting of 200 ml H_20, 200 ml HCl (32%), 20 ml HNO_3 (65%), and 0.6 ml of etching additives.

Detailed microstructural investigations on polished samples were carried out in a JEOL JSM-7800F field emission SEM. EDS and EBSD analysis was carried out using an Oxford X-Max EDS detector and a NordlysNano EBSD detector as well as the Aztec data acquisition software. Additionally, the sample hardness was measured using a LM247 AT Vickers microhardness tester by LECO and a load of 0.1 kg.

RESULTS

Powder Analysis

Figure 3 shows SEM images of the used pre-alloyed CoCrFeNi powder and the elemental Al powder as well as cross sections of both powders. The pre-alloyed CoCrFeNi powder mostly contained spherical particles with a small amount of satellites as well as broken and remelted particles. The average particle diameter was about 70 µm. The chemical composition of the powder is shown in **Table 2**. It was derived from EDS data on powder cross sections. Only small deviations from the desired equimolar ratio of the four elements were detected with a slight deficit in Ni content in particular. The Al powder mostly consisted of irregular shaped elongated particles with a minor

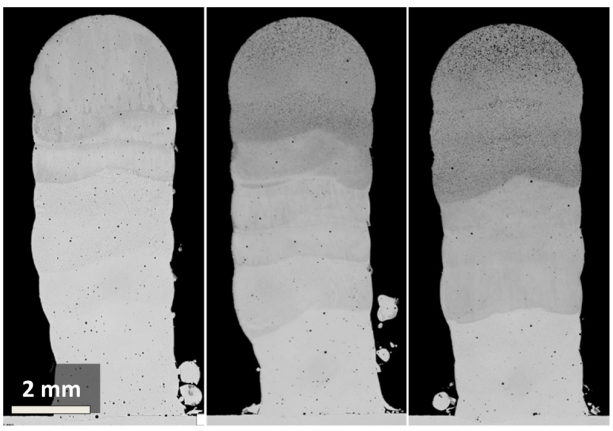

FIGURE 4 | Light microscopic images of the etched as built gradient structures; 5/10/15 at% Al (left); 5/15/25 at% Al (middle); and 10/20/30 at% Al (right).

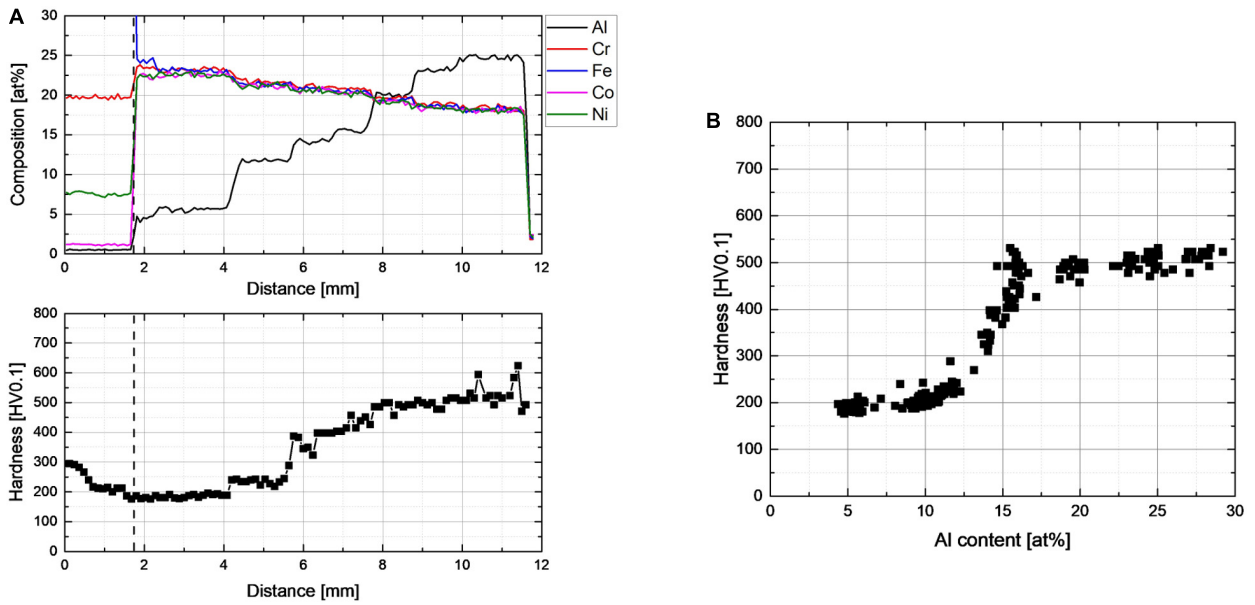

FIGURE 5 | Chemical composition and hardness of the 5/15/25 at% Al as built gradient structure **(A)**; hardness as a function of Al content derived from all three as built gradient structures **(B)**.

axis length between 63 and 150 μm (derived from manufacturer data) and a major axis length up to 300 to 400 μm. Some Ni and Fe rich foreign particles were found within the powder sample. However, no problems in powder feeding and mixing occurred during LMD.

Analysis of the as Built Sample Condition

Light microscopic images of the three different gradient samples in the as built state (**Figure 4**) revealed the nine singular layers of the cladded structures. Each gradient structure was about 4 mm wide and had a height of about 10 mm. Some larger oxide filled pores were identified in the cross sections but no major cracking occurred. Generally, for each of the three stacks, three regions each containing three layers with similar structure and color could be visualized, which is in accordance with the intended and adjusted compositions displayed in **Table 1**. However, due to dilution with the substrate and some intermixing between the individual layers during melting some deviations from the intended chemical composition developed, especially in the transition layers of the three regions. With regard to the screening approach this effect was rather regarded as an advantage. Instead of the intended three different compositions actually five or six different compositions were established in each gradient structure. For all three cladded gradient structures the chemical composition and hardness was determined. As a representative example **Figure 5A** shows the chemical composition and hardness for the gradient structure with 5, 15, and 25 at% Al. Already for this example the comparison of chemical composition and hardness illustrates how strongly the Al content defines the alloys hardness. In **Figure 5B** the hardness measurements on all three gradients are summarized and plotted against the Al content. Up to an Al content of about 10 at% the hardness remained constant at a low level of about 200 HV. In between 10 and 15 at% overall Al content the hardness rapidly increased up to about 500 HV. For Al contents of more than 15 at% the hardness no longer increased but remained at a nearly constant value of 500 HV. The change in hardness in dependence of the Al content correlated well with the change in phase composition from single phase fcc to dual phase bcc as can be seen in **Figure 6** and **Table 3**, respectively. Studying the three gradient samples over the range of 5–25 at% Al content, five major types of microstructures were identified.

Sample position 1 displays a single phase fcc solid solution microstructure with an overall Al content of about 5.0 at% and a hardness of about 200 HV. With increasing Al content more phases started to appear as can be seen at sample position 2 with an overall Al content of about 10.6 at%. Additionally to the previously mentioned fcc phase, a dual and fine-scaled mix of phases, containing more Al than the fcc phase, was found at the interdendritic sites of the microstructure. Further EDS and EBSD analysis which is displayed in **Figure 7** showed that both of these phases exhibit a bcc structure. Furthermore it is worth mentioning that one of the two bcc phases contained more Al than the other. Due to limitations of the EBSD measurements further separation of the two bcc phases was not possible. However, based on the work of Kuwabara et al. (2018) and Wang et al. (2014) it was concluded that this Al rich phase is an ordered bcc B2 phase and the second phase is the solid solution bcc A2 phase. This dual mix of phases will further be referred to as bcc*. The fraction of bcc* rapidly increased with increasing Al content which is displayed at sample positions 3 and 4 which represent an overall Al content of 13.04 at% and 13.4 at%, respectively. This increase in bcc* phase fraction correlated well with the rapid increase in sample hardness between 10 and

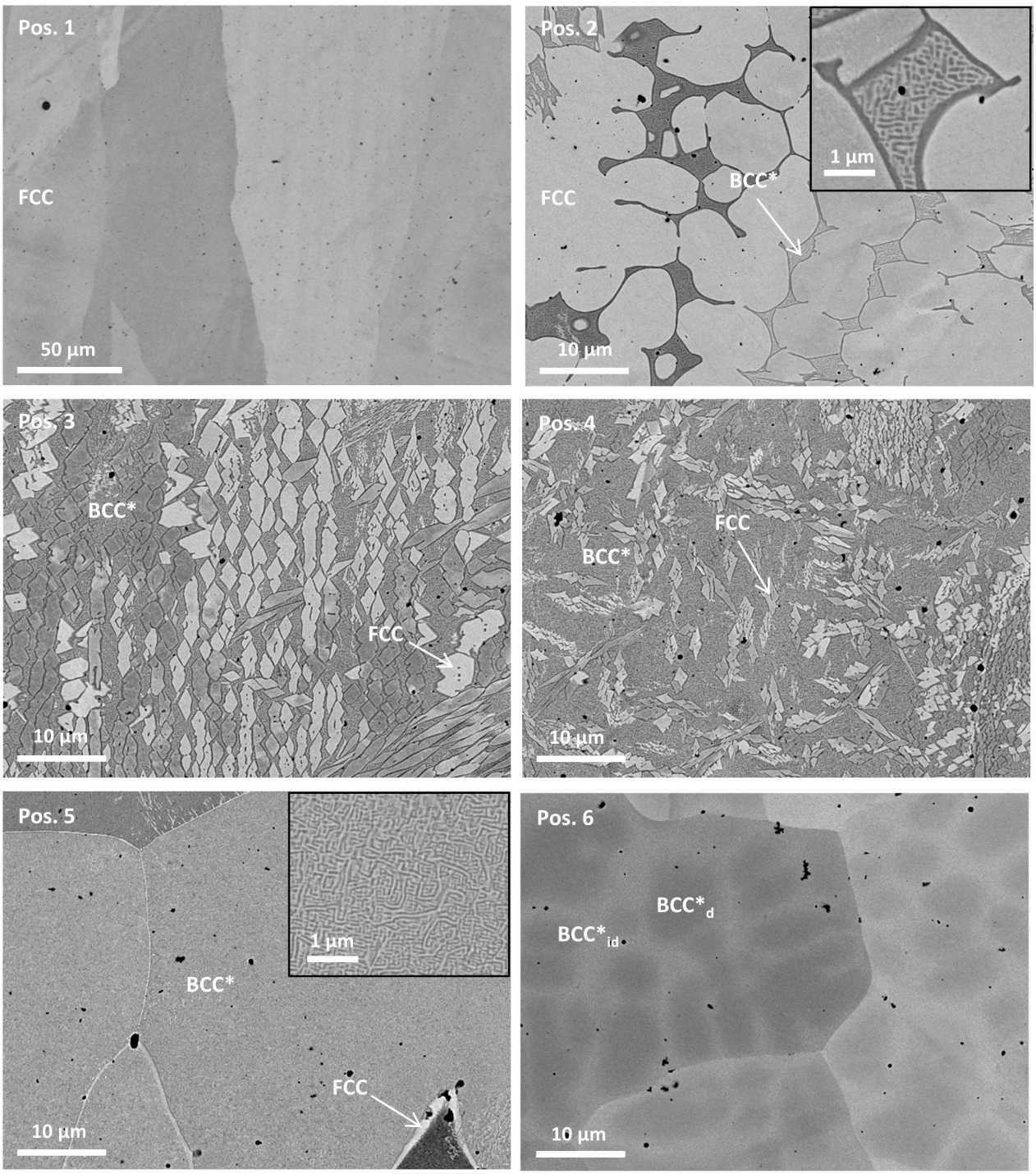

FIGURE 6 | SEM images of the major microstructures of the as built samples with increasing Al content derived from all three cladded gradients: Pos. 1 at 5.0 at% Al, Pos. 2 at 10.6 at% Al, Pos. 3 at 13.0 at% Al, Pos. 4 at 13.4 at% Al, Pos. 5 at 14.2 at% Al, and Pos. 6 at 25.8 at% Al.

15 at% overall Al content. The microstructure at sample position 5 with an overall Al content of 14.2 at% was mostly dominated by bcc* phases showing only some residual fcc phase at the grain boundaries. This is visualized in more detail by the EDS and EBSD measurements displayed in **Figure 7**. In **Figure 6** the detail inlet of the SEM micrograph at position 5 demonstrates the typical very fine-scale dual B2/A2 phase arrangement of bcc*.

At sample position 6 and an overall Al content of 25.8 at% no more residual fcc phase was found and the microstructure fully consisted of bcc* phase mixture. However, besides the

TABLE 3 | Representative EDS analysis of the major microstructures of the as-built samples (at%).

Pos.	Area	Al	Cr	Fe	Co	Ni
1	Overall	5.0	20.6	23.8	24.0	26.7
	fcc	5.0	***20.6***	***23.8***	***24.0***	***26.7***
2	Overall	10.6	19.1	21.4	22.8	26.1
	fcc	8.9	***19.0***	***22.9***	***24.3***	***24.8***
	bcc*	***14.1***	22.1	18.0	20.4	25.4
3	Overall	13.0	18.7	21.0	22.2	25.2
	fcc	9.5	***19.2***	***22.7***	***23.3***	***25.3***
	bcc*	***14.4***	20.1	20.0	21.2	24.3
4	Overall	13.4	18.6	20.9	22.0	25.2
	fcc	9.4	***19.3***	***23.0***	***23.0***	***25.2***
	bcc*	***14.2***	20.8	20.1	21.2	23.8
5	Overall	14.2	18.8	20.1	21.8	25.0
	fcc	-	–	–	–	–
	bcc*	***14.2***	18.8	20.1	21.8	25.0
6	Overall	25.8	15.0	16.6	19.9	22.6
	bcc^*_d	***30.3***	10.9	13.6	19.9	***25.3***
	bcc^*_{id}	20.9	***21.9***	***20.8***	18.9	17.5

The bold values indicate differences in phase composition.

typical grain structure a very fine dendritic structure evolved. The dendritic microstructure is composed of Al rich cores (bcc^*_d) and Cr and Fe rich inter-dendritic areas (bcc^*_{id}). From the observed elemental partitioning it was concluded that the dendrite cores mainly consisted of the bcc B2 phase, whereas the inter-dendritic areas exhibited a fine-scale dual B2/A2 phase arrangement similar to position 5. At this high Al content the sample hardness remained at its peak of about 500 HV.

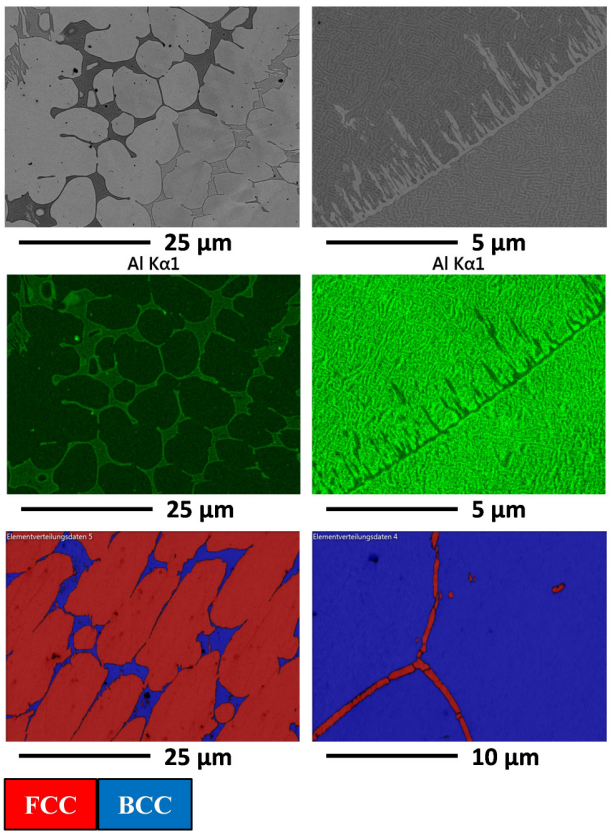

FIGURE 7 | EDS Al maps and EBSD phase maps of sample positions 2 (left) and 5 (right).

Analysis of the Heat Treated Sample Condition

After the homogenizing heat treatment at 1350 K for 20 h the sample hardness and chemical composition were determined for all three gradient structures in the same way as for the as built samples. In **Figure 8** this is shown exemplarily for the 5/15/25 at% Al gradient. In this condition the hardness stayed at 200 HV up to an overall Al content of about 5 at%. In the range from 5 to 18 at% overall Al content the sample hardness increased to its maximum of 700 HV. In the wide range from 5 to 16 at% overall Al content there was only a moderate increase in hardness to 400 HV. However, above 16 at% overall Al content the hardness rapidly jumped to 700 HV. It is worth noting that when the overall Al content exceeded about 20 at%, the hardness dropped to a constant level of about 500 HV, i.e., the same value as in the as built state. Likewise, in the heat treated condition, the change in hardness correlated with a change in microstructure from single phase fcc to dual phase bcc with increasing Al content. This is exemplarily shown in **Figure 9** and **Table 4**, respectively. Over the whole gradient structures five different types of microstructures could be distinguished.

Sample position 1, representing an overall Al content of about 4.8 at% and a hardness of 200 HV, displays a fully solid solution fcc microstructure. Hence, at this alloy composition, the heat treatment did not lead to any structural modifications. At an overall Al content of about 10.4 at% and a hardness of about 280 HV (position 2) additionally to the fcc matrix a small amount of an Al and Ni rich bcc phase was identified. Because of its composition and in accordance to Wang et al. (2014) and Kuwabara et al. (2018) this phase was assumed to be the ordered bcc B2 phase. It should be noted, that in contrast to the as built state no bcc solid solution A2 phase was found at this composition. With increasing Al content the amount of bcc B2 phase increased at the expense of the fcc solid solution phase (position 3). Consequently, the moderate hardness increase in this range of Al content was caused by the increase in bcc B2 phase content. Starting from an overall Al content of 16 at% a third phase could clearly be distinguished leading to a rather complex microstructure. Sample position 4 with an overall Al content of 17.5 at% and a hardness of 700 HV displays such a microstructure (**Figures 9**, **10**). Within the grains it consisted of a mixture of the Al and Ni rich bcc B2 phase and a Fe and Cr rich bcc solid solution A2 (bcc2). Additionally, the solid solution fcc phase had formed along the grain boundaries. Although the phases present at this composition were the same as in the as built state, the homogenizing heat treatment induced substantial changes in the size, distribution, and composition of these phases. It is furthermore remarkable that this microstructure exhibited by far the highest hardness of all conditions analyzed.

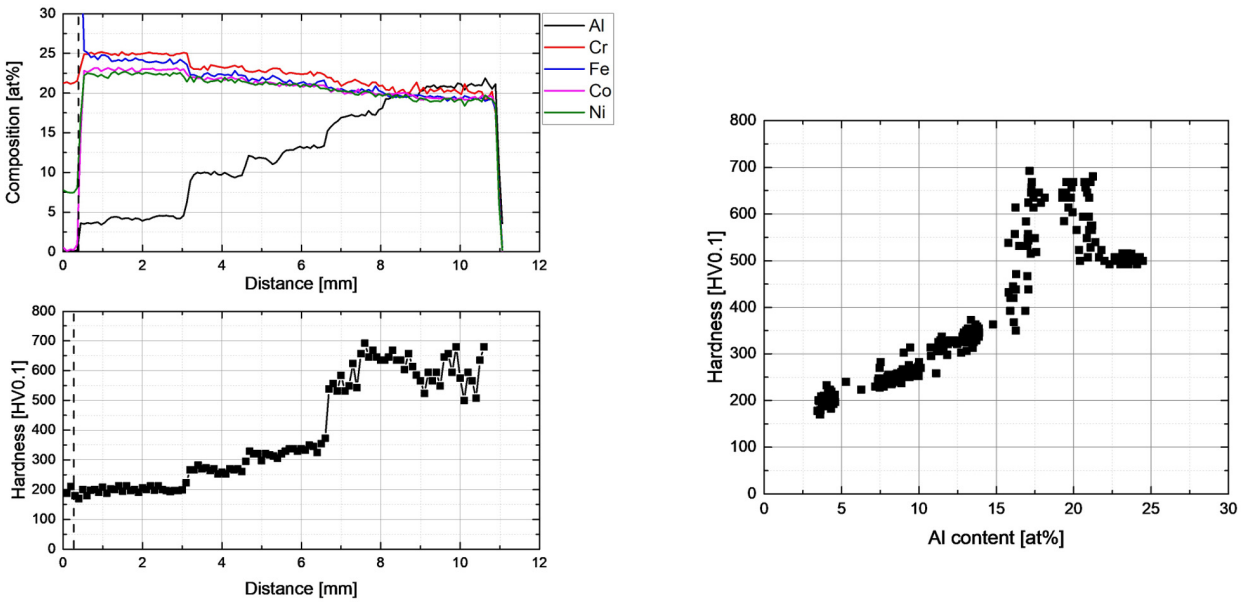

FIGURE 8 | Chemical composition and hardness of the 5/15/25 at% Al gradient structure after heat treatment (left); hardness as a function of Al content derived from all three heat treated gradients (right).

When the overall Al content exceeded 20 at%, as displayed by sample positions 5 and 6, the fcc phase completely vanished and the amount of the Al and Ni rich ordered bcc B2 phase strongly increased. Hence, the predominant phase at this high Al content was the ordered bcc B2 phase. Within this B2 matrix a rather fine and dense arrangement of mainly spherical bcc A2 particles was present. Due to the heat treatment the initially dendritic structure and the accompanying segregations completed vanished. Surprisingly, the hardness of the Al rich B2/A2 dual bcc structure (position 5 and 6) was considerably lower than the hardness of the complex fcc + A2 + B2 bcc structure at an intermediate Al content (position 4).

DISCUSSION

In order to validate thermodynamic calculations as well as effectively produce samples with varying chemical compositions and to build up material libraries for the HEA research, the use of laser and powder based additive manufacturing methods were suggested by Haase et al. (2017) and Li et al. (2018). By varying the powder composition and feed rate and mixing the different powders in situ in the process a wide range of HEA alloy composition can be created very rapidly. In our work this high throughput methodology for HEA alloy fabrication was further developed. By building up tracks that lay on top of each other the Al feed rate was changed every third layer in order to achieve a structure with a gradient in Al content. As a result within only one sample six different compositions of the $Al_xCoCrFeNi$ alloy system could be fabricated. Using this methodology the screening approach could be successfully extended from the alloy fabrication to the analysis of chemical composition, hardness, and structure as well. The obtained results are generally in good agreement with those reported in literature on individual additive manufactured samples while requiring significantly less time for fabrication and analyzing.

Studies on arc-melted and cast samples of $Al_xCoCrFeNi$ reported a transition from a fully fcc phase to a fully dual phase A2/B2 bcc structure in the range from about 10 at% to 19 at% Al content (Kao et al., 2009; Wang et al., 2012). Li et al. (2018) studying 21 different compositions in the $Al_xCoCrFeNi$ alloy system utilizing a laser based LENS process found a similar transition region between about 9 and 21 at%. In contrast, in our work applying LMD to synthesize different alloy compositions of $Al_xCoCrFeNi$, the phase transition occurred in the narrow range from about 10 to 15 at% overall Al content. With increasing Al contents beyond 15 at% only minor microstructural changes in the form of a beginning segregation into Al rich cores (bcc^*_d) and Fe – Cr rich interdendritic areas (bcc^*_{id}) were observed, resulting in a change in local B2/A2 phase fractions. It is proposed that the high laser induced cooling rate of 10^3–10^5 Ks^{-1} associated with the LMD process allowed for a so-called solute trapping that favors sample conditions far from thermal equilibrium and hence the observed phase formation behavior (Xiang et al., 2019). Even though the exact cooling rates of the casting and the LENS process were not given in literature, they were probably lower than for the LMD process. In the case of the casting process much higher melt volumes were involved than in the LMD process leading to lower cooling rates. On the other hand, the LENS process involved several remelting steps and therefore allowed structures closer to the thermal equilibrium compared to the LMD process in our work. The importance of cooling rate and thermal equilibrium to the phase transformation taking place in the $Al_xCoCrFeNi$ alloys system was confirmed

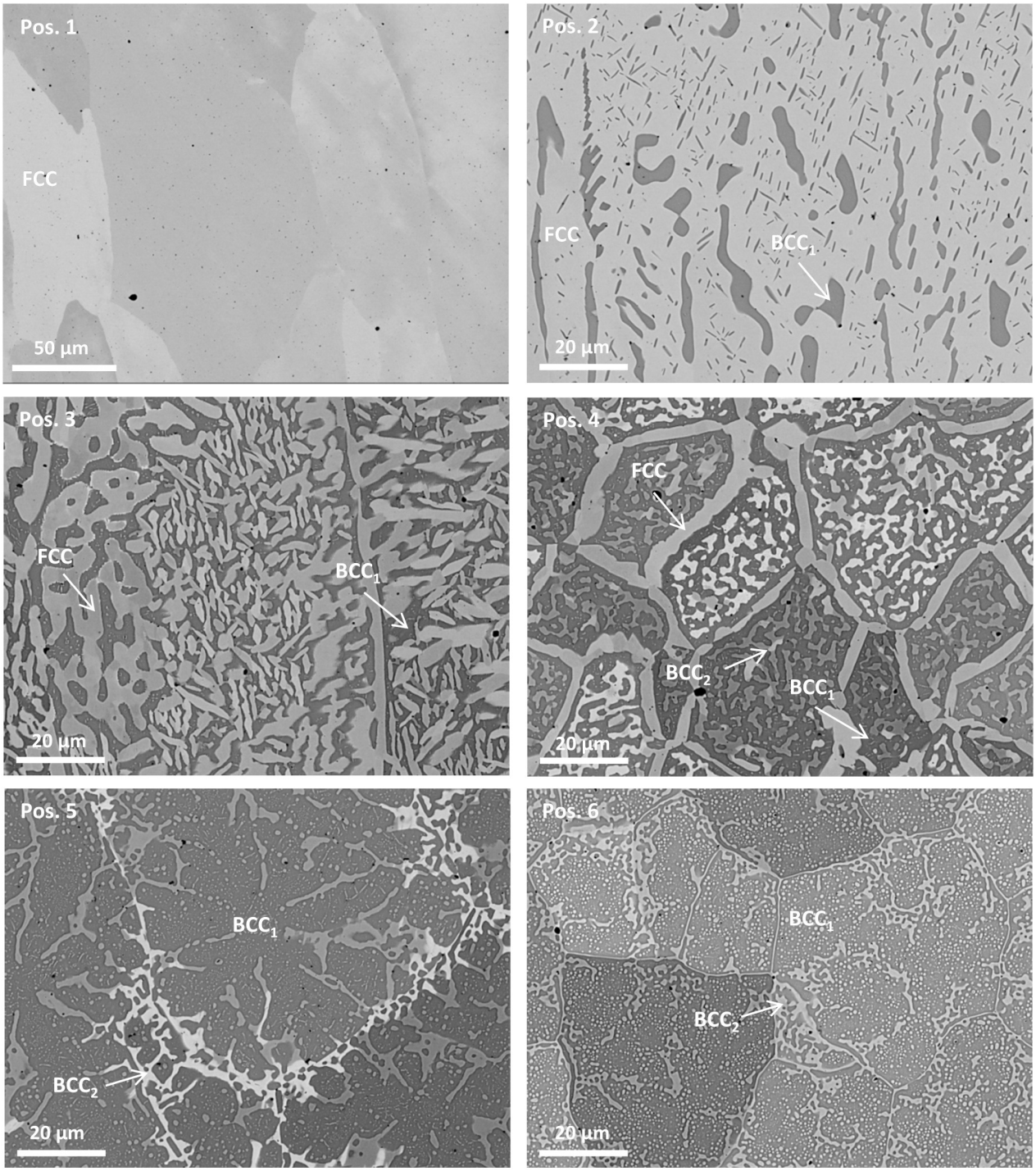

FIGURE 9 | SEM images of the major microstructures of the samples after heat treatment with increasing Al content derived from all three cladded gradients: Pos. 1 at 4.8 at.% Al, Pos. 2 at 10.4 at.% Al, Pos. 3 at 14.7 at.% Al, Pos. 4 at 17.5 at.% Al, Pos. 5 at 23.5 at.% Al, and Pos. 6 at 24.6 at.% Al.

by CALPHAD calculations in literature (Zhang et al., 2016; Butler and Weaver, 2017) and our own work (**Figure 1**). For thermal equilibrium conditions at homogenizing temperature these calculations predicted a very broad range from 5 to 20 at% Al content for the complete transition from fcc to bcc phases.

Another difference between the prediction of the CALPHAD calculations and the experimental results obtained from the LMD as built state regarding the structural evolution was recognized. According to the CALPHAD calculations the transition process from fcc to bcc initiated with the formation of only one

TABLE 4 | Representative EDS analysis of the major regions of the samples after heat treatment (at %).

Pos.	Area	Al	Cr	Fe	Co	Ni
1	Overall	4.8	24.3	23.8	23.8	23.3
	fcc	4.8	***24.3***	***23.8***	***23.8***	***23.3***
2	Overall	10.4	22.4	22.2	22.5	22.5
	fcc	5.9	***25.6***	***24.6***	***23.8***	20.1
	bcc1	***29.1***	7.5	11.6	17.1	***34.7***
3	Overall	14.7	21.2	21.1	21.4	21.6
	fcc	5.7	***27.8***	***27***	***23.3***	16.1
	bcc1	***28.2***	10.2	13.0	18.6	***30.1***
4	Overall	17.5	20.6	20.2	20.6	21.1
	fcc	5.3	***27.3***	***28.7***	***24.1***	14.6
	bcc1	***27.7***	9.0	13.8	20.0	***29.6***
	bcc2	3.4	***44.2***	***27.5***	18.7	6.2
5	Overall	23.5	18.0	18.4	19.8	20.3
	bcc1	***28.8***	10.6	15.2	20.8	***24.7***
	bcc2	4.0	***46.2***	***30.4***	15.1	4.3
6	Overall	24.6	19.5	18.8	18.8	18.3
	bcc1	***28.4***	14.2	16.5	19.8	***21.1***
	bcc2	7.6	***47.7***	***31.8***	10.0	2.9

The bold values indicate differences in phase composition.

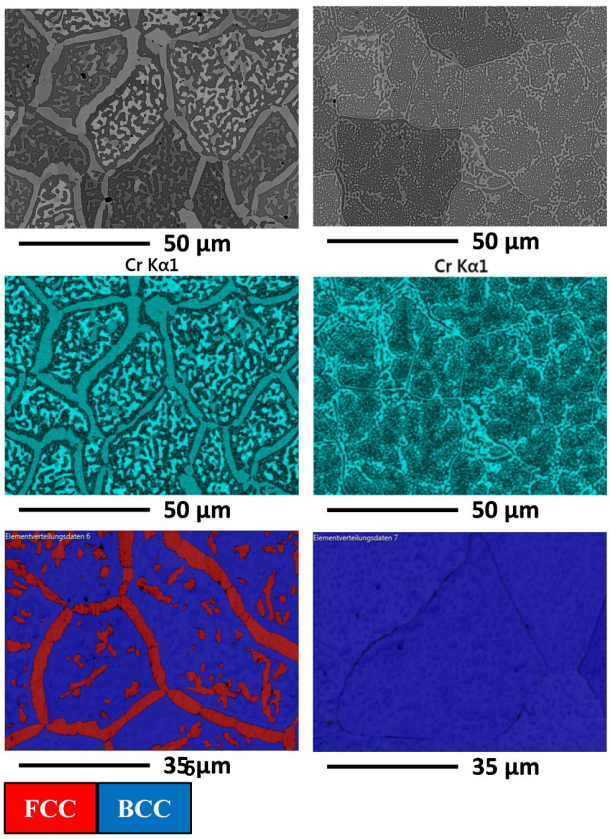

FIGURE 10 | EDS Cr maps and EBSD phase maps of sample positions 4 (left) and 6 (right).

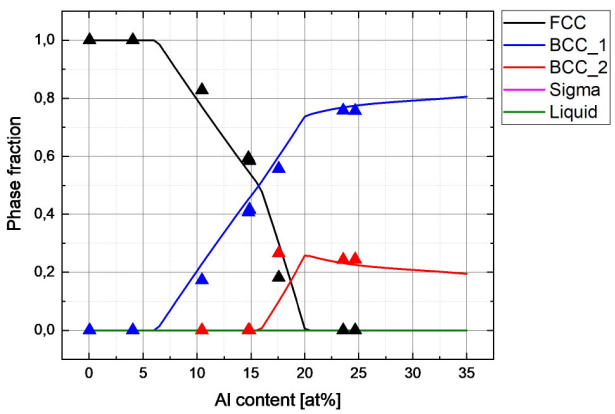

FIGURE 11 | Phase formation in the $Al_xCoCrFeNi$ alloy system homogenized at 1350 K in dependence on the Al content; lines: CALPHAD calculations, symbols: experimental data derived from structural analysis.

bcc phase (bcc1) at about 5 at% Al content. Not until an Al content of about 15 at% Al was exceeded a second bcc phase (bcc2) at a lower phase fraction was predicted. In accordance with Butler and Weaver (2017) bcc1 and bcc2 will be regarded as B2 and A2 phases, respectively. In the as built state of the LMD samples already with the first occurrence of the bcc phase at 10 at% Al the very fine-scaled dual B2/A2 phase arrangement denoted as bcc* formed. This was in contrast to the predictions of the CALPHAD calculations. Although the amount of bcc* increased with increasing Al content, the general appearance of this B2/A2 phase mixture remained unchanged. This is in good agreement with most of the experimental data in literature derived from melting and casting (Wang et al., 2012; Munitz et al., 2016; Lim et al., 2017; Meshi et al., 2019) as well as the additive manufacturing fabrication route (Kunce et al., 2015; Li et al., 2018; Niu et al., 2019; Karlsson et al., 2019b) of $Al_xCoCrFeNi$ alloys. In accordance with the interpretation of Li et al. (2018) and Karlsson et al. (2019b) the very fine-scaled dual B2/A2 phase arrangement is regarded as the result of a spinodal decomposition.

Previous works performed on equiatomic AlCoCrFeNi or near equiatomic $Al_{0.9}CoCrFeNi$ showed that these alloys underwent the following transformation of B2 + A2 → B2 + fcc (A1) + σ during heat treatment at 1123 K (Wang et al., 2014; Meshi et al., 2019). The formation of the brittle σ-phase in $Al_xCoCrFeNi$ alloys at intermediate temperatures has been regarded as a major drawback for industrial applications since it probably limits the operating temperatures to 500°C. According to CALPHAD calculations and the literature discussed in the introduction the avoidance of σ-phase formation during homogenization treatments require temperatures above approximately 1250 K at which the σ-phase dissolves leading to a mixture of A2 + B2 + fcc phases (Munitz et al., 2016; Butler and Weaver, 2017). In our work the homogenization temperature was chosen to be 1350 K, i.e., clearly above this critical temperature. In the range from 5 to 20 at% overall Al content our isothermal CALPHAD calculations at

1350 K predict a combination of fcc, B2, and/or A2 phase depending on the alloy composition (**Figure 1**). Exceeding an overall Al content of 5 at% the phase fraction of the B2 phase increased to the extent of the fcc phase. This prediction was confirmed by our experimental data from annealed LMD samples exhibiting 10.4 and 14.7 at% Al content (positions 2 and 3 in **Figure 9**). Also consistent with the CALPHAD calculations the A2 phase occurred at 17.5 at% Al content (position 4 in **Figure 9**) and the fcc phase completely disappeared at 23.5 and 24.6 at% Al content (position 5 and 6 in **Figure 9**). **Figure 11** visualizes the good agreement of the phase formation behavior of LMD synthesized and annealed $Al_xCoCrFeNi$ alloys with our CALPHAD calculations. A similar good agreement was found in literature with experimental data from vacuum arc-melted, cast and annealed $Al_xCoCrFeNi$ alloys (Butler and Weaver, 2017).

There is a pronounced hardness maximum in the LMD fabricated and annealed $Al_xCoCrFeNi$ alloys in the range from about 17 to about 23 at% overall Al content. At this maximum the hardness of the as built state at the same Al concentrations and also of homogenized samples at higher Al concentrations was exceeded by more than 200 HV. No such hardness maximum was yet reported in vacuum arc-melted, cast, and annealed samples (Kao et al., 2009; Wang et al., 2014). To the best of the authors' knowledge there is no structural and hardness data from additive manufactured and homogenized samples in literature so far to compare the given results with. It is remarkable, however, that the pronounced hardness maximum corresponds directly to the three phase region of fcc + B2 + A2. It is therefore proposed that these three phases arrange to a preferable compound that together with the accompanying grain and phase refinement contributes to this local hardness maximum. However, in order to fully understand the active hardening mechanisms, further structural analysis including TEM is necessary and will be the focus of future research activities.

CONCLUSION

In the present study an experimental methodology based on LMD that allows high throughput experimental screening of HEAs/CCAs including the fabrication and characterization process was introduced. Applying this procedure to the $Al_xCoCrFeNi$ alloy system compositions from 5 to 30 at% Al content were synthesized in gradient structures by LMD and the microstructure and hardness in the as built and homogenized state were investigated in detail. Based on these results the following conclusions were drawn:

(1) LMD utilizing in situ alloying of different pre-alloyed or elemental powders is a very powerful and reliable tool for high throughput screening, fabrication, and the alloy design of HEAs/CCAs.
(2) In the as built condition a microstructural change from single phase solid solution fcc to a fine scaled dual phase bcc microstructure (Fe-Cr rich solid solution bcc phase [A2] and Al-Ni rich ordered bcc phase [B2]) occurred in the narrow range between 10 and 15 at% overall Al content. This structural change correlates to an increase of sample hardness from about 200 to 500 HV. The observed phase formation behavior differs strongly from the CALPHAD calculations at thermal equilibrium. This is due to the typically high cooling rates well known for LMD which promote non-equilibrium conditions.
(3) In the homogenized state the transition from single phase solid solution fcc to ordered B2 phase and finally the dual phase bcc microstructure (B2/A2) occurs in a much wider range from 5 to 23 at% overall Al content. The phase formation and transformation behavior is in very good agreement with homogenized vacuum-arc melted samples and the CALPHAD calculations at thermal equilibrium.
(4) In the homogenized state the structural changes can be correlated to a change in hardness, as well. The maximum hardness of about 700 HV exceeds the hardness of the as built state by more than 200 HV. It is correlated with a favorable formation and arrangement of all three phases (fcc + B2 + A2) and the resulting grain refinement.
(5) The experimental and calculated results in this work demonstrate the effectiveness of CALPHAD methods for the prediction of phase formation in HEAs/CCAs even though a lot of the thermodynamic data from ternary and quaternary systems is still not available.
(6) The mechanical properties of the $Al_xCoCrFeNi$ alloy system can be tuned by the right composition, especially with respect to Al content and using an appropriate annealing heat treatment.

DATA AVAILABILITY STATEMENT

The raw data supporting the conclusions of this article will be made available by the authors, without undue reservation.

AUTHOR CONTRIBUTIONS

JK, MZ, and CL contributed to conception and design of the study. MK performed the CALPHAD calculations and most of the structural analysis. LK performed the cladding experiments by LMD. MK wrote the first draft of the manuscript. JK wrote sections of the manuscript. JK and MZ critically revised the manuscript. All authors read and approved the submitted version.

FUNDING

The research of the present work was supported by internal Fraunhofer funding. Furthermore the financial support from the Federal Ministry for Economic Affairs and Energy in Germany within the "Central Innovation Program for small and medium-sized enterprises (ZIM funding)," Funding code: 16KN081123 is gratefully acknowledged.

REFERENCES

Brueckner, F., Riede, M., Müller, M., Marquardt, F., Willner, R., Seidel, A., et al. (2018). Enhanced manufacturing possibilities using multi-materials in laser metal deposition. *J. Laser Applic.* 30, 1–8. doi: 10.2351/1.5040639

Butler, T. M., and Weaver, M. L. (2017). Investigation of the phase stabilities in AlNiCoCrFe high entropy alloys. *J. Alloys Comp.* 691, 119–129. doi: 10.1016/j.jallcom.2016.08.121

Cantor, B., Chang, I. T. H., Knight, P., and Vincent, A. J. B. (2004). Microstructural development in equiatomic multicomponent alloys. *Mater. Sci. Eng. A* 375-377, 213–218. doi: 10.1016/j.msea.2003.10.257

Fujieda, T., Shiratori, H., Kuwabara, K., Kato, T., Yamanaka, K., Koizumi, Y., et al. (2015). First demonstration of promising selective electron beam melting method for utilizing high-entropy alloys as engineering materials. *Mater. Lett.* 159, 12–15. doi: 10.1016/j.matlet.2015.06.046

Gwalani, B., Gangireddy, S., Shukla, S., Yannetta, C. J., Valentin, S. G., Mishra, R. S., et al. (2019). Compositionally graded high entropy alloy with a strong front and ductile back. *Mater. Today Commun.* 20:100602. doi: 10.1016/j.mtcomm.2019.100602

Haase, C., Tang, F., Wilms, M. B., Weisheit, A., and Hallstedt, B. (2017). Combining thermodynamic modeling and 3D printing of elemental powder blends for high-throughput investigation of high-entropy alloys – Towards rapid alloy screening and design. *Mater. Sci. Eng. A* 688, 180–189. doi: 10.1016/j.msea.2017.01.099

Kao, Y. F., Chen, T. J., Chen, S. K., and Yeh, J. W. (2009). Microstructure and mechanical property of as-cast, -homogenized, and -deformed AlxCoCrFeNi ($0 \leq x \leq 2$) high-entropy alloys. *J. Alloys Comp.* 488, 57–64. doi: 10.1016/j.jallcom.2009.08.090

Karlsson, D., Lindwall, G., Lundbäck, A., Amnebrink, M., Boström, M., Riekehr, L., et al. (2019a). Binder jetting of the AlCoCrFeNi alloy. *Addit. Manuf.* 27, 72–79. doi: 10.1016/j.addma.2019.02.010

Karlsson, D., Marshal, A., Johansson, F., Schuisky, M., Sahlberg, M., Schneider, J. M., et al. (2019b). Elemental segregation in an AlCoCrFeNi high-entropy alloy – A comparison between selective laser melting and induction melting. *J. Alloys Comp.* 784, 195–203. doi: 10.1016/j.jallcom.2018.12.267

Kunce, I., Polanski, M., Karczewski, K., Plocinski, T., and Kurzydlowski, K. J. (2015). Microstructural characterisation of high-entropy alloy AlCoCrFeNi fabricated by laser engineered net shaping. *J. Alloys Comp.* 648, 751–758. doi: 10.1016/j.jallcom.2015.05.144

Kuwabara, K., Shiratori, H., Fujieda, T., Yamanaka, K., Koizumi, Y., and Chiba, A. (2018). Mechanical and corrosion properties of AlCoCrFeNi high-entropy alloy fabricated with selective electron beam melting. *Addit. Manuf.* 23, 264–271. doi: 10.1016/j.addma.2018.06.006

Leino, M., Pekkarinen, J., and Soukka, R. (2016). The role of laser additive manufacturing methods of metals in repair, refurbishment and remanufacturing – enabling circular economy. *Phys. Proc.* 83, 752–760. doi: 10.1016/j.phpro.2016.08.077

Li, M., Gazquez, J., Borisevich, A., Mishra, R., and Flores, K. M. (2018). Evaluation of microstructure and mechanical property variations in Al x CoCrFeNi high entropy alloys produced by a high-throughput laser deposition method. *Intermetallics* 95, 110–118. doi: 10.1016/j.intermet.2018.01.021

Lim, K. R., Lee, K. S., Lee, J. S., Kim, J. Y., Chang, H. J., and Na, Y. S. (2017). Dual-phase high-entropy alloys for high-temperature structural applications. *J. Alloys Comp.* 728, 1235–1238. doi: 10.1016/j.jallcom.2017.09.089

Manzoni, A., Daoud, H., Völkl, R., Glatzel, U., and Wanderka, N. (2013). Phase separation in equiatomic AlCoCrFeNi high-entropy alloy. *Ultramicroscopy* 132, 212–215. doi: 10.1016/j.ultramic.2012.12.015

Marshal, A., Pradeep, K. G., Music, D., Zaefferer, S., De, P. S., and Schneider, J. M. (2017). Combinatorial synthesis of high entropy alloys: introduction of a novel, single phase, body-centered-cubic FeMnCoCrAl solid solution. *J. Alloys Comp.* 691, 683–689. doi: 10.1016/j.jallcom.2016.08.326

Meshi, L., Linden, Y., Munitz, A., Salhov, S., and Pinkas, M. (2019). Retardation of the σ phase formation in the AlCoCrFeNi multi-component alloy. *Mater. Characterization* 148, 171–177. doi: 10.1016/j.matchar.2018.12.010

Miracle, D. B., and Senkov, O. N. (2017). A critical review of high entropy alloys and related concepts. *Acta Mater.* 112, 448–511. doi: 10.1016/j.actamat.2016.08.081

Mohanty, A., Sampreeth, J. K., Bembalge, O., Hascoet, J. Y., Marya, S., Immanuel, R. J., et al. (2019). High temperature oxidation study of direct laser deposited AlXCoCrFeNi (X = 0.3,0.7) high entropy alloys. *Surface Coat. Technol.* 380:125028. doi: 10.1016/j.surfcoat.2019.125028

Munitz, A., Salhov, S., Hayun, S., and Frage, N. (2016). Heat treatment impacts the micro-structure and mechanical properties of AlCoCrFeNi high entropy alloy. *J. Alloys Comp.* 683, 221–230. doi: 10.1016/j.jallcom.2016.05.034

Niu, P. D., Li, R. D., Yuan, T. C., Zhu, S. Y., Chen, C., Wang, M. B., et al. (2019). Microstructures and properties of an equimolar AlCoCrFeNi high entropy alloy printed by selective laser melting. *Intermetallics* 104, 24–32. doi: 10.1016/j.intermet.2018.10.018

Shiratori, H., Fujieda, T., Yamanaka, K., Koizumi, Y., Kuwabara, K., Kato, T., et al. (2016). Relationship between the microstructure and mechanical properties of an equiatomic AlCoCrFeNi high-entropy alloy fabricated by selective electron beam melting. *Mater. Sci. Eng. A* 656, 39–46. doi: 10.1016/j.msea.2016.01.019

Wang, R., Zhang, K., Davies, C., and Wu, X. (2017). Evolution of microstructure, mechanical and corrosion properties of AlCoCrFeNi high-entropy alloy prepared by direct laser fabrication. *J. Alloys Comp.* 694, 971–981. doi: 10.1016/j.jallcom.2016.10.138

Wang, W. R., Wang, W. L., Wang, S. C., Tsai, Y. C., Lai, C. H., and Yeh, J. W. (2012). Effects of Al addition on the microstructure and mechanical property of AlxCoCrFeNi high-entropy alloys. *Intermetallics* 26, 44–51. doi: 10.1016/j.intermet.2012.03.005

Wang, W. R., Wang, W. L., and Yeh, J. W. (2014). Phases, microstructure and mechanical properties of AlxCoCrFeNi high-entropy alloys at elevated temperatures. *J. Alloys Comp.* 589, 143–152. doi: 10.1016/j.jallcom.2013.11.084

Xiang, S., Luan, H., Wu, J., Yao, K. F., Li, J., Liu, X., et al. (2019). Microstructures and mechanical properties of CrMnFeCoNi high entropy alloys fabricated using laser metal deposition technique. *J. Alloys Comp.* 773, 387–392. doi: 10.1016/j.jallcom.2018.09.235

Yeh, J. W., Chen, S. K., Lin, S. J., Gan, J. Y., Chin, T. S., Shun, T. T., et al. (2004). Nanostructured high-entropy alloys with multiple principal elements: novel alloy design concepts and outcomes // nanostructured high-entropy alloys with multiple principal elements: novel alloy design concepts and outcomes. *Adv. Eng. Mater.* 6, 299–303. doi: 10.1002/adem.200300567

Zhang, C., Zhang, F., Diao, H., Gao, M. C., Tang, Z., Poplawsky, J. D., et al. (2016). Understanding phase stability of Al-Co-Cr-Fe-Ni high entropy alloys. *Mater. Des.* 109, 425–433. doi: 10.1016/j.matdes.2016.07.073

Conflict of Interest: The authors declare that the research was conducted in the absence of any commercial or financial relationships that could be construed as a potential conflict of interest.

frontiers in Materials

ORIGINAL RESEARCH
published: 06 August 2020
doi: 10.3389/fmats.2020.00270

Phase Equilibria in the Al–Co–Cr–Fe–Ni High Entropy Alloy System: Thermodynamic Description and Experimental Study

Oleg Stryzhyboroda, Victor T. Witusiewicz, Sergej Gein, Daniel Röhrens and Ulrike Hecht*

Access e.V., Aachen, Germany

In this paper we present and discuss phase equilibria in the quaternary Al–Cr–Fe–Ni and the quinary Al–Co–Cr–Fe–Ni alloy systems based on experimental data from DTA/DSC, SEM/EDS, and SEM/EBSD on as-cast and isothermally annealed samples. These data as well as literature data were used for developing a new Al–Co–Cr–Fe–Ni thermodynamic description by the CALPHAD approach. Considerable efforts in this direction have been made already and commercial databases for high entropy alloys are available, e.g., TCHEA4 and PanHEA. We focus on comparing our new thermodynamic database with computations using TCHEA4 for two section planes, i.e., quaternary $Al_xCrFe_2Ni_2$ and quinary $Al_xCoCrFeNi$, where x is the stochiometric coefficient. According to our new thermodynamic description a single-phase field BCC-B2 is stable over a wider temperature range in both section planes, giving rise to dual-phase microstructures along solid state phase transformation pathways. In the section plane $Al_xCoCrFeNi$ the two-phase field BCC-B2 + σ predicted by the new database is stable between 600 and 800°C, while in TCHEA4 this phase field extends to nearly 1000°C. Furthermore, our new database showed that the solidification interval with primary BCC-B2 phase in quinary as well as quaternary section planes is narrow, being in a good agreement with presented micro-segregation measurements. Additionally, computed phase fields and phase-field boundaries in the quinary section plane correspond well to the experimental results reported in the literature.

Keywords: high entropy alloys, thermodynamic database, CALPHAD, quaternary alloys, quinary alloys, phase diagram

OPEN ACCESS

Edited by:
Liqiang Wang,
Shanghai Jiao Tong University, China

Reviewed by:
Yiping Lu,
Dalian University of Technology, China
Ligang Zhang,
Central South University, China

****Correspondence:***
Oleg Stryzhyboroda
o.stryzhyboroda@access-technology.de

Specialty section:
This article was submitted to Structural Materials, a section of the journal Frontiers in Materials

Received: *31 May 2020*
Accepted: *20 July 2020*
Published: *06 August 2020*

Citation:
Stryzhyboroda O, Witusiewicz VT, Gein S, Röhrens D and Hecht U (2020) Phase Equilibria in the Al–Co–Cr–Fe–Ni High Entropy Alloy System: Thermodynamic Description and Experimental Study. Front. Mater. 7:270. doi: 10.3389/fmats.2020.00270

INTRODUCTION

High entropy alloys (HEAs) and, in particular, alloys from the Al–(Co)–Cr–Fe–Ni alloy system have been subject to numerous investigations due to promising mechanical, magnetic and electrochemical properties (Butler and Weaver, 2016; Gao et al., 2016; Chen et al., 2017; Shi et al., 2017). It was shown that in this alloy system the chemical composition can be adjusted to obtain materials with face centered cubic (FCC) or body centered cubic (BCC) majority phases (Wang et al., 2012, 2014; Yang et al., 2015). However, in the last few years research focused on dual-phase materials (FCC + BCC) (Dong et al., 2016; Ghassemali et al., 2017; Lim et al., 2017) and even

dual phase eutectics (EHEA). Good examples for these two types of dual phase materials are the alloys $Al_{0.7}CoCrFeNi$ with duplex Widmanstätten microstructure (Leo et al., 2017; Rao et al., 2017; Gwalani et al., 2019), and $AlCoCrFeNi_{2.1}$ with a lamellar eutectic microstructure (Lu et al., 2014; Wani et al., 2016; Nagase et al., 2017).

Microstructure and property characterization have progressed significantly for as-cast HEAs and EHEAs including knowledge about solid-state phase transformations along distinct processing routes. Some of them e.g., additive manufacturing, may involve high cooling rates thus leading to non-equilibrium microstructures which can be further optimized through heat treatment schemes. For both alloy design and processing technologies it is therefore important to rely on critically assessed thermodynamic background information.

The challenge with the thermodynamic modeling relates to the fact that the high entropy compositional range involves equiatomic or near equiatomic alloy compositions which have been avoided so far in classical CALPHAD databases. In fact, the databases were designed for alloy families with a well-defined major component e.g., steel, Ni-based superalloys etc. Nonetheless, the CALPHAD approach remains the only efficient tool for the construction of thermodynamic databases. Based on CALPHAD two thermodynamic descriptions were proposed for the quinary alloy system Al–Co–Cr–Fe–Ni being included in high entropy multi-component databases, i.e., TCHEA1 through TCHEA4 (Chen et al., 2018; Thermo-Calc Software, 2020) by Thermo-Calc AB[1] and PanHEA (CompuTherm Plc, 2020) by CompuTherm Plc.[2]

Prediction of phase equilibria for alloys form the Al–(Co)–Cr–Fe–Ni system differ widely in the currently available or published database versions and certainly differ from experimental observations. Necessarily over time these databases will constantly improve both in terms of accuracy and scope. Improvements will also be provided by academic research groups mainly for less ample sub-systems e.g., quaternary and quinary alloy systems. The focus on these sub-systems is essential because simple extrapolations from ternary sub-systems to multicomponent systems may not be straightforward or even problematic as already discussed by Gorsse and Senkov (2018).

In this work we present research results on thermodynamic equilibria in the system Al–Co–Cr–Fe–Ni including key experimental data for selected alloys and annealing conditions as well as a thermodynamic description based on CALPHAD modeling. For selected section planes through the compositional space we will also compare the new description with TCHEA4 results and refer to Zhang et al. (2016) for comparison with PanHEA. The section planes at case are $Al_xCoCrFeNi$ and $Al_xCrFe_2Ni_2$.

EXPERIMENTAL METHODS

To support CALPHAD modeling and complement available literature data we produced a series of experimental alloys using the arc melter MAM-1 (Edmund Bühler GmbH) to melt small 15 g samples from mixtures of high purity elements (>99.9%). The melting process was carried out on a water-cooled copper hearth under Ar atmosphere. Each sample was flipped and re-melted at least three times to ensure chemical homogeneity. To reduce the amount of residual oxygen, the melting chamber was vacuumized and consequently fleshed with Ar at least 3 times before each melting process. **Table 1** list the chemical compositions of the samples measured by energy dispersive X-ray spectrometry (EDS).

The samples were cut in four pieces for isothermal annealing treatments which were performed in a tube furnace RHTC 20-230/15 (Nabertherm GmbH) under high purity Ar atmosphere. The annealing temperatures were 750, 1000, and 1300°C for 48, 24, and 6 h respectively, followed by water quenching (WQ). From these annealing conditions we will mainly report the results for 1300°C/6 h/WQ as well as selected key observations from other annealing temperatures specifically defined in the process of database optimization.

Differential thermal analyses (DTA) were performed with heating and cooling rates of 20 K/min on as-cast samples in alumina crucibles under high purity Ar atmosphere. These measurements were conducted in a high temperature differential scanning calorimeter type Pegasus DSC 404 F3 (NETZSCH-Gerätebau GmbH) operated in DTA mode with two different sensors, i.e., DSC-cp and DSC-DTA both with an S-type thermocouple. Calibration runs were performed using In, Sn, Al, Ag, Au, and Ni from NETZSCH calibration set. The DTA curves were processed according to guidelines of the National Institute of Standards and Technology (NIST) (Boettinger et al., 2006). The first detectable deviation of the peak from the baseline was chosen as the onset of a phase transformation. The end of a phase transformation was defined as corresponding to the inflection point at the return side of the peak.

Microstructural analysis was carried out by scanning electron microscopy (SEM) including EDS and backscattered electron diffraction (EBSD). The specimens were prepared by standard grinding and polishing steps with a final step of vibratory polishing in a Vibromet device (Buehler). SEM/EDS and SEM/EBSD were performed using a ZEISS-Gemini Leo 1550 (Carl Zeiss AG) microscope equipped with EDS and EBSD detectors and the INCA Analysis software (Oxford Instruments Plc). EDS measurements were conducted using an accelerating voltage of 15 kV and a working distance of 10 mm. The EBSD measurements were performed mainly in mapping mode under an accelerating voltage of 25 kV and the working distance of around 16 mm.

KEY EXPERIMENTAL RESULTS

Phase Transformation Temperatures From Differential Thermal Analysis (DTA)

Differential thermal analysis measurements were conducted on as-cast samples. Thus, the micro-segregation inherited from solidification and potentially metastable microstructures are expected to affect the measured phase transformation temperatures upon heating, specifically in the low temperature

[1]https://www.thermocalc.com/products-services/databases/thermodynamic/

[2]https://computherm.com/?docs=pandat-database-manual/database-manual/panhea

TABLE 1 | Integral chemical composition of the Al_xCoCrFeNi alloys measured by EDS.

Alloy	EDS and (nominal) alloy composition in at.%				
	Al	**Co**	**Cr**	**Fe**	**Ni**
$Al_{0.5}$CoCrFeNi	10.7 (11.1)	22.3 (22.2)	22.4 (22.2)	22.2 (22.2)	22.4 (22.3)
$Al_{0.6}$CoCrFeNi	13.1 (13.0)	21.7 (21.7)	22.0 (21.8)	21.2 (21.7)	21.9 (21.8)
$Al_{0.7}$CoCrFeNi	15.1 (14.9)	21.3 (21.2)	21.4 (21.3)	21.1 (21.3)	21.1 (21.3)
$Al_{0.8}$CoCrFeNi	16.6 (16.7)	20.7 (20.8)	21.5 (20.8)	20.6 (20.8)	20.5 (20.9)
$Al_{0.9}$CoCrFeNi	17.9 (18.4)	20.1 (20.4)	21.2 (20.4)	20.2 (20.4)	20.6 (20.4)
$Al_{1.0}$CoCrFeNi	20.3 (20.0)	19.7 (20.0)	20.7 (20.0)	19.9 (20.0)	19.4 (20.0)
$Al_{1.5}$CoCrFeNi	27.6 (27.3)	17.9 (18.2)	18.5 (18.2)	17.9 (18.2)	18.1 (18.1)

range, e.g., below 1000°C. Above this temperature diffusion is considered fast enough to homogenize the samples. Expectedly, solidus and liquidus temperatures are more accurately detected.

Figure 1A shows the DTA heating curves for the Al_xCoCrFeNi HEA alloys listed in **Table 1** in the region of solid-state transformations. The associated endothermic peaks are labeled P1 through P3. Melting peaks are shown in **Figure 1B** labeled P4. Based on microstructure analysis and information from literature we identified the phase transformations corresponding to the individual peaks P1, P2, and P3 as follows. Peak P1 represents the dissolution of the ordered FCC-$L1_2$ phase which is present as needle-like precipitates and stable up to 500–620°C depending on the alloy composition.

Peak P2 around 1000°C is associated with the complete dissolution of the σ-phase. The chromium bonded in σ-phase will be redistributed into the disordered solid solution phases FCC-A1 and/or BCC-A2. Noteworthy alloy $Al_{1.5}$CoCrFeNi shows no σ-phase dissolution in this temperature range.

Peak P3 strongly depends on the alloy composition: for $x \geq 1.0$, P3 is attributed to the dissolution of the disordered BCC-A2 phase; for $0.8 \geq x \geq 1.0$, P3 is attributed to the dissolution of the disordered solid-solution phases BCC-A2 and FCC-A1. Finally, for $0.4 \geq x \geq 0.7$, P3 is attributed to early stages of melting where the disordered solid-solution phases are in equilibrium with the first liquid. These distinctions are made in fact with preliminary knowledge from the thermodynamic computations as well as microstructure information from heat treated specimens. It is noteworthy to see that for $x = 0.6$ and $x = 0.7$ but not for $x = 0.8$ the P3 peaks do not return to the baseline meaning that the P3 corresponds to the solidus temperature of these alloys.

Peak P4 in all the alloys is associated with bulk melting. The broad shape of peak P4 for $x = 1.0$ and $x = 1.5$ is attributed to the latent heat consumed when partition coefficients are greater than 1 as discussed by NIST (Boettinger et al., 2006).

Microstructure Analysis After Isothermal Annealing Experiments

This section mainly describes the microstructural features of Al_xCoCrFeNi samples after annealing at 1300°C/6 h/WQ. Additional information is provided for two dual phase alloys after annealing at 900°C/24 h/WQ ($Al_{0.8}$CoCrFeNi and $Al_{0.7}$CoCrFeNi) mainly with respect to the phase fraction of σ. Furthermore, annealing at 1180°C and 1000°C for alloy $Al_{0.8}$CoCrFeNi provided insight into the location of the binodal line which marks the transition from a compositionally modulated BCC (BCC-A2 + BCC-B2) to a compositionally homogeneous BCC-B2. Indeed, the location of the binodal line in composition and temperature space is one of the critical and most interesting aspects of the Al–(Co)–Cr–Fe–Ni HEA system. We will discuss this in due details in section "Conclusions."

To our best knowledge only few experimental data are available in literature on phase equilibria at temperatures ranging from 1200°C to solidus. Indeed, the stability range of single BCC-B2 phase is at debate. Work from Munitz et al. (2016) show that the BCC-B2 is stable as single phase at 1200°C in alloy $Al_{1.0}$CoCrFeNi. Recently, Aizenshtein et al. (2020) verified experimentally that single BCC-B2 phase is stable at 1300°C in alloy $Al_{2.75}$CoCrFeNi while it coexists with BCC-A2 at 1200°C. The research reported in Abuzaid and Sehitoglu (2018) shows that $Al_{0.6}$CoCrFeNi alloy is dual phase BCC-A2 + BCC-B2 at 1300°C as retained after WQ. However, information is lacking with respect to BCC-B2 phase stability at high temperatures and as function of the Al content. In our annealing series at 1300°C we aimed at screening a wider composition range with a small increment of the Al content e.g., Al_xCoCrFeNi alloys (x = 0.6, 0.7, 0.8, 0.9, and 1.0). The main results are displayed in **Figure 2** showing SEM microstructures at 1000x and 5000x magnification along with phase maps acquired by EBSD.

Alloy $Al_{0.3}$CoCrFeNi shows a single-phase FCC-A1 microstructure. Grain boundaries are not decorated by BCC-B2 precipitates.

Alloys $Al_{0.6}$CoCrFeNi and $Al_{0.7}$CoCrFeNi are dual phase composed of FCC-A1 Widmanstätten laths inside the BCC-B2 parent grains. Grain boundaries in both alloys are decorated by FCC-A1 films. However, in $Al_{0.6}$CoCrFeNi but not in $Al_{0.7}$CoCrFeNi we also observe FCC dendrites close to grain boundary regions. The two samples are very different with respect to the phase fraction of BCC-B2 being 21.5% in $Al_{0.6}$CoCrFeNi and 42% in $Al_{0.7}$CoCrFeNi. In both alloys the BCC-B2 phase is clearly decomposed into nanoscale constituent phases as a consequence of the spinodal decomposition upon quenching. Decomposition of BCC-B2 during quenching has already been reported by Munitz et al. (2016) in alloy $Al_{1.0}$CoCrFeNi to lead to an extremely fine spinodal decomposition wavelength.

Alloy $Al_{0.8}$CoCrFeNi displays a single-phase BCC-B2 structure at 1300°C. As before, upon quenching a spinodal

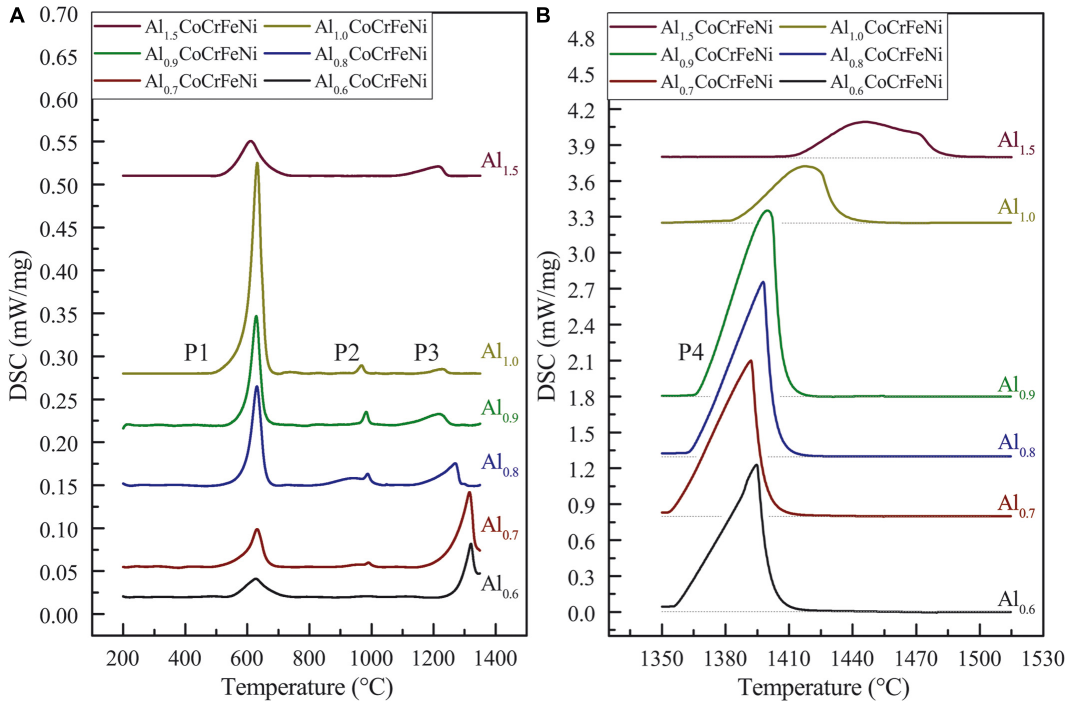

FIGURE 1 | DSC curves for $Al_xCoCrFeNi$ alloys (x = 0.6, 0.7, 0.8, 0.9, 1.0, and 1.5) in solid state **(A)** and in the range of melting **(B)** upon heating with heating rate of 20 K/min.

structure with extremely fine wavelength formed. Some grain boundaries are decorated by thin FCC-A1 films and it is unclear whether these films formed during annealing or upon quenching. Irrespective of this detail we conclude that for $x = 0.8$ the sample is in nearly 100% BCC-B2 state at 1300°C. Very similar microstructures were obtained in alloys $x = 0.9$ and $x = 1.0$. Hence, alloy $Al_{0.8}CoCrFeNi$ almost exactly corresponds to the boundary between BCC-B2 + FCC-A1 and single BCC-B2 at 1300°C.

Figures 3A,B show SEM microstructures of the $Al_{0.8}CoCrFeNi$ alloy annealed at 1000°C/24 h and 1180°C/30 min followed by water quenching, respectively. Both microstructures consist of three phases i.e., FCC-A1 + BCC-A2 + BCC-B2 with vermicular morphology of FCC-A1 phase. The EBSD analysis of the samples confirmed that σ-phase did not form at these temperatures. The microstructure of the samples differs in an important detail: the spinodal structure (BCC-A2 + BCC-B2) is severely coarsened after annealing at 1000°C. On the contrary, in the sample annealed at 1180°C the spinodal structure (BCC-A2 + BCC-B2) is ultrafine which indicates that it has formed upon quenching. This means that the alloy $Al_{0.8}CoCrFeNi$ is above the binodal line at $T = 1180$°C but below the binodal line at $T = 1000$°C.

Further annealing experiments were performed at 900°C/24 h/WQ to verify the composition and phase fraction of σ-phase in alloys $Al_{0.7}CoCrFeNi$ and $Al_{0.8}CoCrFeNi$. For these alloy compositions we expected the maximum of the "σ-bell." We present SEM microstructures along with EBSD maps in **Figures 4**, **5**. Both samples display a three-phase microstructure consisting of FCC-A1, BCC-B2 and σ phases. The σ-phase fraction ranges around 7 area% in $Al_{0.7}CoCrFeNi$ and around 20 area % in $Al_{0.8}CoCrFeNi$. Without showing experimental data, we note that the σ-phase fraction in alloy $Al_{0.7}CoCrFeNi$ annealed at 1000°C is ≤1 area%. Its fraction may further increase after longer annealing time. Therefore, the data were not used for database optimization. Instead, only the chemical composition of the σ-phase was used as an input for CALPHAD modeling.

CALPHAD Database Optimization and Computed Phase Equilibria

The CALPHAD-based thermodynamic description of the quaternary and quinary Al–(Co)–Cr–Fe–Ni alloy systems was optimized based on the key experiments conducted within the scope of the present study as well as experimental data presented in literature. The PARROT module embedded in the Thermo-Calc software was used to optimize the Gibbs energy functions of individual phases in the HEA system. Sub-lattice models were selected as follows: for BCC and FCC ordered and disordered phases we used three sub-lattice models with the third sub-lattice being occupied by vacancies only; for the σ-phase we used a three sub-lattice model with the following sub-lattice occupation – $(Al, Co\%, Fe\%, Ni)_8$:$(Al, Co\%, Cr\%, Fe\%, Ni)_{18}$:$(Cr)_4$.

The available thermodynamic descriptions of the binary, ternary as well as quaternary Al–Co–Cr–Ni (Gheno et al., 2015) sub-systems were included for the extrapolation to the quinary system. Ternary and quaternary systems with incomplete thermodynamic description or descriptions with incompatible

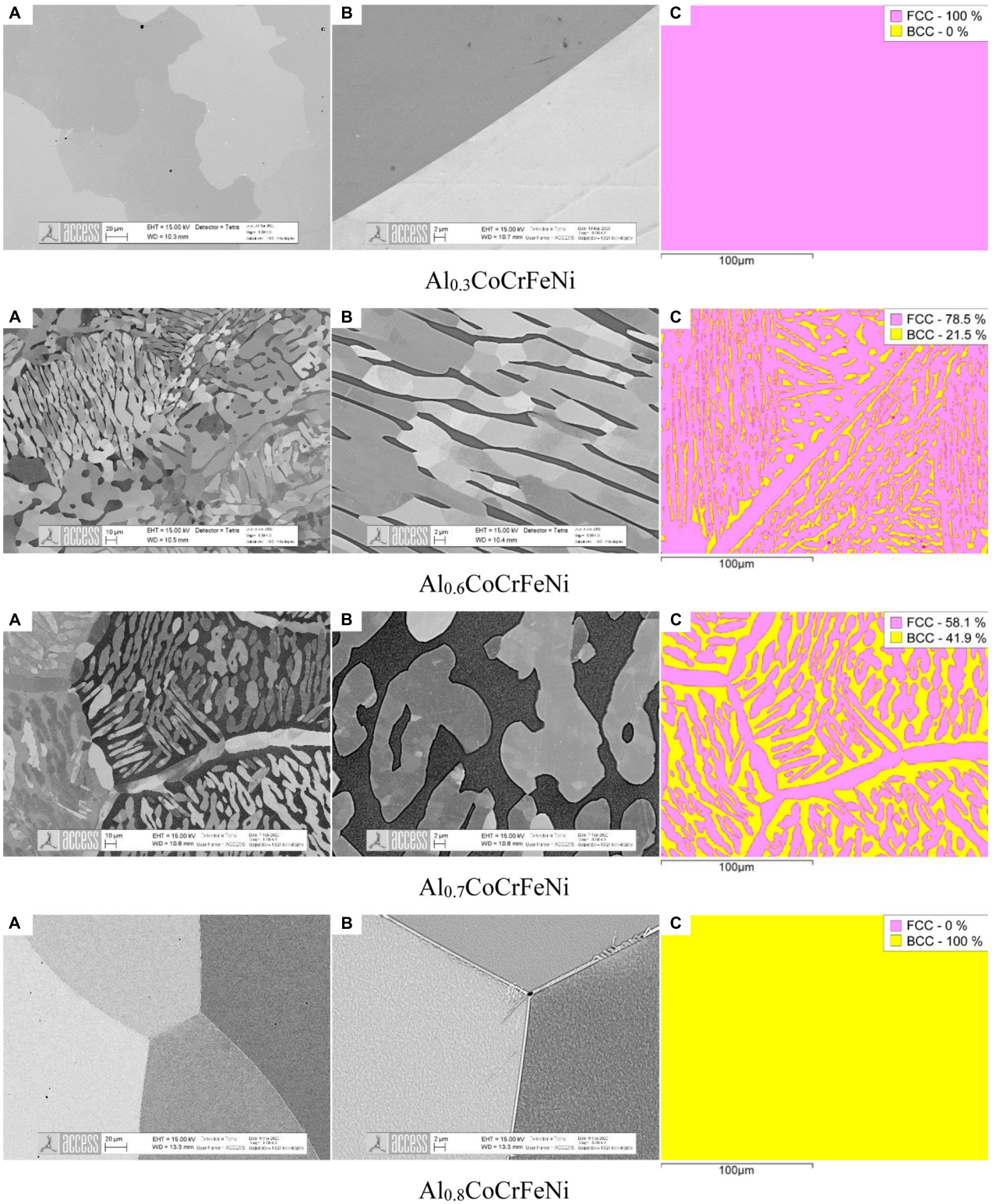

FIGURE 2 | Microstructures **(A)** of $Al_xCoCrFeNi$ samples (x = 0.3, 0.6, 0.7, 0.8) after annealing at 1300°C for 6 h followed by water quenching. **(B)** is a magnified area of interest from **(A)**. The EBSD phase maps show the measured phase fractions in **(C)**. Note that the BCC-B2 phase (dark) in $Al_{0.7}CoCrFeNi$ is spinodally decomposed into BCC-A2 + BCC-B2. The spinodal wavelength suggests that decomposition occurred during the water quenching process.

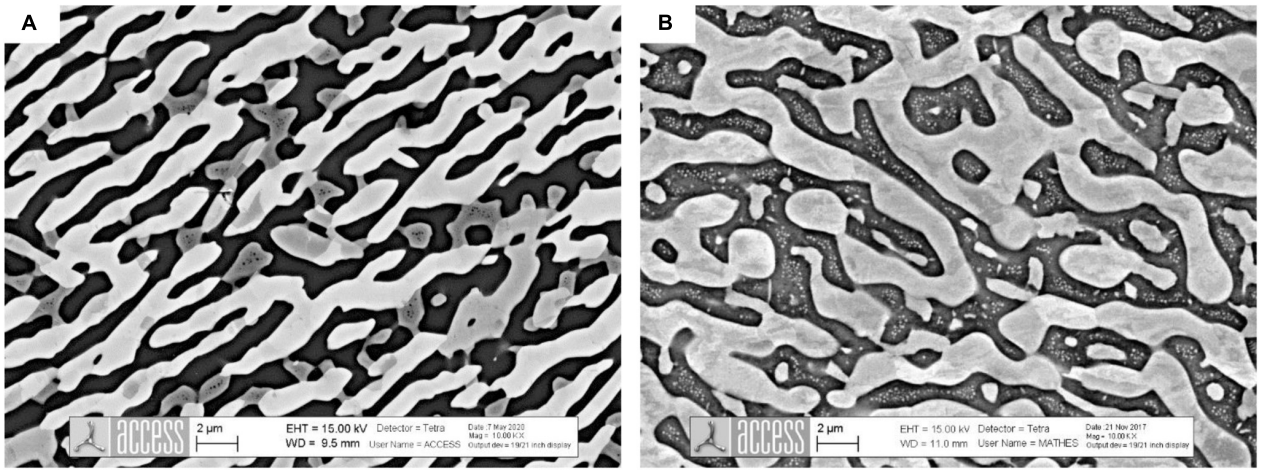

FIGURE 3 | Microstructure of $Al_{0.8}CoCrFeNi$ after annealing at 1000°C/24 h **(A)** followed by water quenching. In **(A)** the microstructure shows three phases: black phase – BCC-B2, dark gray – BCC-A2 and light gray – FCC-A1. The two phases BCC-A2 and BCC-B2 coarsen significantly such that initial spinodal structure cannot be distinguished. In **(B)** the microstructure of $Al_{0.8}CoCrFeNi$ after annealing at 1180°C/30 min is composed of two phases, while the third phase BCC-A2 with nano-size spherical shape formed by spinodal decomposition upon quenching.

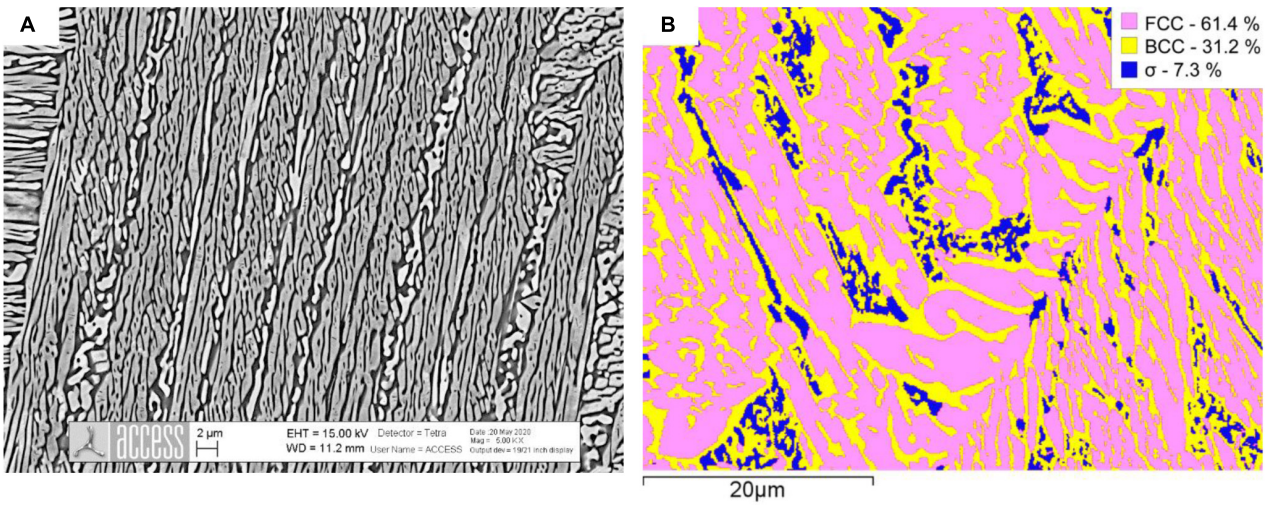

FIGURE 4 | SEM image of the microstructure of $Al_{0.7}CoCrFeNi$ after annealing at 900°C/24 h followed by water quenching **(A)** and EBSD phase map with phase fractions **(B)** given in the legend.

sub-lattice models were re-modeled and optimized. In total, the extrapolation toward quinary Al–Co–Cr–Fe–Ni system requires the reliable thermodynamic description of 10 binary, 10 ternary, and 5 quaternary sub-systems. The description of the ternary sub-system Al–Fe–Ni from Zhang et al. (2009) had to be modified with the respect to phase equilibria between liquid and BCC-B2, BCC-A2, FCC-A1, and FCC-$L1_2$. The quaternary system Al–Fe–Cr–Ni was fully reoptimized and will be presented elsewhere in due details. In the course of the optimization we introduced quaternary and even quinary interaction parameters for the phases with a broad homogeneity range i.e., liquid and BCC-A2, BCC-B2, FCC-A1, FCC-$L1_2$ and σ-phase.

Phase equilibria computed with the new thermodynamic database are displayed in **Figure 6**. Shown are selected sections through the quaternary and quinary composition space, featuring the dependency of phase equilibria on the aluminium content for $Al_xCrFe_2Ni_2$ and $Al_xCoCrFeNi$ alloys. For comparison, the same section planes were calculated with the database TCHEA4. For convenience in all diagrams the boundary of phase regions containing BCC-A2 in various equilibria is represented as bold black line. We highlighted this boundary because in wide parts it corresponds to the binodal line leading to spinodal decomposition of BCC-B2 into Fe, Cr-rich and Al, Ni-rich phases. Note that the Fe, Cr-rich phase (BCC-A2) is disordered. Interestingly in the quinary system the binodal line coincides

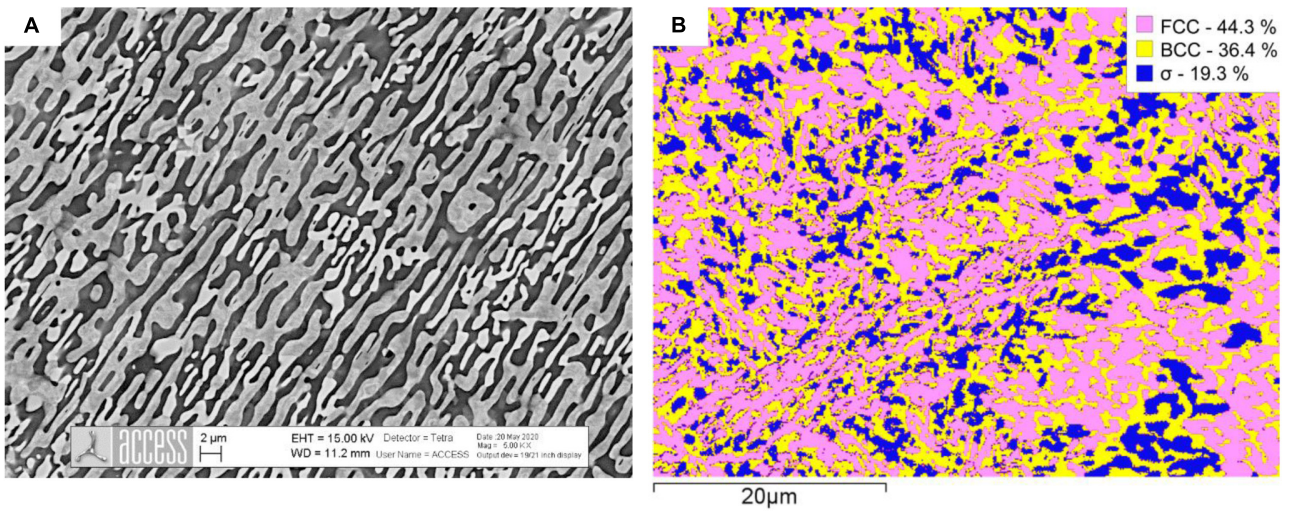

FIGURE 5 | SEM image of the microstructure of $Al_{0.8}CoCrFeNi$ after annealing at 900°C/24 h followed by water quenching **(A)** and EBSD phase map with phase fractions **(B)** given in the legend.

with the order-disorder transition while in the quaternary system the order-disorder transition can be distinguished, being represented by dotted line.

In the following we describe the main differences between the newly developed database and TCHEA4:

1. in the quinary sections (see **Figures 6A,B**), the BCC-B2 phase is more stable, opening a large BCC-B2 single phase region down to temperatures of around 1100°C. Also, the phase boundary BCC-B2/FCC-A1 is shifted to lower Al content at high temperatures. As a consequence, the three-phase field FCC-A1 + BCC-A2 + BCC-B2 appears only at temperatures below 1100°C. This is a key feature to explain the experimental observations described in section "Microstructure analysis after isothermal annealing experiments" relating to phase equilibria and microstructural features in alloy $Al_{0.8}CoCrFeNi$ annealed at 1300°C and at 1180°C respectively (see **Figures 2**, **3B**).
2. the comparison of the quinary sections further reveals that according to TCHEA4 there is an extended two-phase field "BCC-B2 + σ" which encompasses alloys between 15 and 20 at.% Al reaching up to 1000°C. In the new thermodynamic description this two-field is stable only in the temperature range from 600 to 800°C. Instead, the three-phase field FCC-A1 + BCC-B2 + σ and the four-phase field FCC-A1 + BCC-A2 + BCC-B2 + σ are more extended. This is in agreement with experimental observations obtained by annealing experiments at 900°C for alloys $Al_{0.7}CoCrFeNi$ and $Al_{0.8}CoCrFeNi$ (see **Figures 4**, **5**).
3. in the quaternary section $Al_xCrFe_2Ni_2$ (see **Figures 6C,D**) the new thermodynamic description shows the similar extended stability of single-phase BCC-B2 as discussed in (1). This is essential to describe the experimentally observed Widmanstätten and vermicular dual phase microstructures as described in Hecht et al. (unpublished) "The BCC-FCC phase transformation pathways and crystal orientation relationships in dual phase materials from Al–(Co)–Cr–Fe–Ni alloys," submitted for publication in the same topic edition. Furthermore, the liquidus surface differs considerably including melting temperatures. BCC-A2 appears in equilibrium with liquid for small range of alloy compositions followed by a distinct order-disorder transition which does not coincide with the binodal line. Consequently, the FCC-A1 + BCC-B2 phase field predicted by TCHEA4 is confined to a narrow composition range while FCC-A1 + BCC-A2 field is extend up to solidus temperatures. Further differences relate to the stability range of FCC-L12 and σ-phase which need further validations.

Figure 7A picks up the quinary section plane $Al_xCoCrFeNi$ in more detail down to lower temperatures including experimental data points form DSC/DTA analysis which originate from own experiments [see section "Phase transformation temperatures from differential thermal analysis (DTA)"] and from literature as shown in the legend. Most literature data and own measurements related to solidus temperatures for liquid + BCC-B2 equilibria are lower than computed values. This needs further attention either with respect to modeling or to experimental conditions. We performed segregation measurements (see **Figure 8**) to provide more insight into the melting interval but further DTA experiments are needed, especially for homogenized samples which do not show segregation inherited from solidification.

In **Figure 7B** the quinary section plane $Al_xCoCrFeNi$ is re-plotted and contains experimental data points which represent the equilibrium phases obtained from a series of isothermal annealing experiments. The experimental results from Munitz et al. (2016), Butler and Weaver (2017), and He et al. (2017)

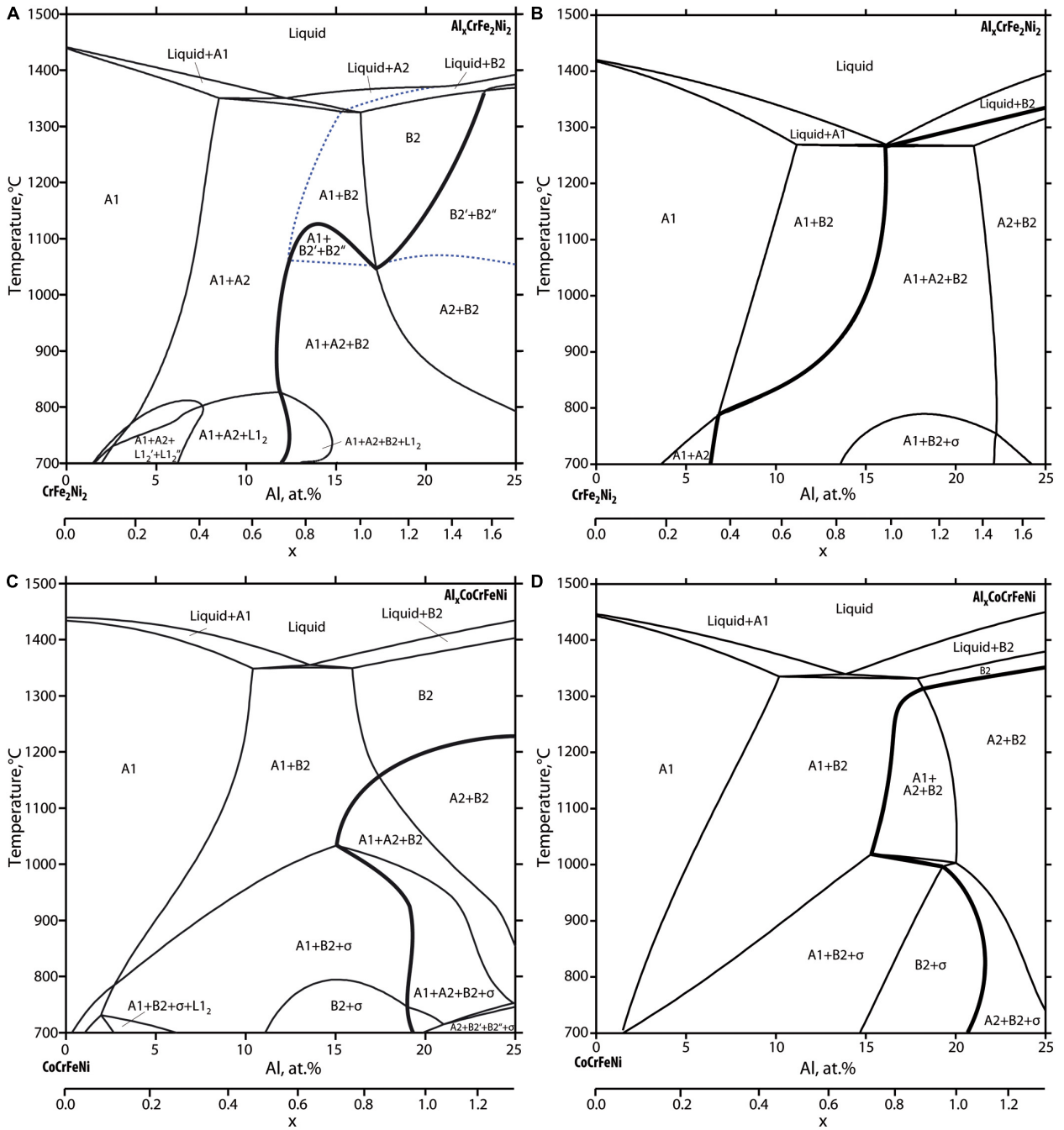

FIGURE 6 | Quaternary $Al_xCrFe_2Ni_2$ and quinary $Al_xCoCrFeNi$ section planes computed with the new thermodynamic description **(A,C)** and compared to TCHEA4 **(B,D)**. The binodal line is highlighted (bold line). BCC-A2/BCC-B2 order-disorder boundary is plotted with dashed line. Except for liquid and σ-phase, the phases are labeled following Strukturbericht designation.

are included. The symbols superimposed on the section plane are selected such that the degree of filling corresponds to the number of experimentally identified phase irrespective of the symbol's shape. For examples, a square symbol filled in a quarter area represents a single-phase microstructure, while full symbols are four phased microstructures. The shaded area below 700°C represents the region in which the FCC-$L1_2$ phase participates in all phase equilibria. The stability limit of all the FCC-$L1_2$ phase fields agrees well with the experimental results of isothermal annealing presented in Gwalani et al. (2016, 2017) and Jones et al. (2016). Due to significantly slower rates of phase transformation and equilibration of the microstructure at low temperatures,

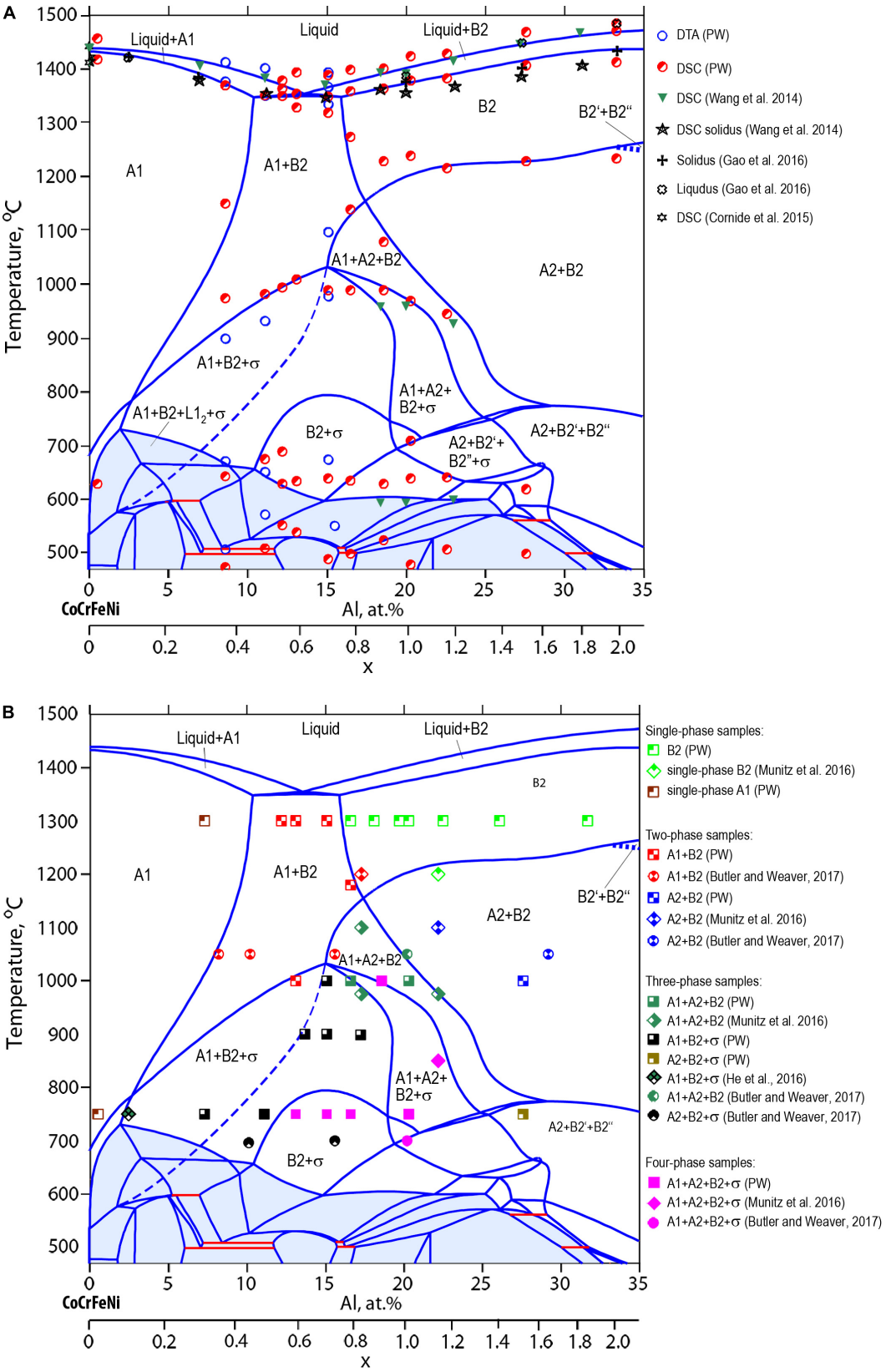

FIGURE 7 | Quinary section plane for Al_xCoCrFeNi alloys superimposed with DSC/DTA data points **(A)** and the equilibrium phases identified after annealing at 750, 1000, and 1300°C **(B)**. Our experimental results (PW) as well as results from the literature are included in the legend.

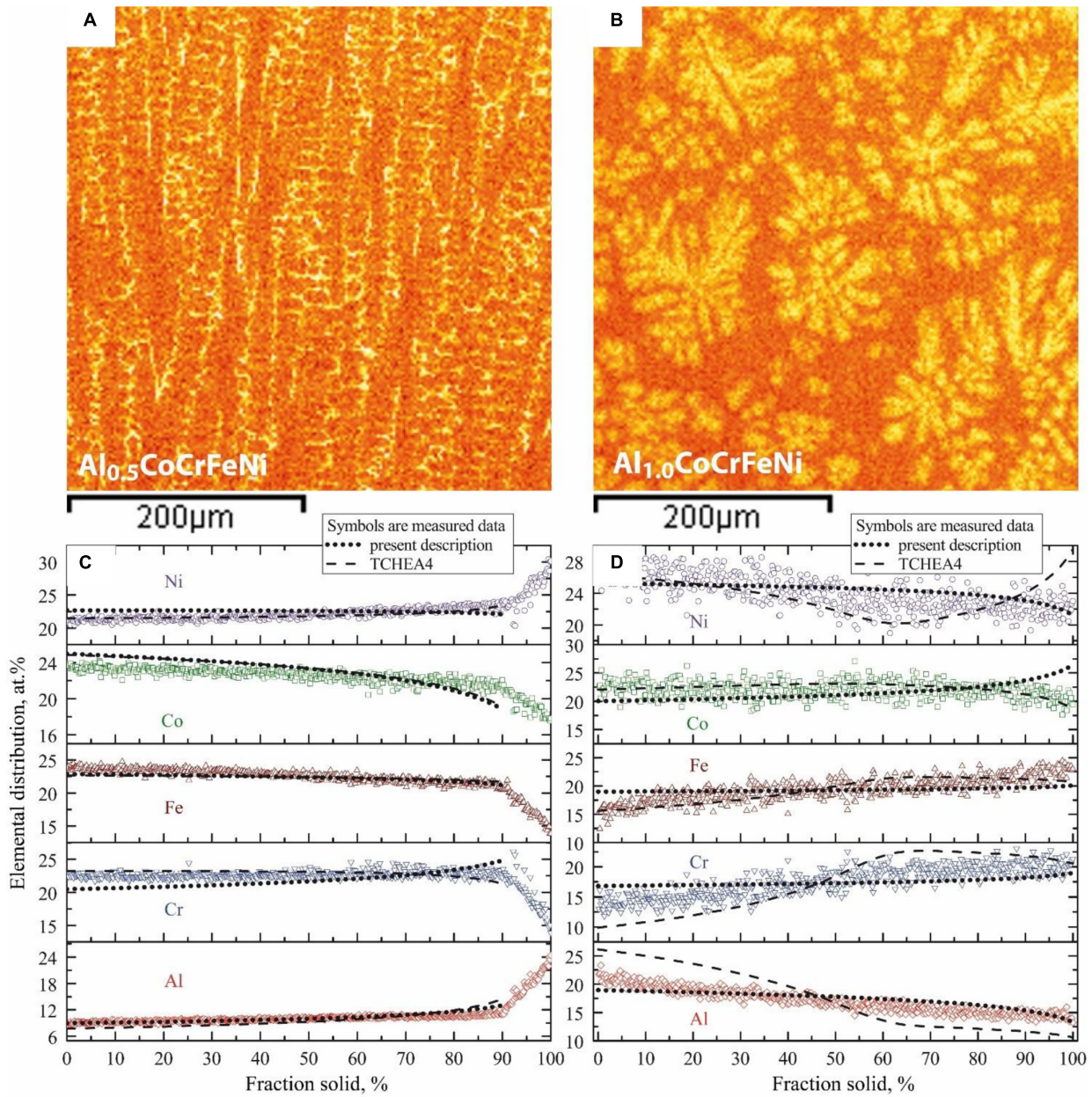

FIGURE 8 | EDS elemental distribution as well as micro-segregation profiles from EDS grid measurements and weighted interval rank sorting (WIRS) in alloys $Al_{0.5}CoCrFeNi$ **(A,C)** and $Al_{1.0}CoCrFeNi$ **(B,D)**. The measurements are compared to computations using Scheil simulation of solidification. Simulation results with present description are represented by dotted line, while TCHEA4 results are represented by dashed line.

the phase fields encapsulated by the shaded area were not experimentally verified in the present work.

Figure 7B allows drawing the following conclusions:

The samples with Al concentration between 10 at.% and 20 at.% annealed at 750°C/48 h show four-phase microstructures i.e., FCC-A1 + BCC-A2 + BCC-B2 + σ. However, the quinary section plane shows that at 750°C these alloy compositions are located in either two- or three phase fields in which BCC-A2 and/or FCC-A1 phases are not present. The difference between the annealed samples and the predictions of the new database is related to non-equilibrium state of the microstructure. Indeed, under conditions when the annealing times are not sufficient to achieve full equilibrium, the BCC-A2 and/or FCC-A1 phases do not transform fully into σ-phase. This is attributed to the slow kinetics of σ-phase formation, possibly also affected by slower diffusion in HEA alloys. As a result, the position of the BCC-A2 phase boundary as well as stability range of σ-phase below 1000°C becomes dependent on the annealing time. A dashed line in the quinary section plane shows the shift of the BCC-A2 phase boundary when σ-phase is suspended. This indicates that

experimental microstructures did not reach full equilibrium. This is in agreement with results reported by Butler and Weaver (2017) on isothermal annealing of the $Al_{0.7}$CoCrFeNi alloy at 700°C for a duration of 1000 h. They report three phase microstructures FCC-A1 + BCC-B2 + σ meaning that the samples are closer to equilibrium compared to our samples. Nonetheless, the two-phase BCC-B2 + σ field is not reached.

At the annealing temperature of 900°C, the microstructure of the $Al_{0.7}$CoCrFeNi and $Al_{0.8}$CoCrFeNi consists of three phases i.e., FCC-A1 + BCC-B2 + σ, in agreement with the computed section plane. At this temperature the BCC-A2 fully transformed into σ-phase.

From all the compositions annealed at 1000°C, a small fraction of σ-phase (0.8 area%) was detected only in $Al_{0.7}$CoCrFeNi alloy. As a result, the highest point of the "σ-bell" in terms of temperature was modeled at this alloy composition. Such position of σ boundary agrees with experimental results presented in Munitz et al. (2016) where AlCoCrFeNi was annealed at 975, 1100, and 1200°C. The authors considered dendritic (DC) and inter-dendritic (ID) regions as two separate alloy compositions. Additionally, the results of Butler and Weaver (2017) were included for $Al_{0.7}$CoCrFeNi annealed at 1050°C/520 h. The reported microstructure is at the border of the computed three-phase field i.e., FCC-A1 + BCC-A2 + BCC-B2 and the neighboring two-phase field FCC-A1 + BCC-B2. Very likely it is in the two-phase field because the authors discussed in detail the formation of BCC-A2 nano-precipitates within the BCC-B2 matrix. Likely the precipitates formed upon spinodal decomposition during quenching, otherwise they should be coarse given the annealing temperature and time. Similar quenching effects were observed in $Al_{0.8}$CoCrFeNi annealed at 1180°C as was discussed in section "Microstructure analysis after isothermal annealing experiments."

Data from annealing at 1300°C/6 h clearly show the limits of the FCC-A1 + BCC-B2 phase field. Starting from $Al_{0.8}$CoCrFeNi and up to $Al_{2.0}$CoCrFeNi the microstructure is single-phase BCC-B2.

As mentioned before, we questioned the width of the solidification interval related to liquid + BCC-B2 equilibria. In the proposed thermodynamic description this interval is narrow and should lead to less severe micro-segregation compared to a wide interval. To address this issue in the Al–Co–Cr–Fe–Ni system we used grid statistical EDS analysis of micro-segregation in as-cast samples together with the weighted interval rank sorting (WIRS) procedure described by Ganesan et al. (2005) for multicomponent systems. For the analysis two alloy compositions were selected, i.e., $Al_{0.5}$CoCrFeNi and $Al_{1.0}$CoCrFeNi and the samples were produced by arc melting. These alloys solidified with primary FCC-A1 or BCC-B2 phase, respectively. EDS measurements were performed on as-cast specimens using equidistant grids with a spacing of 20 μm. A total of 540 grid points was acquired. The compositional differences measured in the grid allow estimating the segregation amplitude, while the WIRS ranking procedure allows plotting the element distribution as a function of the primary phase fraction in the course of solidification. The ranked element distribution plots can be compared to composition profiles from Scheil simulation of solidification. Both databases were used for this comparison.

Figures 8A,B show EDS elemental maps (only Al) in the region of interest where the EDS grid were placed. They qualitatively show that Al partitions to the last solid, i.e., inter-dendritic regions, in alloy $Al_{0.5}$CoCrFeNi while the opposite is true for alloy $Al_{1.0}$CoCrFeNi. The experimental segregation profiles evaluated for each element by grid EDS are plotted in **Figures 8C,D**. Segregation profiles from Scheil simulations are superimposed as dashed and dotted lines. The simulation was done with all phases suspended except liquid and primary phases, i.e., FCC-A1 or BCC-B2. This constraint was applied both to the new thermodynamic description and to TCHEA4. Furthermore, for $Al_{0.5}$CoCrFeNi alloy the Scheil calculations were terminated at fraction solid of 0.9. Such limitation is based on the experimental segregation profiles showing that at this fraction solid the secondary phase, i.e., BCC-B2, emerged along the solidification path. Hence, the slope of the profiles in $Al_{0.5}$CoCrFeNi alloy becomes rapidly steeper due to different solubility of the elements in FCC-A1 and BCC-B2. Since alloy $Al_{1.0}$CoCrFeNi solidified fully with BCC-B2, no constrain was applied.

Generally, the trends of the experimental segregation profiles for $Al_{0.5}$CoCrFeNi alloy are reproduced well both by the proposed thermodynamic description and TCHEA4. Stronger discrepancies are observed for the $Al_{1.0}$CoCrFeNi alloy. Specifically, the Scheil profiles for Cr and Al computed by TCHEA4 deviate strongly from the experimental data points especially at low fraction solid, i.e., starting with much higher Al content. This indicates that the width of the solidification interval is overestimated in TCHEA4. Furthermore, the Scheil profiles for Ni, Cr, and Al show unexpected behavior with changing slopes. Especially for Al and Cr, the amplitudes of the sinusoidal curve are high, extending beyond the measured segregation range.

CONCLUSION

In this work we presented phase equilibria in the Al–Co–Cr–Fe–Ni HEA system from annealing experiments and CALPHAD modeling of the quinary alloy system.

In the first part we described DTA/DSC measurements and microstructures obtained by isothermal annealing for a series of Al_xCoCrFeNi samples with $0.3 < x < 1.5$. Main attention was given to isothermal annealing at 1300°C/6 h, followed by water quenching. We showed that at 1300°C the microstructure of $Al_{0.7}$CoCrFeNi alloy consists of two phases i.e., BCC-B2 and FCC-A1, while alloy $Al_{0.8}$CoCrFeNi is already in the single BCC-B2 phase field. Further key insights were obtained from other annealing conditions as follows:

1. At 1180°C the alloy $Al_{0.8}$CoCrFeNi consists of two phases FCC-A1 and BCC-B2 and does not contain BCC-A2. This phase is formed upon quenching only, meaning that the binodal temperature marking the co-existence of BCC-A2 and BCC-B2 in this alloy must be below 1180°C.

2. Isothermal annealing experiments at 1000 and 900°C allowed concluding about the extent of the σ-bell in the system. The σ-phase is not present above 1000°C.

In the second part we presented computational results from an own thermodynamic database for the quinary Al–Co–Cr–Fe–Ni alloy system developed by the CALPHAD approach on the basis of the experimental results and data from literature. We compared quaternary and quinary section planes i.e., $Al_xCrFe_2Ni_2$ and $Al_xCoCrFeNi$ to computations performed with the TCHEA4 database from Thermo-Calc AB. The computations differ substantially in terms of phase fields and boundaries of the phase fields. The main findings are listed below:

1. According to our new thermodynamic description a rather wide single-phase field BCC-B2 is present in both section planes, giving rise to dual-phase microstructures along solid state phase transformation pathways. The BCC-B2 phase undergoes spinodal decomposition when cooled below the binodal line. The binodal line intersects other phase field boundaries, and as a consequence more complex solid-state transformations are expected and have been observed for appropriate alloy compositions. Further points of interest are the extent of phase fields which contain the σ-phase. The σ-phase reaches a maximum stability for the $Al_{0.7}CoCrFeNi$ alloy composition being stable up to 1000°C. According to our new description the two-phase field (BCC-B2 + σ) predicted with TCHEA4 in $Al_xCoCrFeNi$ is found only between 600 and 800°C and instead we see a four-phase field FCC-A1 + BCC-A2 + BCC-B2 + σ and a three phase field FCC-A1 + BCC-B2 + σ in the respective compositional range. Last but not least our database predicts the FCC-$L1_2$ phase to be stable below 700°C for a wide range of alloy compositions.
2. Equilibria with the liquid phase involve liquid + FCC-A1, liquid + BCC-B2 and in $Al_xCrFe_2Ni_2$ also a narrow region where BCC-A2 is the primary phase. We attempted to estimate the micro-segregation inherited from solidification and compare it to element distribution profiles computed in Scheil approximation for the alloys $Al_{0.5}CoCrFeNi$ and $Al_{1.0}CoCrFeNi$, respectively. We showed that both databases can reproduce the experimental segregation profiles for alloy $Al_{0.5}CoCrFeNi$. Our own database performs better than TCHEA4 for the alloy $Al_{1.0}CoCrFeNi$, suggesting that the equilibrium solidification interval of alloys with primary BCC-B2 is indeed narrow.

Future research on thermodynamic equilibria is requested in several directions, mainly to verify phase field boundaries in these and other section planes. In an upcoming publication we will present interesting section planes to guide experiment design. Further validations will have to include phase equilibria for specified alloys as function of temperature, including the phase fractions and phase compositions for temperatures of interest.

DATA AVAILABILITY STATEMENT

The raw data supporting the conclusions of this article will be made available by the authors, without undue reservation.

AUTHOR CONTRIBUTIONS

OS carried out the experimental work presented in the manuscript including production, isothermal annealing, SEM investigations, and EBSD analysis of the samples. VW developed and optimized the thermodynamic database for quinary Al–Co–Cr–Fe–Ni alloy system. UH performed the EDS measurements of the segregation profiles in the as-cast alloys, assisted with post-processing of the measured data, and actively participated and coordinated the discussion of the experimental results and development of the database. SG and DR provided the additional experimental results for optimization and verification of the quaternary Al–Cr–Fe–Ni section. All authors contributed to the article and approved the submitted version.

FUNDING

The research was supported by the German Federal Ministry for Education and Research (BMBF) under grant number 03XP0163A in the frame of the M-era.Net Joint Call 2017, Project NADEA (no. 5129). Further, the European Funds for Regional Development [*German: Europäischer Fond für regionale Entwicklung (EFRE)*], and the LeitmarktAgentur. NRW supported the research under the grant number EFRE0800625 in the frame of the HEW-Form project.

REFERENCES

Abuzaid, W., and Sehitoglu, H. (2018). Plastic strain partitioning in dual phase Al13CoCrFeNi high entropy alloy. *Mater. Sci. Eng. A* 720, 238–247. doi: 10.1016/j.msea.2018.02.044

Aizenshtein, M., Strumza, E., Brosh, E., and Hayun, S. (2020). Precipitation kinetics, microstructure, and equilibrium state of A2 and B2 phases in multicomponent Al2.75CoCrFeNi alloy. *J. Mater. Sci.* 55, 7016–7028. doi: 10.1007/s10853-020-04487-9

Boettinger, W. J., Kattner, U. R., Moon, K. W., and Perepezko, J. H. (2006). *DTA and Heat-flux DSC Measurements of Alloy Melting and Freezing*. Washington: U.S. Government Printing Office.

Butler, T. M., and Weaver, M. L. (2016). Influence of annealing on the microstructures and oxidation behaviors of Al8(CoCrFeNi)92, Al15(CoCrFeNi)85, and Al30(CoCrFeNi)70 high-entropy alloys. *Metals* 6:222. doi: 10.3390/met6090222

Butler, T. M., and Weaver, M. L. (2017). Investigation of the phase stabilities in AlNiCoCrFe high entropy alloys. *J. Alloy Compd.* 691, 119–129. doi: 10.1016/j.jallcom.2016.08.121

Chen, H. L., Mao, H., and Chen, Q. (2018). Database development and Calphad calculations for high entropy alloys: challenges, strategies, and tips. *Mater. Chem. Phys.* 210, 279–290. doi: 10.1016/j.matchemphys.2017.07.082

Chen, X., Qi, J. Q., Sui, Y. W., He, Y. Z., Wei, F. X., Meng, Q. K., et al. (2017). Effects of aluminum on microstructure and compressive properties of Al-Cr-Fe-Ni eutectic multi-component alloys. *Mater. Sci. Eng. A* 681, 25–31. doi: 10.1016/j.msea.2016.11.019

CompuTherm Plc (2020). *PanHEA*. Available online at: https://computherm.com/?docs=pandat-database-manual/database-manual/panhea (accessed May 20, 2020).

Dong, Y., Gao, X., Lu, Y., Wang, T., and Li, T. (2016). A multi-component AlCrFe2Ni2 with excellent mechanical properties. *Mater. Lett.* 169, 62–64. doi: 10.1016/j.matlet.2016.01.096

Ganesan, M., Dye, D., and Lee, P. D. (2005). Technique for characterizing microsegregation in multicomponent alloys and its application to single-crystal superalloy castings. *Metall. Mater. Trans. A* 36, 2191–2204. doi: 10.1007/s11661-005-0338-2

Gao, M. C., Yeh, J. W., Liaw, P. K., and Zhang, Y. (2016). *High-Entropy Alloys: Fundamentals and Applications*. Cham: Springer.

Ghassemali, E., Sonkusare, R., Biswas, K., and Gurao, N. P. (2017). In-situ study of crack initiation and propagation in a dual phase AlCoCrFeNi high entropy alloy. *J. Alloys Compd.* 710, 539–546. doi: 10.1016/j.jallcom.2017.03.307

Gheno, T., Liu, X. L., Lindwall, G., Liu, Z. K., and Gleeson, B. (2015). Experimental study and thermodynamic modeling of the Al-Co-Cr-Ni system. *Sci. Technol. Adv. Mater.* 16:5. doi: 10.1088/1468-6996/16/5/055001

Gorsse, S., and Senkov, O. N. (2018). About the Reliability of CALPHAD Predictions in Multicomponent Systems. *Entropy* 20:899. doi: 10.3390/e20120899

Gwalani, B., Gangireddy, S., Zheng, Y., Soni, V., Mishra, R. S., and Banerjee, R. (2019). Influence of ordered L12 precipitation on strain-rate dependent mechanical behavior in a eutectic high entropy alloy. *Sci. Rep.* 9:6371. doi: 10.1038/s41598-019-42870-y

Gwalani, B., Soni, V., Choudhuri, D., Lee, M., Hwang, J. Y., Nam, S. J., et al. (2016). Stability of ordered L12 and B2 precipitates in face centered cubic based high entropy alloys - Al0.3CoFeCrNi and Al0.3CuFeCrNi2. *Scr. Mater.* 123, 130–134. doi: 10.1016/j.scriptamat.2016.06.019

Gwalani, B., Soni, V., Lee, B., Mantri, S., Ren, Y., and Banerjee, R. (2017). Optimizing the coupled effects of Hall-Petch and precipitation strengthening in a Al0.3CoCrFeNi high entropy alloy. *Mater. Des.* 121, 254–260. doi: 10.1016/j.matdes.2017.02.072

He, F., Wang, Z., Wu, Q., Li, J., Wang, J., and Liu, C. T. (2017). Phase separation of metastable CoCrFeNi high entropy alloy at intermediate temperatures. *Scr. Mater.* 126, 15–19. doi: 10.1016/j.scriptamat.2016.08.008

Jones, N. G., Izzo, R., Mignanelli, P. M., Christofidou, K. A., and Stone, H. J. (2016). Phase evolution in an Al0.5CrFeCoNiCu high entropy alloy. *Intermetallics* 71, 43–50. doi: 10.1016/j.intermet.2015.12.001

Leo, T. H., Ocelík, V., and De Hosson, J. T. M. (2017). Orientation Relationships in Al0.7CoCrFeNi High-Entropy Alloy. *Microsc. Microanal.* 23:905. doi: 10.1017/S1431927617012442

Lim, K. R., Lee, K. S., Lee, J. S., Kim, J. Y., Chang, H. J., and Na, Y. S. (2017). Dual-phase high-entropy alloys for high-temperature structural applications. *J. Alloys Compd.* 728, 1235–1238. doi: 10.1016/j.jallcom.2017.09.089

Lu, Y., Dong, Y., Guo, S., Jiang, L., Kang, H., Wang, T., et al. (2014). A promising new class of high-temperature alloys: eutectic high-entropy alloys. *Sci. Rep.* 4:6200. doi: 10.1038/srep06200

Munitz, A., Salhov, S., Hayun, S., and Frage, N. (2016). Heat treatment impacts the micro-structure and mechanical properties of AlCoCrFeNi high entropy alloy. *J. Alloys Compd.* 683, 221–230. doi: 10.1016/j.jallcom.2016.05.034

Nagase, T., Takemura, M., Matsumuro, M., and Maruyama, T. (2017). Solidification microstructure of AlCoCrFeNi2.1 eutectic high entropy alloy ingots. *Mater. Trans.* 59:2. doi: 10.11279/jfes.89.119

Rao, J. C., Diao, H. Y., Ocelík, V., Vainchtein, D., Zhang, C., and Kuo, C. (2017). Secondary phases in AlxCoCrFeNi high-entropy alloys: an in-situ TEM heating study and thermodynamic appraisal. *Acta Mater.* 131, 206–220. doi: 10.1016/j.actamat.2017.03.066

Shi, Y., Yang, B., Xie, X., Brechtl, J., Dahmend, K. A., and Liaw, P. K. (2017). Corrosion of AlxCoCrFeNi high-entropy alloys: al-content and potential scan-rate dependent pitting behavior. *Corros Sci.* 119, 33–45. doi: 10.1016/j.corsci.2017.02.019

Thermo-Calc Software (2020). *TCHEA4*. Available online at: https://www.thermocalc.com/products-services/databases/thermodynamic/ (accessed May 20, 2020).

Wang, W. R., Wang, W. L., Wang, S. C., Tsai, Y. C., Lai, C. H., and Yeh, J. W. (2012). Effects of Al addition on the microstructure and mechanical property of AlxCoCrFeNi high-entropy alloys. *Intermetallics* 26, 44–51. doi: 10.1016/j.intermet.2012.03.005

Wang, W. R., Wang, W. L., and Yeh, J. W. (2014). Phases, microstructure and mechanical properties of AlxCoCrFeNi high-entropy alloys at elevated temperatures. *J. Alloys Compd.* 589, 143–152. doi: 10.1016/j.jallcom.2013.11.084

Wani, I. S., Bhattacharjee, T., Sheikh, S., Lu, Y. P., Chatterjee, S., Bhattacharjee, P. P., et al. (2016). Ultrafine-grained AlCoCrFeNi2.1 eutectic high-entropy alloy. *Mater. Res. Lett.* 4, 174–179. doi: 10.1080/21663831.2016.1160451

Yang, T., Xia, S., Liu, S., Wang, C., Liu, S., Zhang, Y., et al. (2015). Effects of Al addition on microstructure and mechanical properties of AlxCoCrFeNi high-entropy alloy. *Mater. Sci. Eng. A* 26, 44–51. doi: 10.1016/j.msea.2015.09.034

Zhang, C., Zhang, F., Diao, D., Gao, M. C., Tang, Z., and Poplawsky, J. D. (2016). Understanding phase stability of Al-Co-Cr-Fe-Ni high entropy alloys. *Mater. Des.* 109, 425–433. doi: 10.1016/j.matdes.2016.07.073

Zhang, L., Wang, J., Du, Y., Hu, R., Nash, P., Lu, X. G., et al. (2009). Thermodynamic properties of the Al-Fe-Ni system acquired via a hybrid approach combining calorimetry, first-principles and CALPHAD. *Acta Mater.* 57:18. doi: 10.1016/j.actamat.2009.07.031

Conflict of Interest: The authors declare that the research was conducted in the absence of any commercial or financial relationships that could be construed as a potential conflict of interest.

frontiers in Materials

ORIGINAL RESEARCH
published: 11 August 2020
doi: 10.3389/fmats.2020.00275

Laser Metal Deposition of Ultra-Fine Duplex $AlCrFe_2Ni_2$-Based High-Entropy Alloy

Veronica Rocio Molina[1], Andreas Weisheit[1], Sergej Gein[2], Ulrike Hecht[2] and Dimitrios Vogiatzief[3]*

[1] Fraunhofer Institute for Laser Technology ILT, Aachen, Germany, [2] Access e.V., Aachen, Germany, [3] Oerlikon AM, Feldkirchen, Germany

A duplex, nano-scale Co-free high-entropy alloy (HEA) based on $AlCrFe_2Ni_2$ was processed using laser material deposition (LMD). Process parameters in various beam diameter configurations, as well as deposition strategies, were used while the alloy microstructure was investigated in the as-built and heat-treated condition. Interlayer regions present a duplex microstructure composed of ultra-fine face-centered cubic (FCC)-platelets nucleated in a nano-scale structured body-centered cubic (BCC) phase. Rapid cooling during LMD induces the decomposition of the BCC phase into ordered and disordered nano-scaled structures. The hard and brittle BCC phase yields a high crack susceptibility during rapid cooling in the LMD process. A suitable processing strategy paired with a post-processing heat treatment was developed to solve this challenge. After heat treatment at 900°C and 6 h annealing time with subsequent furnace cooling, the material presented a homogeneous duplex ultra-fine FCC/BCC microstructure and high bending strength (2310 MPa) compared to a heat-treated cast duplex-steel (1720 MPa) while maintaining excellent ductility (no failure at 20% bending strain).

Keywords: laser material deposition, high-entropy alloy, AlCrFeNi alloy, duplex microstructure, additive manufacturing

OPEN ACCESS

Edited by:
Antonio Caggiano, Darmstadt University of Technology, Germany

Reviewed by:
Yiping Lu, Dalian University of Technology, China
Bharat Gwalani, Pacific Northwest National Laboratory (DOE), United States

****Correspondence:***
Veronica Rocio Molina
veronica.molina@ilt.fraunhofer.de

Specialty section:
This article was submitted to Structural Materials, a section of the journal Frontiers in Materials

Received: *31 May 2020*
Accepted: *23 July 2020*
Published: *11 August 2020*

Citation:
Molina VR, Weisheit A, Gein S, Hecht U and Vogiatzief D (2020) Laser Metal Deposition of Ultra-Fine Duplex $AlCrFe_2Ni_2$-Based High-Entropy Alloy. Front. Mater. 7:275. doi: 10.3389/fmats.2020.00275

INTRODUCTION

The concept of "high-entropy alloys (HEAs)" has been a breakthrough in the field of alloy development (Yeh et al., 2004). As opposed to conventional alloying of metals, this method exploits the high mixing entropy of multi-element compounds in equimolar or near-equimolar ratios, to avoid the formation of brittle intermetallic phases. Thus, various HEA-materials reportedly exhibit both high-strength and ductility as well as good corrosion and wear resistance in cast parts (Chuang et al., 2011; Shi et al., 2017; Chen et al., 2018; Niu et al., 2019). Consequently, these materials hold great potential for the fabrication of parts, such as pump impeller blades, subject to complex stresses (Ma et al., 2016; Yan-dong et al., 2017; Yin et al., 2017). Centrifugal and bending mixed stresses require a high strength material with sufficient ductility for this application. Besides, AlCrCoFeNi-based HEAs have been reported to perform exceptionally in terms of wear resistance, as well as simultaneous strength and ductility properties, which add to the interest toward this material for pump components (Lu et al., 2014; Gao et al., 2017; Shi et al., 2017).

In general, HEA alloy design presumes that a high number of principal elements in the compound – generally above three – will prompt the formation of solid solutions during

solidification (Yeh et al., 2004). This presumption, however, relies on the rapid cooling of the melt to restrict diffusion and thus the growth of intermetallic compounds during solidification (Ocelík et al., 2016). Hence, laser-based additive manufacturing processes such as laser material deposition (LMD), in which cooling rates can reach up to 10^4 K/s, present an interesting prospect as a manufacturing method for HEAs. Various studies report LMD-processed HEA coatings of AlCrCoFeNi-based alloys, which have been found to yield fine-grained solid solution microstructures and allow a crack-free layer deposition (Kuwabara et al., 2018; Cui et al., 2019). Moreover, thin walls and small bulk volumes were fabricated using LMD, resulting in a fine-grained microstructure composed of body-centered cubic (BCC)- and B2 phases in as-built condition (Sistla et al., 2015; Joseph et al., 2017; Wang et al., 2017). Heat treatment trials above 800°C were reported to yield the formation of a softer face-centered cubic (FCC)-phase, reducing the reported brittleness and yield strength, while increasing ductility (Wang et al., 2017).

Despite the promising material properties, the use of cobalt (Co) may be ground for concern given that Co has been reported to carry a high monetary, environmental and human cost in its extraction and refinement (Crundwell et al., 2011). Borkar et al. (2017) performed comparisons between AlCoFeNi and AlCrFeNi alloys by compositionally graded samples produced via LMD. The systematic variation of the $AlCo_xCr_{1-x}FeNi$ HEA composition shows the effect of Co on the microstructure evolution of the material. The presence of an intra-granular (spinoidal) decomposition of the BCC-Matrix into BCC/B2 was found for x = 0.2 and 0. Another Co-free HEA, namely $AlCrFe_2Ni_2$ was proposed by Dong et al. (2016), which presents a microstructure consisting of spinoidally decomposed B2/BCC-phase and an FCC-phase (Shang and Wang, 2017). The material presents a very interesting set of material properties, according to Dong et al. (2016) Cast $AlCrFe_2Ni_2$ was reported to achieve ultimate tensile strength (UTS) of 1228 MPa while withstanding 17% elongation during tensile testing. It was even suggested that these values exceeded those of titanium alloys in as-cast condition (Shang and Wang, 2017). Borkar et al. (2016) reported the fabrication of a Co-free HEA with composition $Al_xCrCuFeNi_2$ ($0 < x < 1.5$). An increase of the Al-content (x = 1.3 and 1.5, vs. 0) in the LMD fabricated HEA was reportedly linked to an increase in microhardness, indicating even higher material strength. In the present study, a near- $AlCrFe_2Ni_2$ alloy with a chemical composition of Al9Cr17Fe36Ni38 (wt.%) was selected for fabrication with LMD to examine the microstructure and material behavior in the as-built and heat-treated condition.

MATERIALS AND METHODS

Two types of samples, named A and B accordingly, correspond to samples built using beam diameters of 0.6 and 1.8 mm, respectively. For a beam diameter of 0.6 mm (A samples), a Laserline LDM 3000-60 fiber-coupled diode laser system paired with a Sulzer Metco Twin 10-C powder feeder (Oerlikon AM) was used. For the 1.8 mm beam diameter configuration, (B samples), an LDF 2000-30 fiber-coupled diode laser and a GTV-PF2/2 powder feeder were employed. In all cases, the powder feeder systems implement argon gas as a protective and conveying medium toward a coaxial powder nozzle. Gas atomized powder with composition Al9Cr17Fe36Ni38 (wt.%), provided by Oerlikon AM was used in this study. A thorough investigation of the powder characteristics of the novel powder material was conducted to rule out powder related material defects. The powders' particle size distribution was analyzed using a CAMSIZER® X2 system and corresponding software.

Hot-work, 10 mm thick 1.2343 (AISI H11) tool steel plates were used as base-plate material in all experiments. Pre-heating of the substrate plate was employed to reduce thermal gradient-related stress. This approach was conducted by placing the substrate material on an electrically heated hot-plate. The temperature was manually adjusted based on a temperature gauge placed on the plate surface. Pre-heating temperatures were set at room temperature (RT), 300 and 450°C for A samples and 450°C for B samples.

Laser material deposition process parameters such as scan speed, laser power, powder feed rate, track overlap, and layer thickness were determined to fabricate cubic bulk volumes with an edge length of 10 mm. For sample type "A" the laser beam diameter was 0.6 mm and for sample type B the laser beam diameter was 1.8 mm. The track overlap was set at 50 and 30%, respectively. The layer thickness employed corresponds to approximately 1/3 of the beam diameter in each case. The track deposition in all sample volumes was conducted in a bidirectional manner, i.e., adjoining tracks are deposited in both directions of a single axis sequentially. An overview of selected process parameter sets for LMD is summarized in **Table 1** and a schematic diagram of the track deposition in a bulk volume is presented in **Figure 1**. Energy density E [J/mm^3] calculations were performed as stated in Equation 1.

Energy density calculation for LMD process:

$$E = \frac{P_L\,[W]}{v\left[\frac{mm}{s}\right] \times \Delta x\,[\mathrm{mm}] \times z_L\,[\mathrm{mm}]} \tag{1}$$

The selection of a certain process parameter window strives toward crack-free build-up and a resulting porosity of max. 0.5%. Both quality characteristics were evaluated utilizing optical microscope analysis on sample cross-sections. The porosity-to-dense material-ratio is measured using "Stream Motion" software from the Olympus Group. Porosity measurements were performed through a gray-scale value analysis of pore vs. dense material surface ratio over the sample cross-section and extrapolated to the entire sample volume. Crack presence in the deposited material was also evaluated using optical microscopy. Crack propagation during metallographic preparation was ruled out by performing dye penetrant testing on selected samples before cutting.

Post-processing heat treatment of selected samples was carried out for microstructure homogenization and stress relaxation purposes for both A- and B- samples. This entails annealing at 900°C in an argon atmosphere for 6 h, followed by air cooling. Microstructure analyses were carried out with the support of Access e.V. with a Zeiss Ultra 55 scanning electron

TABLE 1 | Laser material deposition (LMD) process parameter sets for A- and B Sample production.

Sample type – beam diameter (mm)		Laser power P_L (W)	Scan speed v (mm/min)	Powder feed rate m_P (g/min)	Track overlap Δx (mm)	Layer thickness z_L (mm)	Energy density E (J/mm^3)
A	0.6	365	800	2	0.3	0.2	456.2
B	1.8	550	600	4.3	1.2	0.6	76.4

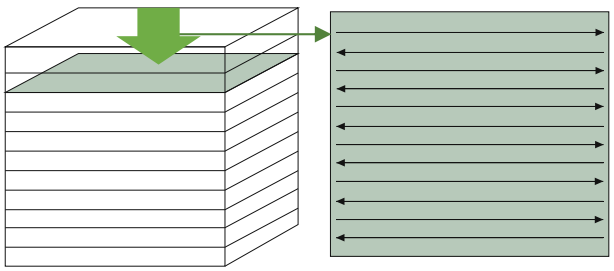

FIGURE 1 | Schematic diagram of bidirectional track deposition pattern in laser material deposition (LMD).

microscopy (SEM) system prior and after heat treatment. SEM analysis was only performed on samples fabricated with the final selected process parameter window for both sample types.

Studies of $AlCrFe_2Ni_2$ report a duplex BCC/FCC microstructure in cast samples and hardness values around 520 HV in vacuum hot pressing coatings of this HEA-material (Dong et al., 2016; Shang and Wang, 2017). In this study, a correspondence between the presence of FCC-phase in the microstructure and lower microhardness values was observed. Microhardness measurements according to Vickers DIN EN ISO 6507 were conducted for all fabricated samples at HV0.3 and 0.5 mm point-to-point distance along the build-height on the sample centerline using a Qness 30A microhardness tester and corresponding Qpix control software.

Additionally, B samples (x:y:z – 10:10:35 mm) were fabricated for a micro-scale three-point bending test before and after heat treatment. For this purpose, an MTI SEMtester 1000 was used. The samples were machined into flat tensile specimens (x:y:z – 10:10:35 mm) from one single LMD sample and bent at a traverse rate of 0.2 mm/min to the point of fraction or up to 20% elongation, which corresponds to the machines' limit. A reference measurement, a DIN 1.4517 duplex steel was used as a reference frame for comparison.

RESULTS

Powder Analysis

Powder analysis results of Al9Cr17Fe36Ni38 (wt.%) material are shown in **Figure 2**. The particle size distribution of a powder sample in terms of particle count (q0) and particle volume (q3) vs. particle equivalent diameter is shown in **Figure 2A**. For clarity purposes, the x-coordinate is transformed into a logarithmic scale. After logarithmic transformation, the variables are named q0* and q3* in **Figure 2A**, respectively.

The volume distribution curve shows a single peak at 44 μm, corresponding to the 50-percentile value of the measurement. That is, roughly 50% of the powder should consist of particles larger than 44 μm in size. The 10-percentile was found at 34 μm and the 90-percentile at 69 μm in a volume distribution. However, the particle count or number distribution curve presents a different profile. A large peak is logged at 2.5 μm, which corresponds to the 10-percentile value. In this case, the 50-percentile is logged at 33 μm and 90-percentile at 47 μm. Hence, roughly 50% of the measured particles are smaller than 33 μm and only about 10% of the particles correspond to a size larger than 47 μm. Considering the nominal particle size range of 20–90 μm, a large number of fine particles are present in the powder material.

A high number of fine particles as well as non-spherical particles could lead to deficient flowability and consequently, inhomogeneous powder layer deposition during LMD. Using SEM micrographs, the powder material was further analyzed by visual examination as shown in **Figure 2B**. Fine particles are found predominantly in agglomerates and sintered to larger particles (satellites). The majority of observed particles present a spherical shape and no surface porosity.

Processability in LMD

The pre-heating temperature was found to have an impact on the inhibition of defect formation during the LMD processing of Al9Cr17Fe36Ni38 (wt.%). An overview of sample cross-sections highlighting arising material defects is presented in **Figure 3**. Large defect formation and cracking were found throughout all used pre-heating temperatures for A samples, namely RT, 300°C, and 450°C. At RT and 300°C surface plate temperature (**Figures 3A,B**), bonding defects between the substrate and deposited material, as well as at interlayers were observed in the evaluated cross-sections. At 450°C, lack of fusion was not observed in the analyzed material, but inhibition of crack formation was not achieved (**Figure 3C**). Moreover, optical microscopy imagery shows the formation of cavities, from which some of the cracks originate. Cavities and cracks are detected exclusively toward the sample outer walls.

The defects visible in **Figures 3A,C** were found similar to reported micro-shrinkage defects in steel casting samples (Ghassemali et al., 2018). As reported by Ghassemali et al. (2018), micro shrinkage defects in the studied steel cast sample occur mainly at the cast "hot-spot," specifically at grain boundary junctions of the present FCC phase in the steel material. The temperature gradients in the cast influence the shrinkage formation in the hottest areas. This phenomenon can also be applied to the present study. Due to the bidirectional track deposition used in this study, the dwell time of the laser radiation

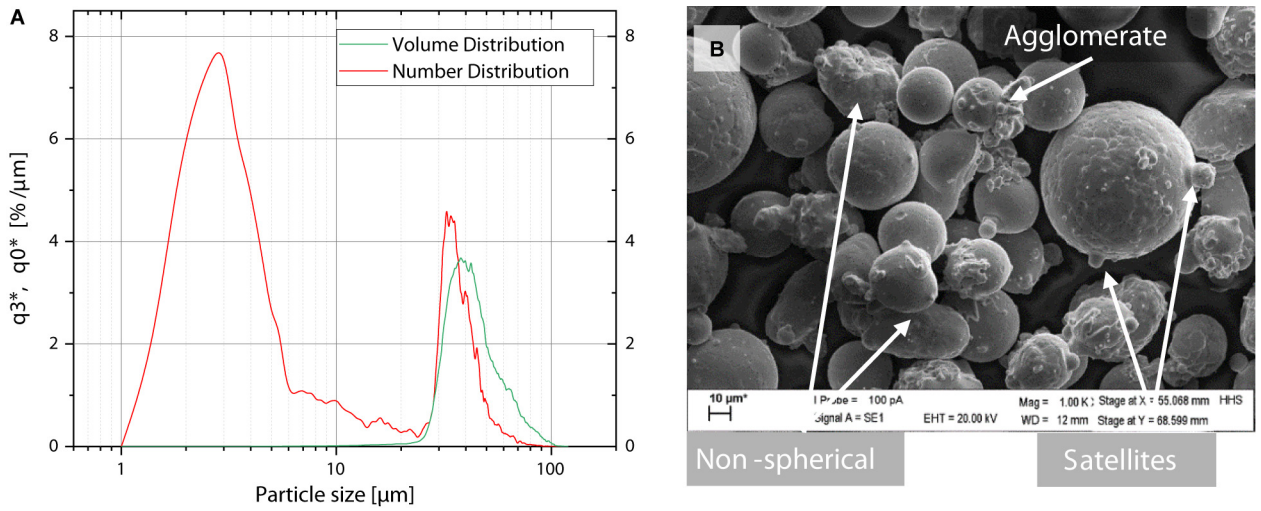

FIGURE 2 | Powder analysis results of Al9Cr17Fe36Ni38 material in 20–90 µm fraction. **(A)** Particle size volume (q3) and number (q0) distribution curves scaled in (%/µm) vs. equivalent particle diameter (µm) showing one maximum in volume distribution and two maxima in number distribution, and **(B)** SEM image of powder material in 1000× magnification showing mainly spherical particles and some irregular shaped particles and satellites.

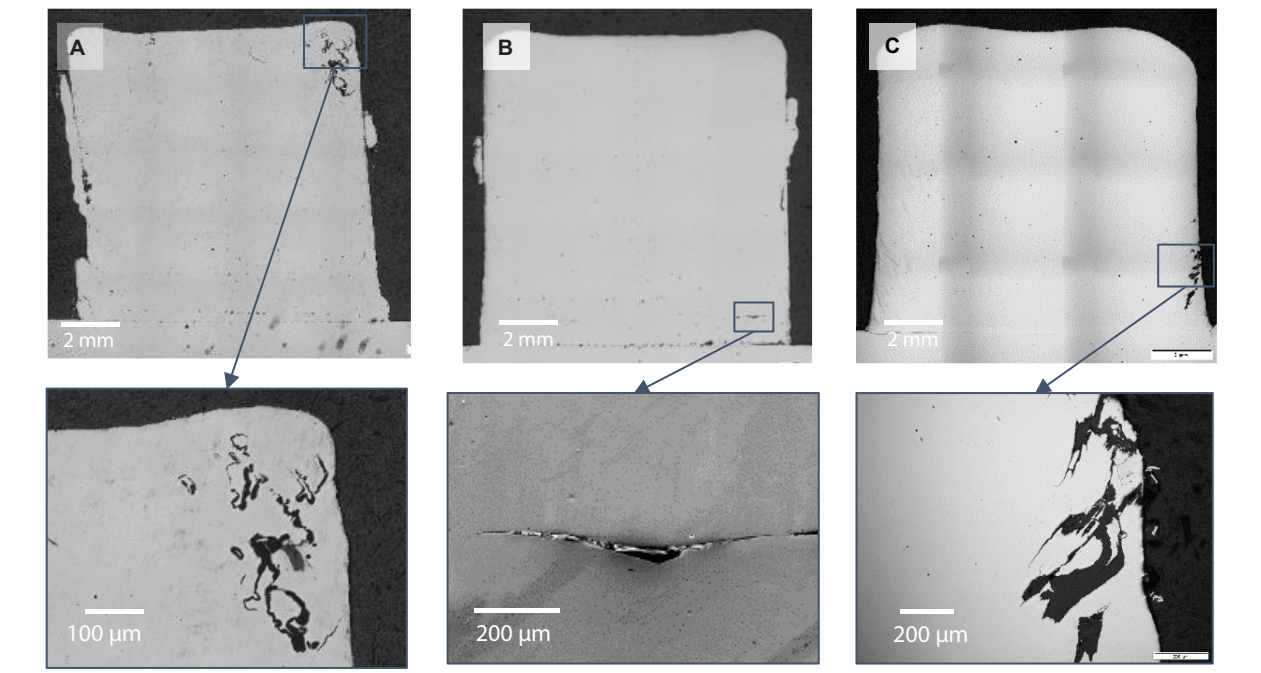

FIGURE 3 | Sample cross-sections of A samples with different pre-heating temperatures on the surface plate during build-up. Respectively at room temperature (RT; **(A)**), 300°C **(B)**, and 450°C **(C)**, including relevant material defects in each case.

is higher at the track tails (beginning and end) than toward the middle of the track. This induces a higher temperature level at the bulk volume walls and thus, a higher temperature gradient between the deposited material and its surroundings. The examination of phase composition in the shrinkage area was not performed at this time.

The effect of the beam diameter size was evaluated by increasing the beam size to 1.8 mm (B Samples, see **Table 1**). Two sample cross-sections of B samples, built at RT and 450°C pre-heating temperature, respectively, are presented in **Figure 4**. No lack of fusion or bonding defects were found in B samples regardless of the pre-heating temperature. Samples built without pre-heating, or RT (**Figure 4A**), present distinctive crack formation along the sample build direction. Cracking seems to be inhibited using a pre-heating temperature of 450°C (**Figure 4B**). Similar crack formation along the build direction in

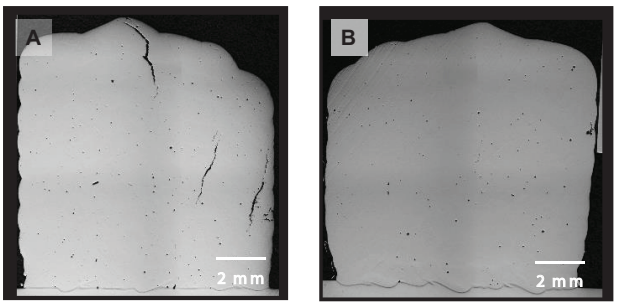

FIGURE 4 | Micrograph images of sample cross-sections of B samples produced at room temperature (RT; **(A)**) and 450°C **(B)** pre-heating temperature showing cracks in build direction at RT and no cracks at 450°C.

LMD-produced samples has been reported for other materials, such as IN718 (Zhou et al., 2018). In that case, cracking was observed at track overlapping regions. A horizontal temperature gradient results from the overlapping of the molten material of a new track over a previously cooled-down neighboring track. The outcome of this is a high-angle boundary, which results in crack formation along its contour. This behavior may apply to the present study, given that cracks formation is inhibited through a higher pre-heating temperature and thus likely because of reduced temperature gradients within the bulk material.

Track length in LMD affects processability of the studied HEA alloy. Given a track length larger than 15 mm, produced (B-type) samples were found prone to crack formation, even at high pre-heating temperatures. Horizontally fabricated samples, with 10:10 mm (*x*:*y*) cross-section and a length of 35 mm presented cracking. Meanwhile, vertically fabricated samples, that is, samples with a 35:10 mm cross-section and a 10 mm length, were crack-free. Sample cross-sections of said results are presented in **Figures 5A–E**. All depicted samples were produced using pre-heating temperatures of 450°C and the B sample parameter set (see **Table 1**). It was found that, if the chosen track length was equal or smaller than 15 mm (**Figures 5A,B**), crack formation was inhibited during LMD-processing. Samples built otherwise equal, but using a track length of 35 mm, presented crack formation in build direction (**Figures 5C,D**). The sample height has no significant effect on crack formation. A micrograph image of a B sample fabricated under "standard" conditions, with 450°C pre-heating temperature and 10 mm long tracks built up to 35 mm sample height is presented in **Figure 5E**. There is a correlation between track length and the elapsed time between "passes" of the laser beam over the surface between the deposition of successive tracks. Longer tracks bring about a longer cooling period of the deposited material before a new track or layer is deposited. Consequently, a larger temperature difference within the cold and molten material is induced, and this results in crack formation in the overlap region between the two tracks in build direction. Shorter tracks and a fast sequence of re-melting allow heat retention inside the sample, reducing temperature gradients in the bulk material during processing.

In samples manufactured with long tracks, as seen in **Figures 5C,D**, the crack formation is more frequent in the lower region of the sample, in the vicinity of the substrate plate. Due to relatively poor heat conductivity of the alloy in comparison to the substrate steel, the cooling rate in the in the lower layers is higher than that in the upper region of the samples. This assumption is supported by the observed outward curvature of the sample outline toward the sample top (**Figures 5A–C**). Given that the number of tracks is identical along the build direction, a bulging in the upper layers of the sample could indicate a larger melt pool during processing and hence, a higher temperature during deposition of the top layers.

Microstructure

As-Built

As proposed by Dong et al. (2016), the $AlCrFe_2Ni_2$ alloy consists of a duplex microstructure formed by an FCC phase, a disordered BCC (A2) phase, and an ordered BCC (B2) phase. The FCC phases were reportedly found as noodle-like structures, while the BCC (A2) phases were found as a precipitate-like structure, combined with inter-precipitate BCC (B2) phases. Borkar et al. (2017) reported elongated grain structures and a pronounced spinoidal decomposition of the BCC (B2) phase on LMD-fabricated AlCrFeNi. In this study, a microstructure with similar visual characteristics to those reported by Dong et al. (2016) and Borkar et al. (2017) was observed. Three SEM micrographs in increasing magnification of the interlayer region in an A-type sample (see **Table 1**) built at 450°C pre-heating temperature, in the as-built condition are shown in **Figure 6**. The low magnification image (**Figure 6A**) shows elongated grains along the build direction of the layers and grain refinement in the interlayer region. Similar results have been reported in the literature for in additively manufactured HEAs (Ocelík et al., 2016; Cui et al., 2019). The interlayer region presents a fine-grained structure, and the presence of bright, small structures that do not appear inside the deposited layers (**Figure 6A**). As seen at higher magnification in **Figure 6B**, a platelet structured phase is homogeneously distributed in this region. Even higher magnification SEM micrographs in this region (**Figure 6C**) reveal the presence of a nano-scaled compositionally de-mixed matrix. Based on the literature about near-$AlCrFe_2Ni_2$ HEA compositions (Dong et al., 2016) and electron backscatter diffraction (EBSD) performed in heat-treated condition (see section "Heat-Treated"), the microstructure is composed of two phases: FCC and BCC. The bright platelet-structures in **Figures 6B,C** correspond to the FCC phase, while the darker-toned matrix corresponds to the parent BCC phase, which is compositionally de-mixed into an Ni, Al-rich ordered and Fe, Cr-rich disordered phase, as reported by Dong et al. (2016) for $AlCrFe_2Ni_2$. Phase fractions were not analyzed in the as-built condition, but only after heat treatment (see section "Heat-Treated").

The presence of FCC-phase platelet structures in the interlayer region is due to the intrinsic heat treatment associated with the cyclic heat input during deposition of consecutive layers during LMD. That is, the BCC phase was found in a so-called metastable state in as-built condition, and an "intrinsic" heat-treatment of the material took place during the deposition of the new layer, which allowed the growth of FCC-platelets

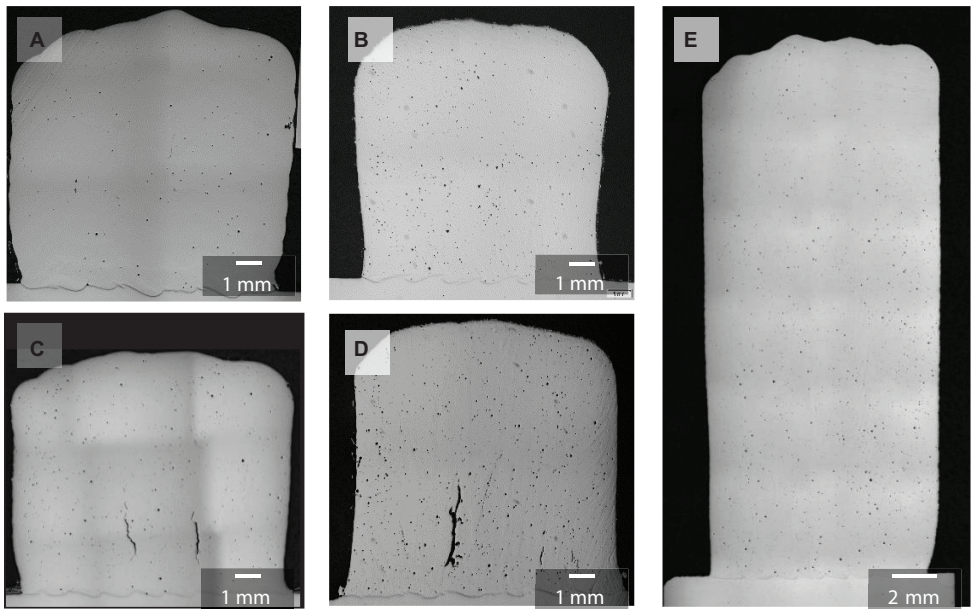

FIGURE 5 | Sample cross-sections of B samples produced with 450°C pre-heating temperature and different track lengths and sample height. 10:10 mm cross-section samples with 15 mm track length **(A,B)** and 35 mm track length **(C,D)** as opposed to 35:10 mm cross-section and 10 mm track length **(E)**. Cracks occur for the longer track length.

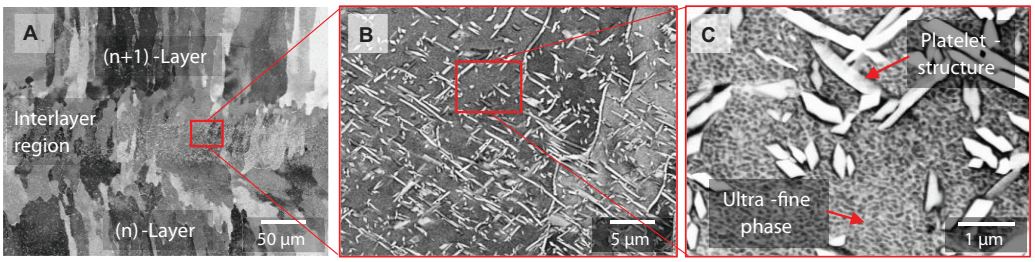

FIGURE 6 | SEM images of laser material deposition (LMD) fabricated A sample (as-built) microstructure at interlayer region in 5000-× **(A)**, 10000-× **(B)**, and 20000-× **(C)** magnification. Homogeneously distributed platelet-structures are visible in the interlayer region only. The matrix is composed of two ultra-fine phases, seen at high magnification.

in the heat affected zone at the interlayer region. A similar microstructure behavior was suggested by Rahul et al. (2020) for a FeCoNiCuAl0.5 HEA during undercooling. High cooling rates in LMD potentially resemble undercooling in the studied conditions for the present HEA, as the solidification takes place at such high rates during processing. Thus the energy input necessary for a new layer deposition is sufficient for the growth of the FCC-phase inside the BCC matrix at boundaries between the two de-mixed BCC-phases.

An SEM image of a B sample in as-built condition (450°C pre-heating), taken just below the interlayer region is shown in **Figure 7**. Analog to A samples, an ultra-fine duplex microstructure and the presence of a bright phase and a darker, compositionally de-mixed matrix is observed. As proposed by Dong et al. (2016), the bright structures correspond to an FCC-phase, while the darker nano-scale compositionally de-mixed matrix corresponds to the decomposed BCC/B2-phases.

Relative to the studied A samples, a higher content of FCC is found in as-built B- samples, even inside the deposited layers, as seen in the SEM image in **Figure 7**. The FCC phase is observed in the form of small platelets (marked circle in **Figure 7**) as well as in longer, Widmanstatten-like structures throughout the studied region. The pronounced formation of the FCC phase within the sample microstructure is consistent with the theory of meta-stability of the BCC phase. Comparatively, the energy density during the processing of A samples is about six times higher than that of B samples, namely $E_B = 76.4$ J/mm^3 vs. $E_A = 456.2$ J/mm^3. As stated in Equation 1, the calculated energy density shows an inverse correlation with both the scan velocity and the beam diameter. Therefore, the formation of a higher content of the FCC phase in B samples compared to A samples can be attributed to two reasons: on one hand, the increased beam diameter has a larger impact area on the plane surface and a higher depth of penetration in the previously deposited layer, thus heating a larger

FIGURE 7 | SEM image of laser material deposition (LMD) fabricated B sample with 450°C pre-heating at the vicinity of the interlayer region in as-built condition. FCC platelets (exemplified inside red circle) and Widmanstatten-like structures over a BCC/(B2) nano-scale compositionally de-mixed matrix are visible.

volume of the sample. Secondly, the slower scan velocity results in a longer laser beam dwell time on the plane surface. These two effects overlap, allowing not only the formation of small FCC-platelets in the material but also the growth of the FCC phase within the material over a longer period.

Heat-Treated

After heat treatment at 900°C for 6 h, the resulting microstructure presents a homogeneously distributed duplex microstructure throughout the sample cross-sections. SEM images of heat treated A and B samples, including an EBSD phase analysis of an A sample are presented in **Figure 8**. The microstructure of the heat-treated A sample presents a homogeneous two-phase microstructure composed of larger, intertwined platelets over a homogeneous matrix (**Figure 8A**). According to the phase distribution analysis (**Figure 8B**), heat-treated A samples exhibit a duplex microstructure composed of 46% FCC-phase (bright, platelet structures) and 57% BCC-phase (dark, matrix). Heat-treated B samples present platelet-structures over a homogenous matrix, as seen in **Figure 8C**. Thus, heat treatment yields an equivalent structure of the FCC and BCC phases for both sample types A and B, as opposed to the previously observed differences in FCC-phase structures in as-built condition. After the applied heat treatment, the compositionally de-mixed matrix is no longer present in the analyzed microstructure in either sample type.

Hardness

Hardness measurement profiles along the centerline of both an A sample and a B sample are shown in **Figure 9, comparing as-built** and **heat**-treated condition. Samples in as-built condition present an inhomogeneous hardness value distribution consistent with the findings in microstructure analyses. Measured hardness values fluctuate along the sample build direction. Moreover, for as-built condition, A samples show higher hardness values than B samples, namely 507 ± 37 HV0.3 vs. 386 ± 59 HV0.3. This leads to the conclusion that the observed higher FCC content in B samples (see section "Microstructure") effectively leads to the increase of material ductility and reduction of strength. After heat treatment, the hardness profiles in both sample types show a homogeneous profile. Moreover, the hardness values of both sample types converge into a similar trend line at around 300 HV0.3. Again, this result correlates with

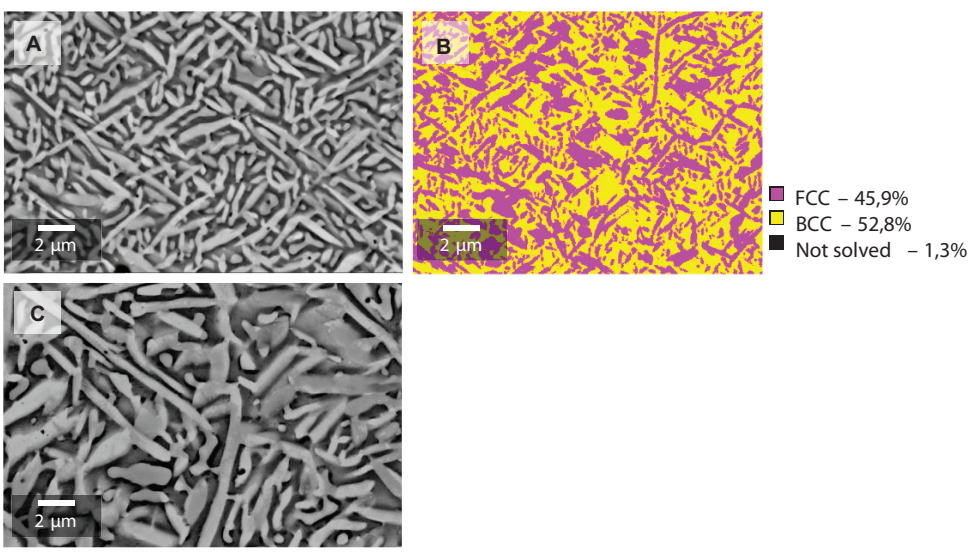

FIGURE 8 | SEM images of laser material deposition (LMD) fabricated samples with 450°C pre-heating temperature. A samples **(A)** and B samples **(C)** after heat treatment at 900°C for 6 h, and an EBSD phase analysis of A sample microstructure after heat treatment **(B)**. A duplex FCC/BCC microstructure is visible, and a 46%/53% (FCC/BCC) phase composition is determined.

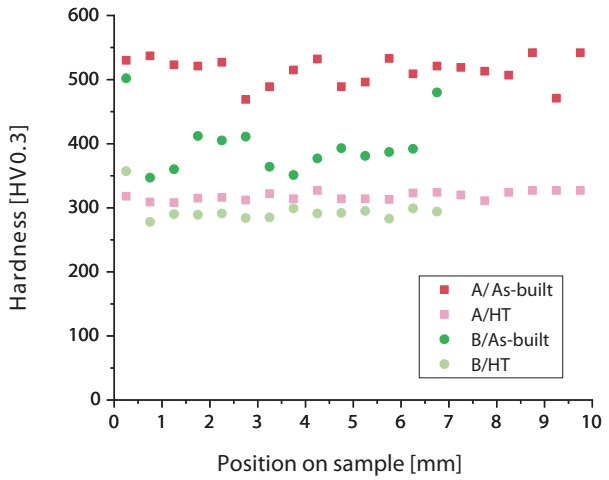

FIGURE 9 | Hardness values along sample centerline for A and B samples in as-built and heat treated condition.

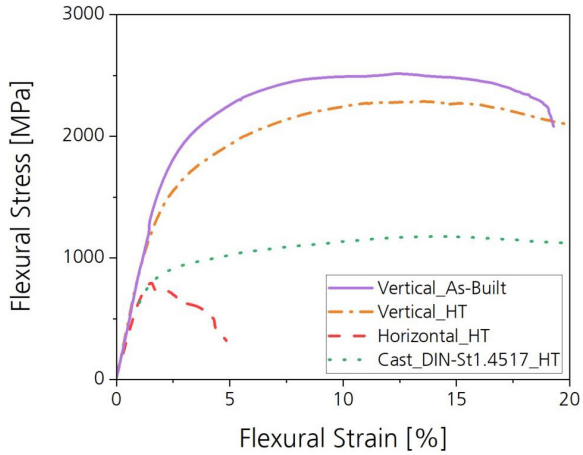

FIGURE 10 | Bending test trendlines–stress (MPa) vs. strain (%) for laser material deposition fabricated B samples in as-built and heat-treated condition in a vertical build orientation (Vertical_As-Built, Vertical_HT), heat treated in a horizontal build orientation (Horizontal_HT), and a reference heat-treated DIN St.1.4517 cast sample material (Cast_DIN-St1.4517_HT).

the findings of microstructure analysis, which shows a very similar microstructure for both sample types after heat treatment, whereas A samples sustain a slightly higher hardness average than B samples, even after heat treatment.

Bending Strength

The resulting stress vs. strain diagram from bending tests performed on selected samples is shown in **Figure 10**. Due to the high susceptibility to cracking in A samples, bending tests were only performed on B samples in this study. The presented diagram shows the test results for LMD samples fabricated in a vertical orientation build (*x*:*y*:*z* 10:10:35 mm) in both as-built (*Vertical_As-Built*) and heat-treated condition (*Vertical_HT*) and LMD samples in a horizontal orientation build (*x*:*y*:*z* 10:35:10 mm) in heat-treated condition (*Horizontal_HT*). A reference cast duplex-steel in heat-treated condition (*Cast_DIN St.1.4517_HT*) is depicted in the diagram as well.

In as-built condition, the LMD fabricated material exhibits a maximal bending strength of 2601 MPa and failure at 19.2% bending strain. This case is only depicted for the vertically built samples, since horizontally built samples presented premature failure during testing, which made bending testing impossible. After heat treatment, the maximal strength is achieved at 2286 MPa, and no failure behavior is observed up to the machine strain limit of 20% for vertically built samples. In comparison to the reference material, a strength increase of 50% is achieved by the studied HEA, while maintaining similar ductility.

Horizontally built samples reach the point of fracture at 4.5% bending strain even in heat-treated condition. Around 240 MPa and ∼0.2% strain, plastic deformation begins for the horizontally built, heat-treated LMD sample. This leads to the conclusion that inherent material defects propagate in the analyzed horizontally built B samples after this point. This material behavior correlates with the findings on material processability in LMD. Horizontally built samples present higher susceptibility to crack formation in build direction. Hence, lengthwise cut bending test samples will present transverse cracks, which cause failure at a low stress level.

SUMMARY

An Al9Cr17Fe36Ni38 (wt.%) HEA was fabricated by means of LMD using two beam diameter sizes: 0.6 and 1.8 mm. The fabricated samples were evaluated in as-built and heat-treated condition regarding microstructure, hardness, and bending strength.

Processability

- Samples with dimensions 10 mm × 10 mm × 10 mm were fabricated successfully by LMD.
- Pre-heating of the substrate plate is necessary for crack-free fabrication. A temperature of 450°C of the base substrate plate was used to inhibit temperature-gradient-induced crack formation during processing.
- Using a 0.6 mm beam diameter, crack and shrinkage cavity formation in LMD-built samples were observed despite 450°C pre-heating.
- Using a 1.8 mm beam diameter, crack free samples of surface area 10 mm × 10 mm were successfully produced using LMD. Crack formation was observed when track lengths larger than 15 mm were used. A sample volume of 10:10:35 mm (*x*:*y*:*z*) was successfully fabricated using LMD and a 1.8 mm beam diameter producing crack-free samples with residual porosity <0.5%.

Microstructure

- In as-built condition, the material presents an inhomogeneous microstructure along the build height consistent with the layer-wise additive fabrication.

- Using a 0.6 mm beam diameter, the resulting microstructure *in-layer* presents elongated grains along the build direction and grain refinement in the interlayer region. The presence of homogeneously distributed platelet-like structures (FCC-phase) was observed only in the interlayer region. The presence of a nano-scale, compositionally de-mixed matrix (ordered/disordered BCC/B2 phases) was observed throughout the sample cross-section.
- Using a 1.8 mm beam diameter, an ultra-fine duplex microstructure was found throughout the sample. The microstructure is composed of an FCC phase in form of platelets and Widmanstatten-like structures and a compositionally de-mixed BCC matrix (ordered/disordered BCC/B2 phases).
- After heat treatment, a homogenization of the microstructure throughout the samples was observed in both 0.6 and 1.8 mm samples resulting in a duplex microstructure with a phase content of 46% vs. 53% for FCC/BCC-phases, respectively. The compositionally de-mixed matrix observed in as-built condition was no longer present after heat treatment. Samples built with a 1.8 mm beam diameter present coarser structures than 0.6 mm samples in heat-treated condition.

Mechanical Properties

- In as-built condition, all samples present an inhomogeneous hardness profile along build height. Hardness values reach 507 ± 37 HV0.3 for 0.6 mm beam diameter samples and 386 ± 59 HV0.3 for 1.8 mm beam diameter samples.
- After heat treatment, the hardness profiles of both sample types level-out at ∼300 HV.
- A three-point bending test was performed for samples built with a 1.8 mm beam diameter. A high strength/high ductility of the material using a vertical sample production (short tracks, high number of layers) was achieved. Using a horizontal sample production (long tracks, low number of layers), results in a low-ductility material.
- The maximal bending strength is achieved in a vertically produced 1.8 mm beam diameter sample in as-built condition, reaching 2601 MPa and failure at 19.2%.
- After heat treatment of the 1.8 mm beam diameter vertically built sample, the bending strength reaches 2286 MPa and no failure up to 20% bending strain (test machine limit). That is, the novel Al9Cr17Fe36Ni38 (wt.%) HEA produced my means of LMD presents, in heat-treated condition, an over 50% increase in strength compared to a DIN-St.1.4517 duplex steel, while maintaining similar ductility.

DATA AVAILABILITY STATEMENT

The raw data supporting the conclusions of this article will be made available by the authors, without undue reservation.

AUTHOR CONTRIBUTIONS

VM performed the process development in laser metal deposition as well as material analysis and result discussion. AW advised VM with material science and project development topics. UH provided with consulting support on the AlCrFeNi-HEA. SG performed a flexural test on LMD-produced material. DV and Oerlikon AM provided the novel HEA powder material used for the LMD process development. All authors contributed to the article and approved the submitted version.

FUNDING

The authors acknowledge the financial support by the Federal Ministry of Education and Research of Germany (Bundesministerium für Bildung und Forschung – BMBF) in the framework of the project NADEA (grant number 03XP0163B)[1].

[1]Das diesem Bericht zugrundeliegende Vorhaben wurde mit Mitteln des Bundesministeriums für Bildung und Forschung unter dem Förderkennzeichen 03XP0163B gefördert. Die Verantwortung für den Inhalt dieser Veröffentlichung liegt beim Autor.

REFERENCES

Borkar, T., Chaudhary, V., Gwalani, B., Choudhuri, D., Mikler, C. V., Soni, V., et al. (2017). A combinatorial approach for assessing the magnetic properties of high entropy alloys: role of Cr in AlCo x Cr 1- x FeNi. *Adv. Eng. Mater.* 19:1700048. doi: 10.1002/adem.201700048

Borkar, T., Gwalani, B., Choudhuri, D., Mikler, C. V., Yannetta, C. J., Chen, X., et al. (2016). A combinatorial assessment of AlxCrCuFeNi2 ($0 < x < 1.5$) complex concentrated alloys: Microstructure, microhardness, and magnetic properties. *Acta Mater.* 116, 63–76. doi: 10.1016/j.actamat.2016.06.025

Chen, M., Shi, X. H., Yang, H., Liaw, P. K., Gao, M. C., Hawk, J. A., et al. (2018). Wear behavior of Al 0.6 CoCrFeNi high-entropy alloys: effect of environments. *J. Mater. Res.* 33, 3310–3320. doi: 10.1557/jmr.2018.279

Chuang, M.-H., Tsai, M.-H., Wang, W.-R., Lin, S.-J., and Yeh, J.-W. (2011). Microstructure and wear behavior of AlxCo1.5CrFeNi1.5Tiy high-entropy alloys. *Acta Mater.* 59, 6308–6317. doi: 10.1016/j.actamat.2011.06.041

Crundwell, F. K., Moats, M. S., Ramachandran, V., Robinson, T. G., and Davenport, W. G. (2011). "Cobalt – occurrence, production, use and price," in *Extractive Metallurgy of Nickel, Cobalt and Platinum Group Metals*, eds F. Crundwell, M. Moats, V. Ramachandran, T. Robinson, and W. G. Davenport (Amsterdam: Elsevier), 357–363. doi: 10.1016/b978-0-08-096809-4.10028-0

Cui, W., Karnati, S., Zhang, X., Burns, E., and Liou, F. (2019). Fabrication of AlCoCrFeNi high-entropy alloy coating on an AISI 304 substrate via a CoFe2Ni intermediate layer. *Entropy* 21:2. doi: 10.3390/e21010002

Dong, Y., Gao, X., Lu, Y., Wang, T., and Li, T. (2016). A multi-component $AlCrFe_2Ni_2$ alloy with excellent mechanical properties. *Mater. Lett.* 169, 62–64. doi: 10.1016/j.matlet.2016.01.096

Gao, X., Lu, Y., Zhang, B., Liang, N., Wu, G., Sha, G., et al. (2017). Microstructural origins of high strength and high ductility in an AlCoCrFeNi2.1 eutectic high-entropy alloy. *Acta Mater.* 141, 59–66. doi: 10.1016/j.actamat.2017.07.041

Ghassemali, E., Jarfors, A., and Diószegi, A. (2018). On the formation of micro-shrinkage porosities in ductile iron cast components. *Metals* 8:551. doi: 10.3390/met8070551

Joseph, J., Stanford, N., Hodgson, P., and Fabijanic, D. M. (2017). Tension/compression asymmetry in additive manufactured face centered

cubic high entropy alloy. *Scripta Mater.* 129, 30–34. doi: 10.1016/j.scriptamat.2016.10.023

Kuwabara, K., Shiratori, H., Fujieda, T., Yamanaka, K., Koizumi, Y., and Chiba, A. (2018). Mechanical and corrosion properties of AlCoCrFeNi high-entropy alloy fabricated with selective electron beam melting. *Addit. Manufact.* 23, 264–271. doi: 10.1016/j.addma.2018.06.006

Lu, Y., Dong, Y., Guo, S., Jiang, L., Kang, H., Wang, T., et al. (2014). A promising new class of high-temperature alloys: eutectic high-entropy alloys. *Sci. Rep.* 4:6200. doi: 10.1038/srep06200

Ma, X. D., Li, X. L., Zhu, Z. Q., Li, C. J., and Gao, S. (2016). The stress analysis of a heavy liquid metal pump impeller. *IOP Conf. Ser.: Mater. Sci. Eng.* 129:12023. doi: 10.1088/1757-899X/129/1/012023

Niu, P. D., Li, R. D., Yuan, T. C., Zhu, S. Y., Chen, C., Wang, M. B., et al. (2019). Microstructures and properties of an equimolar AlCoCrFeNi high entropy alloy printed by selective laser melting. *Intermetallics* 104, 24–32. doi: 10.1016/j.intermet.2018.10.018

Ocelík, V., Janssen, N., Smith, S. N., and de Hosson, J. T. M. (2016). Additive manufacturing of high-entropy alloys by laser processing. *JOM* 68, 1810–1818. doi: 10.1007/s11837-016-1888-z

Rahul, M. R., Samal, S., and Phanikumar, G. (2020). Metastable microstructures in the solidification of undercooled high entropy alloys. *J. Alloys Comp.* 821:153488. doi: 10.1016/j.jallcom.2019.153488

Shang, C. Y., and Wang, Y. (2017). AlCrFeNi high-entropy coating fabricated by mechanical alloying and hot pressing sintering. *MSF* 898, 628–637. doi: 10.4028/www.scientific.net/msf.898.628

Shi, Y., Yang, B., Xie, X., Brechtl, J., Dahmen, K. A., and Liaw, P. K. (2017). Corrosion of Al CoCrFeNi high-entropy alloys: al-content and potential scan-rate dependent pitting behavior. *Corros. Sci.* 119, 33–45. doi: 10.1016/j.corsci.2017.02.019

Sistla, H. R., Newkirk, J. W., and Frank Liou, F. (2015). Effect of Al/Ni ratio, heat treatment on phase transformations and microstructure of AlxFeCoCrNi2-x (x=0.3, 1) high entropy alloys. *Mater. Design* 81, 113–121. doi: 10.1016/j.matdes.2015.05.027

Wang, R., Zhang, K., Davies, C., and Wu, X. (2017). Evolution of microstructure, mechanical and corrosion properties of AlCoCrFeNi high-entropy alloy prepared by direct laser fabrication. *J. Alloys Comp.* 694, 971–981. doi: 10.1016/j.jallcom.2016.10.138

Yan-dong, G. U., Shou-qi Yuan, Ji Pei, and Fan Meng. (2017). *Numerical Analysis of Stress and Deformation of Impeller in the Mixed Flow Pump Based on Fluid-structure Interaction*. Toronto, ON: DEStech.

Yeh, J.-W., Chen, S.-K., Lin, S.-J., Gan, J.-Y., Chin, T.-S., Shun, T.-T., et al. (2004). Nanostructured high-entropy alloys with multiple principal elements: novel alloy design concepts and outcomes. *Adv. Eng. Mater.* 6, 303–306. doi: 10.1002/adem.200300578

Yin, T., Pei, J., Yuan, S., Osman, M. K., Wang, J., and Wang, W. (2017). Fluid-structure interaction analysis of an impeller for a high-pressure booster pump for seawater desalination. *J. Mech. Sci. Technol.* 31, 5319–5328. doi: 10.1007/s12206-017-1026-z

Zhou, Z., Huang, L., Shang, Y., Li, Y., Jiang, L., and Lei, Q. (2018). Causes analysis on cracks in nickel-based single crystal superalloy fabricated by laser powder deposition additive manufacturing. *Mater. Design* 160, 1238–1249. doi: 10.1016/j.matdes.2018.10.042

Conflict of Interest: DV is employed by the company Oerlikon AM.

The remaining authors declare that the research was conducted in the absence of any commercial or financial relationships that could be construed as a potential conflict of interest.

frontiers in Materials

CORRECTION
published: 18 September 2020
doi: 10.3389/fmats.2020.594883

Corrigendum: Laser Metal Deposition of Ultra-Fine Duplex $AlCrFe_2Ni_2$-Based High-Entropy Alloy

Veronica Rocio Molina[1]*, *Andreas Weisheit*[1], *Sergej Gein*[2], *Ulrike Hecht*[2] and *Dimitrios Vogiatzief*[3]

[1] Fraunhofer Institute for Laser Technology ILT, Aachen, Germany, [2] Access e.V., Aachen, Germany, [3] Oerlikon AM, Feldkirchen, Germany

Keywords: laser meterial deposition, high-entropy alloy, AlCrFeNi alloy, duplex microstructure, additive manufacturing

OPEN ACCESS

Approved by:
Frontiers Editorial Office, Frontiers Media SA, Switzerland

***Correspondence:**
Veronica Rocio Molina
veronica.molina@ilt.fraunhofer.de

Specialty section:
This article was submitted to Structural Materials, a section of the journal Frontiers in Materials

Received: *14 August 2020*
Accepted: *31 August 2020*
Published: *18 September 2020*

Citation:
Molina VR, Weisheit A, Gein S, Hecht U and Vogiatzief D (2020) Corrigendum: Laser Metal Deposition of Ultra-Fine Duplex $AlCrFe_2Ni_2$-Based High-Entropy Alloy. Front. Mater. 7:594883. doi: 10.3389/fmats.2020.594883

A Corrigendum on

Laser Metal Deposition of Ultra-fine Duplex $AlCrFe_2Ni_2$-based High-Entropy Alloy
by Molina, V. R., Weisheit, A., Gein, S., Hecht, U., and Vogiatzief, D. (2020). Front. Mater. 7:275. doi: 10.3389/fmats.2020.00275

In the original article, there was a mistake in **Figure 10** as published. The legend colors did not match to the depicted lines, which confuses the reader. The corrected **Figure 10** appears below.

The authors apologize for this error and state that this does not change the scientific conclusions of the article in any way. The original article has been updated.

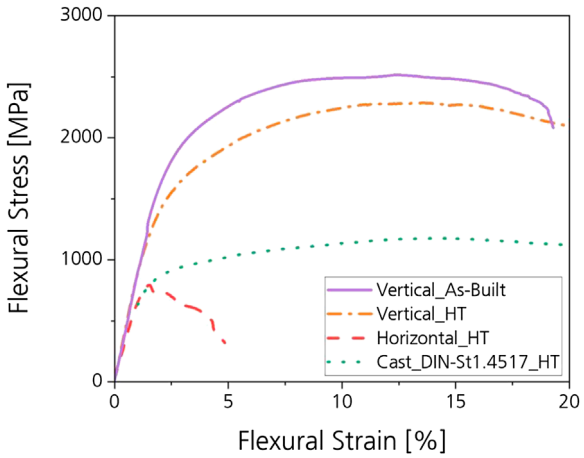

FIGURE 10 | Bending test trendlines–stress (MPa) vs. strain (%) for laser material deposition fabricated B samples in as-built and heat-treated condition in a vertical build orientation (Vertical_As-Built, Vertical_HT), heat treated in a horizontal build orientation (Horizontal_HT), and a reference heat-treated DIN St.1.4517 cast sample material (Cast_DIN-St1.4517_HT).

frontiers in Materials

ORIGINAL RESEARCH
published: 14 August 2020
doi: 10.3389/fmats.2020.00287

The BCC-FCC Phase Transformation Pathways and Crystal Orientation Relationships in Dual Phase Materials From Al-(Co)-Cr-Fe-Ni Alloys

Ulrike Hecht[1], Sergej Gein[1], Oleg Stryzhyboroda[1], Eyal Eshed[2] and Shmuel Osovski[2]*

[1] Access e.V., Aachen, Germany, [2] Technion-Israel Institute of Technology, Faculty of Mechanical Engineering, Haifa, Israel

The alloy system Al-(Co)-Cr-Fe-Ni contains compositional ranges where a solid state BCC-FCC phase transformation leads to dual-phase materials composed of face-centered cubic (FCC) and body-centered cubic (BCC) phases with nearly equal volume fraction. The microstructure arising from this transformation at slow cooling rates is the classical Widmanstätten structure, with FCC-laths and colonies growing from grain boundaries into the parent BCC-B2 grain. Very distinct microstructures are obtained, when Widmanstätten growth is kinetically suppressed e.g., during continuous cooling with high cooling rates. These novel microstructures are associated with the spinodal decomposition of the parent BCC-B2 such that FCC growth occurs during the spinodal decomposition or upon annealing from a metastable, fully spinodal state. We review the microstructures at case as function of the imposed cooling regimes for the Co-free medium entropy alloy $AlCrFe_2Ni_2$. One of them, termed ultrafine vermicular microstructure, involves a characteristic and novel crystal orientation relationship (OR) between FCC and BCC. We identify the common planes and directions of this OR using electron backscatter diffraction maps to be $\{111\}^{FCC} \parallel \{12\bar{1}\}^{BCC}$ and $\langle\bar{1}01\rangle^{FCC} \parallel \langle\bar{1}0\bar{1}\rangle^{BCC}$, respectively. Embedded is a second OR with $\{1\bar{3}\bar{1}\}^{FCC} \parallel \{\bar{1}03\}^{BCC}$ and $\langle101\rangle^{FCC} \parallel \langle010\rangle^{BCC}$. We further show that the vermicular FCC phase contains a high amount of lattice strain and sub-grain boundaries with disorientation angles in the range from 2 to 12°, as a result of the solid-state phase transformation.

Keywords: high entropy alloy, medium entropy alloys, phase transformation pathways, crystal orientation relationships, dual phase materials

OPEN ACCESS

Edited by:
Liqiang Wang,
Shanghai Jiao Tong University, China

Reviewed by:
Liang Zhang,
Chongqing University, China
Xinwang Liu,
Huazhong University of Science & Technology, China

****Correspondence:***
Ulrike Hecht
u.hecht@access-technology.de

Specialty section:
This article was submitted to Structural Materials, a section of the journal Frontiers in Materials

Received: *31 May 2020*
Accepted: *29 July 2020*
Published: *14 August 2020*

Citation:
Hecht U, Gein S, Stryzhyboroda O, Eshed E and Osovski S (2020) The BCC-FCC Phase Transformation Pathways and Crystal Orientation Relationships in Dual Phase Materials From Al-(Co)-Cr-Fe-Ni Alloys. Front. Mater. 7:287. doi: 10.3389/fmats.2020.00287

INTRODUCTION

High entropy and medium entropy alloys attracted wide interest, driven by the quest for multicomponent, yet single phase materials with face-centred-cubic (FCC), body-centred-cubic (BCC) and hexagonal-close-packed (HCP) structures while eliminating secondary (and tertiary) phases (Steurer, 2020). More recently, research on dual-phase (or multi-phase) materials gained momentum, because their heterophase nature allows tailoring mechanical properties and achieving well-balanced property profiles (Bönisch et al., 2018). The quinary alloy system of major interest is

Al-Co-Cr-Fe-Ni offering a composition range for dual-phase alloy design around $Al_xCoCrFeNi$ with $0.5 < x < 0.9$ (Kao et al., 2009; Wang et al., 2014, Gangireddy et al., 2019). The dual-phase alloys provide considerable strength while retaining about ∼20% tensile ductility (Gangireddy et al., 2019) and also show promising corrosion resistance, comparable to stainless steels (Shi et al., 2017). Since alloy design strategies attach increasing importance to cost reduction and resource-conserving aspects, the quaternary alloy system Al-Cr-Fe-Ni proved equally prolific around compositions $AlCrFe_2Ni_2$ (Dong et al., 2016 and Li et al., 2020) thus avoiding expensive and resource-critical elements like Cobalt (Tkaczyk et al., 2018).

Alloys like $Al_{0.7}CoCrFeNi$, $Al_{0.8}CoCrFeNi$ and certainly many other alloys with reduced or fully eliminated Co content like $AlCrFe_2Ni_2$, are dual-phase materials composed of FCC and BCC phases with nearly equal volume fraction, typically with a Widmanstätten lath morphology of the FCC phase (De Jeer et al., 2017; Abuzaid and Sehitoglu, 2018). This microstructure type, known as "duplex microstructure", is similar though not identical to the one well known from duplex steels (Ohmori et al., 1995; Knyazeva and Pohl, 2013). The major difference relates to the nature of the parent BCC phase, being a disordered d-ferrite (BCC-A2) in the case of duplex steels but an ordered BCC-B2 phase in the case of Al-(Co)-Cr-Ni alloys. The most remarkable and eminently important difference arises from the limited stability of this BCC-B2 phase, which is prone to spinodal decomposition into a Fe, Cr- rich BCC-A2 phase and a Ni, Al-rich BCC-B2 phase. The domain ordering of the BCC-B2 in the spinodally decomposed state was investigated in detail by Linden et al. (2017), while also accounting for microsegregation inherited from solidification.

The spinodal decomposition of the BCC-B2 phase and more specifically its interaction with the BCC-FCC phase transformation is one of the most fascinating aspects in the alloy system Al-(Co)-Cr-Fe-Ni, leading to novel phase transformation pathways and unique microstructures. The purpose of this paper is to accurately describe the distinct transformation pathways for distinct cooling regimes, while referring to the most recent thermodynamic data. Emphasis is placed on the crystal orientation relationships (ORs) established between the BCC and FCC phases. We will introduce a new crystal OR, which pertains to a novel and unique microstructure termed "ultrafine vermicular microstructure" (UVM). Vermicular structures have first been reported in Dong et al. (2016) for an as cast $AlCrFe_2Ni_2$ alloy, but are likewise forming in $Al_{0.7}CoCrFeNi$, $Al_{0.8}CoCrFeNi$ at sufficiently high cooling rates, e.g., during permanent mold casting. Dong et al. (2016) described this microstructure as "noodle-like", but gave no explanation about its origin, while alluding to a "eutectic" design principle. The microstructure captured our attention because it compares to no other structure that we saw in many years of research on different metallic and intermetallic materials. We thus engaged into an ample experimental investigation, also including further alloy design, heat treatments and mechanical property characterization, as presented by S. Gein et al. in this Frontier's edition.

This paper focuses on microstructure characterization only, being structured as follows: the experimental methods used for sample preparation and microstructure characterization are briefly described in section 2; an overview on the distinct dual-phase microstructures and the associated phase transformation pathways are described in section 3. The newly identified crystal orientation relationship pertaining to ultrafine vermicular microstructures is presented with due details in section 3. Finally, a short summary and main conclusion are given in section 4.

EXPERIMENTAL METHODS OF SAMPLE PREPARATION AND CHARACTERIZATION

Samples presented in section 3 and 4 were prepared by arc melting under Argon gas (Ar6.0) in an Edmund Bühler device type AM500 using elemental mixtures of the desired alloy composition close to $AlCrFe_2Ni_2$. The melted and solidified buttons of 50 and 300 g each were flipped and repeatedly molten for at least 3 times, to insure chemical homogeneity. The elements used for alloy preparation had a purity of at least 99.98 wt-%. For completeness of the overview on the distinct dual-phase microstructures we also present a sample which was produced by additive manufacturing using powder bed fusion (L-PBF) in order to reach high cooling rates i.e., $>10^3$ K/min. The L-PBF sample was provided by Oerlikon AM GmbH in the as-build condition and was further annealed under Argon (Ar4.8) in a horizontal tube furnace at 950°C for a duration of 6 h followed by water quenching.

Sample characterization encompassed microstructure analysis in a scanning electron microscope SEM type Zeiss Gemini 1550 equipped with energy dispersive X-ray analysis (EDS) and electron backscatter diffraction (EBSD) detectors. The EDS-spectra and EBSD-patterns were acquired and analyzed using the Oxford-INCA software. Samples for microstructure characterization in SEM were cut from the arc melted buttons, embedded in conductive resin, grinded and polished. After standard polishing steps a final step of vibratory polishing (Buehler VibroMet 2) was applied, which allows acquiring good Kikuchi patterns during EBSD mapping.

Selected samples were investigated by conventional transmission electron microscopy (TEM) and scanning transmission electron microscopy (STEM) including energy dispersive X-ray analysis. TEM images and selected area electron diffractions (SAED) were obtained using a FEI Tecnai G2 T20 200 KeV TEM with a LaB6 electron source. A Titan Themis G^2 60–300 (FEI/Thermo Fisher) was used for high resolution STEM Imaging and EDS maps. **Samples for** microstructure characterization in TEM and STEM were prepared by focused ion beam cutting (FIB) of thin lamellae using a dual-beam FEI Helios NanoLab G3 scanning microscope.

DUAL-PHASE MICROSTRUCTURES IN AL-(CO)-CR-FE-NI ALLOYS

Three very distinct dual-phase microstructures evolve upon cooling certain Al-(Co)-Cr-Fe-Ni alloys, whenever the alloy

composition is such that two solid-state transformations are involved along the transformation pathway, the allotropic transformation BCC-B2 → FCC-A1 and the spinodal decomposition BCC-B2 → BCC-A2# + BCC-B2#. In the following, we describe the formation of these microstructures and highlight their characteristic morphological features based on the alloy composition $AlCrFe_2Ni_2$. For sake of clarity, the hash symbol is used to denote the product phases of the spinodal decomposition and the Strukturbericht designations A1, A2 and B2 are used in addition to the crystal structure type, as to distinguish ordered (B2) from disordered (A2) BCC phases. The presented information is essentially drawing on results from many experiments with distinct cooling rates, e.g., casting into ceramic and permanent molds, arc melting of buttons with different size (weight) and suction casting, additive manufacturing etc., which are not presented in detail. The typical cooling rates reported in literature range from ∼20 K/min (sand and ceramic mold casting), ∼200 K/min (permanent mold casting), ∼2000 K/min (suction casting) and above $\sim 10^4$ K/min for laser based additive manufacturing.

As will be seen, the term "dual-phase" used to describe FCC-BCC microstructures is not strictly correct, because the BCC phase decomposes spinodally into two BCC-phases with distinct composition sets. However, the vast majority of literature, i.e., De Jeer et al., 2017; Abuzaid and Sehitoglu, 2018, Gangireddy et al., 2019, uses this term, since it is simple and captures the quintessence.

Dual-Phase Microstructures and Associated Phase Transformation Pathways

An overview of characteristic dual-phase microstructures is displayed in **Figure 1** for the Co-free alloy $AlCrFe_2Ni_2$, along with schematic icons of the microstructure and a sketch of the related phase transformation pathways. Other alloys with similar transformation pathways will develop similar microstructure features and indeed we observed them in alloy $Al_xCoCrFeNi$ alloys with $0.7 < x < 0.8$ without showing them in detail. Three distinct dual-phase structure types can be distinguished, being labeled CWM, UVM, and UMM, respectively. They all form from the BCC-B2 parent phase as described below:

(1) The conventional Widmanstätten microstructure (CWM) is formed at low cooling rates, typically less than ∼50 K/min, by diffusion controlled growth of FCC-A1 plates into the parent BCC-B2 grains. The FCC-A1 plates originate from FCC-A1 films at grain boundaries of BCC-B2 and grow into the volume of the grains with a plate-like morphology forming colonies of parallel plates. For other nucleation scenarios a pattern of intersecting plates may develop. Growth requires a small undercooling below the BCC-B2 → FCC-A1 transformation temperature. FCC-A1 growth thus occurs before the spinodal decomposition of the BCC-B2 parent grains. The remaining BCC-B2 phase, located in between the FCC laths will later decompose spinodally into BCC-B2#2 and BCC-A2#. The sequence of phase transformations along the CWM transformation pathway reads:

Pathway (1): BCC-B2 → FCC-A1 + BCC-B2 → FCC-A1 + BCC-B2# + BCC-A2#

The group from the University of Groningen (Rao et al., 2016; De Jeer et al., 2017) investigated the crystallographic orientation relationship between FCC-A1 and BCC (BCC-B2# + BCC-A2#) in a sample from alloy $Al_{0.7}CoCrFeNi$ with Widmannstätten microstructure. The authors report a continuum from the Pitsch OR to the Kurdjumov-Sachs OR. Our own measurements in CWM-samples form alloys $AlCrFe_2Ni_2$, $Al_{0.7}CoCrFeNi$ and $Al_{0.8}CoCrFeNi$ show the Nishiyama-Wassermann OR (Nishiyama, 1934; Wassermann, 1935) extending to the Kurdjumov-Sachs OR (Kurdjumow and Sachs, 1930). This is quite similar to Bunge et al. (2003) who reported a similar spread of ORs in an iron meteorite with Widmanstätten structure formed during the FCC → BCC phase transformation.

(2) The ultrafine vermicular microstructure (UVM) was reported as a "noodle-like" structure by Dong et al. (2016), but its formation and morphological peculiarities have not been described, leaving room to speculations about its origins. Some authors alluded to possible eutectic or eutectoid reactions, simply because the structure is ultrafine and vaguely lamellar in appearance. Our own research shows that this microstructure forms at moderate to high cooling rates, typically ranging from ∼100 K/min to ∼1000 K/min such that Widmanstätten growth is kinetically suppressed. Under these conditions, the undercooling below the BCC-B2 → FCC-A1 transformation temperature increases to some 10 to 100 K eventually going below the binodal line of the phase diagram. The spinodal decomposition of the BCC-B2 phase then triggers the growth of FCC-A1, in what we call a "*duplex spinodal reaction*". The associated transformation pathway reads:

Pathway (2): BCC-B2 → FCC-A1 + BCC-B2# + BCC-A2#

It is currently unclear whether the transformation is fully or at least partly diffusion controlled, given the small length scales involved and the elevated transformation temperature around ∼1000°C. It is, however, possible that the structural transformation to FCC-A1 precedes the chemical part of the transformation. More research is required to clarify this aspect. The most remarkable feature is, however, the ultrafine size of the vermicular FCC-A1 phase, typically with a thickness of about 200 to 500 nm, which is slightly above the wavelength of the spinodal decomposition. We thus propose that the formation of the ultrafine vermicular structure requires large undercooling below the BCC-B2 → FCC-A1 transformation temperature and some limited undercooling below the binodal line and into the three phase field "FCC-A1 + BCC-B2# + BCC-A2#". The ultrafine vermicular microstructure displays special and characteristic morphological features, including a

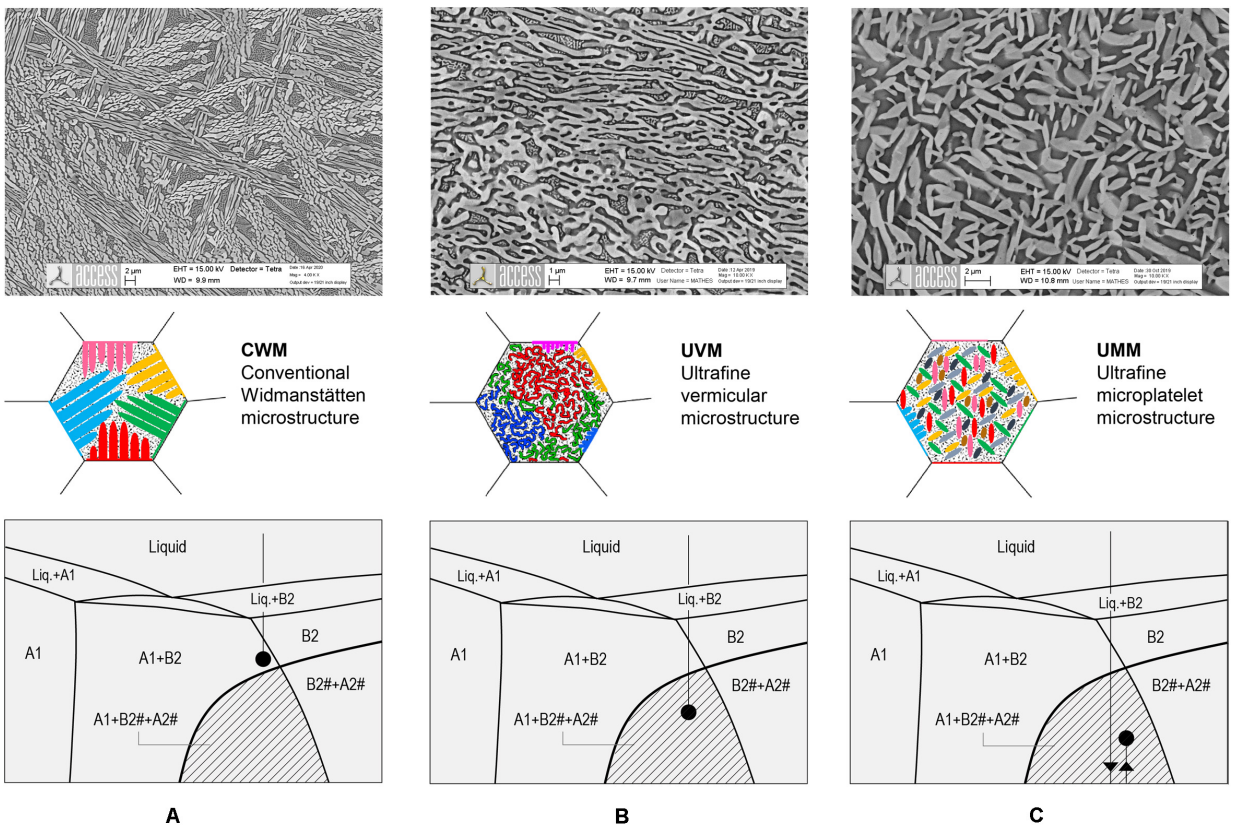

FIGURE 1 | Overview of dual phase microstructures forming in Al-(Co)-Cr-Fe-Ni alloys from the parent BCC-B2 phase under different cooling regimes. The cooling rate increases from left to right. According to the morphology of the FCC phase we distinguish **(A)** classical Widmanstätten laths and colonies, **(B)** ultrafine vermicular network and **(C)** ultrafine micro-platelets. The colors in the icons represent different crystal orientations of the FCC phase inside one parent BCC-B2 grain. The corresponding transformation pathways are schematically depicted on simplified phase diagram sections. The micrographs in the top row are taken from $AlCrFe_2Ni_2$ samples produced by arc melting of 300 g buttons **(A)**, 50 g buttons **(B)** and laser powder bed fusion, L-PBF, with a post-build heat treatment at 950°C/6 h **(C)**.

pronounced contiguity of the FCC-A1 phase, which appears fully interwoven with the spinodally decomposed BCC phase at nearly equal phase fractions. Furthermore, it is associated with a novel crystallographic orientation relationship. Sections 3.1 and section 4 contain more details about this special dual-phase microstructure.

(3) The formation of the ultrafine micro-platelet microstructure (UMM) requires highest cooling rates, e.g., above 1000 K/min and forms only during annealing heat treatments after cooling. Cooling itself must be so fast, that formation of FCC-A1 is fully suppressed, leaving behind a metastable and spinodally decomposed BCC microstructure (BCC-A2# + BCC-B2#). Precipitation of FCC-A1 occurs by isothermal annealing at a temperature in the three-phase field "FCC-A1 + BCC-B2# + BCC-A2#". Our observations show that the metastable spinodal structure offers a high density of nucleation sites for the FCC-A1 phase, such that micro-platelets with distinct crystal orientations form in high number. In fact all 12 variants of the crystallographic OR (Nishiyama-Wassermann) are present. The phase transformation pathway is as follows:

Pathway (3): BCC-B2 → BCC-B2# + BCC-A2# → FCC-A1 + BCC-B2# + BCC-A2# (annealing)

This topical Frontier's edition contains more details about this structure obtained along additive manufacturing routes with post-build annealing, as described by D. Vogiatzief et al. and V. Rocio Molina Ramirez et al. We point out, that nucleation triggered by the compositional modulations of a spinodal decomposition occurs in Fe-Mn alloys, being confined to crystalline defects (Da Silva et al., 2018). Furthermore, Loh et al., 2017 reported spinodal decomposition as the first step in a multistep nucleation of gold and silver nanocrystals in aqueous solutions.

We would like to remark that in a sample or cast part the conventional Widmanstätten structure may coexist with the ultrafine vermicular structure for moderate cooling rates. These mixed structures form successively during continuous cooling with the 1st generation of Widmanstätten plates being well developed along pathway (1), while the remaining BCC-B2 transforms to the ultrafine vermicular microstructure following pathway (2). We summarize this section with pointing out that

the ultrafine vermicular microstructures as well as the micro-platelet microstructures are unique and have not been reported for other alloy systems. Their formation requires the spinodal decomposition of BCC-B2 to trigger the nucleation and growth of FCC-A1. From a thermodynamic point of view their formation requires that a three-phase field "FCC-A1 + BCC-B2# + BCC-A2#" exists in the phase diagram in the region corresponding to the alloy composition. The subject is new, calling for modeling and simulation at all scales.

Ultrafine Vermicular Microstructure in $AlCrFe_2Ni_2$

The nearly fully UVM is obtained in small arc melted buttons (50 g) of alloy $AlCrFe_2Ni_2$, as displayed in **Figure 2**. **Table 1** lists the integral alloy composition measured by EDS. The SEM image in **Figure 2A** reveals three grains with one of the grain boundaries showing a narrow region of Widmanstätten laths protruding from the boundary into one grain. The bright phase with vermicular morphology is FCC-A1, while the dark phase is spinodally decomposed BCC-B2. The inserted micrograph taken at higher magnification shows that the width of the FCC phase in the vermicular network is about the size of the spinodal wavelength. The TEM images in **Figure 2B** show a close-up view of the microstructure constituents: the bright FCC-A1 phase is as small as ∼250 nm in width and contains sub-grains as well as a high density of dislocations; the dark "matrix" phase is spinodally decomposed into an Al-,Ni- rich BCC-B2# (labeled ①) and Cr-, Fe- rich BCC-A2# particles (labeled ②). The diffraction patterns of the two BCC phases are equally displayed for a < 100 > zone axis. A subtle difference in the intensity of the {100} planes, relative to the {110} planes, was observed when comparing the diffractions of the BCC-B2# and BCC-A2# phases. **Table 2** lists the measured phase compositions and lattice parameters for the three phases. The structural features are similar to the ones reported in Dong et al. (2016).

TABLE 1 | Chemical composition of the alloy $AlCrFe_2Ni_2$ measured by EDS in an SEM.

Element	Al	Cr	Fe	Ni
Nominal (at %)	16.67	16.67	33.34	33.34
Mean, Std. dev. (at %)	16.6 ± 0.3	17.4 ± 0.2	33.1 ± 0.3	32.9 ± 0.2
Mean, Std. dev. (wt %)	8.7 ± 0.1	17.7 ± 0.1	36.0 ± 0.3	37.7 ± 0.3

TABLE 2 | Chemical composition and lattice parameters of the phases in an as-cast $AlCrFe_2Ni_2$ sample with ultrafine vermicular microstructure, measured by high resolution EDS in STEM.

Phase	Phase composition, at % (TEM, HR-EDS)				Lattice parameter, a, Å
	Al	Cr	Fe	Ni	
FCC-A1	8.3	19.7	43.5	28.5	a = 3.554
BCC-B2	34.3	3.1	15.1	47.5	a = 2.889
BCC-A2	6.1	32.2	48.5	13.3	not analyzed

CRYSTAL ORIENTATION RELATIONSHIP PERTAINING TO ULTRAFINE VERMICULAR MICROSTRUCTURES

EBSD mapping was used extensively in order to identify the crystal orientation relationship (OR) between the vermicular

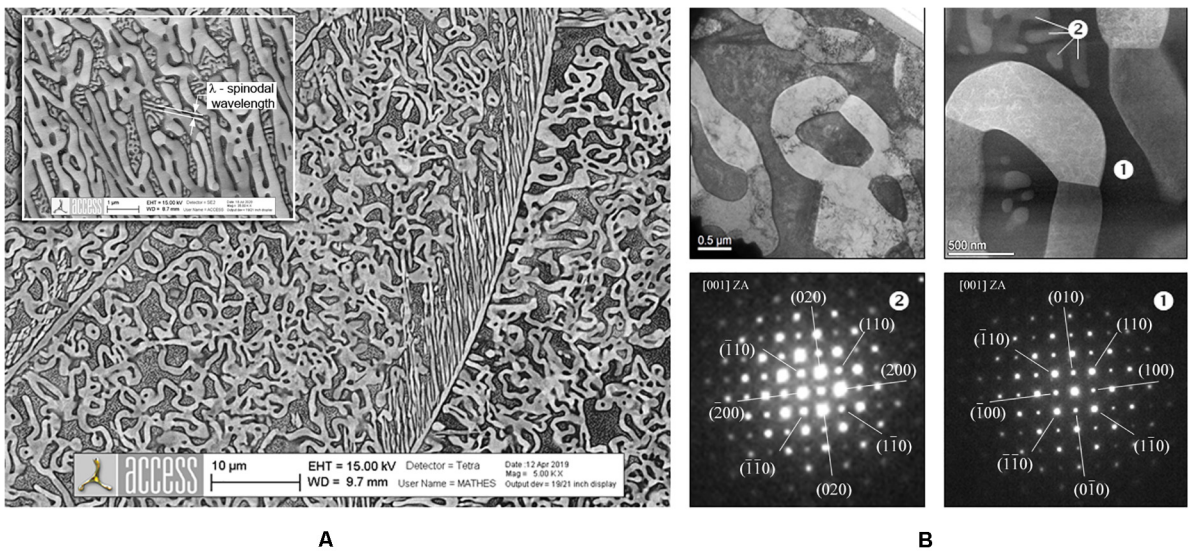

FIGURE 2 | SEM **(A)** and BFTEM as well as STEM **(B)** micrographs of an as-cast $AlCrFe_2Ni_2$ sample featuring the ultrafine vermicular microstructure of FCC-A1 in a spinodally decomposed BCC matrix. The product phases of the spinodal decomposition are labeled ① (BCC-B2#) and ② (BCC-A2). Diffraction patterns taken along a [001] zone axis show subtle difference in the intensity of the {100} planes, relative to the {110} planes, when comparing BCC-B2# and BCC-A2# phases. Note the high dislocation density in the FCC-A1 phase as well as sub-grain boundaries.

FCC and the parent BCC phase, which in turn is spinodally decomposed into a mixture of BCC#1 = BCC-B2 and BCC#2 = BCC-A2 phases. The product phases of the spinodal reaction have different composition and lattice parameter, but identical crystal orientation, and hence no distinction between is made between them. The phases used for mapping were Iron (BCC, space group no. 229) and Nickel (FCC, space group no. 225).

We illustrate the EBSD mapping and results of the analysis based on a mapping region with an area S_a = 1384.384 μm^2 (**Figure 3**) scanned with a resolution of 1 pixel = 0.007 μm^2. The mapping region contains two distinct grains with vermicular microstructure, separated by a grain boundary. A thin FCC film decorates the grain boundary between the neighboring grains. A narrow region of FCC Widmanstätten laths with the crystal orientation of grain 2 grow from the boundary into the opposite BCC grain, i.e., grain 1. For convenience, the crystal mimic of the involved phases is equally depicted. It is noted here, and will be outlined later in more detail, that the FCC phase displays considerable lattice strain and a high density of low angle grain boundaries (LAGBs) with disorientation angles ranging from 2 to 12 degree. Accordingly, the FCC crystal orientation in each grain is rather broadly scattered around a specific average orientation and the FCC pole figures show wider poles compared to the BCC phase, as seen in **Figures 4**, **5**. The two figures display selected pole figures for grain 1 and grain 2, respectively, which illustrate the crystal orientation relationship between vermicular FCC and the parent BCC. It turns out that this is a novel crystallographic OR, which is not only distinct from the ORs observed in samples with classical Widmanstätten (CWM) or ultrafine micro-platelet (UMM) structure, but also different from all other ORs reported for the BCC/FCC systems. In fact, before identifying the new OR we first performed a careful verification of the known ORs, which have been reviewed and tabulated e.g., in (Verbeken et al., 2009).

The new OR described below was found in many samples from different alloys including not only $AlCrFe_2Ni_2$ but also $Al_{0.8}CoCrFeNi$ and $AlCrFe_2Ni_2$ with Mo additions. It is characteristic for dual-phase medium and high entropy alloys with ultrafine vermicular microstructure; we found no exception from it.

Figure 4A shows the relevant pole figures for grain 1 and highlights the poles which correspond to the common planes and directions of the OR. Common planes and directions are indexed and marked in green color with full and dotted circles, respectively. In grain 1 the two crystals imbricate such that:

$$\begin{aligned} &\text{Common plane(s):} && (111)^{FCC} \parallel (12\bar{1})^{BCC} \text{ and} \\ &&& (1\bar{1}1)^{FCC} \parallel (\bar{1}21)^{BCC} \\ &\text{Common direction:} && [\bar{1}01]^{FCC} \parallel [\bar{1}0\bar{1}]^{BCC} \end{aligned}$$

Interestingly, for the given crystal orientations in grain 1, a second set of low index planes and directions was found to superpose as shown in **Figure 4B**. The common planes and directions are indexed and marked in red color with full and dotted circles, respectively.

$$\begin{aligned} &\text{Common plane(s):} && (1\bar{3}\bar{1})^{FCC} \parallel (\bar{1}03)^{BCC} \text{ and} \\ &&& (\bar{1}\bar{3}1)^{FCC} \parallel (\bar{3}01)^{BCC} \\ &\text{Common direction:} && [101]^{FCC} \parallel [010]^{BCC} \end{aligned}$$

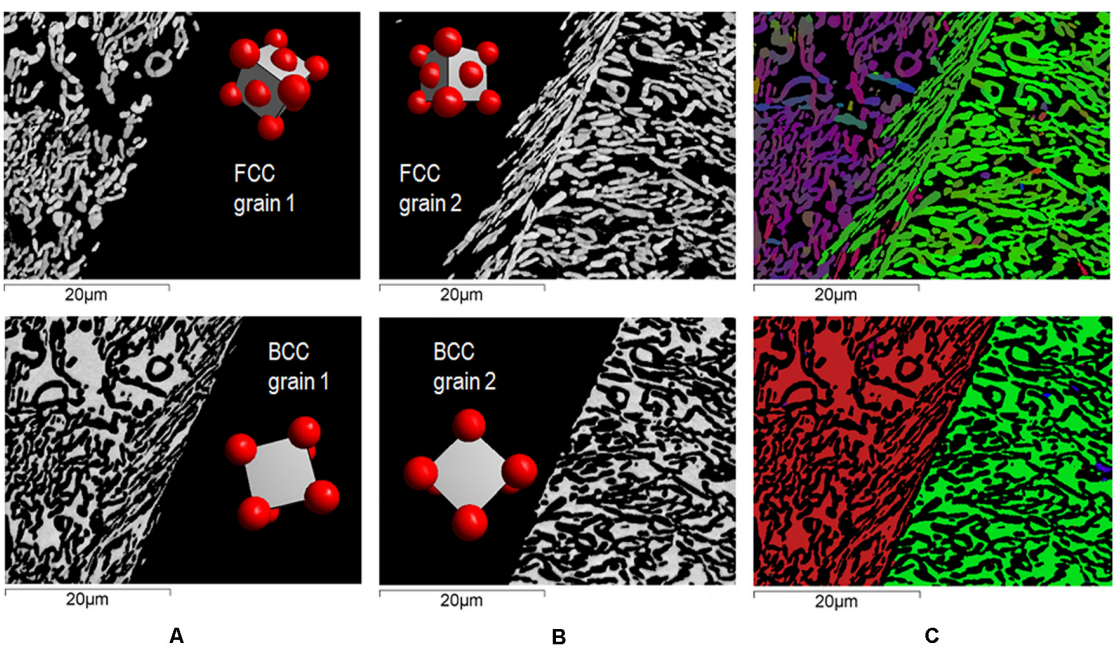

FIGURE 3 | EBSD map in sample $AlCrFe_2Ni_2$ with ultrafine vermicular microstructure in a region of interest containing a grain boundary of the parent BCC-B2 phase. The phases and their crystal mimic are shown for each grain **(A,B)**. An overall view is presented in **(C)** using an inverse pole figure color map for the FCC phase (top) and the BCC phase (bottom), respectively.

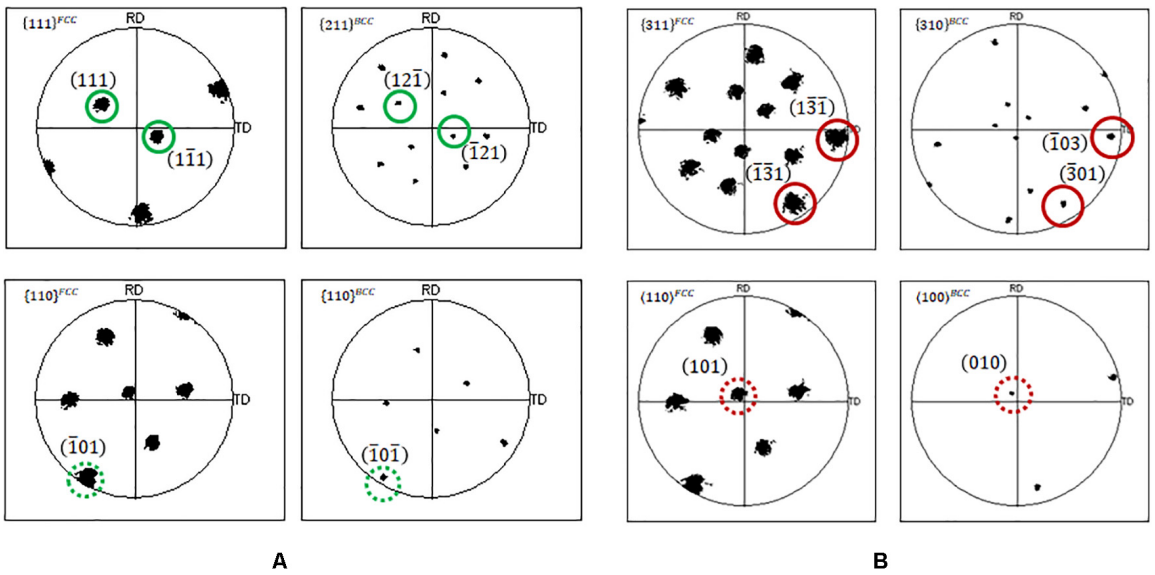

FIGURE 4 | Selected pole figures for grain 1, see **Figure 3A**, illustrating the primary **(A)** and the secondary **(B)** crystallographic orientation relationship between FCC and the parent BCC phase. Full circles mark the superposing poles, which correspond to the common planes. Dotted circles mark the superposing poles, which correspond to the common direction. Common planes and directions are indexed with the corresponding {hkl}-triplets.

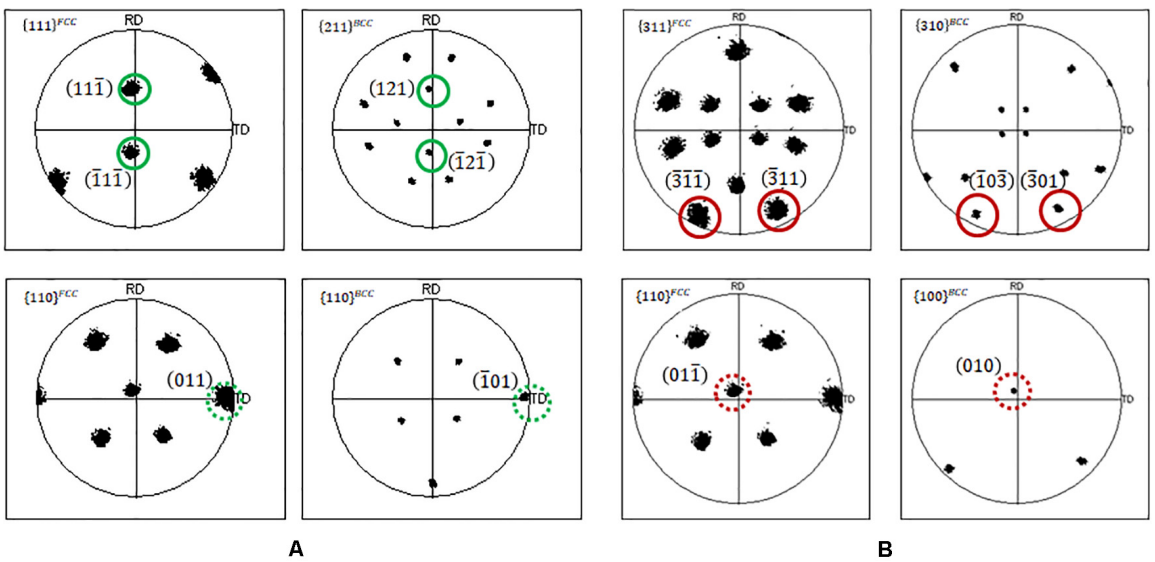

FIGURE 5 | Selected pole figures for grain 2, see **Figure 3B**, illustrating the primary **(A)** and the secondary **(B)** crystallographic orientation relationship between FCC and the parent BCC phase. Full circles mark the superposing poles, which correspond to the common planes. Dotted circles mark the superposing poles, which correspond to the common direction. Common planes and directions are indexed with the corresponding {hkl}-triplets.

Figures 5A,B confirm that the same ORs are present in grain 2, naturally with permuted {hkl}-indices for the common planes and directions. **Table 3** summarizes the results for both grains. The two ORs listed above are simultaneously valid and the system can choose to align phase boundaries to any of the common planes in order to reduce the phase boundary energy. For convenience, we call the ORs primary and secondary ORs. Likely, the primary OR provides deeper energy minima and more pronounced energy anisotropy compared to the secondary OR. The presence of the secondary and presumably less anisotropic OR may indeed explain the poor alinement of FCC/BCC interfaces observed in the ultrafine vermicular microstructures.

Noteworthy, the planes of the BCC phase pertaining to the above ORs are twinning planes, e.g., {112} and even {013}, as reviewed in Christian and Mahajan (1995). This suggests that twinning is possibly triggering the nucleation of vermicular FCC

TABLE 3 | Crystal orientation relationship(s) identified in an as-cast sample $AlCrFe_2Ni_2$ with ultrafine vermicular microstructure; the primary and secondary OR hold simultaneously.

No	EBSD map	Primary OR	Secondary OR
G1	Grain 1/**Figure 3**	$(111)^{FCC} \parallel (12\bar{1})^{BCC}$ $(1\bar{1}1)^{FCC} \parallel (\bar{1}21)^{BCC}$ $[\bar{1}01]^{FCC} \parallel [\bar{1}0\bar{1}]^{BCC}$	$(1\bar{3}\bar{1})^{FCC} \parallel (\bar{1}03)^{BCC}$ $(\bar{1}\bar{3}1)^{FCC} \parallel (\bar{3}01)^{BCC}$ $[101]^{FCC} \parallel [010]^{BCC}$
G2	Grain 2/**Figure 3**	$(11\bar{1})^{FCC} \parallel (121)^{BCC}$ $(\bar{1}1\bar{1})^{FCC} \parallel (\bar{1}2\bar{1})^{BCC}$ $[011]^{FCC} \parallel [\bar{1}01]^{BCC}$	$(\bar{3}\bar{1}1)^{FCC} \parallel (\bar{1}0\bar{3})^{BCC}$ $(\bar{3}11)^{FCC} \parallel (\bar{3}01)^{BCC}$ $[01\bar{1}]^{FCC} \parallel [010]^{BCC}$
V1	Variant 1/**Figure 6**	$(\bar{1}1\bar{1})^{FCC} \parallel (211)^{BCC}$ $(111)^{FCC} \parallel (\bar{2}11)^{BCC}$ $[\bar{1}01]^{FCC} \parallel [01\bar{1}]^{BCC}$	$(13\bar{1})^{FCC} \parallel (013)^{BCC}$ $(\bar{1}31)^{FCC} \parallel (031)^{BCC}$ $[101]^{FCC} \parallel [\bar{1}00]^{BCC}$
V2	Variant 2/**Figure 6**	$(\bar{1}\bar{1}\bar{1})^{FCC} \parallel (21\bar{1})^{BCC}$ $(1\bar{1}1)^{FCC} \parallel (\bar{2}1\bar{1})^{BCC}$ $[\bar{1}01]^{FCC} \parallel [011]^{BCC}$	$(1\bar{3}\bar{1})^{FCC} \parallel (01\bar{3})^{BCC}$ $(\bar{1}\bar{3}1)^{FCC} \parallel (03\bar{1})^{BCC}$ $[101]^{FCC} \parallel [\bar{1}00]^{BCC}$
V3	Variant 3/**Figure 6**	$(111)^{FCC} \parallel (121)^{BCC}$ $(1\bar{1}1)^{FCC} \parallel (\bar{1}2\bar{1})^{BCC}$ $[10\bar{1}]^{FCC} \parallel [\bar{1}01]^{BCC}$	$(1\bar{3}\bar{1})^{FCC} \parallel (\bar{3}0\bar{1})^{BCC}$ $(\bar{1}\bar{3}1)^{FCC} \parallel (\bar{1}0\bar{3})^{BCC}$ $[101]^{FCC} \parallel [010]^{BCC}$

inside the spinodally decomposing BCC-B2 parent phase. The elastic strain associated with the compositional modulation may suffice to promote local twinning at the atomic level and trigger the BCC-FCC structural transition with these unusual ORs.

We observed, without showing details here, that nucleation events are, however, rare, meaning that vermicular domains within one single parent grain are large. In fact, these domains are crystallographic variants of the above given ORs. From a total of 12 possible variants we typically observe 3 to 4 variants in one parent grain. **Figure 6** shows an EBSD mapping region, which encompasses three vermicular domains evolved from the same parent grain. The phase map in **Figure 6A** shows the fractions of the two phases, with FCC reaching about 58 area%. **Figure 6B** shows the Euler map, with all Euler angles for both phases, **Figures 6C,D** show selected inverse pole figure color maps for BCC and FCC, respectively, being superposed to the pattern quality map. Finally, **Figure 6E** displays the crystal mimic of the parent BCC and of the three variants of the vermicular FCC

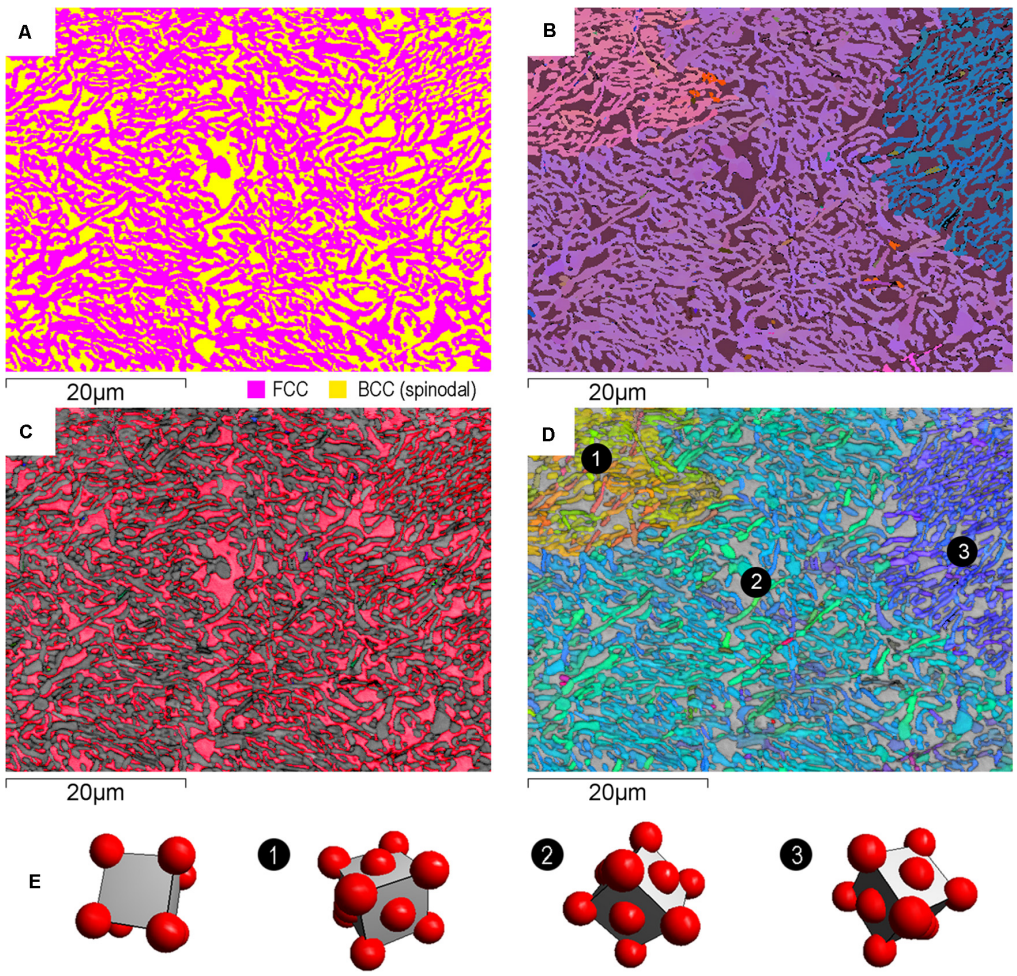

FIGURE 6 | EBSD map in sample $AlCrFe_2Ni_2$ with ultrafine vermicular microstructure in a region of interest containing three vermicular domains inside one parent BCC-B2 grain. The phase map **(A)** reveals the fraction of FCC ~58%. The Euler map **(B)** outlines the three distinct FCC domains. A better view of the phase orientation is given in the inverse pole figure color maps **(C,D)** superposed to the pattern quality maps. The crystal mimic of the phases in (E) shows the three FCC variants corresponding to the three vermicular domains. The full crystal OR is listed in **Table 3** for each variant.

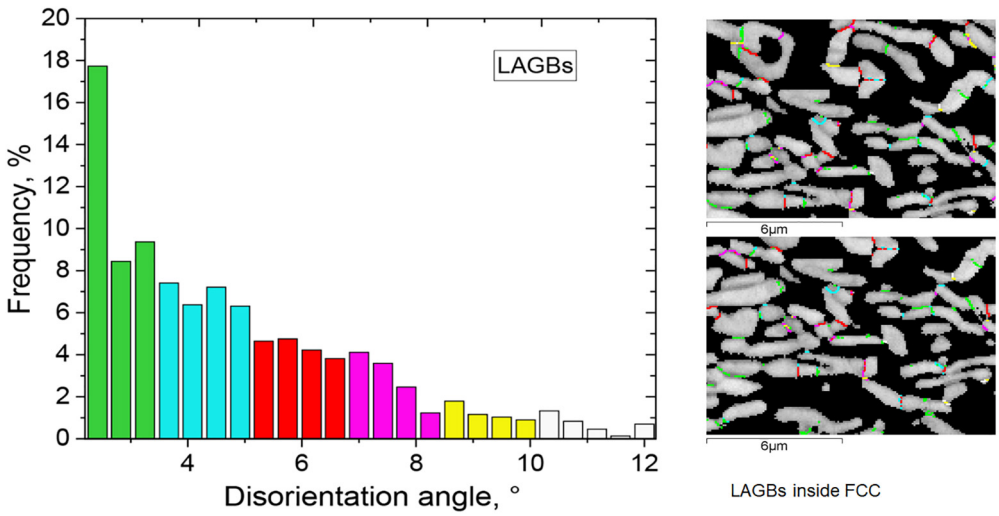

FIGURE 7 | Disorientation angle distribution inside the vermicular FCC phase of grain 2 (compare **Figures 3B,C**) in the range from 2 to 12° and associated sub-grain boundaries, i.e., low angle grain boundaries (LAGBs).

phase. **Table 3** lists the common planes and directions identified for each of the variants following the primary and secondary OR.

Finally, we recall that the vermicular FCC phase displays considerable lattice strain and a high density of low angle grain boundaries (LAGBs). These features result from the solid state phase transformation following the dynamic relaxation of phase transformation stresses accomplished through dislocation networks, dislocation slip, lattice rotations etc., which are known mechanisms of phase transformation plasticity (Denis et al., 1985). Due to the involved stresses, the elastoplastic deformation processes are complex, as shown by the simulations reported i.e., in Cottura et al., 2015 and Yamanaka et al., 2010 for other alloys. For the BCC-FCC transformation at case here, the spinodal decomposition of the parent phase induces yet another stress/strain field, which will affect the relaxation processes involved. From today's perspective, understanding the elastoplastic aspects of this solid state transformation and its impact on the observed lattice strain of the vermicular FCC phase is a true challenge.

A quantitative analysis of the lattice strain is beyond the scope of this paper. However, a convenient way to estimate the associated deformation is by analyzing the disorientation angle distribution inside the FCC phase (single grain including subgrains) using EBSD mapping data (Humphreys, 2001; Brough et al., 2006). The analysis is included in commercial EBSD software packages, here INCA Crystal. The relative disorientation (or misorientation) for a given data point is expressed as an angle-axis pair corresponding to the operation of rotating the crystal from each individual data point into coincidence with the average crystal orientation of the grain. The average disorientation angle is then calculated over all data points. The results are further used to outline low angle boundaries (LAGBs) according to predefined angular ranges. We illustrate the results of this analysis for the FCC-Grain 2 data (compare **Figure 3**) in **Figure 7**. The frequency of the measured disorientation angles are plotted for the range from 2 to 12° and color-coded for predefined ranges. LAGBs within the FCC phase are shown using the same color code. The average disorientation ranges around 5.8° being higher compared to a typical value of ∼3.8° found in a package of Widmanstätten laths. This rather high number reflects the lattice strain associated with the phase transformation when FCC growth occurs along with the spinodal decomposition of the parent BCC-B2 phase.

SUMMARY AND CONCLUSION

The spinodal decomposition of the BCC-B2 phase and more specifically its interaction with the BCC-FCC phase transformation is one of the most fascinating aspects in the alloy system Al-(Co)-Cr-Fe-Ni. In certain compositional regions, e.g., in alloys $Al_{0.8}CoCrFeNi$ and $AlCrFe_2Ni_2$, the sequence of phase transformations, involving the structural transformation BCC-B2 → FCC-A1 and the spinodal decomposition BCC-B2 → BCC-B2# + BCC-A2# change, when changing the cooling conditions. Three distinct phase transformation pathways are accessible, leading to very distinct microstructures.

- Upon slow cooling the classical Widmanstätten microstructure forms, however, with the remaining BCC phase being spinodally decomposed after completion of the BCC-B2 → FCC-A1 transformation.
- For moderate to high cooling rates an ultrafine vermicular microstructure forms with the FCC-A1 phase displaying a contiguous network, neatly interwoven with spinodally decomposed BCC. The thickness of the individual FCC "veins" is about the size of the spinodal wavelength. This structure is formed upon cooling into the three phase field "BCC-B2# + BCC-A2# + FCC-A1", i.e., when Widmanstätten growth is kinetically supressed due to the applied cooling conditions.

- For high and very high cooling rates the FCC formation can be fully supressed, leading to a metastable BCC spinodal state. It offers a high density of nucleation sites for FCC-A1 upon annealing in the three phase field "BCC-B2# + BCC-A2# + FCC-A1". The resulting morphology of FCC-A1 is best described by the term "micro-platelets" and it is unique because all crystallographic variants (Nishiyama-Wassermann) are present and randomly distributed within a parent grain.

In all cases, the phase fraction of FCC-A1 finally reaches about 50% to 60%, depending on the alloy composition. This nearly "duplex" phase balance makes these alloys very interesting for structural applications. Moreover, the distinct and unique microstructures described above are accessible along distinct manufacturing routes, e.g., sand casting, permanent mold casting, and additive manufacturing. Further research is needed to explore the mechanical properties associated to the distinct microstructures. Some properties, e.g., fatigue, will sensitively depend on the microstructural features, while other will show less pronounced dependency.

In the second part, we described the ultrafine vermicular microstructure in more detail, with emphasis on the crystal orientation relationship between FCC and BCC. The OR differs from Nishiyama-Wassermann and from any other BCC/FCC relationship known from literature on steels. It reads $\{111\}^{FCC} \parallel \{\bar{2}11\}^{BCC}$; $\bar{1}01^{FCC} \parallel 01\bar{1}^{BCC}$. A secondary, embedded OR reads $\{\bar{1}31\}^{FCC} \parallel \{031\}^{BCC}$; $101^{FCC} \parallel \bar{1}00^{BCC}$. The secondary and presumably less anisotropic OR may indeed explain the poor alinement of FCC/BCC interfaces observed in the ultrafine vermicular microstructures. Whether the OR is triggered by local twinning at the atomic level, remains to be investigated.

We finally emphasize that the phase transformations presented here and the associated microstructure features do not genuinely relate to high entropy or medium entropy effects as were originally postulated (Murty et al., 2014). They are a direct consequence of the thermodynamic equilibria of the alloy systems Al-Cr-Fe-Ni and Al-Co-Cr-Fe-Ni and the corresponding phase fields accessible by cooling. We note, however, that limited diffusion kinetics, if applicable (Divinski et al., 2018), may ease the transition to off-equilibrium transformation pathways, which in this case lead to very distinct microstructures. Our own research continues with focus on comparing the associated mechanical properties, specifically the fatigue resistance.

DATA AVAILABILITY STATEMENT

The raw data supporting the conclusions of this article will be made available by the authors, without undue reservation.

AUTHOR CONTRIBUTIONS

UH conducted the research and performed the analysis of crystal ORs. SG and OS prepared the samples by arc melting and performed EBSD measurements, as part of their Ph.D. research. EE performed TEM and STEM measurements including high resolution EDS measurements as part of his Ph.D. thesis. SO guided and supervised the research of EE. All authors contributed to the article and approved the submitted version.

FUNDING

The German Federal Ministry for Education and Research (BMBF) supported this research under grant number 03XP0163A in the frame of the M-era.Net Joint Call 2017, Project NADEA (no. 5129).

ACKNOWLEDGMENTS

EE and SO acknowledge funding through the Ministry of Science, Technology and Space, of the State of Israel in the frame of the M-era.Net Joint Call 2017, Project NADEA (no. 5129). We wish to thank Dimitrios Vogiatzief from Oerlikon AM GmbH for providing a sample from alloy $AlCrFe_2Ni_2$ in the as-build state, being produced by laser powder bed fusion.

REFERENCES

Abuzaid, W., and Sehitoglu, H. (2018). Plastic strain partitioning in dual phase Al13CoCrFeNi high entropy alloy. *Mater. Sci. Eng. A* 720, 238–247. doi: 10.1016/j.msea.2018.02.044

Bönisch, M., Wu, Y., and Sehitoglu, H. (2018). Twinning-induced strain hardening in dual-phase FeCoCrNiAl0.5 at room and cryogenic temperature. *Sci. Rep.* 8:10663. doi: 10.1038/s41598-018-28784-1

Brough, I., Bate, P. S., and Humphreys, F. J. (2006). Optimising the angular resolution of EBSD. *Mater. Sci. Technol.* 22, 1279–1286. doi: 10.1179/174328406X130902

Bunge, H. J., Weiss, W., Klein, H., Wcislak, L., Garbe, U., and Schneider, J. R. (2003). Orientation relationship of Widmannstätten plates in an iron meteorite measured with high-energy synchrotron radiation. *J. Appl. Crystallogr.* 36, 137–140. doi: 10.1107/S0021889802021386

Christian, J. W., and Mahajan, S. (1995). Deformation twinning. *Prog. Mater. Sci* 39, 1–157. doi: 10.1016/0079-6425(94)00007-7

Cottura, M., Benoît, A., Finel, A., and Le Bouar, Y. (2015). Plastic relaxation during diffusion-controlled growth of Widmanstätten plates. *Scripta Mat.* 108, 117–121. doi: 10.1016/j.scriptamat.2015.06.032

Da Silva, A. K., Ponge, D., Peng, Z., Inden, G., Lu, Y., Breen, A., et al. (2018). Phase nucleation through confined spinodal fluctuations at crystal defects evidenced in Fe-Mn alloys. *Nat. Commun.* 9, 1–11. doi: 10.1038/s41467-018-03591-4

De Jeer, L. T. H., Ocelík, V., and De Hosson, J. T. M. (2017). Orientation Relationships in Al0.7CoCrFeNi high-entropy alloy. *Microsc. Microanal.* 23, 905–915. doi: 10.1017/S1431927617012442

Denis, S., Aeby-Gautier, E., Simon, A., and Beck, G. (1985). Stress–phase-transformation interactions – basic principles, modelling, and calculation of internal stresses. *Mater. Sci. Technol.* 1, 805–814. doi: 10.1179/026708385790124071

Divinski, S. V., Pokoev, A., Neelamegan, E., and Paul, A. (2018). A mystery of "sluggish diffusion" in high-entropy alloys: the truth or a myth?. *Diffus. Fundam.* 17:69. doi: 10.4028/www.scientific.net/DF.17.69

Dong, Y., Gao, X., Lu, Y., Wang, T., and Li, T. (2016). A multi-component AlCrFe2Ni2 alloy with excellent mechanical properties. *Mater. Lett.* 169, 62–64. doi: 10.1016/j.matlet.2016.01.096

Gangireddy, S., Gwalani, B., Soni, V., Banerjee, R., and Mishra, R. S. (2019). Contrasting mechanical behavior in precipitation hardenable AlXCoCrFeNi high entropy alloy microstructures: single phase FCC vs. dual phase FCC-BCC. *Mat. Sci. Eng. A* 739, 158–166. doi: 10.1016/j.msea.2018.10.021

Humphreys, F. J. (2001). Review Grain and subgrain characterisation by electron backscatter diffraction. *J. Mater. Sci.* 36, 3833–3854. doi: 10.1023/A:1017973432592

Kao, Y. F., Chen, T. J., Chen, S. K., and Yeh, J. W. (2009). Microstructure and mechanical property of as-cast, -homogenized, and -deformed AlxCoCrFeNi (0 = x = 2) high-entropy alloys. *J. Alloys Compd.* 488, 57–64. doi: 10.1016/j.jallcom.2009.08.090

Knyazeva, M., and Pohl, M. (2013). Duplex steels: part I: genesis, formation, structure. *Metallogr. Microstruct. Anal.* 2, 113–121. doi: 10.1007/s13632-013-0066-8

Kurdjumow, G., and Sachs, G. (1930). Über den mechanismus der stahlhärtung. *Z. Phys.* 64, 325–343. doi: 10.1007/BF01397346

Li, C., Qu, Y., Zhang, Y., Lv, Q., and Qi, H. (2020). Effect of deep cryogenic treatment on the microstructure and mechanical properties of AlCrFe2Ni2 High-entropy alloy. *Mater. Res. Express* 7:036504. doi: 10.1088/2053-1591/ab7a5f

Linden, Y., Pinkas, M., Munitz, A., and Meshi, L. (2017). Long-period antiphase domains and short-range order in a B2 matrix of the AlCoCrFeNi high-entropy alloy. *Scr. Mater.* 139, 49–52. doi: 10.1016/j.scriptamat.2017.06.015

Loh, N. D., Sen, S., Bosman, M., Tan, S. F., Zhong, J., Nijhuis, C. A., et al. (2017). Multistep nucleation of nanocrystals in aqueous solution. *Nat. Chem.* 9, 77–82. doi: 10.1038/nchem.2618

Murty, B. S., Yeh, J. W., and Ranganathan, S. (2014). *High-Entropy Alloys*. Oxford: Butterworth-Heinemann.

Nishiyama, Z. (1934). X-ray investigation of the mechanism of the transformation from face centered cubic lattice to body centered cubic lattice. *Sci. Rep. Tohoku Imp. Univ.* 23:637.

Ohmori, Y., Nakai, K., Ohtsubo, H., and Isshiki, Y. (1995). Mechanism of widmanstätten austenite formation in a δ/γ duplex phase stainless steel. *ISIJ Int.* 35, 969–975. doi: 10.2355/isijinternational.35.969

Rao, J. C., Ocelík, V., Vainchtein, D., Tang, Z., Liaw, P. K., and De Hosson, J. T. M. (2016). The fcc-bcc crystallographic orientation relationship in AlxCoCrFeNi high-entropy alloys. *Mater. Lett.* 176, 29–32. doi: 10.1016/j.matlet.2016.04.086

Shi, Y., Yang, B., Xie, X., Brechtl, L., Dahmen, K. A., and Liaw, P. K. (2017). Corrosion of Al xCoCrFeNi high-entropy alloys: al-content and potential scan-rate dependent pitting behavior. *Corros. Sci.* 119, 33–45. doi: 10.1016/j.corsci.2017.02.019

Steurer, W. (2020). Single-phase high-entropy alloys – A critical update. *Mater. Charact.* 162:110179. doi: 10.1016/j.matchar.2020.110179

Tkaczyk, A. H., Bartl, A., Amato, A., Lapkovskis, V., and Petranikova, M. (2018). Sustainability evaluation of essential critical raw materials: cobalt, niobium, tungsten and rare earth elements. *J. Phys. D Appl. Phys.* 51:203001. doi: 10.1088/1361-6463/aaba99

Verbeken, K., Barbé, L., and Raabe, D. (2009). Evaluation of the crystallographic orientation relationships between FCC and BCC phases in TRIP steels. *ISIJ Int.* 49, 1601–1609. doi: 10.2355/isijinternational.49.1601

Wang, W. R., Wang, W. L., and Yeh, J. W. (2014). Phases, microstructure and mechanical properties of AlxCoCrFeNi high-entropy alloys at elevated temperatures. *J. Alloys Compd.* 589, 143–152. doi: 10.1016/j.jallcom.2013.11.084

Wassermann, G. (1935). *Über den Mechanismus der α-γ Umwandlung des Eisens Mitteilungen aus dem Kaiser-Wilhelm-Institut für Eisenforschung zu Düsseldorf*. Stuttgart: Verlag Stahleisen. doi: 10.1016/j.jallcom.2013.11.084

Yamanaka, A., Takaki, T., and Tomita, Y. (2010). Elastoplastic phase-field simulation of martensitic transformation with plastic deformation in polycrystal. *Int. J. Mech. Sci.* 52, 245–250. doi: 10.1016/j.ijmecsci.2009.09.020

Conflict of Interest: The authors declare that the research was conducted in the absence of any commercial or financial relationships that could be construed as a potential conflict of interest.

frontiers in Materials

ORIGINAL RESEARCH
published: 27 August 2020
doi: 10.3389/fmats.2020.00284

TEM and High Resolution TEM Investigation of Phase Formation in High Entropy Alloy $AlCrFe_2Ni_2$

Eyal Eshed[1,2], Suzan Abd El Majid[3], Menachem Bamberger[3] and Shmuel Osovski[1]*

[1] Faculty of Mechanical Engineering, Technion Israel Institute of Technology, Haifa, Israel, [2] Technion Research and Development Foundation, Israel Institute of Metals, Haifa, Israel, [3] Faculty of Materials Science and Engineering, Technion Israel Institute of Technology, Haifa, Israel

The $AlCrFe_2Ni_2$ high entropy alloy exhibits an interesting microstructure, which changes considerably when various thermal treatments are applied. These changes are manifested mostly through the precipitation and dissolution of several BCC and FCC phases. To gain better understanding as to the phase evolution in $AlCrFe_2Ni_2$ with respect to the thermal history, the microstructures of four thermal states were investigated using Transmission Electron Microscope (TEM) and high resolution TEM. The thermal states included as-cast, homogenized at 1185°C for 75 min, homogenized and aged at 750°C for 4 h, and homogenized and aged at 930°C for 3 h. Common phases to all of the examined thermal states are Fe-rich FCC phase, ordered Ni-Al -rich BCC phase (B2), and disordered Cr-Fe -rich BCC phase. Following homogenization at 1185°C dissolution of the submicron-sized BCC phase particles in the ordered B2 phase was observed. Aging at 750°C resulted in the precipitation of nano-sized B2 platelets and needle-like particles inside the FCC phase domain, while the re-precipitation of nano-sized Cr-Fe globules occurred in the B2 phase. Aging at 930°C resulted mainly in the formation of submicron sized B2 platelets in the FCC phase domain.

Keywords: high entropy alloy, transmission electrom microscopy, microstructural evolution in metal, iron-nickel alloy, phase precipitation behavior

OPEN ACCESS

Edited by:
Sheng Guo, Chalmers University of Technology, Sweden

Reviewed by:
Zhiqiang Fu, South China University of Technology, China
Bharat Gwalani, Pacific Northwest National Laboratory (DOE), United States

****Correspondence:***
Eyal Eshed
eyale@trdf.technion.ac.il

Specialty section:
This article was submitted to Structural Materials, a section of the journal Frontiers in Materials

Received: *01 June 2020*
Accepted: *27 July 2020*
Published: *27 August 2020*

Citation:
Eshed E, Abd El Majid S, Bamberger M and Osovski S (2020) TEM and High Resolution TEM Investigation of Phase Formation in High Entropy Alloy $AlCrFe_2Ni_2$. Front. Mater. 7:284. doi: 10.3389/fmats.2020.00284

INTRODUCTION

The 3d transition metals based high entropy alloys (HEAs) have been the focus of attention since the early stages of this branch of metallurgy. These alloys gained attention due to their balanced combination of desired properties: mechanical behavior (strength, ductility), corrosion resistance and high thermal stability (Zhang et al., 2014; Miracle and Senkov, 2017). The most common family of HEAs in this class is the quinary AlCrCoFeNi HEA with various ratios among the constituting elements (Kao et al., 2009, 2011; Qiao et al., 2011; Dong et al., 2014; Munitz et al., 2016; Niu et al., 2019).

Non-equimolar HEAs in the AlCrCoFeNi alloy family have also been investigated. Reddy et al. (2019) found that severe deformation of $AlCoCrFeNi_{2.1}$ eutectic high entropy alloy by cryo-rolling and subsequent warm-rolling at 600°C imparts high ductility and strength due to the unique lamellar structure ($L1_2$+B2) that is formed.

Recently, the search for a more affordable HEA led to the elimination of the expensive Co. One of the emerging Co-free alloys, which holds great promise, is the non-equimolar $AlCrFe_2Ni_2$ alloy (Dong et al., 2016). While the number of publications dedicated to the study of the $AlCrFe_2Ni_2$ HEA is still quite limited, its microstructure is known to bear remarkable similarities with that of the AlCrCoFeNi alloy, and it shares its microstructural sensitivity to the cooling rate (Dong et al., 2016; Li C. et al., 2020; Li Z. et al., 2020).

Thermodynamically, Fe and Cr tend to concentrate more in a disordered FCC solid solution phase, while Ni and Al are typically concentrated in the ordered BCC arrangement (B2 phase). When the cooling rate is extremely high (such as in additive manufacturing) there is not enough time for the solidification route to go through the formation of an FCC phase, and a spinodal decomposition occurs, partitioning the alloy to Fe- and Cr-rich regions and Al- and Ni- rich regions (Wang et al., 2008; Manzoni et al., 2013; Dong et al., 2016; Munitz et al., 2016; Rogal et al., 2019; Li C. et al., 2020; Li Z. et al., 2020). Both regions possess a BCC crystal structure, with the Cr-Fe- rich phase being a configurationally disordered solid solution, and the Al-Ni- rich phase being an ordered B2 (Manzoni et al., 2013; Rogal et al., 2019; Li C. et al., 2020). Both regions share the same lattice parameter (2.88 Å) and therefore their orientation can be identical, thus forming a large contiguous BCC domain. When the solidification rate is slower, or when different post-production heat treatments are performed, the FCC phase, with a lattice parameter of 3.55 Å becomes favorable and grows at the expense of the Cr- and Fe-rich disordered BCC phase.

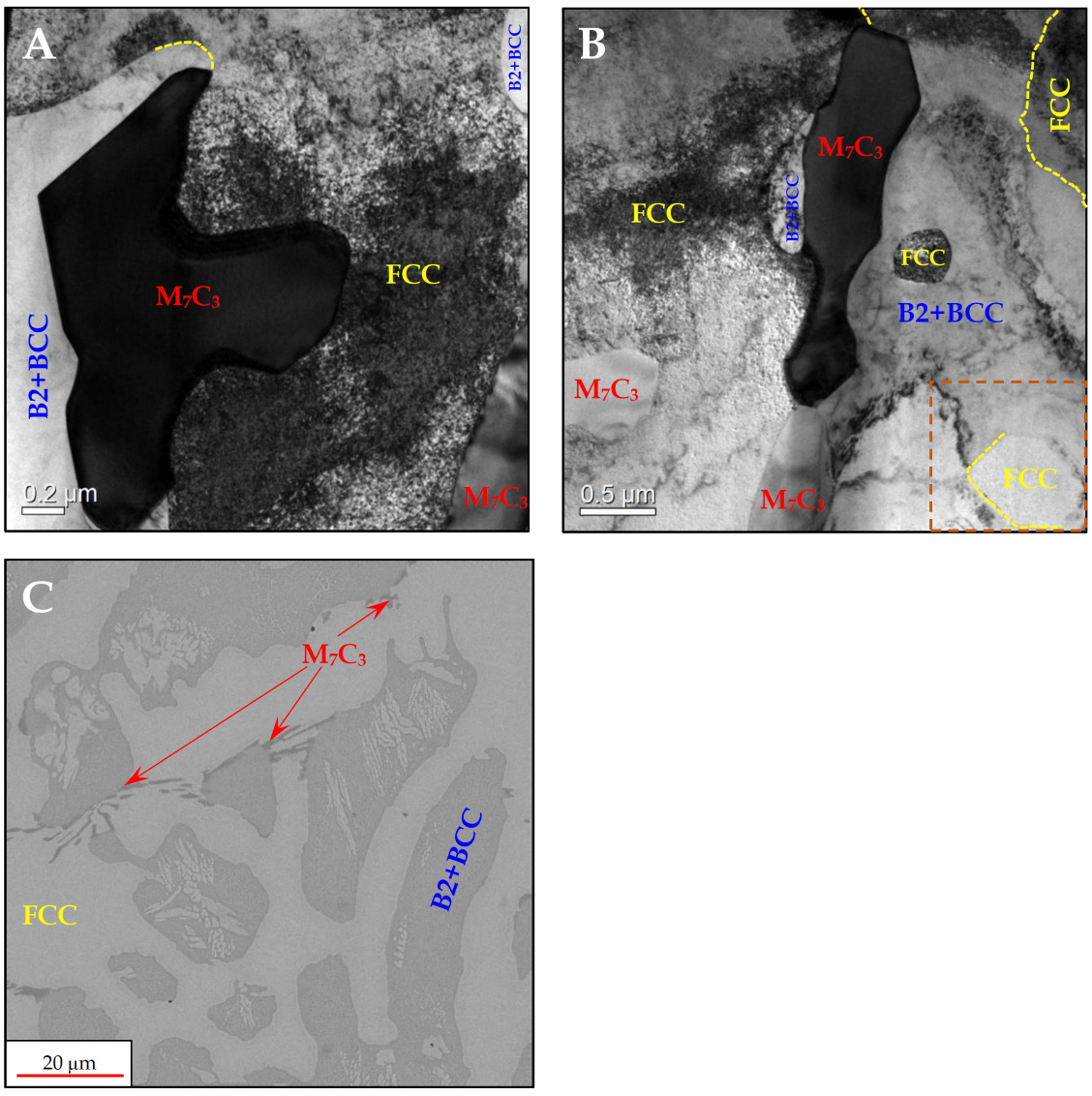

FIGURE 1 | BF-TEM micrographs showing the general morphology of the phases comprising the microstructure in as-cast $AlCrFe_2Ni_2$ alloy **(A,B)**. HRSEM micrograph showing the general microstructure in as-cast $AlCrFe_2Ni_2$ alloy **(C).**

Munitz et al. (2016) showed that for the AlCrCoFeNi alloy, the as-cast state contained almost no detectable FCC phase, and its volume fraction increased with treatment temperature in the range of $650°C \leq T < 1200°C$. When heat treated at 1200°C, the reverse phenomenon was observed and all of the formed FCC particles dissolved back into the BCC matrix. Li Z. et al. (2020) showed that for the $AlCrFe_2Ni_2$ alloy, an increased carbon content results in a general increase in the volume fraction of the FCC phase. Aside from determining which phases form during the solidification process and their volumetric ratio, the cooling rate and the carbon content can also affect the morphologies of the formed phases, ranging from needle-like particles, globules and plates to elongated worm-shaped domains.

Adding to the previously described microstructural complexity, chromium based carbides are sometimes observed alongside the occasional CrFe σ phase (Munitz et al., 2016; Rogal et al., 2019).

EXPERIMENTAL PROCEDURE

Alloying Procedure

The complete melting of a mixture of the pure elements (Al, Cr, Fe, and Ni) placed in a zirconia crucible, was achieved via a "Consarc" vacuum induction melting furnace. To avoid oxidation, a two-stage procedure was adopted. The furnace chamber was initially vacuumed to a pressure of $1.33 \cdot (10^{-6}–10^{-5})$ MPa, followed by the injection of a protective argon environment at a slight over-pressure of 0.11 MPa. Casting was performed by manual tilting of the crucible in the furnace into a high-density graphite mold. The obtained product was rod-shaped with approximate dimensions of $20 \times 20 \times 200$ mm^3.

Heat Treatments

Heat treatments were performed using an electric fiber-insulated chamber furnace. The temperature inside the furnace was monitored via a W-Re thermocouple. Homogenization treatment

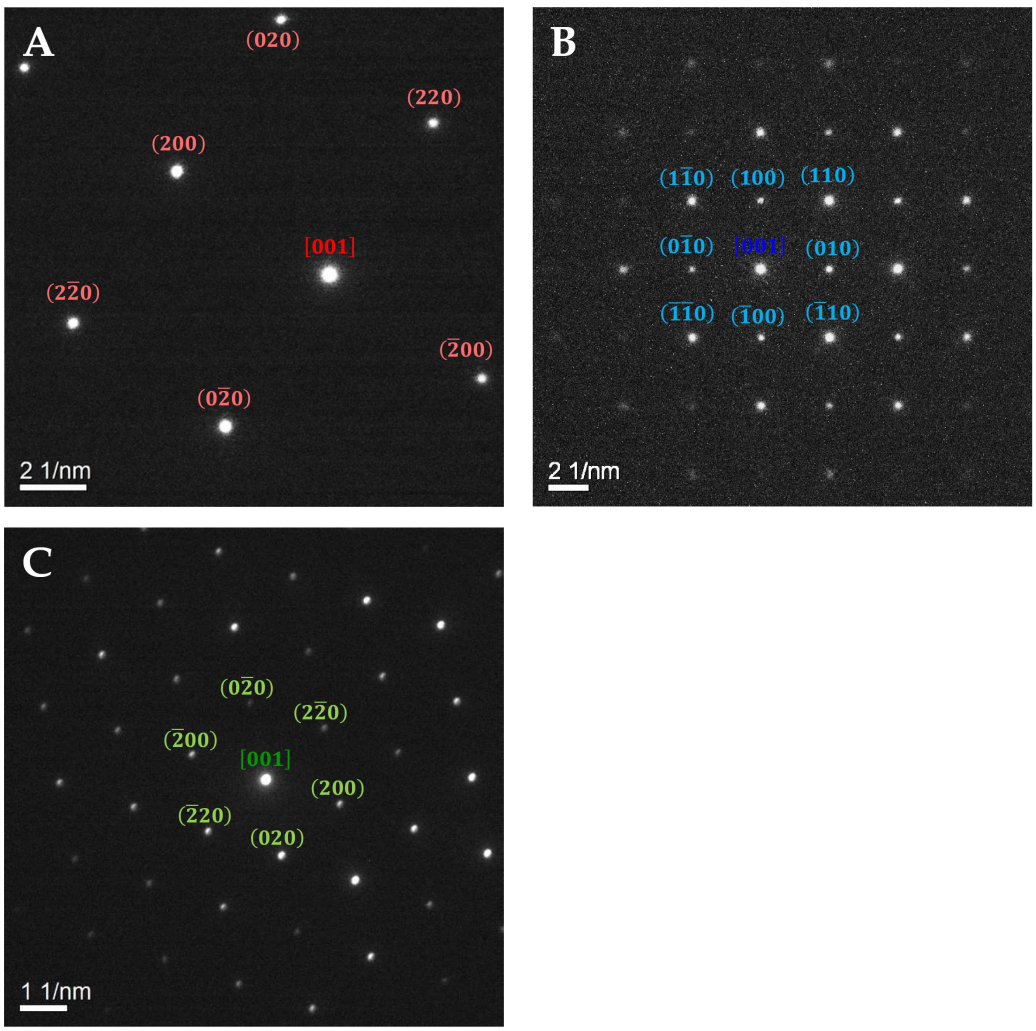

FIGURE 2 | SAED patterns in as-cast $AlCrFe_2Ni_2$ alloy – obtained from **(A)** the FCC phase in zone axis (Z.A.) <001>; **(B)** the B2 and BCC phases in Z.A. <001> and **(C)** the M_7C_3 phase in Z.A. <001>.

was performed at 1185°C for 75 min, and the subsequent aging treatments were performed at 750°C for 4 h, and 930°C for 3 h. The aforementioned heat treatments were terminated by water quenching.

Scanning Electron Microscopy (SEM)

A high resolution TESCAN MIRA3 Field Emission Gun SEM was used to observe the micron-scale microstructure. Specimens were prepared via mechanical polishing with SiC papers (1000 grit) and diamond slurries (down to 3 microns). Following the mechanical preparation stages, the specimens were electropolished at 18V for 3 s using a Struers LectroPol machine and A3 solution.

Transmission Electron Microscopy (TEM)

The preparation of TEM samples was performed using a dual-beam FEI Helios NanoLab G3 focused ion beam (FIB) HR-SEM.

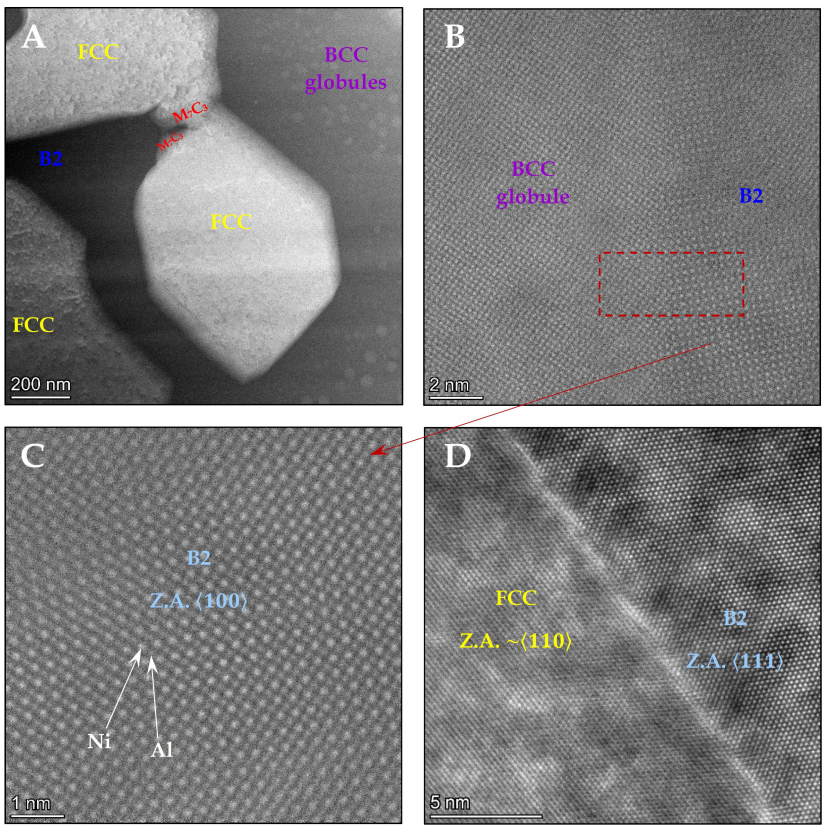

FIGURE 3 | (A) STEM image taken from the dashed square region in **Figure 1B** showing the brighter globules compared with the darker B2 background; **(B)** HAADF showing a lattice image in the <100> zone axis of the BCC and B2 domain, and the characteristic order-disorder transition through the interface between the B2 phase and the BCC globules; **(C)** HAADF of the B2 parent phase in the <001> zone axis showing the ordering of Ni and Al atoms in the lattice; **(D)** HAADF image showing the interface between an FCC particle and the B2 phase – demonstrating the near perfect Kurdjumov-Sachs orientation relationship.

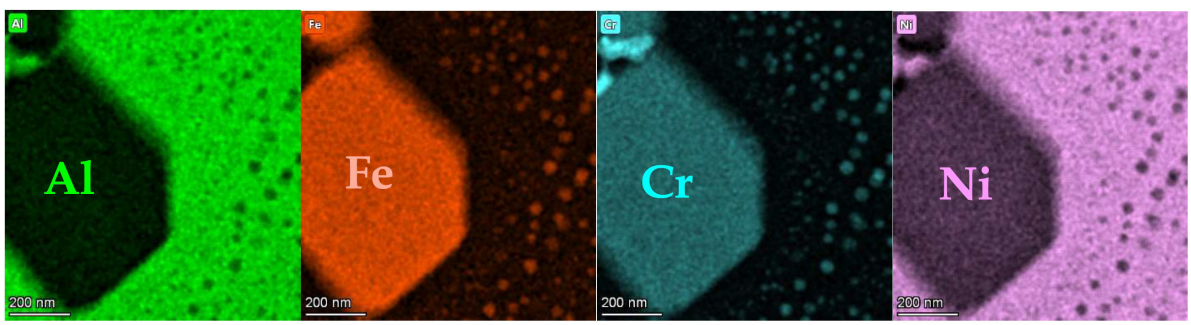

FIGURE 4 | High Resolution S/TEM EDS map (STEM mode) of the area captured in **Figure 3A** in the as-cast $AlCrFe_2Ni_2$ alloy.

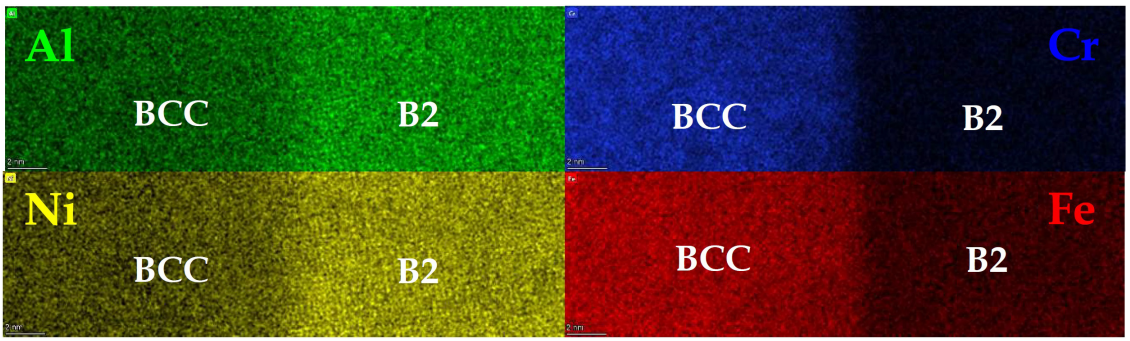

FIGURE 5 | High Resolution S/TEM EDS map (STEM mode) of the B2-BCC interface in as-cast $AlCrFe_2Ni_2$ alloy.

TABLE 1 | Characteristic EDS measurements of phases in as-cast $AlCrFe_2Ni_2$ in atomic fractions.

Phase	C (at%)	Al (at%)	Cr (at%)	Fe (at%)	Ni (at%)
FCC	–	7.74	18.71	44.06	29.49
B2	–	32.47	–	16.70	50.83
BCC	–	1.81	38.72	53.42	6.05
M_7C_3	28.55	–	63.08	8.37	–

Electron diffractions and TEM images were obtained using an FEI Tecnai G2 T20 200 KeV TEM with a LaB_6 electron source and an FEI Supertwin objective lens. This microscope is also equipped with a plate camera and a 1K × 1K Gatan 694 retractable slow scan CCD.

High Resolution TEM Imaging and EDS maps were obtained via an FEI Titan Themis 60–300 kV S/TEM equipped with HAADF and an EDS system for local chemical analysis.

RESULTS AND DISCUSSION

As-Cast $AlCrFe_2Ni_2$

The as-cast alloy was first investigated using TEM. Four main phases were identified: FCC, ordered BCC (B2), disordered BCC and a hexagonal carbide of the M_7C_3 type. The carbide is most likely a result of a carbon containing substance found within the furnace, however, the exact source of contamination could not be pinpointed. Overall the alloy contains 0.18 wt% carbon.

Figures 1, **2** provide bright field (BF) micrographs and selected area electron diffraction (SAED) patterns obtained from each phase, respectively. A low magnification HRSEM micrograph is also added in **Figure 1C** to give an overview of the distribution of phases comprising the microstructure.

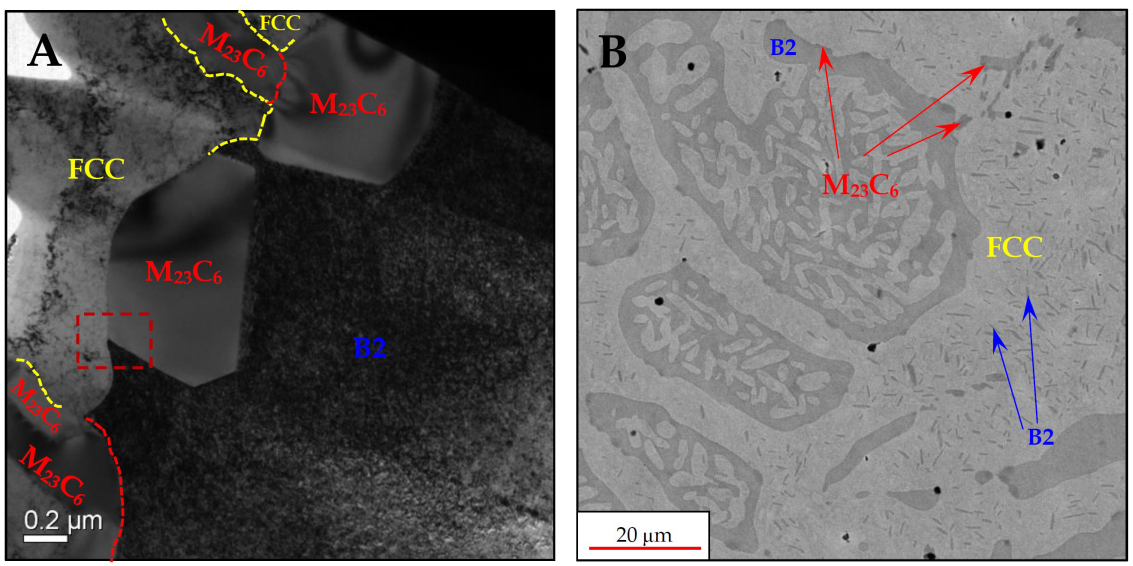

FIGURE 6 | (A) BF-TEM micrographs showing the general morphology of the phases comprising the microstructure in homogenized $AlCrFe_2Ni_2$ alloy; **(B)** An HRSEM micrograph showing the general microstructure in homogenized $AlCrFe_2Ni_2$ alloy.

The ranges of the different phases lattice parameters of, as calculated from the SAED are:

$$FCC\ -\ 3.5Å < a < 3.6Å$$

$$B2 + BCC\ -\ 2.85Å < a < 2.9Å$$

$$M7C3\ -\ 14.00 < a < 14.25Å;\ 4.52 < c < 4.6Å$$

It should be noted that since the BCC globules were extremely small, it was impossible to obtain a separate diffraction pattern from this phase.

Since the B2 and BCC phases shared the same orientation, and their diffraction patterns were indistinguishable from each other due to the very small size of the BCC phase, a high-resolution STEM analysis was performed. **Figure 3** shows the BCC particles in the B2 phase in increasing magnifications. Additionally, the FCC-B2 interface was also investigated revealing a dominant Kurdjumov-Sachs orientation relationship.

A high-resolution EDS map was obtained from the area captured in **Figure 3A**, in order to better understand the elemental distribution in each of the participating phases in the microstructure.

The HR-EDS analysis presented in **Figure 4** suggests that there is a ∼50 nm long precipitate-free zone in the B2 parent phase bordering the FCC particle. Outside of the precipitate-free zone, BCC globules form, ranging in size from a few nanometers to 20–30 nm. Additionally, the M_7C_3 phase is almost devoid of Ni, and its metallic component is primarily Cr, with some Fe.

As evident from **Figure 3B**, even though both the BCC and B2 phases share the same orientation, there is a clear

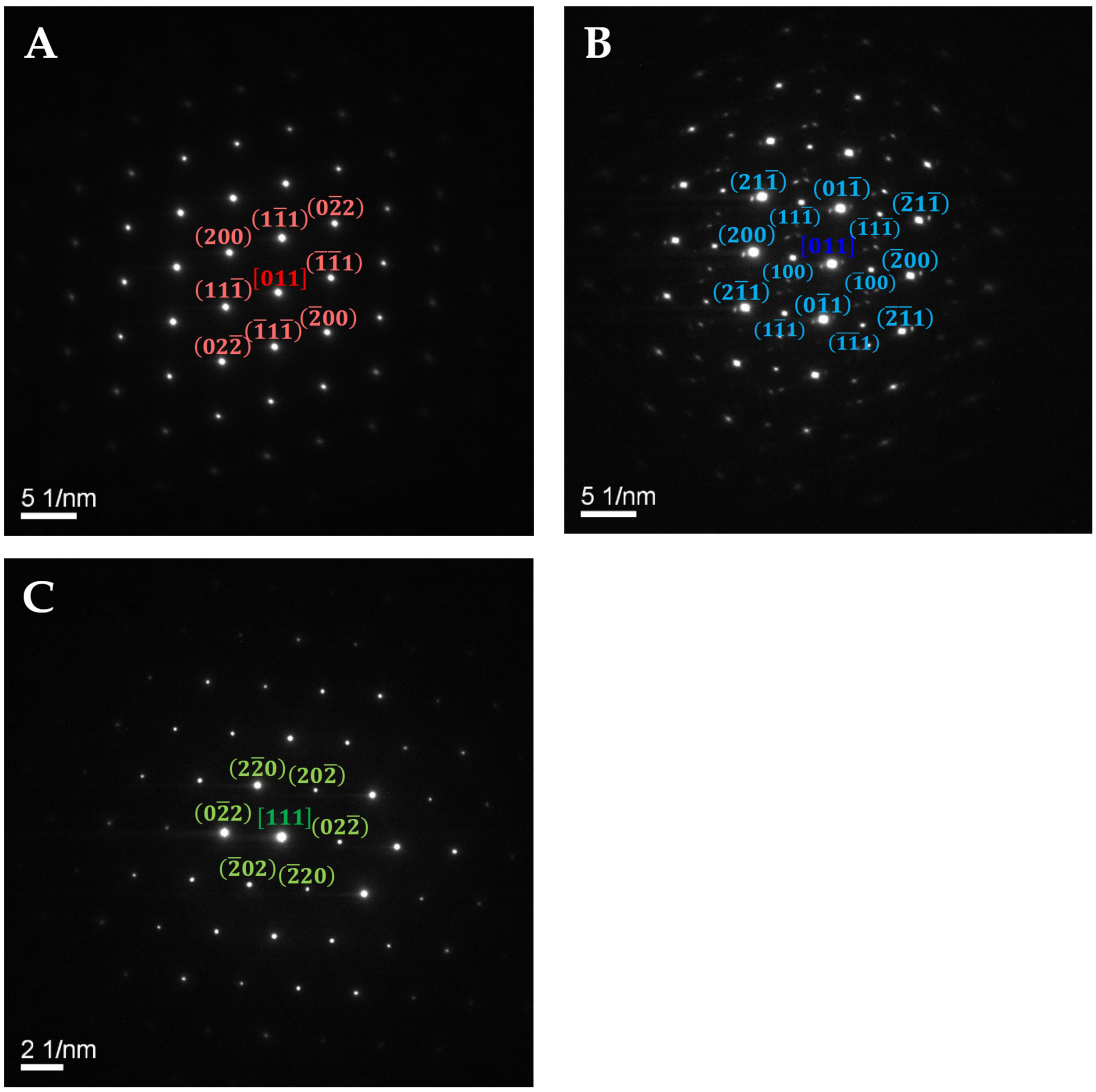

FIGURE 7 | SAED patterns in the homogenized $AlCrFe_2Ni_2$ alloy – obtained from **(A)** the FCC phase in Z.A. <011> **(B)** the B2 phase in Z.A. <011>; **(C)** the FCC $M_{23}C_6$ phase in Z.A. <111>.

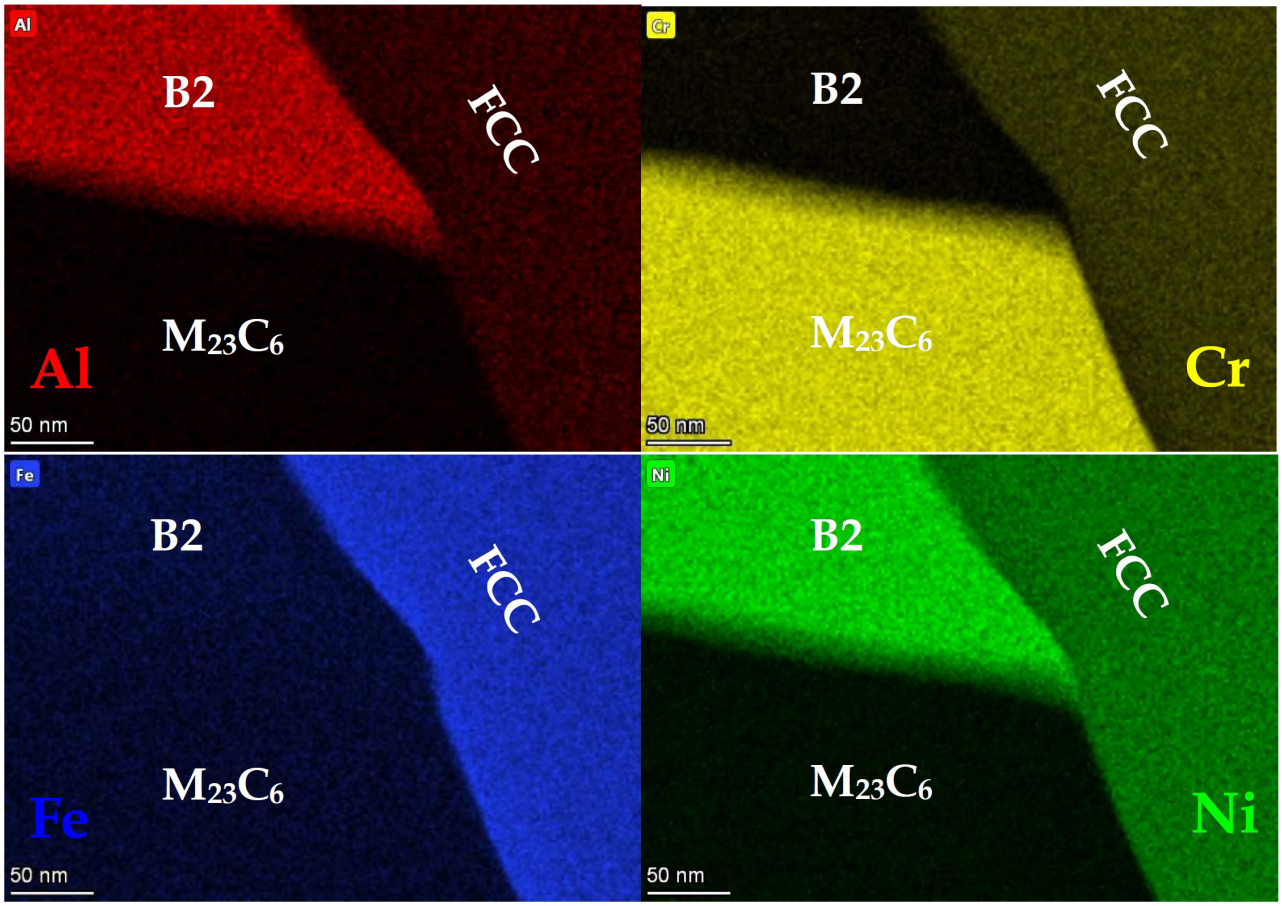

FIGURE 8 | High Resolution S/TEM EDS map (STEM mode) of the area marked in **Figure 6** in the homogenized $AlCrFe_2Ni_2$ alloy.

order-to-disorder transition going from the B2 parent phase to the BCC particles.

The morphology of the globules, and the fact that both the B2 parent phase and the BCC globules embedded in it share the same orientation, suggests that a spinodal decomposition took place. In order to establish the nature of the elemental separation taking place here, a high resolution EDS map of the interface between a BCC globule and the B2 parent phase (taken from the dashed square in **Figure 3B**) was performed (**Figure 5**):

The maps clearly show that during the spinodal decomposition process Cr and Fe concentrate in the disordered BCC globules, while Ni and Al concentrate more in the ordered B2 phase. The fact that elemental Cr and Fe, and $AlNi_{0.5}Fe_{0.5}$ all have a BCC crystal structure with the same lattice parameter of 2.87–2.89 Å enables this separation to take place coherently, while preserving the shared orientation of both phases (Kotov et al., 1972; Hermann, 2011).

The globular morphology and increased Cr-Fe content of the BCC globules, together with their shared orientation with the B2 matrix they are embedded in, was also found in publications dealing with similar Co-containing HEAs such as $AlCo_{0.5}Cr_{0.5}FeNi$ (Chaudhary et al., 2018) and $Al_{0.7}CoCrFeNi$ (Gwalani et al., 2019), especially after aging at relatively low temperatures (~600°C).

Finally, in order to complete the analysis of the as-cast product, a high-resolution EDS point analysis was performed. The results are presented in **Table 1**.

Homogenized $AlCrFe_2Ni_2$

The microstructural investigation of the homogenized $AlCrFe_2Ni_2$ revealed the following phases: FCC, ordered BCC (B2), and a cubic carbide phase of the $M_{23}C_6$ type (FCC). Therefore, the two main microstructural changes that occurred due to the homogenization treatment were the dissolution of the Cr-Fe- rich disordered BCC globules

TABLE 2 | Characteristic EDS measurements of phases in homogenized $AlCrFe_2Ni_2$ in atomic fractions.

Phase	C (at%)	Al (at%)	Cr (at%)	Fe (at%)	Ni (at%)
FCC	–	8.22	17.66	45.47	28.65
B2	–	29.33	3.23	18.93	48.51
$M_{23}C_6$	21.87	–	63.23	14.90	–

and the transformation of the hexagonal M_7C_3 carbide into the cubic $Cr_{23}C_6$ carbide. Additional precipitation of B2 platelets/whiskers inside the FCC phase was observed in SEM images, perhaps indicating that for this alloy this treatment is more of an extreme form of aging rather than pure homogenization.

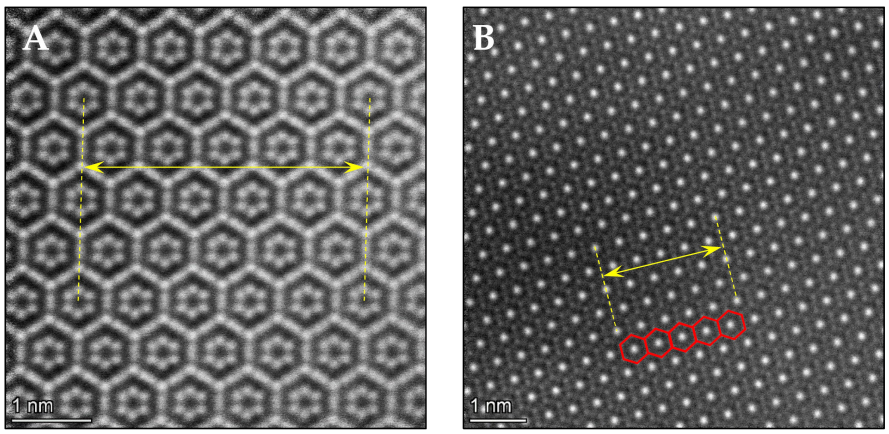

FIGURE 9 | (A) HAADF showing a lattice image in Z.A. <001> of the hexagonal M_7C_3; **(B)** HAADF showing a lattice image in Z.A. <111> of the cubic $M_{23}C_6$.

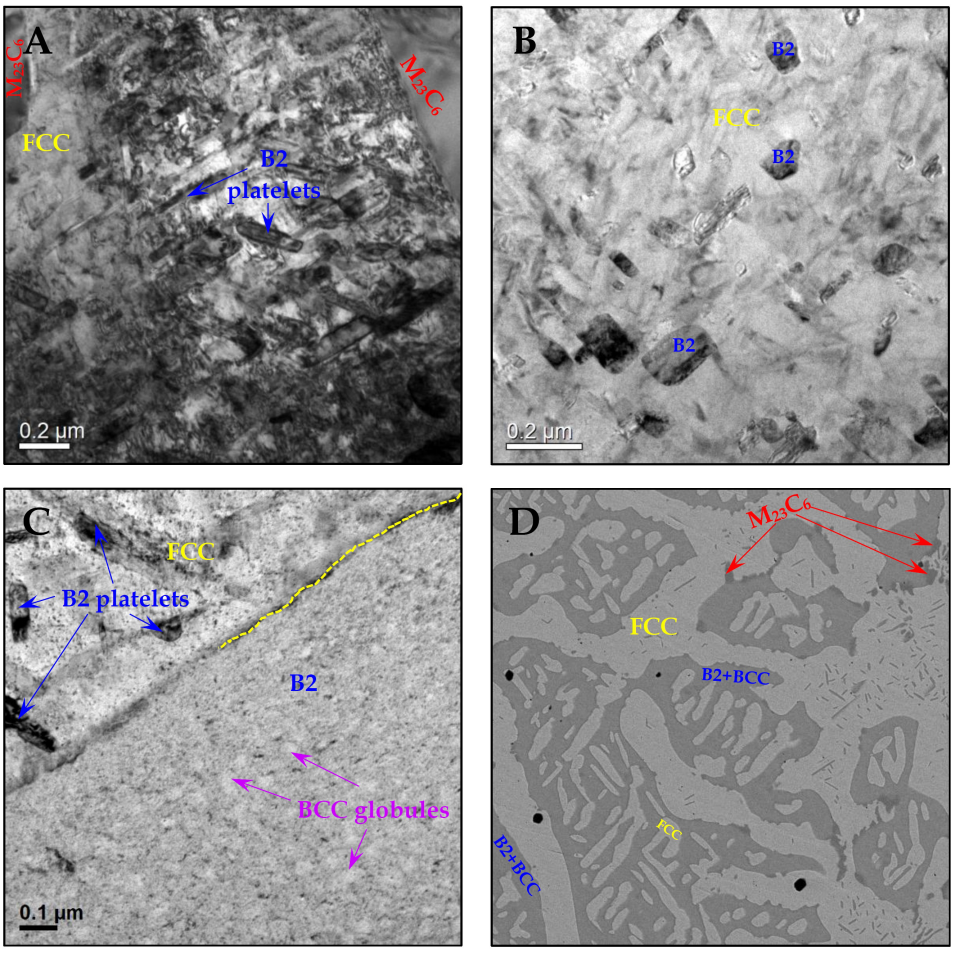

FIGURE 10 | (A–C) BF-TEM micrographs showing the general morphology of the phases and precipitates comprising the microstructure in homogenized and aged (750°C) $AlCrFe_2Ni_2$ alloy; **(D)** HRSEM micrograph showing the general microstructure in aged (750°C) $AlCrFe_2Ni_2$ alloy.

Figures 6, **7** provide BF-TEM micrographs and SAED patterns obtained from each phase in the homogenized alloy, respectively. **Figure 6B** shows an HRSEM image of the general microstructure:

The lattice parameter of the $M_{23}C_6$ phase was calculated from the SAED to be: a= 10.8 Å, which is slightly higher than the theoretical value for $Cr_{23}C_6$ of a = 10.66 Å (Powder Diffraction, 1985). The difference in lattice parameter could be due to measurement errors associated with the TEM, or the deviation from the perfect stoichiometry due to incorporation of Fe atoms or increased C content.

High resolution EDS mapping of the tri-phase junction shown in the dashed square in **Figure 6** is presented in **Figure 8**:

The elemental separation among the three phases, is very similar to the as-cast alloy, including the carbide phase.

A high-resolution EDS point analysis was performed in the homogenized alloy as well. The results are presented in **Table 2**.

The transformation of the carbide may seem surprising, since the M_7C_3 carbide is more stable than the $M_{23}C_6$, and in a binary Cr-C system, heating $Cr_{23}C_6$ carbide will result in the formation of Cr_7C_3, and not the other way around. The reverse trend we observed is rationalized for the $AlCrFe_2Ni_2$ alloy using the fact that as the temperature rises, more carbon can be dissolved in the surrounding B2 and FCC phases, which leaves the carbide phase with a lower carbon-to-metal ratio, resulting in the M_7C_3-to-$M_{23}C_6$ transformation.

A look at the lattice images of both carbides, viewed from their threefold symmetry zone axes, shows their similarity (**Figure 9**).

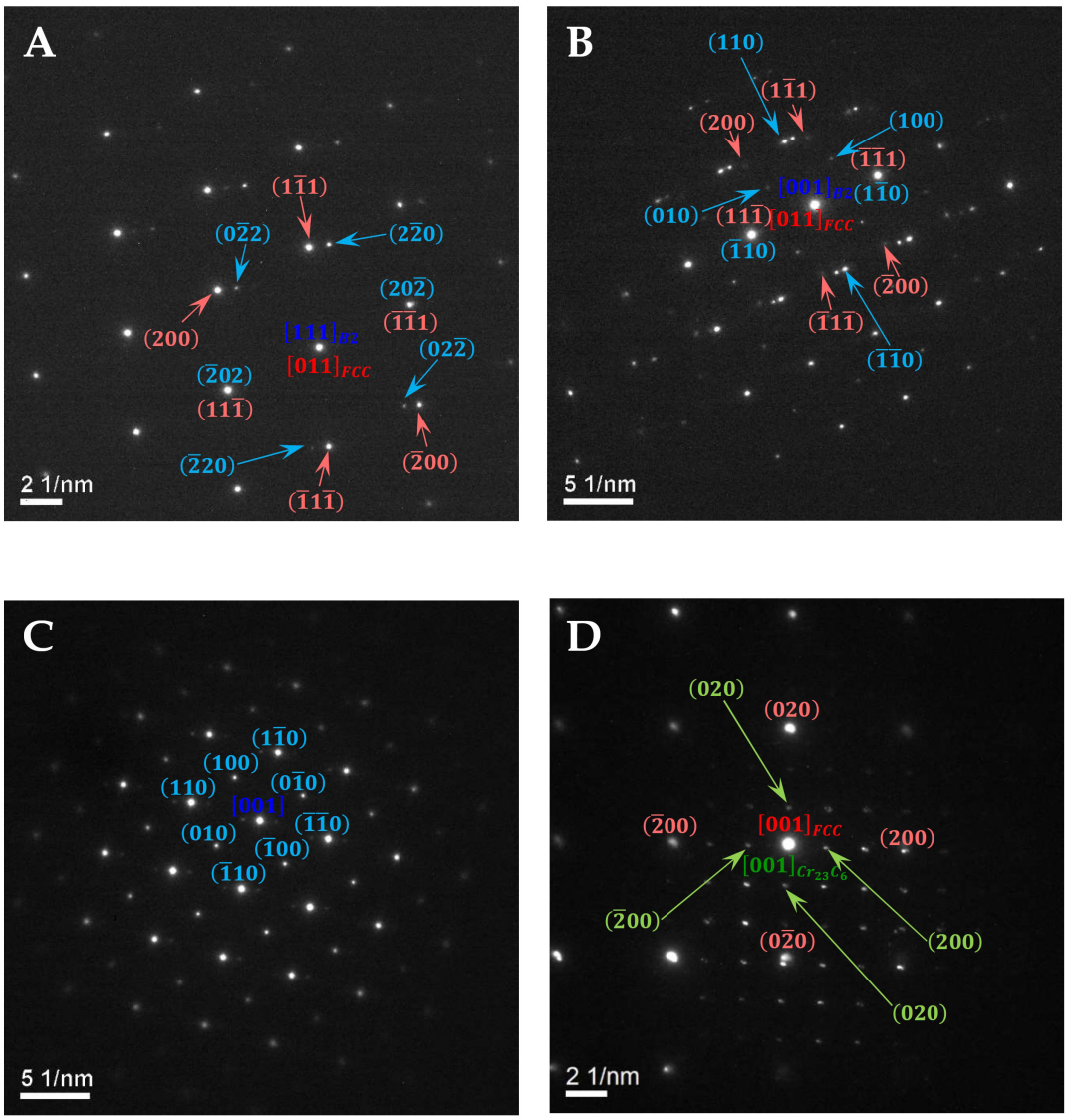

FIGURE 11 | SAED diffraction patterns in the homogenized and aged (750°C) $AlCrFe_2Ni_2$ alloy – obtained from **(A)** a B2 platelet in Z.A. <111> inside the FCC phase in Z.A. <110>; **(B)** a B2 platelet in Z.A. <100> inside the FCC phase in Z.A. <110>; **(C)** the B2+BCC phase domain in Z.A. <100>; **(D)** a $M_{23}C_6$ particle bordering the FCC phase.

Noteworthy is that the loss of carbon is also accompanied by a reduction in the corresponding d-space defined by the periodic hexagonal structure.

Homogenized and Aged (750°C) $AlCrFe_2Ni_2$

Post-homogenization aging treatment at 750°C for 4 h resulted in the re-precipitation of nano-globular BCC particles within the B2 phase domain. Additional precipitation occurred inside the FCC phase, in the form of nano sized B2 platelets. The $M_{23}C_6$ carbide remained unchanged.

Figure 10 presents BF-TEM micrographs and an HRSEM micrograph, depicting the general microstructure obtained following homogenization at 1185°C for 75 min and subsequent aging at 750°C for 4 h.

As shown in **Figure 10**, the characteristic thickness of the platelets is 20–50 nm, while their length ranges from 100 to 300 nm. The BCC globules inside the B2 phase were observed to be quite uniform in size – approximately 30–50 nm.

The SAED pattern obtained from each phase are given in **Figure 11**. A clear SAED of the BCC globules could not be obtained due to their small dimensions.

Figure 11 clearly shows that each B2 precipitate can possess a different orientation relative to that of the FCC parent phase such as the Kurdjumov-Sachs relationship in **Figure 11A** or the Nishiyama–Wasserman relationship in **Figure 11B**. Since the $M_{23}C_6$ carbide also possesses an FCC structure, it was no surprise that some crystals showed almost identical orientation to that of the neighboring FCC parent phase (**Figure 11D**). The diffraction pattern in **Figure 11D** also exhibits the 1:3 ratio of the lattice parameters of both phases.

HR-TEM images and lattice images were also obtained in order to further investigate the BCC nano-globules and the B2 nano-precipitates in the FCC phase.

The nature of the ordered B2 platelets and the order-to-disorder transition in the B2-BCC globules' interface are only evident in HRTEM analyses as shown in **Figure 12**.

Comparing the obtained microstructure in this research, with similar alloys having undergone aging treatment (Chaudhary et al., 2018; Gwalani et al., 2019), It appears that the slightly higher aging temperature here resulted in the

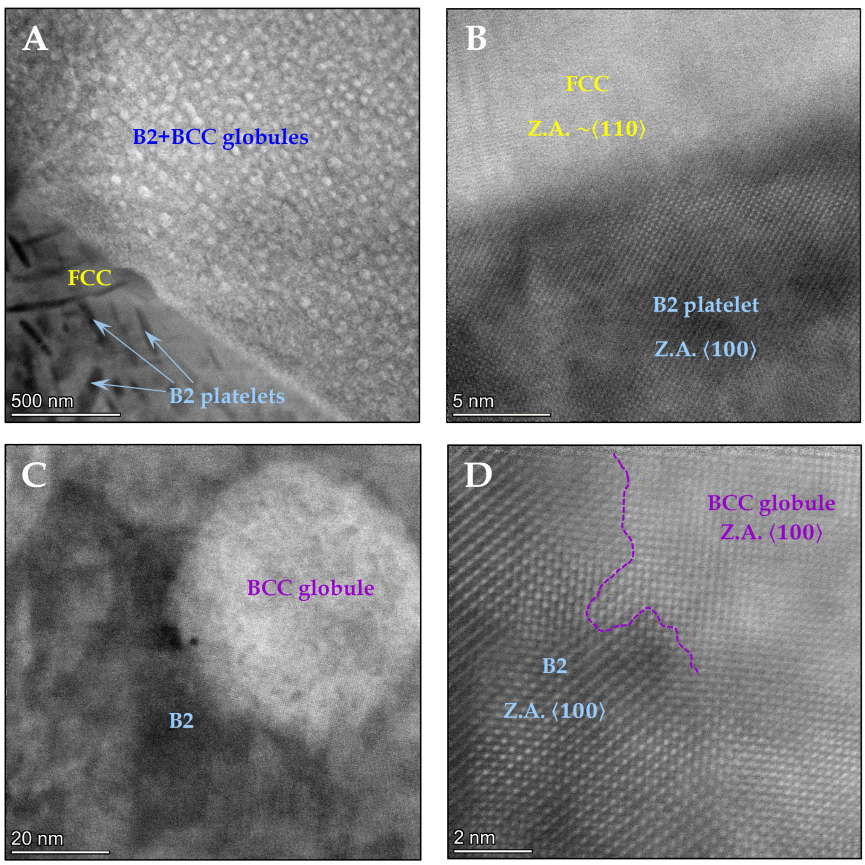

FIGURE 12 | (A) STEM image showing the extremely fine precipitates in the B2 and FCC phases characteristic of the microstructure of the homogenized and aged (750°C) $AlCrFe_2Ni_2$ alloy. **(B)** HAADF of a B2 platelet showing a lattice image in the <100> zone axis, relative to the FCC parent phase whose zone axis is close to <110>; **(C)** Low magnification HAADF of the B2+BCC domain in the <100> zone axis, showing the outlines of a globule; **(D)** HAADF image showing the interface between the ordered B2 parent phase and the BCC globule.

precipitation of B2 precipitates inside the FCC parent phase instead of $L1_2$.

Homogenized and Aged (930°C) $AlCrFe_2Ni_2$

Post-homogenization aging at 930°C for 3 h resulted in the dissolution of the majority of the BCC nano-globules in the B2 parent phase. Few globules were able to grow large enough (around 100 nm) without dissolving. The B2 nano-platelets have also grown considerably due to aging at a higher temperature (200–500 μm in length and width; less than 100 μm in thickness), but were much more ubiquitous than the BCC globules. Most likely, the interfacial incoherence and crystallographic mismatch between the platelets and the FCC parent phase, require higher temperatures to initiate dissolution than in the case of the coherent BCC globules. The $M_{23}C_6$ carbide remained unchanged.

Figure 13 presents bright field TEM micrographs and an HRSEM image, depicting the general microstructure obtained following homogenization at 1185°C for 75 min and aging at 930°C for 3 h. The corresponding SAED pa[3-8]tterns are shown in **Figure 14**.

Since many of the platelets and BCC globules are still very thin, the background of their respective parent phases is still visible in the diffraction patterns.

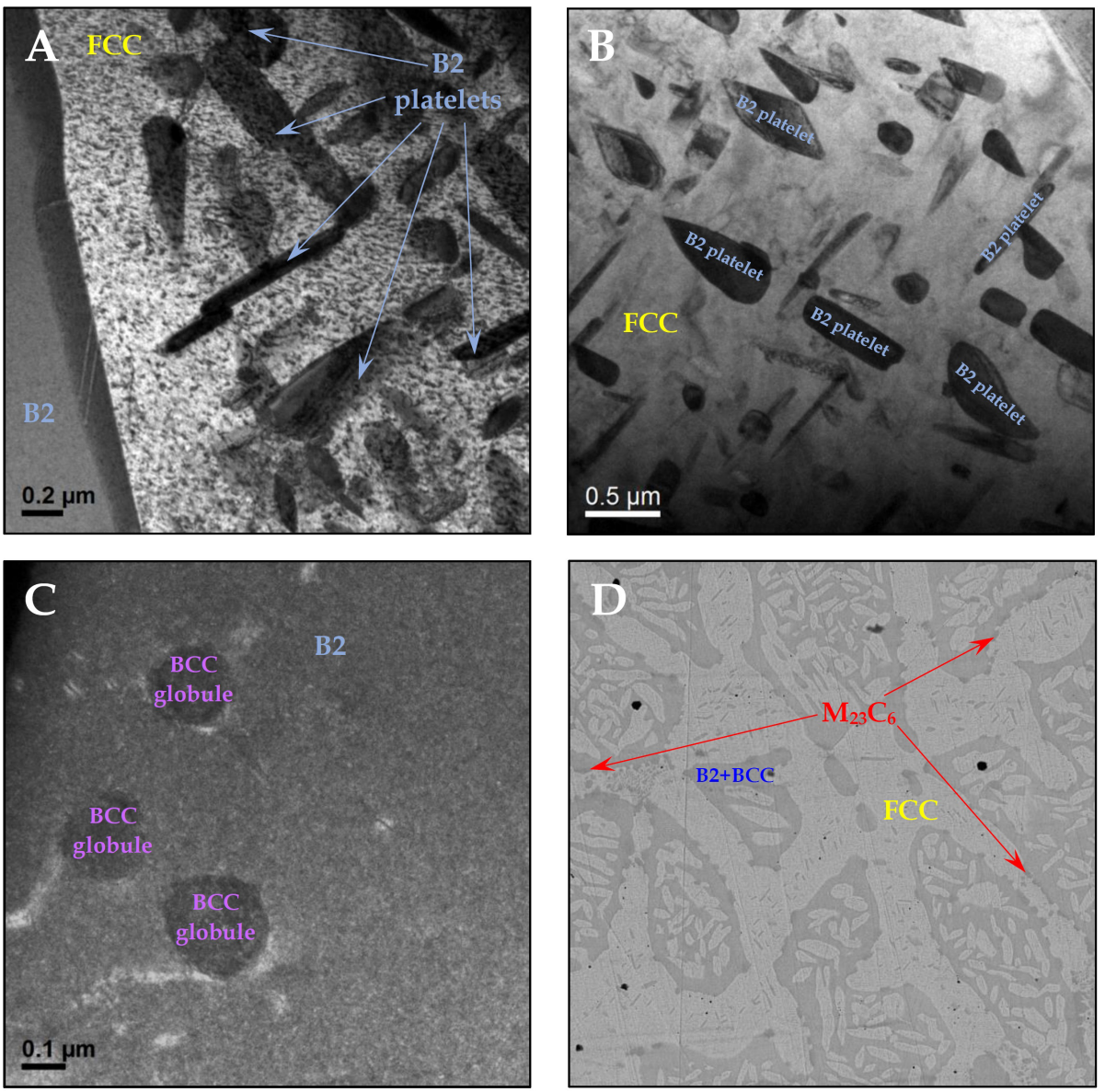

FIGURE 13 | (A–C) BF-TEM micrographs showing the general morphology of the phases and precipitates comprising the microstructure of the homogenized and aged (930°C) $AlCrFe_2Ni_2$ alloy; **(D)** HRSEM micrograph showing the general microstructure in aged (930°C) $AlCrFe_2Ni_2$ alloy.

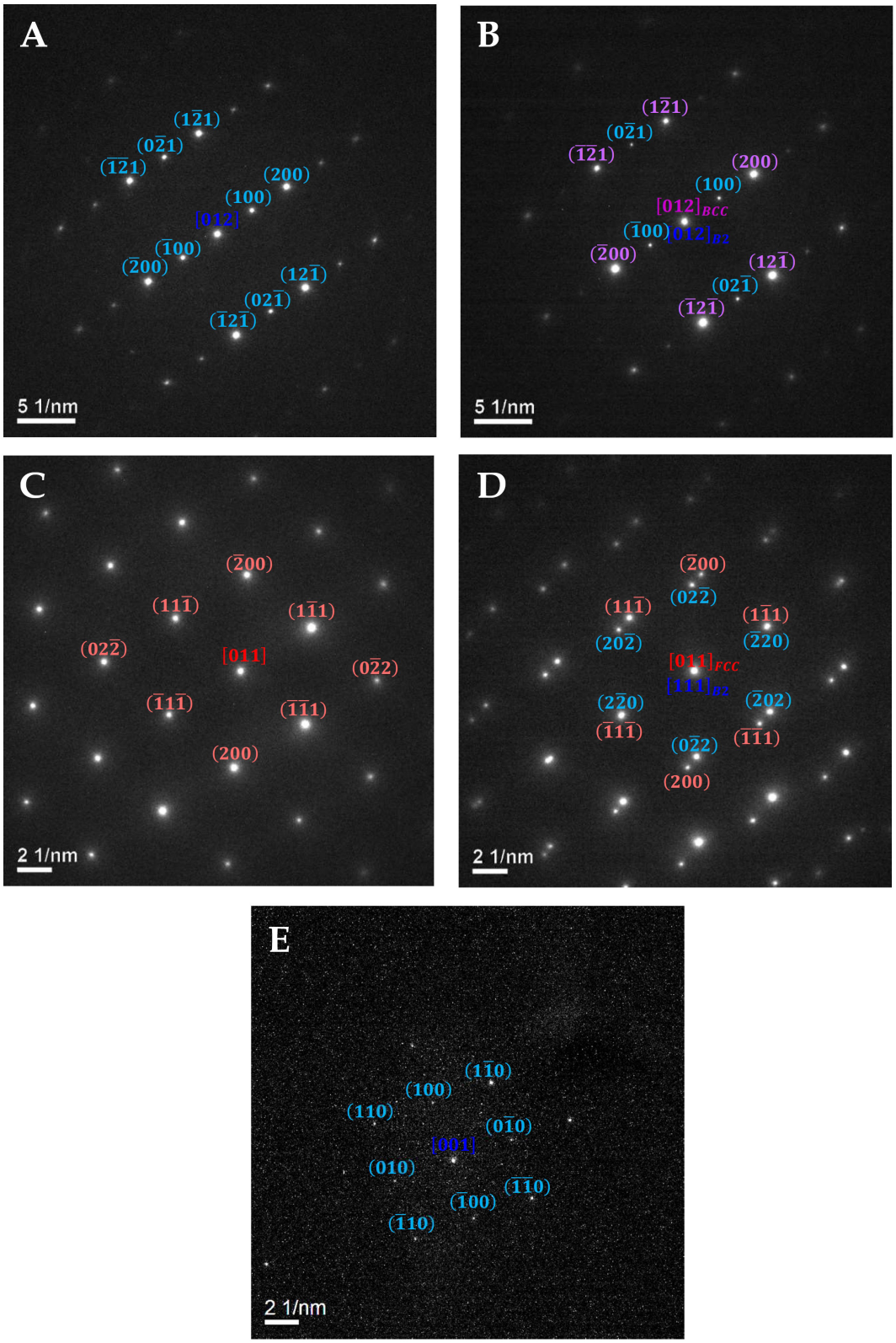

FIGURE 14 | SAED patterns in the homogenized and aged (930°C) $AlCrFe_2Ni_2$ alloy – obtained from **(A)** the B2 parent phase in Z.A. <210>; **(B)** a BCC globule in Z.A. <210> inside the B2 phase; **(C)** the FCC parent phase in Z.A. <110>; **(D)** a B2 platelet in Z.A. <111> inside the FCC parent phase in Z.A. <110> exemplifying the Kurdjumov-Sachs orientation relationship; **(E)** a B2 platelet in Z.A. <001> inside the FCC parent phase.

TABLE 3 | Phase identity and morphology as function of the thermal state of $AlCrFe_2Ni_2$ alloy.

Thermal state	FCC	B2 (Al-Ni rich)	BCC (Cr-Fe rich)	M_7C_3	$M_{23}C_6$
As-cast	✓ (parent phase)	✓ (parent phase)	✓ (globular precipitates inside B2)	✓	x
Homogenized	✓ (parent phase)	✓ (parent phase, whiskers inside FCC phase)	x	x	✓
Homogenized and aged at 750°C	✓ (parent phase)	✓ (parent phase, nano-platelets inside FCC)	✓ (globular nano-precipitates inside B2)	x	✓
Homogenized and aged at 930°C	✓ (parent phase)	✓ (parent phase, micro-platelets inside FCC)	✓ (few globular micro-precipitates inside B2)	x	✓

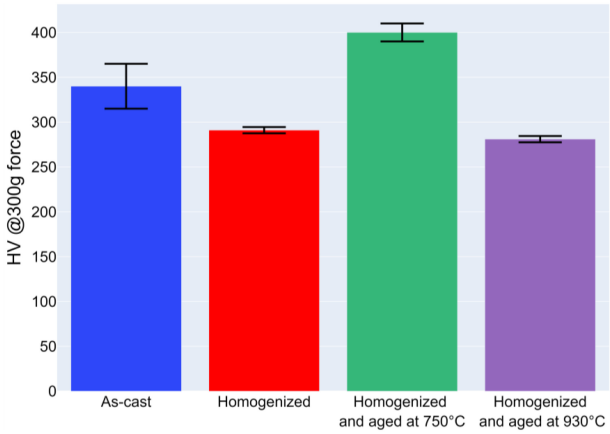

FIGURE 15 | Vickers microhardness test results of $AlCrFe_2Ni_2$ alloy in various thermal states.

Summary of Microstructural Changes

The following table summarizes the main microstructural features present in each thermal state of the $AlCrFe_2Ni_2$ alloy:

Microhardness Tests

To get a preliminary indication of the expected effect of the investigated four thermal states on the mechanical properties, Vickers microhardness tests were conducted (**Figure 15**). For the as-cast state, the Vickers hardness was measured to be 340 ± 25, which is roughly 10% higher than the value reported in Li C. et al. (2020), for a similar alloy (albeit without the 1%a carbon presence). Upon homogenization, which resulted in some grain growth and carbide transformation, the hardness decreased to 291 ± 3.5. For the two aging treatments considered in this work, considerable hardening (with respect to the homogenized state) was observed for the 750°C aged state (400 ± 10), while aging at 930°C led to a slight decrease in hardness (281 ± 3.5). The difference in measured hardness between the two aged state agrees with the observed microstructures summarized in **Table 3**. Under the 930°C aging treatments, both the B2 platelets (inside FCC) and BCC precipitates (inside B2) were observed to be larger in size, while the BCC precipitates appeared to be rather sparse, suggesting that 3 h at 930°C lead to over-aging.

SUMMARY

The microstructure of the $AlCrFe_2Ni_2$ high entropy alloy was studied under four thermal conditions, namely: As-cast; Homogenized (75 min at 1185°C); Homogenized and aged (240 min at 750°C) and homogenized and aged (180 min at 930°C). The as cast alloy was found to comprise three metallic phases and a carbide phase: FCC; B2; BCC globules embedded in the B2 matrix and a hexagonal M_7C_3 carbide, where Cr is the dominant metal. Upon being subjected to the homogenization treatment, the Cr-Fe-rich BCC globules were observed to dissolve, while the M_7C_3 phase has transformed into a cubic $Cr_{23}C_6$ phase. The carbide transformation was accompanied by an increase in the Fe-to-Cr atomic ratio in the carbide and a lower carbon-to-metal ratio, the latter, most likely, resulting from the increased dissolution of C in the neighboring FCC and B2 parent phases, due to the higher temperature. Subsequent Aging treatments resulted in re-precipitation of the BCC particles within the parent B2 phase, accompanied by the precipitation of nano sized B2 platelets in the parent FCC phase. With increasing aging temperature, the size of both BCC and B2 precipitates was found to increase. A striking difference between the two aging treatments was found in the distribution and size of the two precipitating phases. Aging at 750°C, resulted in smaller, more ubiquitous BCC globules, when compared with the larger, less frequent BCC particles observed in the alloy aged at 930°C. The B2 nano-platelets, embedded in the FCC phase, were observed to grow larger with increasing aging temperature, however their distribution in the parent phase was not observed to vary much between the two studied aging treatments.

DATA AVAILABILITY STATEMENT

All datasets presented in this study are included in the article/supplementary material.

AUTHOR CONTRIBUTIONS

SA and EE: TEM work. EE: TEM diffractions analysis. EE, SO, and MB: writing the revised manuscript. All authors contributed to the article and approved the submitted version.

FUNDING

This research was supported by the Ministry of Science, Technology and Space, the State of Israel in the frame of the M-era.Net Joint Call 2017, Project NADEA (No. 5129).

REFERENCES

Chaudhary, V., Gwalani, B., Soni, V., Ramanujan, R. V., and Banerjee, R. (2018). Infuence of Cr substitution and temperature on hierarchical phase decomposition in the AlCoFeNi high entropy alloy. *Sci. Rep.* 8:15578.

Dong, Y., Gao, X., Lu, Y., Wang, T., and Lu, Y. (2016). A multi-component $AlCrFe_2Ni_2$ alloy with excellent mechanical properties. *Mater. Lett.* 169, 62–64. doi: 10.1016/j.matlet.2016.01.096

Dong, Y., Zhou, K., Lu, Y., Gao, X., Wang, T., and Lu, Y. (2014). Effect of vanadium addition on the microstructure and properties of AlCoCrFeNi high entropy alloy. *Mater. Design* 57, 67–72. doi: 10.1016/j.matdes.2013.12.048

Gwalani, B., Gangireddy, S., Zheng, Y., Soni, V., Mishra, R. S., and Banerjee, R. (2019). Infuence of Ordered $L1_2$ precipitation on strain-rate dependent mechanical behavior in a eutectic high entropy alloy. *Sci. Rep.* 9, 1–13.

Hermann, K. (2011). *Crystallography and Surface Structure: An Introduction for Surface Scientists and Nanoscientists*. Weinheim: Wiley-VCH Verlag GmbH & Co, 265–266.

Kao, Y.-F., Chen, S.-K., Chen, T.-S., Chu, P.-C., Yeh, J.-W., and Lin, S.-W. (2011). Electrical, magnetic, and Hall properties of $Al_xCoCrFeNi$ high-entropy alloys. *J. Alloys Compounds* 509, 1607–1614.

Kao, Y.-F., Chen, T.-S., Chen, S.-K., and Yeh, J.-W. (2009). Microstructure and mechanical property of as-cast, -homogenized, and -deformed $Al_xCoCrFeNi$ ($0 \leq x \leq 2$) high-entropy alloys. *J. Alloys Compounds* 488, 57–64. doi: 10.1016/j.jallcom.2009.08.090

Kotov, A. P., Zelenin, L. P., Bronfin, M. B., Sidorenko, F. A., and Gel'd, P.V (1972). Structure and magnetic properties of solid solutions of iron and nickel monoaluminides in each other. *Phys. Met. Metall.* 33, 142–146.

Li, C., Qu, Y., Zhang, Y., Lv, Q., and Qi, H. (2020). Effect of deep cryogenic treatment on the microstructure and mechanical properties of $AlCrFe_2Ni_2$ High-entropy alloy. *Mater. Res. Express* 7:036504.

Li, Z., You, J. H., Guo, Y., Li, C., Zhang, Y., and Liu, Z. (2020). Phase transition mechanism and mechanical properties of $AlCrFe_2Ni_2$ high-entropy alloys with changes in the applied carbon content. *Adv. Eng. Mater.* 22, 1–7.

Manzoni, A., Daoud, H., Völkl, R., Glatzel, U., and Wanderka, N. (2013). Phase separation in equiatomic AlCoCrFeNi high-entropy alloy. *Ultramicroscopy* 132, 212–215. doi: 10.1016/j.ultramic.2012.12.015

Miracle, D. B., and Senkov, O. N. (2017). A critical review of high entropy alloys and related concepts. *Acta Materialia* 122, 448–511. doi: 10.1016/j.actamat.2016.08.081

Munitz, A., Salhov, S., and Frage, S. H. N. (2016). Heat treatment impacts the micro-structure and mechanical properties of AlCoCrFeNi high entropy alloy. *J. Alloys Compounds* 683, 221–230. doi: 10.1016/j.jallcom.2016.05.034

Niu, P. D., Li, R., Yuan, T. C., Zhu, S. Y., Chen, C., Wang, M. B., et al. (2019). Microstructures and properties of an equimolar AlCoCrFeNi high entropy alloy printed by selective laser melting. *Intermetallics* 104, 24–32. doi: 10.1016/j.intermet.2018.10.018

Powder Diffraction (1985). *00-035-0783, in Powder Diffraction 1985*. Newtown Square, PA: International Centre for Diffraction Data.

Qiao, J. W., Ma, S. G., Huang, E. W., Chuang, C. P., Liaw, P., and Zhang, Y. (2011). Microstructural characteristics and mechanical behaviors of AlCoCrFeNi high-entropy alloys at ambient and cryogenic temperatures. *Mater. Sci. Forum* 688, 419–425. doi: 10.4028/www.scientific.net/msf.688.41

Reddy, S. R., Yoshida, S., Bhattacharjee, P. P., Sake, N., Lozinko, A., Guo, S., et al. (2019). Nanostructuring with structural-compositional dual heterogeneities enhances strength-ductility synergy in eutectic high entropy alloy. *Sci. Rep.* 9, 1–9.

Rogal, L., Szklarz, Z., Bobrowski, P., Kalita, D., Garzeł, G., Tarasek, A., et al. (2019). Microstructure and mechanical properties of Al-Co-Cr-Fe-Ni base high entropy alloys obtained using powder metallurgy. *Metals Mater. Int.* 25, 930–945. doi: 10.1007/s12540-018-00236-5

Wang, Y. P., Li, B. S., Ren, M. X., Yang, C., and Fu, H. Z. (2008). Microstructure and compressive properties of AlCrFeCoNi high entropy alloy. *Mater. Sci. Eng. A* 491, 154–158.

Zhang, Y., Zuo, T. T., Tang, Z., Gao, M. C., Dahmen, K. A., Liaw, P. K., et al. (2014). Microstructures and properties of high-entropy alloys. *Prog. Mater. Sci.* 61, 1–93.

Conflict of Interest: EE was employed by the company Technion Research and Development Foundation Ltd.

The remaining authors declare that the research was conducted in the absence of any commercial or financial relationships that could be construed as a potential conflict of interest.

frontiers in Materials

ORIGINAL RESEARCH
published: 23 September 2020
doi: 10.3389/fmats.2020.00296

The Influence of Mo Additions on the Microstructure and Mechanical Properties of $AlCrFe_2Ni_2$ Medium Entropy Alloys

Sergej Gein, Victor T. Witusiewicz and Ulrike Hecht*

Access e.V., Aachen, Germany

The alloy system Al-Cr-Fe-Ni provides means for developing novel duplex materials composed of face-centered cubic (FCC) and body-centered cubic (BCC) phases with nearly equal volume fraction. We performed an alloy development study starting from the medium entropy alloy $AlCrFe_2Ni_2$ and adding small amounts of molybdenum in the following series (at.%): $Al_{17}Cr_{17}Fe_{33}Ni_{33}$, $Al_{17}Cr_{17}Fe_{33}Ni_{33}Mo_1$, $Al_{16}Cr_{16}Fe_{33}Ni_{33}Mo_2$, and $Al_{16}Cr_{16}Fe_{33}Ni_{33}Mo_3$. We focused the research on samples with an ultrafine vermicular duplex microstructure, a unique structure requiring sufficiently high cooling rates to suppress the conventional Widmanstätten colony formation. The samples were produced by arc melting in buttons of 300 g each. We characterized the microstructure of the samples using scanning electron microscopy (SEM), energy-dispersive X-ray spectroscopy (EDS), and electron backscatter diffraction (EBSD). The EBSD data revealed significant strain in the FCC phase resulting from the BCC→FCC phase transformation. We investigated mechanical properties of the samples by micro-indentation and 3-point bending in a miniature testing device. The test specimens were in the as-cast condition, as well as in distinct annealed conditions. Annealing treatments were carried out at 950 and 1100°C under argon. The annealing lasted from 10 min to 6 h, followed by water quenching. Prolonged annealing at 950°C of Mo-containing samples resulted in the formation of sigma-phase. Annealing at 1100°C safely avoided sigma-phase formation, while leading to a good balance between the flexural strength and ductility of these samples. Mechanical testing also included the well-established superduplex steel 1.4517 (DIN EN 10283/ASTM A890) as reference material.

Keywords: duplex microstructure, medium entropy alloys, mechanical properties, spinodal decomposition, sigma-phase, alloy development

OPEN ACCESS

Edited by:
Liqiang Wang,
Shanghai Jiao Tong University, China

Reviewed by:
Zhiming Li,
Central South University, China
Yan Wang,
Xi'an University of Architecture and Technology, China

****Correspondence:***
Sergej Gein
s.gein@access-technology.de

Specialty section:
This article was submitted to Structural Materials, a section of the journal Frontiers in Materials

Received: *29 May 2020*
Accepted: *06 August 2020*
Published: *23 September 2020*

Citation:
Gein S, Witusiewicz VT and Hecht U (2020) The Influence of Mo Additions on the Microstructure and Mechanical Properties of $AlCrFe_2Ni_2$ Medium Entropy Alloys. Front. Mater. 7:296. doi: 10.3389/fmats.2020.00296

INTRODUCTION

In the last two decades, research on high entropy alloys (HEAs) aimed at finding alloys that would allow obtaining single-phase equiatomic HEAs exhibiting face-centered-cubic (FCC), body-centered-cubic (BCC), and hexagonal-close-packed (HCP) structures while eliminating secondary (and tertiary) phases (Kozak et al., 2015; Steurer, 2020). However, in recent years a paradigm shift has taken place that puts the focus on dual-phase (or multi-phase) HEAs and intentionally takes advantage of their heterophase nature to achieve superior mechanical properties

(Bönisch et al., 2018). Furthermore, increasing attention is given to medium entropy alloys with less than five elements, not at least with the aim of avoiding expensive and resource-critical elements like Cobalt (Tkaczyk et al., 2018). This opens opportunities to develop novel materials for industrial applications, whenever clear development targets are set forward. The alloy system Al-(Co)-Cr-Fe-Ni is one interesting candidate for the development of dual phase materials, building on rich knowledge from the ternary subsystems Fe-Cr-Ni (Jönsson, 1995; Wróbel et al., 2015), Fe-Ni-Al (Eleno et al., 2006), etc. These subsystems host the well-known family of duplex steels (Alvarez-Armas and Degallaix-Moreuil, 2013), B2-ordered intermetallic alloys, and a series of eutectic alloys (Misra and Gibala, 1997). The alloy system Al-(Co)-Cr-Fe-Ni also offers means to exploit some features of spinodal decomposition (Langer, 1971) for microstructure tailoring. Novel dual phase materials have been reported in the system Al-(Co)-Cr-Fe-Ni (Dong et al., 2016; Abuzaid and Sehitoglu, 2018; Bönisch et al., 2018; Gwalani et al., 2019; Li C. et al., 2020; Li Z. et al., 2020). Unique so far are vermicular duplex microstructures (Dong et al., 2016; Li C. et al., 2020) composed of an ultrafine vermicular FCC phase intertwined with a spinodally decomposed BCC in nearly equal volume fraction. They were first reported in 2016 by Dong et al. (2016) in an $AlCrFe_2Ni_2$ alloy, being termed "noodle-like" and suggested to be of eutectic origin. Similar microstructures are equally found in Co-containing alloys.

During the exploration of the Al-Cr-Fe-Ni and the Al-Co-Cr-Fe-Ni systems with respect to the addition of further alloying elements, molybdenum was investigated by Hsu et al. (2010), Zhu et al. (2010), and Dong et al. (2013), respectively. Dong et al. (2013) investigated a series of alloys $AlCrFeNiMo_x$ with the molar ratio x ranging from 0 to 1, explicitly $x = 0.0, 0.2, 0.5, 0.8, 1.0$. All alloys $x < 0.5$ displayed BCC-based microstructures. For Mo exceeding $x > 0.5$, the primary phase was identified as sigma phase. Compression tests for $x = 0.2$, corresponding to a Mo content of 4.8 at.–%, revealed fracture strength as high as 3.22 GPa and a plastic strain of 28.7%, however with a cleavage-like appearance of the fracture surface. To our best knowledge, molybdenum additions to the alloy $AlCrFe_2Ni_2$ were not reported in literature, despite the increasing interested in alloys, which form dual-phase microstructures.

In this study, we selected the $AlCrFe_2Ni_2$ alloy to revisit the microstructure and further develop the alloy by minor additions of molybdenum in the range from 1–3 at.–% to the baseline composition. The study encompasses four alloys, that is, $Al_{17}Cr_{17}Fe_{33}Ni_{33}$ (Mo_0), $Al_{17}Cr_{17}Fe_{33}Ni_{33}Mo_1$ (Mo_1), $Al_{16}Cr_{16}Fe_{33}Ni_{33}Mo_2$ (Mo_2), and $Al_{16}Cr_{16}Fe_{33}Ni_{33}Mo_3$ (Mo_3) (at.–%). An industrial superduplex steel 1.4517 (DIN EN 10283/ASTM A890) is included as reference material. The research is embedded in a targeted European effort aiming at applications, which require a good balance between strength, ductility, and toughness along with wear and corrosion resistance in areas commonly served by duplex and superduplex steels. In this paper, we present and discuss the contribution of molybdenum to phase stability and describe the effects of annealing heat treatments on microstructure and selected mechanical properties. Main attention is given to alloys Mo_0 and Mo_2.

EXPERIMENTAL PROCEDURES

We investigated samples with an ultrafine vermicular duplex microstructure in a series of alloys $AlCrFe_2Ni_2Mo_x$ (molar ratio) starting from the initial composition $AlCrFe_2Ni_2$. Molybdenum additions ranged from $x = 0.06$ to 0.18 molar ratio, corresponding to 1–3 at.–%. Samples were produced by arc melting (Edmund Bühler AM500) of large 300 g buttons from raw elemental metals with a purity above 99.8 wt.–%. The samples were molten under 0.7 bar argon (purity 5.0) with a Ti-getter after having evacuated the chamber to 10^{-5} bar followed by repeated purging with argon to prevent oxygen pickup. The samples were then flipped and remolten three times to ensure chemical homogeneity. **Table 1** shows the nominal and measured alloy compositions as determined by energy dispersive x-ray spectrometry (EDS).

The arc-melted buttons were cut by wire electrical discharge machining (Excetek V400G) to produce specimens for microstructure characterization and instrumented micro-indentation before and after defined annealing treatments. Furthermore, from the samples, Mo_0 and Mo_2 rectangular specimens with the dimensions $30 \times 5 \times 1.6$ mm were extracted for 3-point-bending tests and subjected to annealing heat treatments at 950°C for 6 h followed by water quenching. Moreover, specimens from Mo_2 were annealed at 1100°C for varying holding times, that is, 10 min to 3 h followed by water quenching. Annealing was carried out in a horizontal tube furnace (Nabertherm RHTC 80-230/15) under argon flow.

Sample preparation for microstructure analysis consisted of standard metallographic grinding and polishing steps with a final polishing step in a vibromet device (Buehler VibroMet^{TM}). Samples were analyzed in scanning electron microscopes (Zeiss, Gemini Ultra 55 and Gemini Leo 1550) equipped with detectors for EDS analysis (Oxford Instruments X-max 150) and electron backscatter diffraction (EBSD) (Nordlys HKL). Micro-indentation measurements were performed in an Anton Paar MHT^3 using a Vickers indenter at a loading speed of 2000 mN/min and a maximum load of 500 mN. The 3-point-bending tests were carried out in a miniature testing device (MTI SEMtester 1000 EBSD) using a constant displacement of 0.2 mm/min (strainrate $\sim$0.3% s^{-1}) until a maximum strain of 20% or sample failure was reached. For improved statistics three to five specimen were tested per alloy composition and annealing condition.

EXPERIMENTAL RESULTS AND DISCUSSION

In section "Microstructure Characterisation," we describe the microstructure in the arc melted condition and after annealing heat treatments with focus on morphological and crystalline features of the dual phase structure, the phase fractions, and compositions. In section "Mechanical Properties," we present

TABLE 1 | Nominal and integral composition of fabricated $AlCrFe_2Ni_2Mo_x$ samples by EDS (at.%).

Alloy	Nominal composition	Chemical composition by EDS in at.%				
		Al	Cr	Fe	Ni	Mo
Mo_0	$Al_{17}Cr_{17}Fe_{33}Ni_{33}$	17.1 ± 0.1	16.9 ± 0.1	32.6 ± 0.3	33.3 ± 0.4	–
Mo_1	$Al_{17}Cr_{17}Fe_{33}Ni_{33}Mo_1$	16.3 ± 0.1	17.1 ± 0.1	32.5 ± 0.2	33.0 ± 0.1	1.0 ± 0.1
Mo_2	$Al_{16}Cr_{16}Fe_{33}Ni_{33}Mo_2$	16.1 ± 0.1	17.0 ± 0.1	32.8 ± 0.1	32.2 ± 0.1	2.0 ± 0.1
Mo_3	$Al_{16}Cr_{16}Fe_{33}Ni_{33}Mo_3$	16.0 ± 0.1	17.0 ± 0.1	32.3 ± 0.2	31.7 ± 0.1	3.0 ± 0.1

EDS measurements were performed on five randomly placed areas on the sample and the values represent the mean and standard deviation of the five measurements.

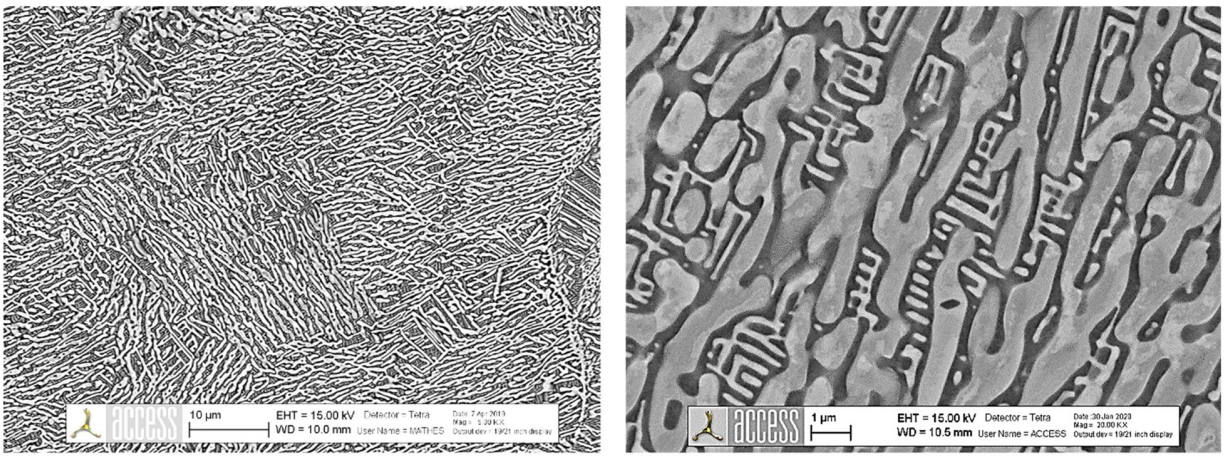

FIGURE 1 | SEM-BSE micrographs of the as-cast microstructure in sample Mo_2 **(A)** displays a low magnifcation overview while **(B)** shows the ultrafine vermicular duplex structure with the FCC phase (bright) closely entangled with the spinodal decomposed BCC phase (dark).

the mechanical properties from micro-indentation and 3-point-bending, respectively.

Microstructure Characterization

Initial Condition After Arc Melting

Figure 1 – shows an overview of the microstructure in the initial "as-cast" condition of the Mo_2 sample at different magnifications, which allows identifying the multiscale structural features as follows: **Figure 1A** – At low magnifications, one distinguishes large dual-phase grains, which are former (parent) BCC-B2 grains. **Figure 1B** – Inside the grains, an ultrafine vermicular FCC phase is present (bright color), while the BCC matrix is spinodally decomposed at nanoscale. The decomposition products are BCC-B2#2 (dark) and BCC-A2# (bright). The vermicular FCC and the spinodal BCC are visibly entangled, the FCC phase fraction reaching about 60 area–%. Two types of boundaries are visible (i) grain boundaries, decorated by a continuous film of FCC and (ii) domain boundaries, which separate regions of similar FCC directionality, being in fact boundaries between crystallographic FCC variants. Sometimes, grain boundaries show small regions with Widmanstätten rather than vermicular FCC. These features are similar to those reported by Dong et al. for the Mo-free alloy $AlCrFe_2Ni_2$; however, Mo additions greatly reduce the extent of Widmanstätten regions. Hecht et al. discuss more details about the competition between Widmanstätten and vermicular FCC in this Frontier's edition, "The BCC-FCC phase transformation pathways and crystal orientation relationships in dual phase materials from Al-(Co)-Cr-Fe-Ni alloys."

Molybdenum additions, even in small quantities, have a pronounced effect on the FCC phase fraction formed upon continuous cooling through the BCC→FCC phase transformation, but also on the morphological anisotropy. **Figure 2** displays high magnification micrographs of the as-cast microstructure in the four alloys Mo_0 through Mo_3. The FCC phase fraction evaluated by image analysis ranges from 50% in Mo_0, 60% Mo_1 and Mo_2 and finally 45% in Mo_3. This is surprising, because Mo is a BCC stabilizing element. The increase of the FCC fraction from 50 to 60% seems counterintuitive but relates to the fact that Mo additions implicitly decrease the aluminum content, simply by dilution. This indicates that Mo is a less strong BCC stabilizing element compared with Al. Only above 2 at.–% Mo, for example, in Mo_3, the BCC stabilizing effect of Mo compensates for the dilution of Al, thus leading to a decrease of the FCC phase fraction to 45%.

From **Figure 2**, it is perceivable that molybdenum additions lead to an increasing microstructural anisotropy, both regarding the directionality of the vermicular FCC structure but also regarding the nanoscale pattern inside the spinodally

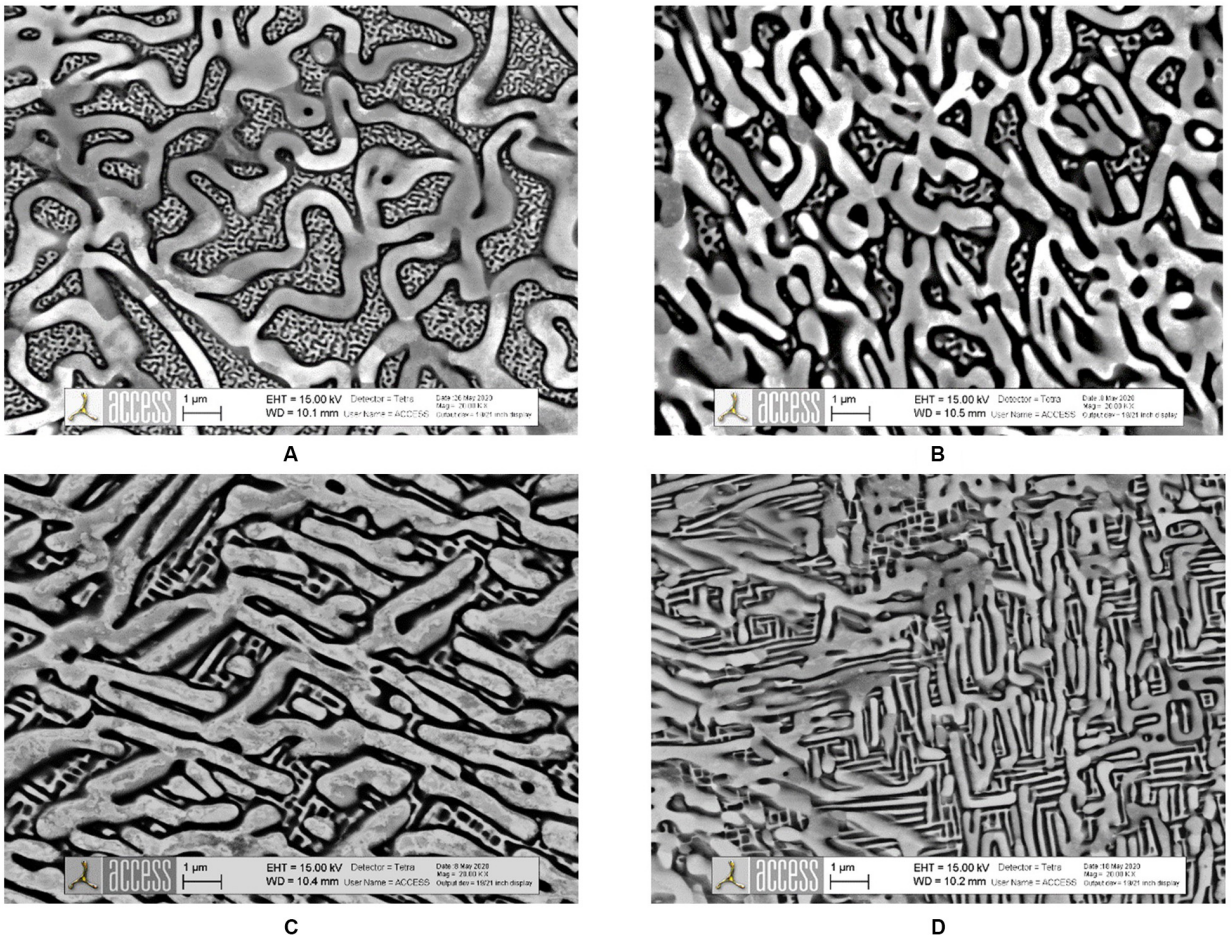

FIGURE 2 | SEM-BSE images of the ultrafine vermicular duplex structure in as-cast Mo_x samples, showing increasing morphological anisotropie with increasing Mo: **(A)** Mo-free, **(B)** 1 Mo, **(C)** 2 Mo, and **(D)** 3 Mo (at.-%).

TABLE 2 | Morphological and crystallographic features of the FCC phase in of Mo_0 and Mo_2: Phase fraction, average thickness, average and 95th percentile intergranular misorientation.

Sample	FCC phase fraction (%)	Average thickness (μm)	Intergranular misorientation (°)	
			Average	95th percentile
Mo_0 as-cast	52 ± 0	0.54 ± 0.03	5.2 ± 2.5	8.8
Mo_0 950°C 6 h	58 ± 2	0.89 ± 0.18	4.0 ± 2.0	8.0
Mo_2 as-cast	59 ± 2	0.48 ± 0.09	4.9 ± 2.2	9.5
Mo_2 950°C 6 h*	44 ± 1	0.86 ± 0.14	4.4 ± 1.8	7.9
Mo_2 1100°C 10 min	58 ± 1	0.79 ± 0.14	5.7 ± 2.5	10.3
Mo_2 1100°C 1 h	60 ± 3	1.09 ± 0.12	4.0 ± 1.9	7.8
Mo_2 1100°C 2 h	56 ± 1	1.13 ± 0.17	4.6 ± 2.2	8.6
Mo_2 1100°C 3 h	57 ± 1	1.31 ± 0.14	5.3 ± 2.6	10.4

**Sigma phase 17%; Composition by EDS in at.%: Al 4.7 ± 1.0 Cr 36.2 ± 0.9 Fe 39.9 ± 0.8 Ni 11.8 ± 0.9 Mo 7.5 ± 0.3.*

decomposed BCC phase. The increased anisotropy is attributed to an increase of the BCC-A2 phase fraction inside the spinodal structure but likely also to an increase of the interfacial energy anisotropy. The simulation study by Vidyasagar et al. (2018) illustrates the importance of interfacial energy anisotropy during spinodal decomposition.

Table 2 lists all measured quantitative data regarding the FCC phase fraction and the average thickness of the FCC vermicelli, also including the lattice strain observed by EBSD and analyzed by the MTEX software. Indeed, the EBSD analysis of the ultrafine vermicular samples in the as-cast as well as annealed conditions revealed that the FCC phase is significantly strained, containing a

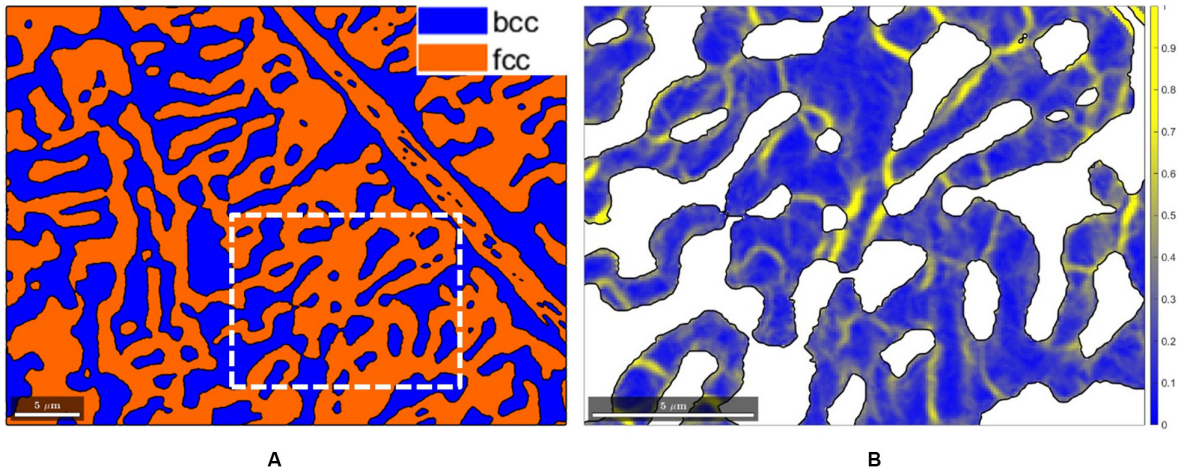

FIGURE 3 | (A) EBSD Phase map of Mo_2 after annealing at 1100°C for 3 h and **(B)** magnified region with a map of the kernel average misorientation within the FCC phase.

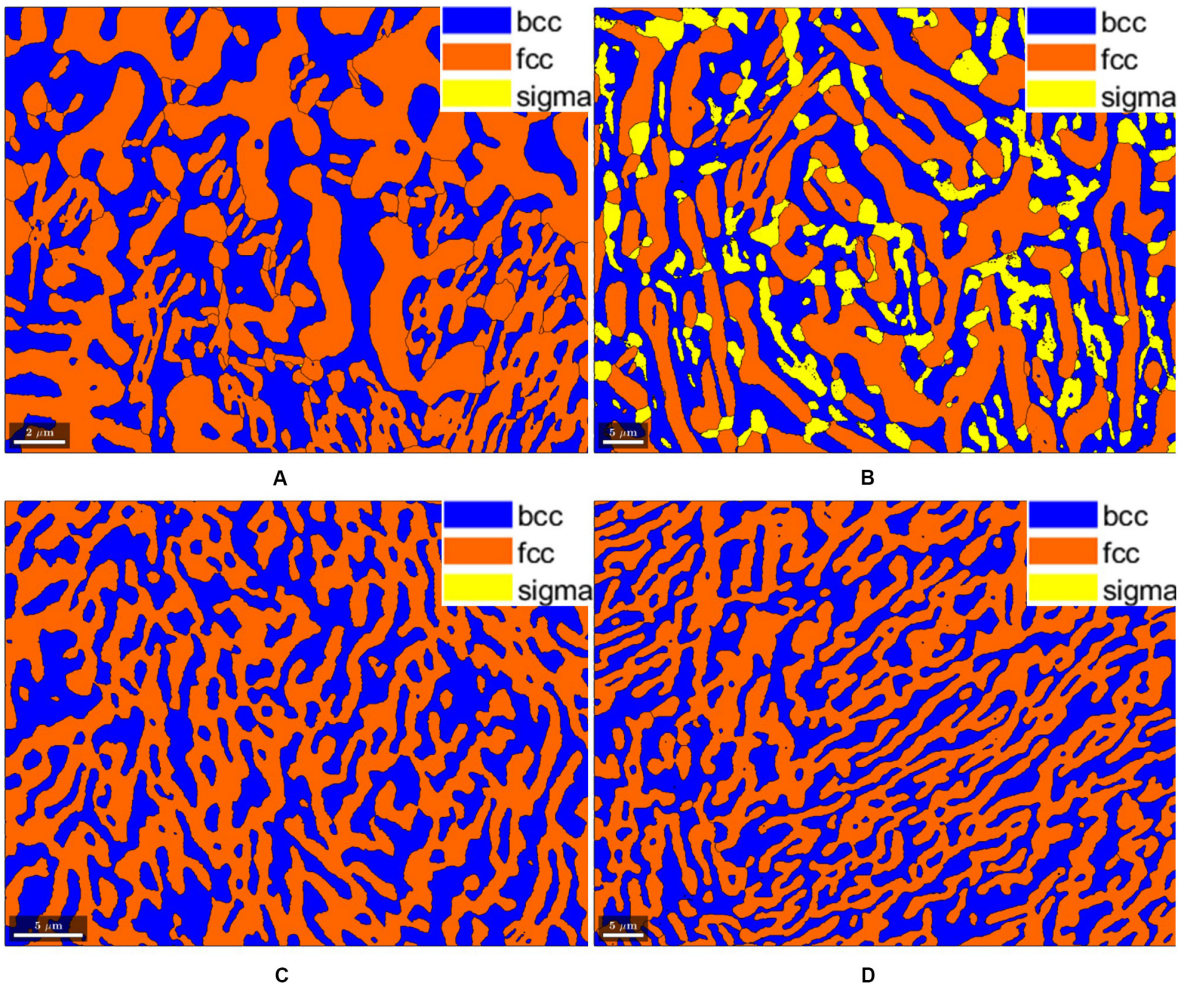

FIGURE 4 | EBSD map of samples **(A)** Mo_0 in as-cast condition, **(B)** Mo_2 after annealing at 950°C/6 h, **(C)** after annealing at 1100°C/1 h, and **(D)** 1100°C/3 h. Sigma phase is only present in Mo_2 950°C/6 h.

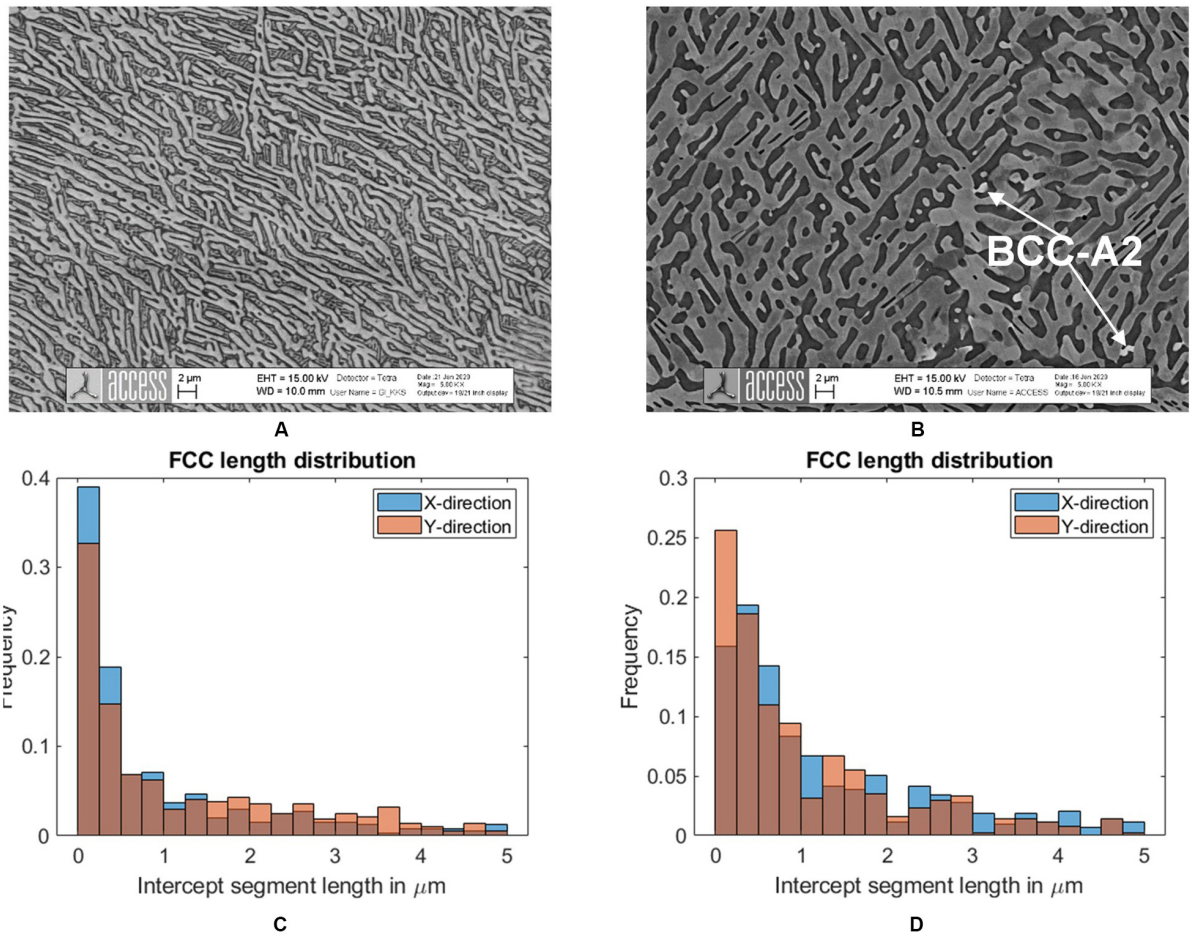

FIGURE 5 | FCC size distribution in sample Mo_2 in as-cast conditions **(A,C)** and after annealing at 1100°C for 3 h **(B,D)**. The size distribution was measured by the line intercept method using both vertical and horizontal lines.

TABLE 3 | Phase compositions in Mo_0 and Mo_2 after annealing at 1100°C/3 h measured by EDS.

AlCrFe$_2$Ni$_2$	**Al (at.%)**	**Cr (at.%)**	**Fe (at.%)**	**Ni (at.%)**	**Mo (at.%)**
FCC (A1)	5.4 ± 0.1	23.5 ± 0.2	46.5 ± 0.3	24.6 ± 0.3	–
BCC (A2)	20.7 ± 0.2	23.7 ± 1.1	27.2 ± 0.4	28.5 ± 0.8	–
BCC (B2)	30.7 ± 1.3	8.8 ± 2.7	16.3 ± 1.8	44.2 ± 3.2	–
AlCrFe$_2$Ni$_2$Mo$_{0.1}$	**Al (at.%)**	**Cr (at.%)**	**Fe (at.%)**	**Ni (at.%)**	**Mo (at.%)**
FCC (A1)	7.3 ± 0.1	22.0 ± 0	41.3 ± 0.5	26.5 ± 0.3	2.8 ± 0.1
BCC (A2)	6.9 ± 0.6	33.2 ± 0.1	41.3 ± 0.4	13.5 ± 0.3	5.1 ± 0.1
BCC (B2)	33.0 ± 0.3	5.6 ± 0.7	15.1 ± 0.7	46.0 ± 1.3	0.4 ± 0.2

high density of subgrain boundaries. The strain originates from the BCC→FCC phase transformation, which involves lattice rotation and dilatation relative to the parent BCC. **Figure 3** shows the subgrain network for sample Mo_2 after annealing at 1100°C/3 h based on the kernel average misorientation map (the average misorientation angle of a given point with all its first neighbors) plotted by MTEX. We believe that apart from classical transformation strain, the observed subgrain network relates to the growth conditions of the vermicular FCC from the initial BCC-B2 parent phase. Unlike Widmanstätten FCC plates, which grow into chemically homogeneous BCC-B2, the vermicular FCC was observed to grow into spinodally decomposing BCC-B2 (see Hecht et al. in this Frontier's edition). The compositional modulation in the parent grain is likely causing additional strain.

Annealed Condition After Isothermal Heat Treatments

Annealing heat treatments were carried out at 950°C for 6 h mainly to verify the propensity of the Mo_0 and Mo_2 alloys to

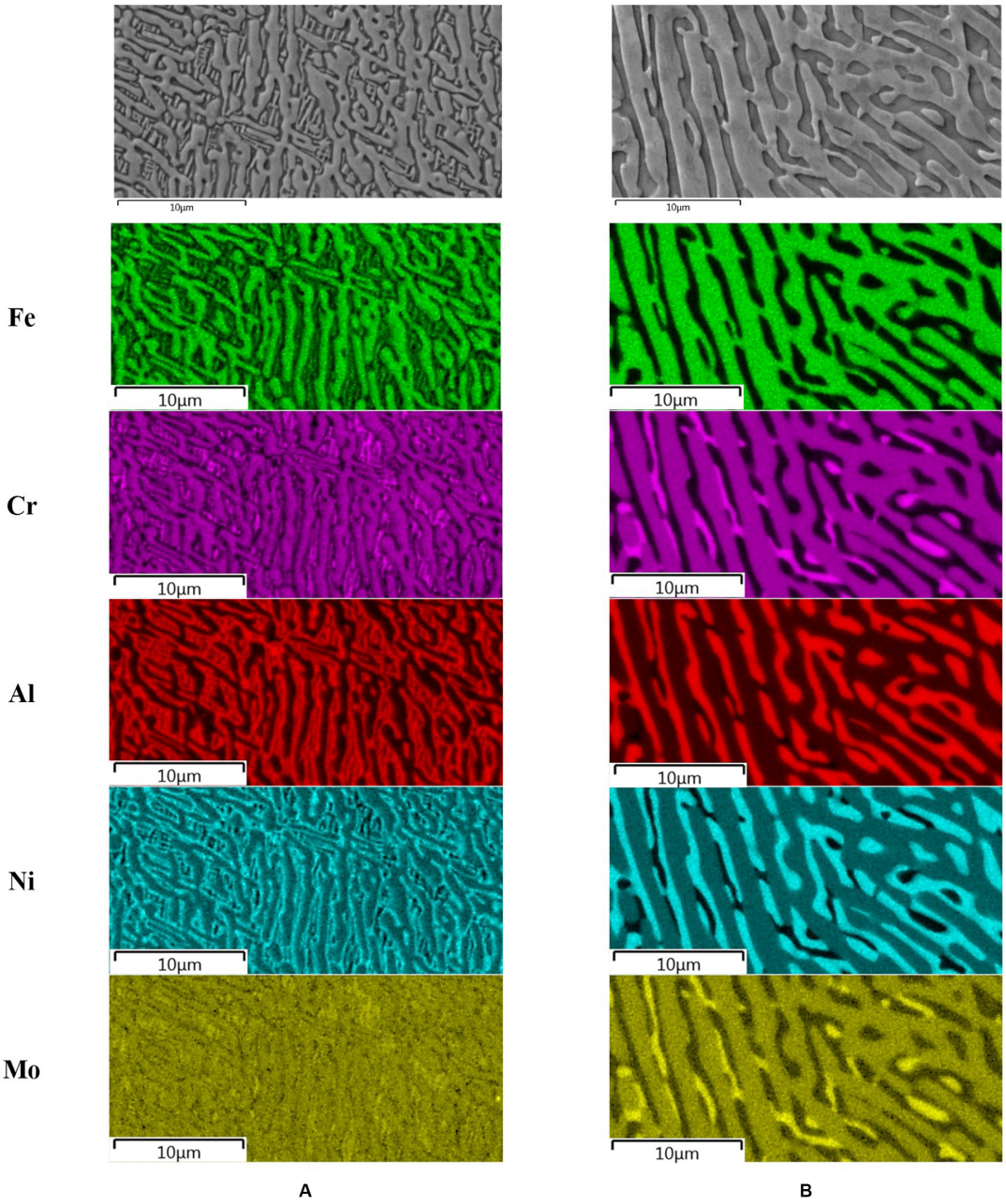

FIGURE 6 | Element distribution from EDS mapping in the sample Mo_2 for **(A)** as-cast condition and **(B)** after annealing at 1100°C for 3 h. Noteworthy is the sluggish partitioning of molybdenum in the as-cast condition, which is recovered after heat treatment.

form the brittle sigma phase (tetragonal, space group no.136). EBSD analysis shows the absence of the sigma phase in Mo_0, while in alloy Mo_2 about 17% sigma-phase is present with a composition around Al = 6 ± 2, Cr = 35 ± 2, Fe = 39 ± 1, Ni = 13 ± 2 and Mo = 7 ± 1 (at.–%). **Figure 4** displays the EBSD phase maps for (**Figure 4A**) Mo_0 950°C/6 h, (**Figure 4B**) Mo_2 950°C/6 h, (**Figure 4C**) Mo_2 1100°C/1 h, and (**Figure 4D**) Mo_2 1100°C/3 h. The sigma phase is particularly present in Mo_2 950°C/6 h at FCC phase boundaries but also in regions where former BCC-A2 was present (**Figure 4B**). Sigma phase formation can be successfully prevented, even in sample Mo_2, after annealing at 1100°C up to 3 h followed by water quenching. Such heat treatment parameters are common practice for duplex steels, even for thick section castings, to avoid sigma phase formation (Fritz, 2014; Llorca-Isern et al., 2017).

A small series of annealing treatments were performed for Mo_2 at 1100°C with distinct holding durations of 10 min, 1, 2, and 3 h, followed by water quenching. The series aimed

TABLE 4 | Overview of mechanical properties for all tested conditions for Mo_0 and Mo_2.

Sample	HV 0.05	E_{it} (GPa)	YS (0.2%) (MPa)	Flexural UTS (MPa)	Elongation at fracture (%)
Mo_0	326 ± 6	190 ± 12	1140 ± 40	2150 ± 60	16.0
Mo_0 950°C 6 h	304 ± 6	197 ± 12	1000 ± 50	2050 ± 30	14.3
Mo_2	384 ± 6	193 ± 7	1330 ± 90	2200 ± 90	15.6
Mo_2 950°C 6 h	392 ± 8	183 ± 13	1100 ± 50	1900 ± 40	4.2
Mo_2 1100°C 10 min	333 ± 8	189 ± 9	1150 ± 60	2060 ± 25	>20.0
Mo_2 1100°C 1 h	324 ± 7	189 ± 12	1020 ± 50	2040 ± 110	>20.0
Mo_2 1100°C 2 h	315 ± 7	192 ± 6	930 ± 50	1950 ± 130	>20.0
Mo_2 1100°C 3 h	315 ± 3	188 ± 10	900 ± 30	2000 ± 30	>20.0
Superduplex 1.4517	185 ± 15	155 ± 9	1110 ± 50	1620 ± 80	>20.0

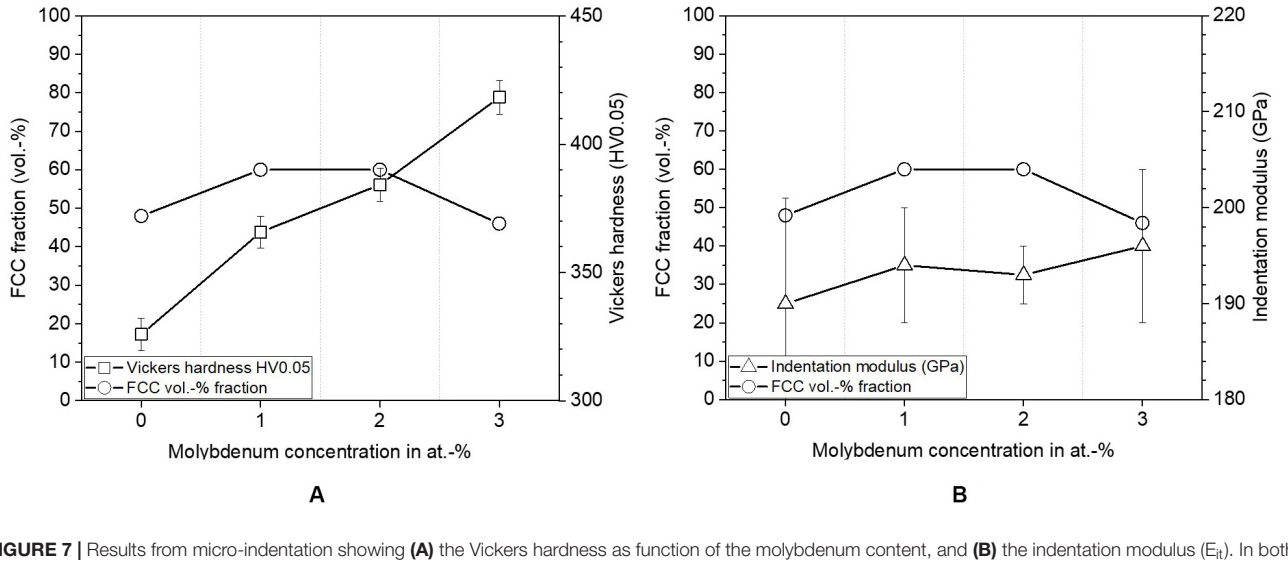

FIGURE 7 | Results from micro-indentation showing **(A)** the Vickers hardness as function of the molybdenum content, and **(B)** the indentation modulus (E_{it}). In both diagrams, the FCC phase fraction is equally plotted.

at verifying the coarsening of the ultrafine vermicular FCC phase and of the spinodal structure. **Figures 5A,B** illustrates the effects of coarsening by comparing the as-cast (**Figure 5A**) and annealed microstructures after 1100°C/3 h (**Figure 5B**). The comparison shows that the FCC phase thickens considerably, without changes in the phase fraction (see **Table 2**). The average thickness increases from 0.5 μm in the as-cast state to 1.3 μm in the annealed state. Coarsening is associated with an increasing contiguity of the FCC network. **Figures 5C,D** displays the size distribution of the FCC phase measured by the line intercept method along horizontal and vertical lines. The most dramatic coarsening is seen in the spinodal structure, which vanishes nearly completely, leaving behind few globulitic BCC-A2 particles. Without having analyzed the BCC-A2 fraction quantitatively, we qualitatively see a decrease of the BCC-A2 fraction, which is in agreement with the thermodynamics of the system. By heat treatment, the subgrain network inside the FCC phase is not changed significantly. We do not observe significant changes of the intergranular misorientation or of the low angle grain boundary distribution. **Table 2** summaries the morphological and crystallographic features of the FCC phase for Mo_0 and Mo_2 for all heat treatment conditions.

Due to coarsening, it was feasible to measure the chemical composition of the individual phases in Mo_0 and Mo_2 by EDS. **Table 3** summarizes the results. As can be seen, molybdenum partitions mainly to the BCC-A2 phase, while being <0.5 at.% in the BCC-B2 phase. The FCC phase contains 2.8 at.% Mo. EDS maps provided in **Figure 6** show the elemental partitioning between the phases for Mo_2 in the as-cast and annealed 1100°C/3 h condition. An interesting and noteworthy observation is that molybdenum partitioning occurs only during heat treatment. The as-cast sample (**Figure 6**, left column) shows a sluggish Mo-partitioning, even though the other elements are clearly partitioned. This is likely due to kinetic effects, which are commonly termed as "solute trapping," being associated to limited diffusion of Mo in BCC-B2. After heat treatment (**Figure 6**, right column), molybdenum partitioning is complete, and mainly to the BCC-A2 and the FCC-A1 phases. The Mo-content of the BCC-B2 phase is below 0.5 at.–%.

Mechanical Properties

The basic mechanical properties investigated on small samples in the as-cast and annealed states relate to results from micro-indentation and 3-point-bending, as presented below

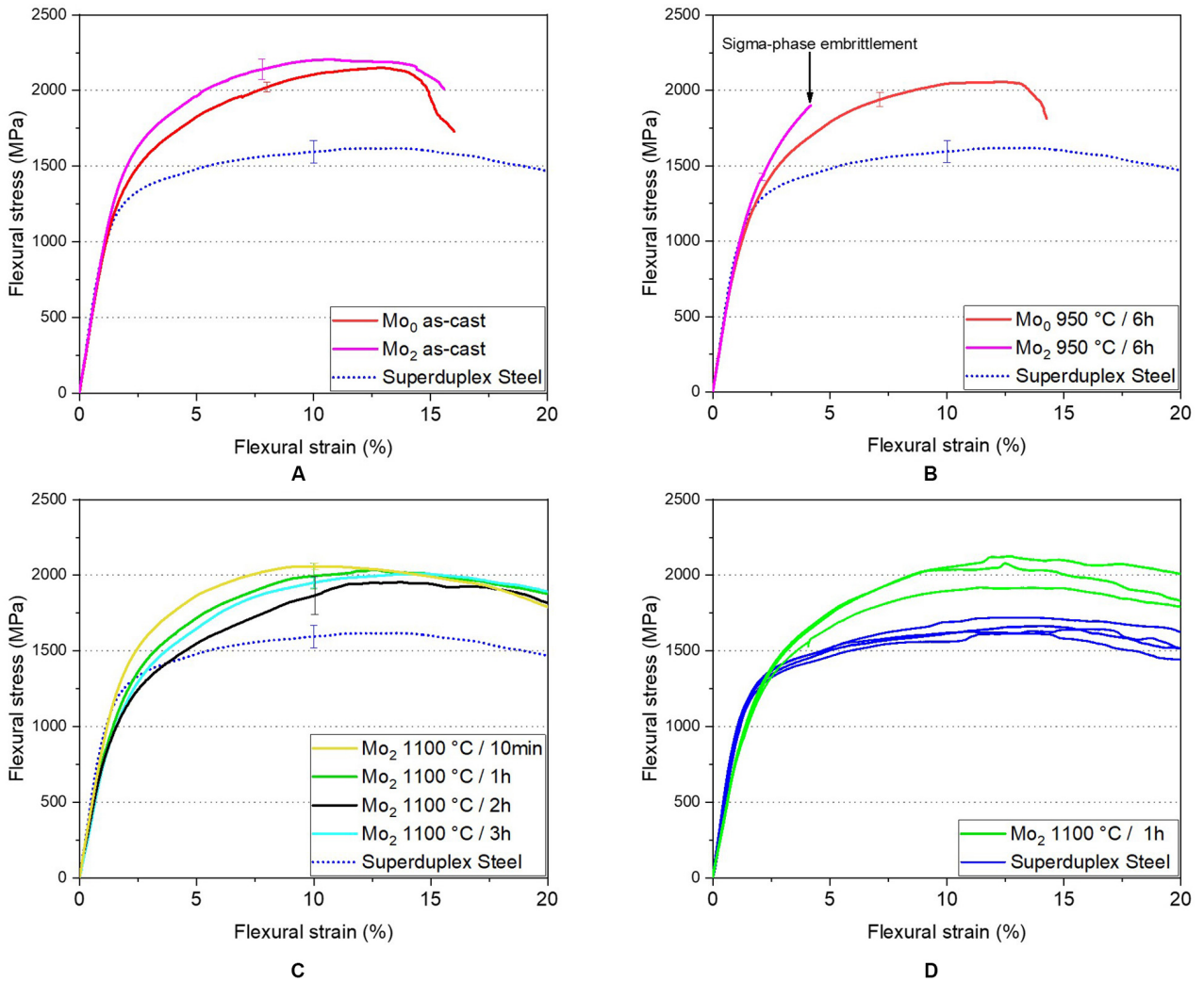

FIGURE 8 | (A) Flexural stress-strain curves in as-cast conditions: $AlCrFe_2Ni_2$ (Mo_0) in red, $AlCrFe_2Ni_2Mo_{0.1}$ (Mo_2) in magenta, superduplex steel reference 1.4517 in blue, **(B)** after annealing at 950°C/6 h: Mo_0 in red, Mo_2 in magenta, **(C)** Mo_2 after annealing at 1100°C for 10 min (yellow), 1 h (green), 2 h (black), and 3 h (light blue). Illustration of the spread shown in **(D)** for Mo_2 1100°C/1 h and the reference superduplex steel.

and summarized in **Table 4** for the Mo_0 and Mo_2 in all tested conditions.

Micro-Indentation

Figures 7A,B provide the Vickers hardness (HV0.05) and the indentation modulus (E_{it}) as function of the molybdenum content for samples in the as-cast state along with the values of the FCC phase fraction. The Vickers hardness increases markedly with increasing Molybdenum content from 326 ± 6 HV0.05 in Mo_0 to 418 ± 7 HV0.05 in Mo_3, independent of the BCC/FCC phase ratio. The origin of this increase may relate to increased density and bulk modulus of the alloy as was reported by Ledbetter et al. for the Fe-Cr-Ni system (Ledbetter and Austin, 1988; Ledbetter and Kim, 1988). However, we remind the microstructure observations (compare **Figure 2**), which showed that Mo increases the BCC-A2 phase fraction inside the spinodal BCC, leading to a plate-like morphology. At this stage, the quantitative analysis of the BCC-A2 fraction is still pending. As shown in **Figure 7B**, the indentation modulus increases only slightly from 190 to 196 GPa.

The evolution of hardness and indentation modulus for the annealed samples (Mo_0 and Mo_2) are listed in **Table 4** along with results from 3-point-bending. As expected, upon annealing the hardness decreases with increasing temperature and/or annealing time. The lowest hardness of around 315 HV0.05 is reached in Mo_2 after annealing at 1100°C for 3 h, which is still significantly higher than the hardness of the reference superduplex steel 1.4517 with 185 HV0.05.

Three-Point Bending Tests

Three-point-bending tests of miniature specimens 30 × 5 × 1.6 mm reveal the potential of the alloy Mo_2 for applications as structural material compared to the reference superduplex steel. Furthermore, the tests also shed light on means

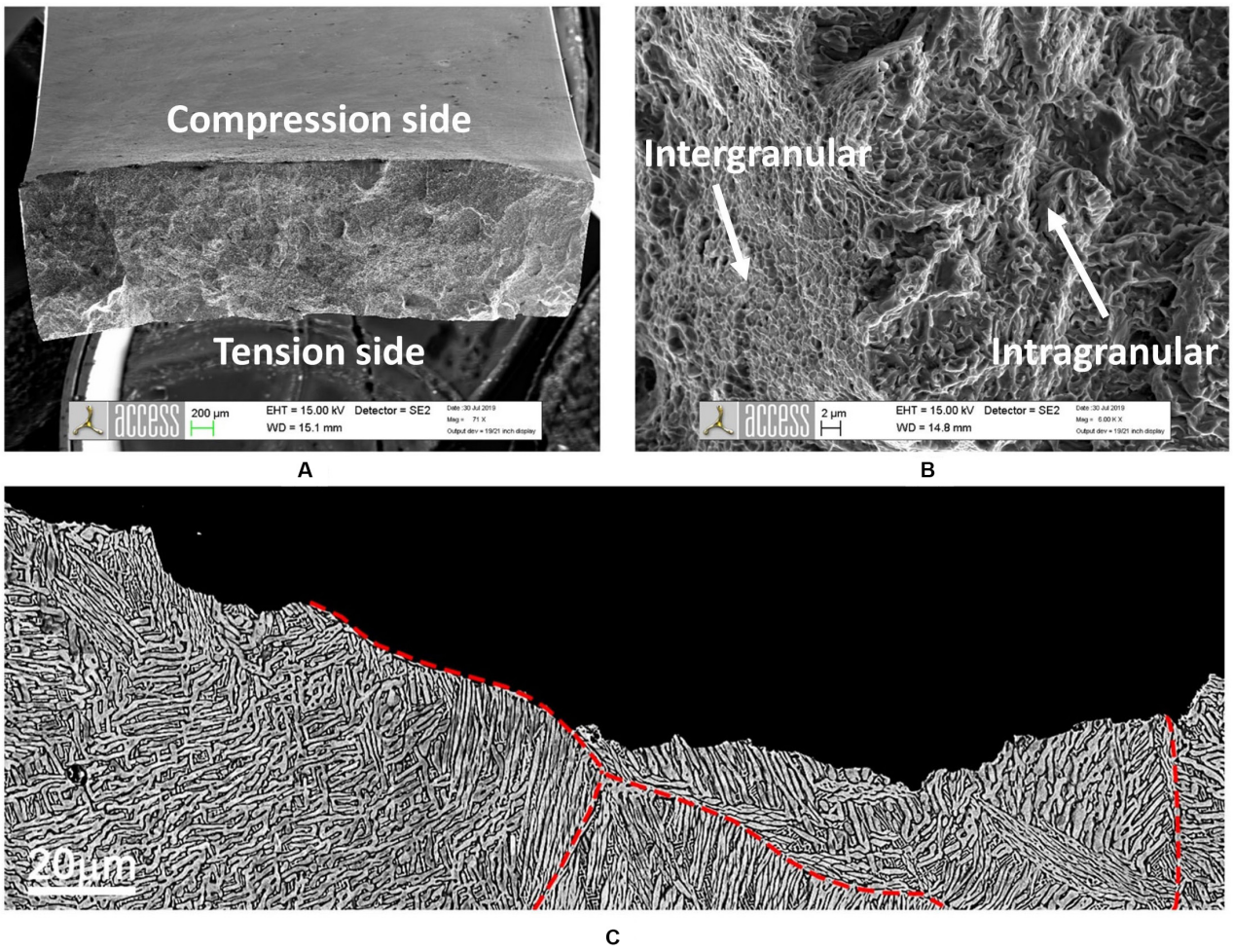

FIGURE 9 | Overview SEM-SE image of an as-cast Mo_2 specimen fractured surface in **(A),** in **(B)** a high magnification fracture surface image with (left) an intergranular fracture region and (right) an intragranular fracture region. **(C)** shows a perpendicular metallographic section plane of the fracture surface with (red strokes) outlined grain boundaries.

of balancing strength and ductility by annealing treatments. The main results are shown in **Figure 8** as follows: **Figure 8A** compares the as-cast Mo_0 and Mo_2 samples to the as received and heat treated (1150°C for 3 h) superduplex steel 1.4517. Both alloys show pronounced and similar strain hardening, with the Mo-containing Mo_2 being slightly stronger than the Mo-free Mo_0. Both materials outpace the superduplex steel in terms of maximum flexural strength, however at the expense of ductility. The ductility is none the less considerably high, reaching about 15% flexural strain at fracture. **Figure 8B** compares the Mo_0 and Mo_2 in the heat-treated condition 950°C/6 h and reveals the embrittlement by sigma phase in the Mo_2 sample. **Figure 8C** compares distinct annealing durations at 1100°C for Mo_2 samples and shows that the yield strength decreases with increasing annealing durations, while the ductility increases significantly to flexural stains above 20%. The flexural UTS remains as high as 2000 MPa compared to 1600 MPa of the superduplex reference steel, while the yield stress falls down to the level of the reference steel. In all above figures, the plotted stress-strain curves are averaged over 3 to 5 tested specimens. **Figure 8D** illustrates the spread, taking as representative example all tested Mo_2 specimens annealed at 1100°C/1 h as well as the reference steel. All specimens reach the flexural strain of 20% being the limit of the testing device.

Further, the fracture surface of one as-cast Mo_2 specimen, failed during bending, was inspected in SEM as well as in a metallographic section plane placed perpendicular to the fracture surface. We identified both, inter- and intragranular fracture paths, as shown in **Figure 9**. In **Figure 9A**, we outline the grain boundaries to highlight that a part of the fracture path follows a grain boundary. Grain boundaries are decorated by a thin layer of FCC phase. **Figure 9B** displays a SEM-SE view of the fractures specimen with labels indicating the tensile and compression side. Finally, **Figure 9C** shows a high magnification of the fracture surface including a region of intergranular fracture on the left side and a region with intragranular fracture on the right side.

Taken together, the bending results clearly prove a remarkable strain hardening capability of the investigated alloys, which

is indeed one of the most prominent properties of HEAs as already discussed by Wang and Misra (2011) and Basu et al. (2018). Current work is directed toward better understanding the strain partitioning between BCC and FCC phases and identify the mechanisms behind strain hardening. Furthermore, the vermicular and highly contiguous microstructure is expected to show attractive fatigue properties, which are currently investigated. The hardness values, which outpass the superduplex steel by far, may improve the wear resistance, while calling for a careful investigation of the impact toughness.

SUMMARY AND CONCLUSION

We have investigated the effects of minor additions of molybdenum to the medium entropy alloy $AlCrFe_2Ni_2$ regarding the microstructure and basic mechanical properties with focus on annealing heat treatments. The alloy develops an ultrafine vermicular microstructure composed of 60% FCC and 40% BCC, the BCC being spinodally decomposed into BCC-A2 + BCC-B2. The vermicular microstructure displays a high contiguity, the phases forming a neatly entangled network. The following main conclusions are drawn:

- The ultrafine vermicular microstructure formed in the Mo-free baseline alloy $AlCrFe_2Ni_2$ is retained for Mo additions up to 3 at.%; however the directionality of the FCC phase increases, as does the anisotropy of the spinodal pattern. The latter is attributed to an increasing fraction of the BCC-A2 phase but may also relate to stronger interfacial anisotropy between the product phases of the spinodal decomposition.
- The FCC phase in the ultrafine vermicular microstructure displays significant strain and a network of low angle grain boundaries. The average intragranular misorientation does not change significantly during annealing treatments.
- Alloy Mo_2 with 2 at.% Mo is prone to sigma formation and related embrittlement. Annealing heat treatments must exceed the stability limit of the sigma phase, that is, ∼1000°C. At 950°C the sigma fraction is as high as 17%. Annealing at 1100°C safely avoids sigma formation.
- Alloy Mo_2 with 2 at.% Mo shows promising mechanical properties, which can be balanced by annealing at 1100°C. With increasing annealing duration, the ductility (flexural strain) increases at the expense of the yield strength. The ultimate flexural strength remains nearly unchanged at ∼2000 MPa, well exceeding the strength of the reference superduplex steel 1.4517. Like all investigated medium and HEAs, Mo_2 shows a remarkable strain hardening behavior, expected to prove beneficial to the wear resistance.
- An annealing treatment at 1100°C for the duration of 30 min to 1 h with subsequent water quenching is recommended.

DATA AVAILABILITY STATEMENT

The raw data supporting the conclusions of this article will be made available by the authors, without undue reservation, to any qualified researcher.

AUTHOR CONTRIBUTIONS

SG designed the study, performed all the experiments and analyzed the experimental results as part of his Ph.D. research. VW performed the thermodynamic calculations which guided the selection of annealing conditions. UH supervised the research and contributed to the process of writing the manuscript. All authors contributed to the article and approved the submitted version.

FUNDING

The German Federal Ministry for Education and Research (BMBF) supported this research under Grant No. 03XP0163A in the frame of the M-era.Net Joint Call 2017, Project NADEA (No. 5129).

ACKNOWLEDGMENTS

We kindly thank Otto Junker GmbH for providing the superduplex steel EN 1.4517 (ASTM A890 Grade 1B) in the cast and fully heat-treated condition to serve as reference material.

REFERENCES

Abuzaid, W., and Sehitoglu, H. (2018). Plastic strain partitioning in dual phase Al13CoCrFeNi high entropy alloy. *Mater. Sci. Eng. A* 720, 238–247. doi: 10.1016/j.msea.2018.02.044

Alvarez-Armas, I., and Degallaix-Moreuil, S. (eds) (2013). *Duplex Stainless Steels*. Hoboken, NJ: John Wiley & Sons Inc, doi: 10.1002/9781118557990

Basu, I., Ocelík, V., and De Hosson, J. T. M. (2018). BCC-FCC interfacial effects on plasticity and strengthening mechanisms in high entropy alloys. *Acta Mater.* 157, 83–95. doi: 10.1016/j.actamat.2018.07.031

Bönisch, M., Wu, Y., and Sehitoglu, H. (2018). Twinning-induced strain hardening in dual-phase FeCoCrNiAl0.5 at room and cryogenic temperature. *Sci. Rep.* 8, 1–9. doi: 10.1038/s41598-018-28784-1

Dong, Y., Gao, X., Lu, Y., Wang, T., and Li, T. (2016). A multi-component AlCrFe2Ni2 alloy with excellent mechanical properties. *Mater. Lett.* 169, 62–64. doi: 10.1016/j.matlet.2016.01.096

Dong, Y., Lu, Y., Kong, J., Zhang, J., and Li, T. (2013). Microstructure and mechanical properties of multi-component AlCrFeNiMo x high-entropy alloys. *J. Alloys Compd.* 573, 96–101. doi: 10.1016/j.jallcom.2013.03.253

Eleno, L., Frisk, K., and Schneider, A. (2006). Assessment of the Fe-Ni-Al system. *Intermetallics* 14, 1276–1290. doi: 10.1016/j.intermet.2005.11.021

Fritz, J. D. (2014). "Heat treating of austenitic and duplex stainless steels[1]," in *Heat Treating of Irons and Steels*, eds J. L. Dossett and G. E. Totten (Cleveland, OH: ASM International), 370–381. doi: 10.31399/asm.hb.v04d.a0005990

Gwalani, B., Gangireddy, S., Zheng, Y., Soni, V., Mishra, R. S., and Banerjee, R. (2019). Influence of ordered L1 2 precipitation on strain-rate dependent

mechanical behavior in a eutectic high entropy alloy. *Sci. Rep.* 9, 1–13. doi: 10.1038/s41598-019-42870-y

Hsu, C. Y., Wang, W. R., Tang, W. Y., Chen, S. K., and Yeh, J. W. (2010). Microstructure and mechanical properties of new AlCoxCrFeMo 0.5Ni high-entropy alloys. *Adv. Eng. Mater.* 12, 44–49. doi: 10.1002/adem.200900171

Jönsson, B. (1995). Assessment of the mobilities of Cr, Fe and Ni in bcc Cr-Fe-Ni Alloys. *ISIJ Int.* 35, 1415–1421. doi: 10.2355/isijinternational.35.1415

Kozak, R., Sologubenko, A., and Steurer, W. (2015). Single-phase high-entropy alloys – an overview. *Zeitschrift. Krist.* 230, 55–68. doi: 10.1515/zkri-2014-1739

Langer, J. (1971). Theory of spinodal decomposition in alloys. *Ann. Phys.* 65, 53–86. doi: 10.1016/0003-4916(71)90162-X

Ledbetter, H. M., and Austin, M. W. (1988). Molybdenum effect on volume in Fe-Cr-Ni alloys. *J. Mater. Sci.* 23, 3120–3124. doi: 10.1007/BF00551282

Ledbetter, H. M., and Kim, S. A. (1988). Molybdenum effect on Fe—Cr—Ni-alloy elastic constants. *J. Mater. Res.* 3, 40–44. doi: 10.1557/JMR.1988.0040

Li, C., Qu, Y., Zhang, Y., Lv, Q., and Qi, H. (2020). Effect of deep cryogenic treatment on the microstructure and mechanical properties of AlCrFe2Ni2 High-entropy alloy. *Mater. Res. Express* 7:36504. doi: 10.1088/2053-1591/ab7a5f

Li, Z., You, J., Guo, Y., Li, C., Zhang, Y., and Liu, Z. (2020). Phase transition mechanism and mechanical properties of AlCrFe 2 Ni 2 High-entropy alloys with changes in the applied carbon content. *Adv. Eng. Mater.* 22:1901363. doi: 10.1002/adem.201901363

Llorca-Isern, N., López-Jiménez, I., López-Luque, H., Biezma, M. V., and Roca, A. (2017). Study of the precipitation of secondary phases in duplex and superduplex stainless steel. *Mater. Sci. Forum* 879, 2537–2542. doi: 10.4028/www.scientific.net/msf.879.2537

Misra, A., and Gibala, R. (1997). Room-temperature deformation behavior of directionally solidified multiphase Ni-Fe-Al alloys. *Metall. Mater. Trans. A Phys. Metall. Mater. Sci.* 28, 795–807. doi: 10.1007/s11661-997-1007-4

Steurer, W. (2020). Single-phase high-entropy alloys – A critical update. *Mater. Charact.* 162:110179. doi: 10.1016/j.matchar.2020.110179

Tkaczyk, A. H., Bartl, A., Amato, A., Lapkovskis, V., and Petranikova, M. (2018). Sustainability evaluation of essential critical raw materials: cobalt, niobium, tungsten and rare earth elements. *J. Phys. D. Appl. Phys.* 51:aaba99. doi: 10.1088/1361-6463/aaba99

Vidyasagar, A., Krödel, S., and Kochmann, D. M. (2018). Microstructural patterns with tunable mechanical anisotropy obtained by simulating anisotropic spinodal decomposition. *Proc. R. Soc. A Math. Phys. Eng. Sci.* 474:535. doi: 10.1098/rspa.2018.0535

Wang, J., and Misra, A. (2011). An overview of interface-dominated deformation mechanisms in metallic multilayers. *Curr. Opin. Solid State Mater. Sci.* 15, 20–28. doi: 10.1016/j.cossms.2010.09.002

Wróbel, J. S., Nguyen-Manh, D., Lavrentiev, M. Y., Muzyk, M., and Dudarev, S. L. (2015). Phase stability of ternary fcc and bcc Fe-Cr-Ni alloys. *Phys. Rev. B Condens. Matter Mater. Phys.* 91:108. doi: 10.1103/PhysRevB.91.024108

Zhu, J. M., Fu, H. M., Zhang, H. F., Wang, A. M., Li, H., and Hu, Z. Q. (2010). Microstructures and compressive properties of multicomponent AlCoCrFeNiMox alloys. *Mater. Sci. Eng. A* 527, 6975–6979. doi: 10.1016/j.msea.2010.07.028

Conflict of Interest: The authors declare that the research was conducted in the absence of any commercial or financial relationships that could be construed as a potential conflict of interest.

frontiers in Materials

ORIGINAL RESEARCH
published: 07 October 2020
doi: 10.3389/fmats.2020.567793

Microstructure and Mechanical Properties of BCC-FCC Eutectics in Ternary, Quaternary and Quinary Alloys From the Al-Co-Cr-Fe-Ni System

Daniel Röhrens[1], Niloofar Navaeilavasani[1], Oleg Stryzhyboroda[1], Fabian Swientek[2], Paul Pavlov[2], Dirk Meister[2], Amber Genau[3] and Ulrike Hecht[1]*

[1] Access e.V., Aachen, Germany, [2] Anton Paar Germany GmbH, Ostfildern-Scharnhausen, Germany, [3] Department of Materials Science and Engineering, The University of Alabama at Birmingham, Birmingham, AL, United States

This study aimed at understanding the structure and properties of dual-phase eutectics in ternary, quaternary, and quinary alloys of the Al-Co-Cr-Fe-Ni system. The alloys at case were i) $Ni_{48}Fe_{34}Al_{18}$, ii) $Ni_{44}Fe_{20}Cr_{20}Al_{16,}$ and iii) $Ni_{34.4}Fe_{16.4}Co_{16.4}Cr_{16.4}Al_{16.4}$. Samples in the form of cylindrical bars, diameter 10 mm × 150 mm, were produced by arc melting and suction casting from pure elements (>99.9 wt%). Bridgman solidification at low growth velocity was used to produce additional samples with large eutectic spacing and lamellae thickness of the two phases body-centered cubic (BCC)-B2 and face-centered cubic (FCC) in order to facilitate phase characterization by energy-dispersive X-ray analysis (scanning electron microscopy/energy-dispersive spectroscopy) and nano-indentation. In agreement with thermodynamic calculations, each of the phases was found to be multi-component and contain all alloying elements in distinct amounts. The mechanical properties of the individual phases were analyzed in relation to their composition using nano-indentation experiments. These measurements revealed some insights into "high-entropy effects" and their contribution to the elastoplastic response to indentation loading. Further analysis focused on as-cast as well as heat-treated samples comprising phase fraction measurements, micro-indentation, and miniature testing in three-point bending configuration. For optimum heat treatment conditions, a good balance of strength and ductility was obtained for each of the investigated alloys. Further work is necessary in order to assess their capability as structural materials.

Keywords: high entropy alloy, eutectic, nano-indentation, microindentation, miniature testing, heat treatment

OPEN ACCESS

Edited by:
Liqiang Wang,
Shanghai Jiao Tong University, China

Reviewed by:
Jose Eduardo Spinelli,
Federal University of São Carlos, Brazil
Lei Wang,
Xi'an University of Technology, China

****Correspondence:***
Daniel Röhrens
d.roehrens@access-technology.de

Specialty section:
This article was submitted to Structural Materials a section of the journal Frontiers in Materials

Received: *30 May 2020*
Accepted: *27 August 2020*
Published: *07 October 2020*

Citation:
Röhrens D, Navaeilavasani N, Stryzhyboroda O, Swientek F, Pavlov P, Meister D, Genau A and Hecht U (2020) Microstructure and Mechanical Properties of BCC-FCC Eutectics in Ternary, Quaternary and Quinary Alloys From the Al-Co-Cr-Fe-Ni System. Front. Mater. 7:567793. doi: 10.3389/fmats.2020.567793

INTRODUCTION

The intermetallic compound NiAl has long been proposed as a potential alloy for high temperature structural applications due to its high melting-point, good thermal conductivity and excellent corrosion resistance (Miracle, 1993; Noebe et al., 1993; Liu, 1995). Because of the relatively low density (5.7 g/cm^3) it was especially considered for lightweight applications (Bei and George, 2005). Resulting from a high degree of order in the crystal structure and corresponding limitations in slip transfer, NiAl suffers from low room temperature ductility and low fracture toughness. This

TABLE 1 | Alloy designation and composition of the samples as measured by energy dispersive spectroscopy.

Alloy designation and content, at%	Ternary $Ni_{48}Fe_{34}Al_{18}$	Quaternary $Ni_{44}Fe_{20}Cr_{20}Al_{16}$	Quinary $Ni_{34.4}Fe_{16.4}Co_{16.4}Cr_{16.4}Al_{16.4}$
Ni	47.2	43.4	34.1
Fe	33.9	20.4	15.5
Al	18.9	15.7	15.8
Cr	—	20.5	17.0
Co	—	—	17.5

drawback is further complemented by low strength and creep resistance at higher temperatures (>600 °C). Numerous approaches have been proposed in order to improve the mechanical properties of NiAl (Shang et al., 2012; Hu et al., 2013; Wang et al., 2014; Wang et al., 2019; Wang et al., 2017). For example, alloying with refractory metals such as Cr, Mo, Re, and V produced binary BCC-B2 eutectic alloys with improved toughness and creep strength (Misra et al., 1998; Bei and George, 2005). Another successful approach by Misra and Gibala involved the addition of large amounts of iron to produce BCC-B2/FCC eutectic alloys with much improved room temperature ductility (Misra and Gibala, 1997). The possible tailoring of microstructure and interfacial properties with the target of promoting slip transfer and ductility was further advanced by investigating directionally solidified $Ni_{50}Fe_{30}Al_{20}$ (Misra and Gibala, 1999). The authors studied slip transfer across the phase boundaries and could identify several compatible slip systems, given the Kurdjumow–Sachs orientation relationship (Kurdjumow and Sachs, 1930) between the BCC and FCC lamellae (Misra and Gibala, 1999). In particular, they found that the interphase slip transfer is similar to the transfer across grain boundaries, and as a result, the active slip system can be predicted by utilizing criteria that had been proposed for grain boundaries (Shen et al., 1988).

The idea of creating a eutectic microstructure with improved ductility and an increasing number of constituents was advanced further by Jin et al. (2019). By the addition of Cr to a Ni-Fe-Al alloy, for example, $Ni_{44}Fe_{20}Cr_{20}Al_{16}$, a eutectic microstructure composed of FCC and BCC-B2 was found and investigated. The authors reported good mechanical strength and ductility for this material, which they ascribed to the so-called high-entropy effect (Cantor et al., 2004; Chen et al., 2004). Many authors, including the study of Jin et al. postulate a thermodynamic explanation for the improved mechanical properties of those materials (Jin et al., 2019). However, there is currently an ongoing discussion about the fundamental reasoning behind and the validity of the high-entropy-effect, which is discussed in depth in an extensive review by Miracle and Senkov et al. (2017). Independent of the fundamental physical reasoning behind the effect, the class of multicomponent materials offers numerous possibilities for improving and tailoring alloys related to NiAl. This is especially true for eutectic materials with the nominal composition of $Ni_{34.4}Fe_{16.4}Co_{16.4}Cr_{16.4}Al_{16.4}$ (Lu et al., 2014; Gao et al., 2017), which turned out to be composed of FCC and BCC-B2 and was termed an eutectic high-entropy alloy (EHEA). A particularly good combination of high fracture strength and high ductility was reported to be retained even at temperatures of 700°C. The ratio of fracture stress to yield stress was shown to be about 1 order of magnitude larger for this EHEA than for NiAl-based alloys. Beneficial mechanical properties were both found and investigated by several groups (Gao et al., 2017; Nagase et al., 2017), including thermomechanical processing (Wani et al., 2016; Bhattacharjee et al., 2018). Summarizing, we found that FCC/BCC-B2 eutectics with lamellar microstructure were reported for ternary Al-Ni-Fe, quaternary Al-Ni-Fe-Cr, and quinary Al-Ni-Fe-Cr-Co alloys. The quaternary Co-free eutectic alloy could be preferable due to economic, societal, and political reasons (Tkaczyk et al., 2018).

The aim of this study was to take up the early work by Misra and Gibala (1997), Misra et al. (1998), Misra and Gibala (1999), and Misra et al. (2005) and compare the microstructure and properties of ternary FCC/BCC-B2 eutectics to the recent EHEAs reported by Lu et al. (2014), Gao et al. (2017), Jin et al. (2019). The main emphasis is given to the analysis of element partitioning between the two phases of the eutectic, the analysis of the nano- and micro-hardness, and a comparison of mechanical properties determined by three-point bending on as-cast and heat treated specimens.

EXPERIMENTAL METHODS

Sample Preparation

Specimens were produced using a commercial arc-melting setup (AM 500, Edmund Bühler GmbH, Germany) equipped with a suction casting unit. The furnace operates under argon atmosphere after having evacuated the chamber several times to ensure that the residual oxygen partial pressure is small. Samples were produced in 100 g batches from high-purity elements, being molted in the arc-melter and rapidly cooled down, either in the form of buttons or suction cast into cylindrical samples of Ø 10 mm × 150 mm. All samples were remolted three times to ensure chemical homogeneity. The overall chemical composition of the samples produced for this study is given in **Table 1** in at%.

We found that the composition of the ternary eutectic was slightly different from that of $Ni_{50}Fe_{30}Al_{20}$ given by Misra and Gibala (1999). According to our observations, the composition given in Misra's study is slightly off-eutectic and yields BCC-B2 dendrites as a primary phase. For the composition listed in **Table 1** we were able to avoid primary phases and achieve a two-phase FCC/BCC-B2 eutectic microstructure.

The specimens were analyzed in the as-cast state, and in addition, directional solidification at low growth velocity was

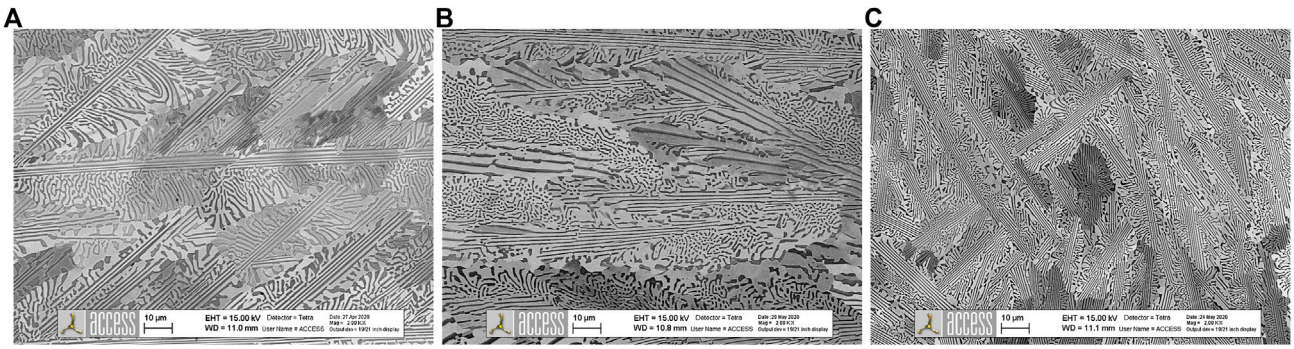

FIGURE 1 | Scanning electron microscopy backscatter-electron micrographs in 2000 X magnification of polished cross sections of as-cast arc-melted cylindrical samples of the $Ni_{48}Fe_{34}Al_{18}$ **(A)**, $Ni_{44}Fe_{20}Cr_{20}Al_{16}$ **(B)**, and $Ni_{34.4}Fe_{16.4}Co_{16.4}Cr_{16.4}Al_{16.4}$ alloys **(C)**.

carried out on the suction cast rods, in order to achieve planar coupled growth and provide equilibrium data about the phase composition. As-cast samples from the $Ni_{44}Fe_{20}Cr_{20}Al_{16}$ and $Ni_{34.4}Fe_{16.4}Co_{16.4}Cr_{16.4}Al_{16.4}$ eutectic alloys were further subjected to different annealing treatments which were carried out in a horizontal tube furnace under an argon (Ar 5.0) atmosphere at 750°C for 24 h and at 950°C for 15 h, respectively.

Directional solidification was carried out in a vertical Bridgman–Stockbarger furnace. This furnace features a heating zone on the top and a liquid metal cooling zone on the bottom, separated from one another by an isolation zone (baffle). The furnace operates under a protective argon (Ar 4.8) atmosphere. The setup was described in another article in more detail (Drevermann et al., 2004). For this study, the samples measuring Ø 8 mm × 150 mm were placed in an alumina tube, directionally molted over about 2/3rd of their length, and subsequently solidified at a velocity of 5 μm/sec over a length of 40 mm. The heater temperatures were set to 1,600°C. Directional solidification was finished by a quenching operation, achieved by a rapid, pneumatically driven movement of the cooler over the sample. The directionally solidified samples were cut along longitudinal and transverse section planes for further analysis. Phase composition measurements were performed on longitudinal sections close to the quenched solidification front.

Electron Microscopy, Energy Dispersive Spectroscopy, and Electron Backscatter Diffraction

The three alloys were analyzed by scanning electron microscopy (SEM) using ZEISS Gemini LEO 1550 and ZEISS Gemini Ultra 55 microscopes equipped with detectors for energy-dispersive spectroscopy (EDS) and electron backscatter diffraction (EBSD), that is, X-MaxN 150 and HKL Nordlys, respectively, being controlled and operated by INCA-software (Oxford Instruments). Sample preparation included conventional embedding, grinding, and polishing steps, with a final step of vibratory polishing (Vibromet, Buehler). EDS measurements were conducted in point-, line-scan, and area modes at 15 kV acceleration voltage and a working distance of 10 mm. EDS line scans were conducted perpendicular to the lamellar microstructure for all three alloys to determine the chemical composition of the individual phases in the two-phase eutectic. Crystallographic information was obtained using EBSD maps. Additionally, phase fractions were determined from backscatter-SEM images (1,024 pixels × 768 pixels) in 2,000× magnification using the open-source software ImageJ (Schneider et al., 2012). For each of the as-cast alloys, three individual pictures were analyzed.

Indentation Experiments

Micro-indentation

Micro-indentation experiments were carried out in the indentation MHT3 from Anton Paar GmbH, Germany. The system allows for a continuous measurement of the penetration depth of a defined indentation tip as a function of the loading force (load–depth profiles). Positioning of the imprints on the sample surface is facilitated by an in-built light microscope. Micro-indentation measurements were carried out using a diamond indentation tip in Vickers geometry, which had been calibrated before to determine the area function. Load-depth curves were recorded in the load-controlled mode using 1,000 mN maximum load, a 2,000 mN/min loading and unloading rate, and a 10-sec pause on maximum load. Indents were placed in the form of a predefined matrix across the surface. The distance between each individual indent was 75 μm, while the diagonal for the imprint under these conditions was about 25 μm. The Oliver–Pharr algorithm was applied to determine the microhardness and Young's modulus from the unloading characteristics. The selected set of parameters

TABLE 2 | Phase fractions in as-cast samples from image analysis and electron backscatter diffraction (EBSD) mapping, in area%.

Phase fraction	Image analysis $Ni_{48}Fe_{34}Al_{18}$	EBSD map $Ni_{48}Fe_{34}Al_{18}$	Image analysis $Ni_{44}Fe_{20}Cr_{20}Al_{16}$	Image analysis $Ni_{34.4}Fe_{16.4}Co_{16.4}Cr_{16.4}Al_{16.4}$
FCC	60	59.2	68	70
BCC-B2	40	40.8	32	30

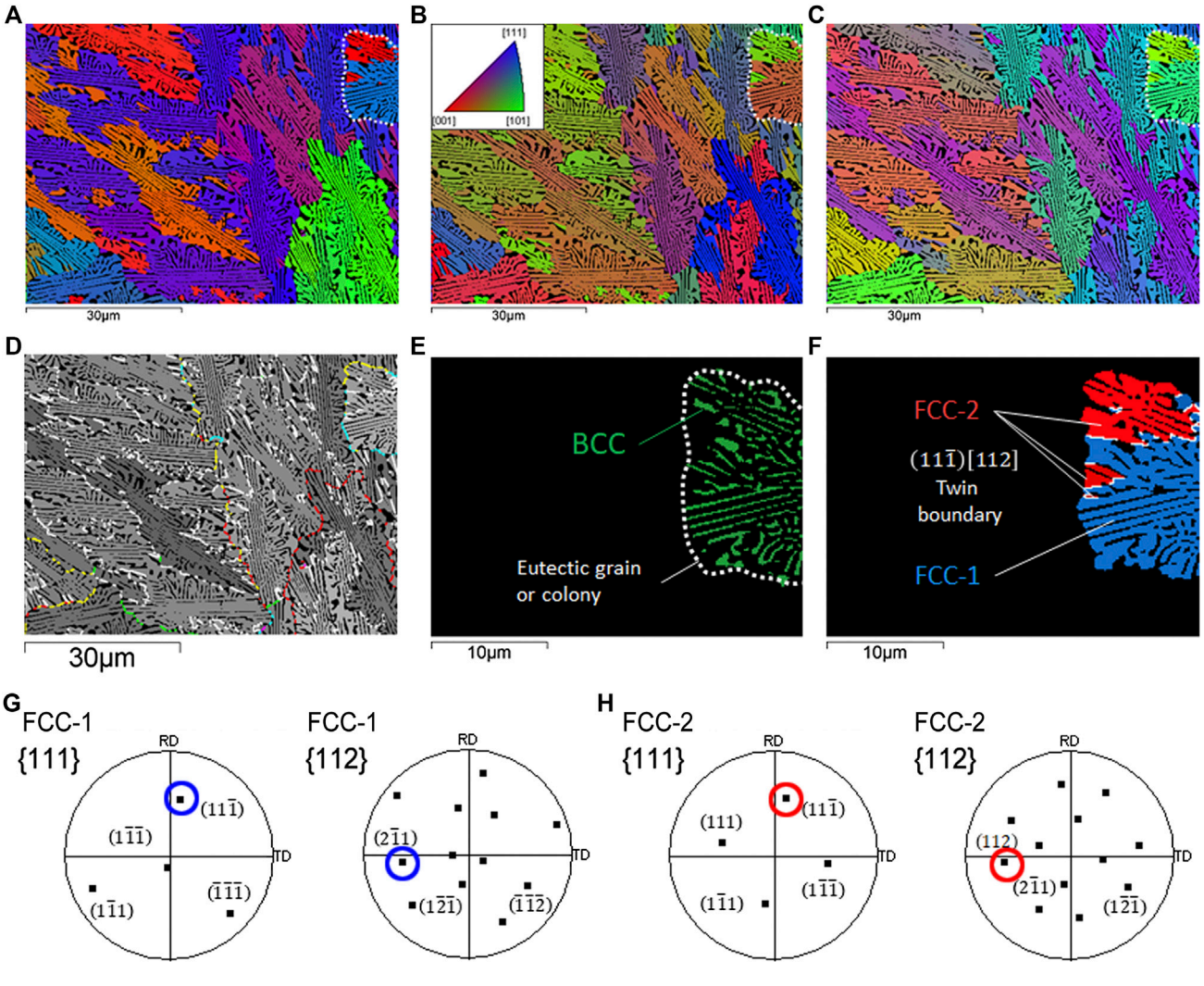

FIGURE 2 | FCC twins in the as-cast quinary eutectic alloy $Ni_{34.4}Fe_{16.4}Co_{16.4}Cr_{16.4}Al_{16.4}$ based on electron backscatter diffraction mapping results: **(A–C)** inverse pole figure coloring of the FCC orientation, **(D)** grain boundaries (colored lines) and twin boundaries (white lines) in the mapping region, **(E, F)** zoom-in view into one eutectic grain which features a single BCC orientation but two distinct FCC orientations separated by $(11\bar{1})[112]$ twin boundaries, **(G, H)** pole figures for {111} and {112} plane families corresponding to FCC-1 and FCC-2, respectively. The common planes/directions are marked with circles.

ensured a sufficiently large size of the imprint encompassing several lamellae, while at the same time being small enough to capture individual grain properties. Additionally, the selected load is in a range for optimal signal-to-noise characteristics in the raw data.

Nano-Indentation

Nano-indentation measurements twere carried out by Anton Paar GmbH, Germany, on a nanohardness tester (NHT). As with the micro-indentation system, a continuous measurement of penetration depth as a function of an applied axial load was recorded. All nano-indentation experiments were carried out using a diamond indentation tip in Berkovich geometry (cube corner). The indentations followed a predefined 11 × 11 matrix across a polished cross section of the specific samples, set up as lines of equi-distant points with a 3-μm distance, which ensures a sufficient spacing so that none of the neighboring indentations are affected by localized strain. Load–depth curves were recorded in load-controlled procedures using 1.0 mN maximum load, a 2.0-mN/min loading and unloading rate, and a 10-sec pause on maximum load. The Oliver–Pharr algorithm was used to determine the nano-hardness and Young's modulus from the unloading characteristics. Surface detection limits were set to 0.1 mN for each measurement. The resulting imprints were comparatively small with around 60 nm depth and 300 nm diagonal width. Most of them were well inside specific phases (lamellae), which allowed for the collection of phase specific indentation curves and properties.

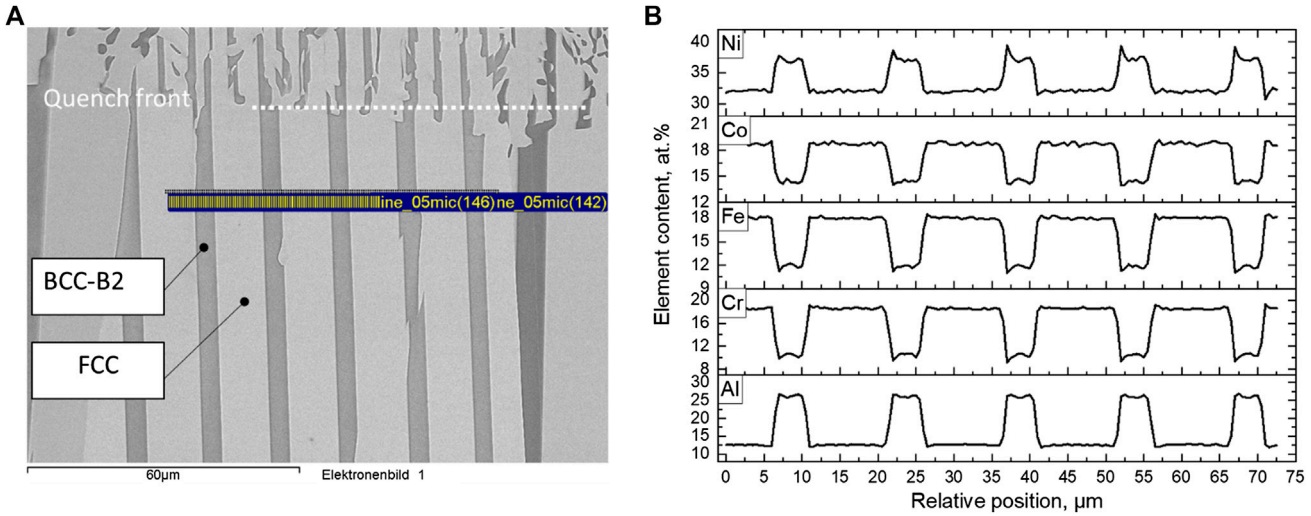

FIGURE 3 | Energy dispersive spectroscopy line scan and measured element partitioning between the two phases of the eutectic exemplarily shown for the quinary alloy $Ni_{34.4}Fe_{16.4}Co_{16.4}Cr_{16.4}Al_{16.4}$ at the quenched front of the directional solidified sample **(A)**. The composition profiles displayed in **(B)** show that both phases are multicomponent: while the BCC-B2 phase is rich in Ni and Al, the FCC phase is rich in Fe and Cr. Co partitions to the FCC phase.

Three-Point Bending Tests

Three-point bending tests were conducted on $Ni_{48}Fe_{34}Al_{18}$, $Ni_{44}Fe_{20}Cr_{20}Al_{16}$, and $Ni_{34.4}Fe_{16.4}Co_{16.4}Cr_{16.4}Al_{16.4}$ specimens using a micromechanical stage SEMtester 1000 EBSD instrument (MTI Instruments Inc., United States). Rectangular specimens measuring 30.0 mm × 5.0 mm× 1.6 mm were cut from suction cast bars and by wire erosion cutting and tested in the as-cast state. Samples from the $Ni_{44}Fe_{20}Cr_{20}Al_{16}$ and $Ni_{34.4}Fe_{16.4}Co_{16.4}Cr_{16.4}Al_{16.4}$ alloys were also tested in heat-treated conditions, for example, at 750°C/24 h and at 950°C/15 h, respectively. Flexural stress-strain curves were calculated following the procedures outlined in the ASTM testing standard (Raheem, 2019).

TABLE 3 | Quantitative energy dispersive spectroscopy-analysis of directionally solidified samples close to the solidification front.

	Eutectic (at%)	BCC-B2		FCC-A1	
		(at%)	Std. dev.	(at%)	Std. dev.
$Ni_{48}Fe_{34}Al_{18}$					
Al	18.9	25.5	0.4	14.8	0.4
Fe	33.9	26.6	0.5	39.7	0.4
Ni	47.2	47.9	0.3	45.5	0.2
$Ni_{44}Fe_{20}Cr_{20}Al_{16}$					
Al	15.7	25.8	0.3	10.8	0.2
Cr	20.5	12.2	0.8	24.4	0.2
Fe	20.4	13.5	0.4	23.7	0.2
Ni	43.4	48.5	1.0	41.1	0.2
$Ni_{34.4}Fe_{16.4}Co_{16.4}Cr_{16.4}Al_{16.4}$					
Al	15.8	26.1	0.4	12.4	0.2
Cr	17.0	10.4	0.5	18.6	0.2
Fe	15.5	11.8	0.3	18.0	0.2
Co	17.5	14.4	0.2	18.8	0.2
Ni	34.1	37.4	0.7	32.1	0.2

RESULTS AND DISCUSSION

Microstructure

As-cast samples from arc-melting and suction casting were prepared metallographically and subsequently analyzed by SEM according to the information given in chapter 2. All samples in the as-cast state showed a two-phase lamellar eutectic microstructure, low porosity, and no cracks. The as-cast microstructure is shown in **Figure 1**. The eutectic has a clear cellular/"dendritic" appearance with a sharply defined lamellar morphology in the trunk center and radially branching lamellae toward the cell sides. The FCC phase (bright) is the majority phase, while the BCC-B2 phase (dark) is the minority phase. While the three alloys look similar, the microstructure is finer in the $Ni_{44}Fe_{20}Cr_{20}Al_{16}$ and $Ni_{34.4}Fe_{16.4}Co_{16.4}Cr_{16.4}Al_{16.4}$ samples, which exhibit smaller lamellar spacings in the trunc region, and a higher fraction of the FCC phase. Lamellar spacings were estimated to be in the range around 1.2–1.4 µm in the $Ni_{44}Fe_{20}Cr_{20}Al_{16}$ and $Ni_{34.4}Fe_{16.4}Co_{16.4}Cr_{16.4}Al_{16.4}$ samples, while being slightly larger in the $Ni_{48}Fe_{34}Al_{18}$ sample, for example, 1.4–2.1 µm, due to faster diffusion owing to higher liquidus and solidus temperatures. The spacing estimation was done by the line intercept method and limited to the core region of eutectic colonies, where the lamellar structure is prominent and clear.

Quantitative phase analysis using the open-source software ImageJ was used to measure phase fractions. For the $Ni_{48}Fe_{34}Al_{18}$ alloy, the phase fractions were also verified by EBSD mapping. The results are listed in **Table 2**. The $Ni_{48}Fe_{34}Al_{18}$ sample consists of roughly 60% FCC, while both the $Ni_{44}Fe_{20}Cr_{20}Al_{16}$ and $Ni_{34.4}Fe_{16.4}Co_{16.4}Cr_{16.4}Al_{16.4}$ alloys show an increase in the FCC fraction to about 70%.

In all samples, we observed that the FCC phase inside the eutectic grains or colonies, which were formed as a result of

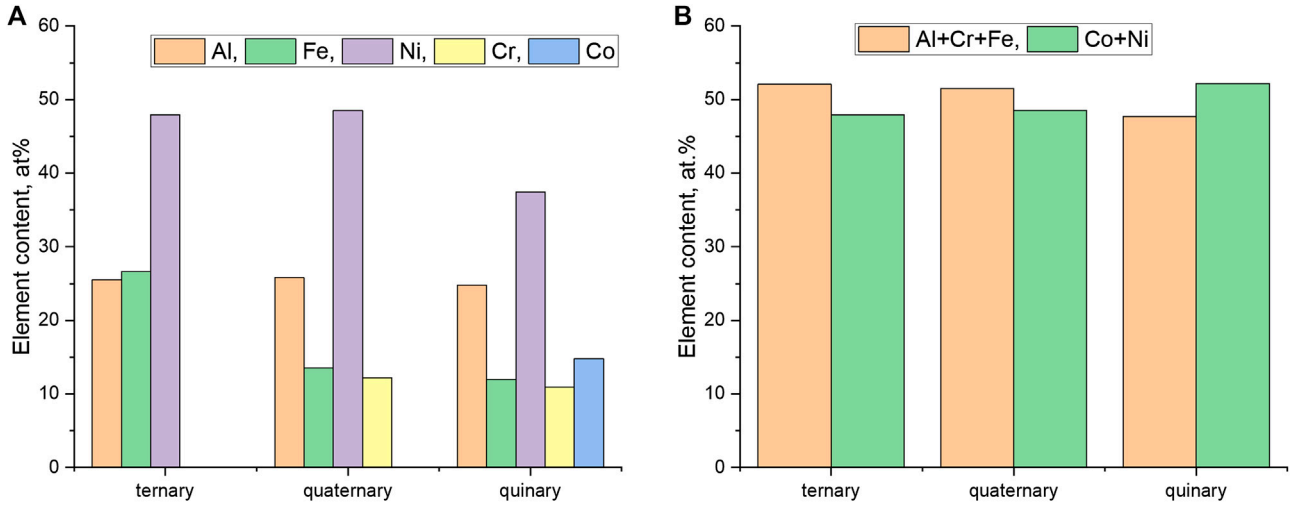

FIGURE 4 | Graphical visualization of the compositional data of the BCC-B2 phase for all three alloys given in **Table 3 (**A**)** and grouping of the elements according to two separate crystallographic sites in the BCC-B2 phase **(B)**.

Mullins–Sekerka instabilities (Plapp and Karma, 2002) in large columnar eutectic grains, displays growth twins. Twinning of the FCC phase is illustrated in **Figure 2** for the as-cast quinary eutectic $Ni_{34.4}Fe_{16.4}Co_{16.4}Cr_{16.4}Al_{16.4}$ based on EBSD mapping results. The orientation of the FCC phase is shown using inverse pole figure coloring for the normal direction (**Figure 2A**), the rolling direction (**Figure 2B**) and the transverse direction (**Figure 2C**). In the upper right corner of these inverse pole figure maps, one grain is outlined with a dotted white line. As seen in **Figure 2D**, the grain is bounded by yellow and turquoise

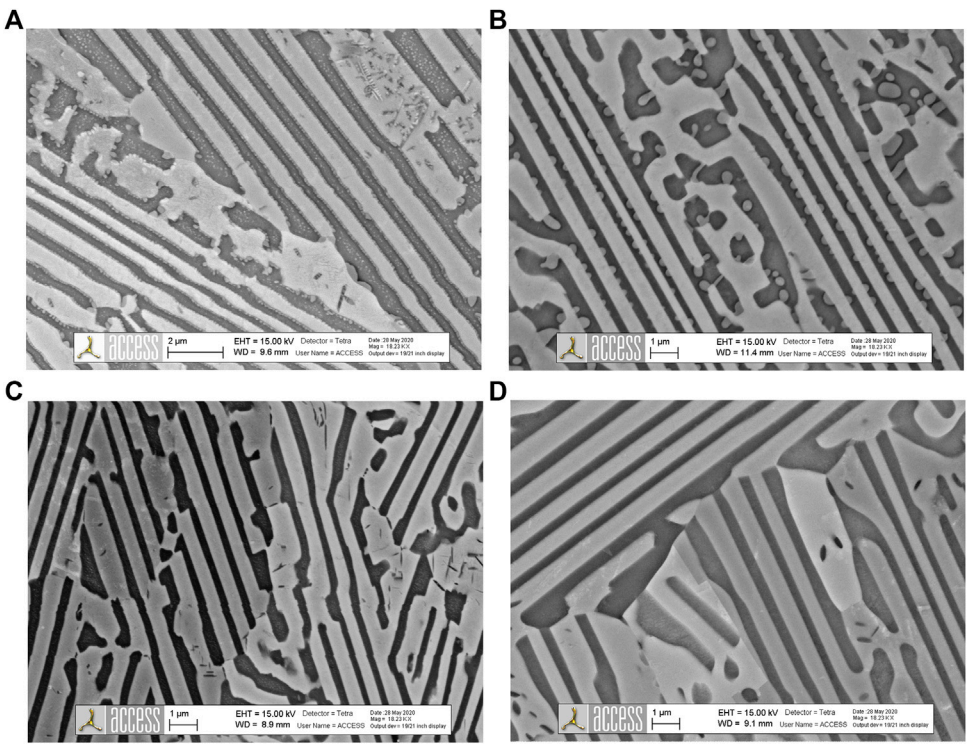

FIGURE 5 | Scanning Electron Microscopy micrographs of samples of the $Ni_{44}Fe_{20}Cr_{20}Al_{16}$ alloy after treatment at 750°C **(A)** and after 950°C **(B)**, the $Ni_{34.4}Fe_{16.4}Co_{16.4}Cr_{16.4}Al_{16.4}$ samples after 750°C **(C)** and after 950°C **(D)**.

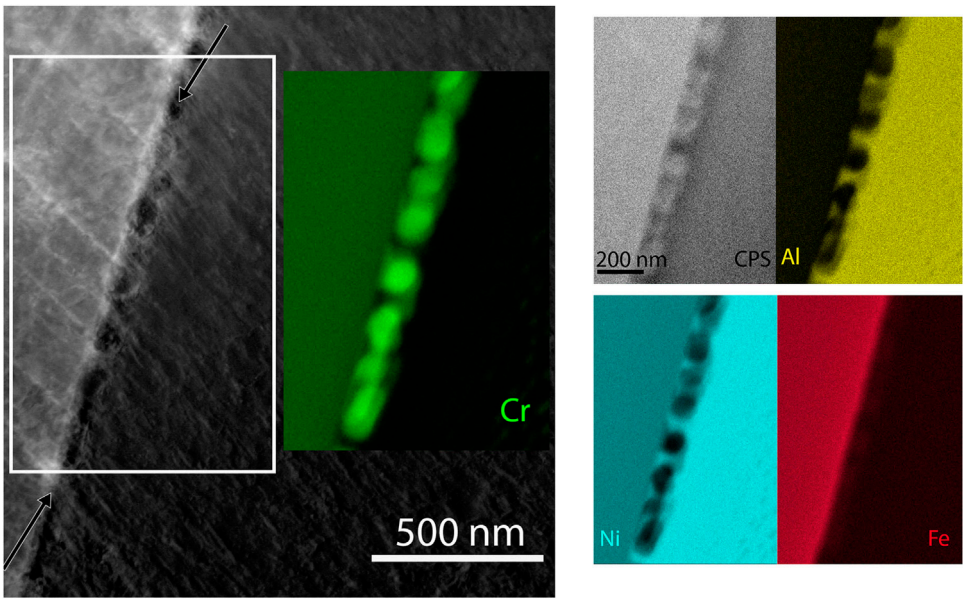

FIGURE 6 | Scanning transmission electron microscopy image in high-angle annular dark-field mode and transmission electron microscopy-energy dispersive spectroscopy map of a characteristic interface region between the FCC and BCC-B2 lamellae of a sample of the directionally solidified $Ni_{44}Fe_{20}Cr_{20}Al_{16}$ alloy.

borders toward neighboring grains, but internally it contains distinct regions separated by white boundaries. In fact, the white boundaries are twin boundaries. A zoom-in view of the FCC twin boundaries in this grain is provided in **Figure 2F**, while **Figure 2E** shows that a single BCC orientation prevails in the eutectic grain. We identified the twinning plane and direction between the two regions FCC-1 and FCC-2 to be $(11\bar{1})[112]$. The corresponding pole figures for {111} and {112} plane families are presented in **Figure 2G** for FCC-1 and in **Figure 2H** for FCC-2. The twinning system is characteristic for FCC growth twins. We observed a remarkably high amount of twin boundaries in the mapping region (compare **Figure 2D**). More details about twinning in this EHEA will be presented in an upcoming publication.

Directional Solidification

Directionally solidified samples with planar growth front and coupled eutectic growth patterns with large lamellae size were used to accurately measure the phase composition using EDS line scans across several lamellae. A step size of 0.5 µm was used. EDS analysis has been shown previously to be an adequate method for elemental quantification (Newbury and Ritchie, 2013). Line scans have been conducted a few below the quenched front in the directionally solidified area. We present the data from a single line scan for each of the three alloys, containing about 150 single-point spectra. **Figure 3** exemplarily shows a line scan and the measured element distribution across the FCC and BCC-B2 lamellae from the alloy $Ni_{34.4}Fe_{16.4}Co_{16.4}Cr_{16.4}Al_{16.4}$. **Table 3** contains the phase composition data for all three investigated alloys measured by the same procedure.

The ordered BCC-B2 phase in all three alloys is derived from the ordered compound NiAl, which is known to crystallize in a CsCl-type structure (space-group 221, Pearson symbol cP2). From the data presented in **Table 3** and **Figure 4** it is deduced that an approximate composition of $(Ni, Co)_{50}$ $(Al, Cr, Fe)_{50}$ is valid for the BCC-B2 phase, with Co occupying Ni sites, while Fe and Cr prefer the Al-sites. If elements Al, Cr, and Fe are grouped together and a second group of Ni, and Co is established, the summation of the data in **Table 3** leads to an equally distributed elemental composition within the two groups (see **Figure 4B**). These findings are consistent with literature data: Duncan et al. used atom probe field ion microscopy to show Fe preferentially occupying Al sites in NiAl (Duncan et al., 1994). Other studies found Cr clearly preferring Al sites (Medvedeva et al., 1998), while Co is found on the Ni sites, which is to be expected from the chemical similarity of the two elements (Li et al., 2016). It has to be noted that all these studies were conducted for very low concentrations of the substituting elements (Jones, 2003). This consideration has been conducted only for the ordered BCC-B2 phase since in the FCC phase all the atoms share all sites statistically.

To our knowledge, single-phase specific compositional data for the $Ni_{48}Fe_{34}Al_{18}$ and $Ni_{44}Fe_{20}Cr_{20}Al_{16}$ eutectics have not been published so far. For the $Ni_{34.4}Fe_{16.4}Co_{16.4}Cr_{16.4}Al_{16.4}$ alloy, Gao et al. determined elemental distributions for single phase lamellae with atom probe tomography that deviate significantly from our results (Gao et al., 2017). We believe this deviation can be attributed to both the atom probe tomography method of quantification in Gaos's study which is sensitive to local fluctuations and a different method of preparation of the specimens. Wang et al. published phase-specific compositional data obtained by SEM-EDS for the eutectic $Ni_{34.4}Fe_{16.4}Co_{16.4}Cr_{16.4}Al_{16.4}$ which exhibits similar results to this study (Wang et al., 2020).

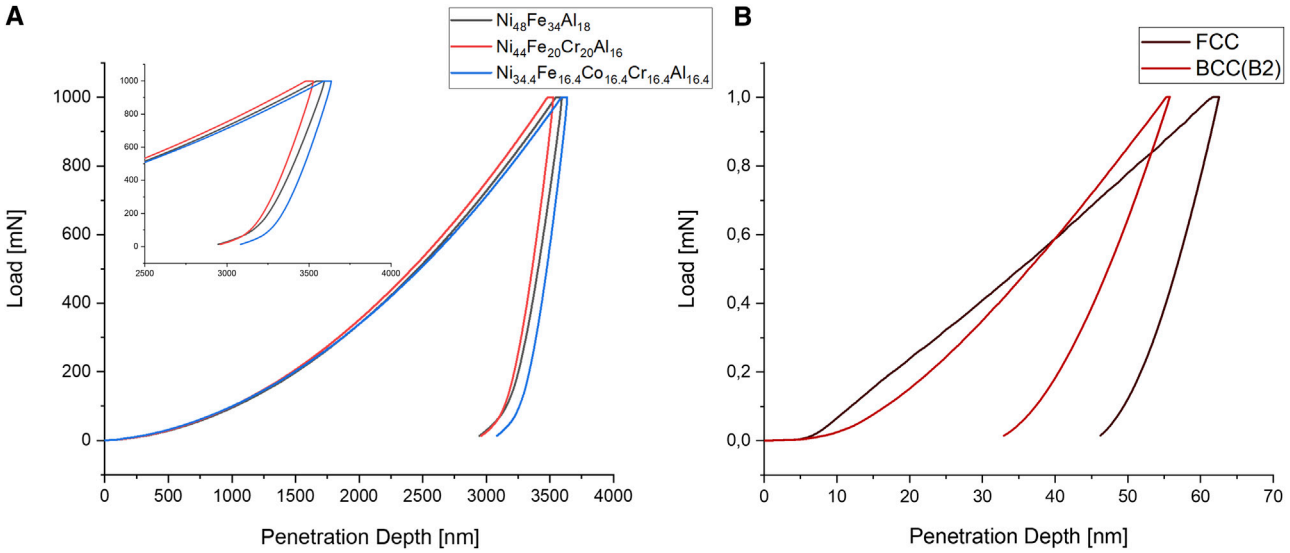

FIGURE 7 | Mean load-depth profiles of the three alloys from micro-indentation experiments **(A)** and mean load-depth profiles of nano-indentation probing of the individual phases of the $Ni_{44}Fe_{20}Cr_{20}Al_{16}$ alloy **(B)**.

As can be deduced from these results, the BCC-B2 phase is rich in Al and Ni, while the FCC phase is rich in Fe, and where applicable Cr, and Co. While this finding holds true for all the analyzed regions in this study, we want to emphasize that always all the elements are present in each individual phase in significant amounts (>10 at%), which is an important finding in regard to the discussion of a potential high-entropy effect.

Isothermal Heat Treatment

In order to assess the potential for altering the mechanical properties of the eutectic alloys, two different heat treatments were conducted for the $Ni_{44}Fe_{20}Cr_{20}Al_{16}$ and $Ni_{34.4}Fe_{16.4}Co_{16.4}Cr_{16.4}Al_{16.4}$ samples, that is, 750 °C for 24 h and 950 °C for 15 h. In this case, the $Ni_{48}Fe_{34}Al_{18}$ alloy was not included. In the SEM analysis of the heat-treated $Ni_{44}Fe_{20}Cr_{20}Al_{16}$ samples we observed needle-like precipitation in the FCC phase and a new Cr-rich phase. The phase boundaries appear fully and densely covered with small particles of this new phase. As shown in **Figure 5A** for samples heat-treated at 750°C and **Figure 5B** for samples heat-treated at 950°C the thickness of this layer increases with temperature and time, a result of coarsening. Along with coarsening at 950°C, the Cr-rich particle layer no longer fully covers the interface. The nature of the Cr-rich phase could not be identified unambiguously, but we expect it to be a Cr-rich BCC-A2 phase. A potential σ-phase could be excluded by EBSD. Interestingly, as revealed by transmission electron microscopy analysis, we found that this Cr-rich layer was already present for an as-cast sample of the $Ni_{44}Fe_{20}Cr_{20}Al_{16}$ alloy. This is shown in **Figure 6**. We attribute this behavior to the relatively large Cr content of the $Ni_{44}Fe_{20}Cr_{20}Al_{16}$ eutectic alloy, which is 20.5 vs. 17.0 at% for the $Ni_{34.4}Fe_{16.4}Co_{16.4}Cr_{16.4}Al_{16.4}$. In contrast, the $Ni_{34.4}Fe_{16.4}Co_{16.4}Cr_{16.4}Al_{16.4}$ alloy did not exhibit a Cr-rich layer at the lamellar interface after the same heat treatments at 750°C (**Figure 5C**) and 950°C (**Figure 5D**). We observed needle-like precipitates in the FCC-phase of the $Ni_{34.4}Fe_{16.4}Co_{16.4}Cr_{16.4}Al_{16.4}$ samples, which also showed a tendency toward coarsening at 950°C.

In summary, applying the afore-mentioned heat treatments to the $Ni_{44}Fe_{20}Cr_{20}Al_{16}$ and $Ni_{34.4}Fe_{16.4}Co_{16.4}Cr_{16.4}Al_{16.4}$ samples revealed significant differences between the two alloys, which will impact the mechanical behavior in the three-point bending experiments shown in *Three-Point Bending Experiments*. The appearance and coarsening of the Cr-rich layer that covers the lamellar interfaces of the $Ni_{44}Fe_{20}Cr_{20}Al_{16}$ samples demonstrated the necessity for a heat treatment that is adapted to this system, and the 950°C treatment may constitute a starting point for further research.

TABLE 4 | Instrumented hardness (H_{IT}) and Young's modulus (E_{IT}) for the three alloys as determined by micro-indentation experiments and for the individual phases of the Ni44Fe20Cr20Al16 alloy as determined by nano-indentation.

	H_{IT} (MPa)	Std. dev.	E_{IT} (GPa)	Std. dev	N
Micro-indentation alloy					
$Ni_{48}Fe_{34}Al_{18}$	3472.1	67.9	158.0	6.7	52
$Ni_{44}Fe_{20}Cr_{20}Al_{16}$	3537.5	93.7	188.1	7.6	46
$Ni_{34.4}Fe_{16.4}Co_{16.4}Cr_{16.4}Al_{16.4}$	3310.1	71.2	185.9	8.5	44
Nano-indentation phase					
$Ni_{44}Fe_{20}Cr_{20}Al_{16}$-FCC	4721.9	215.5	190.1	9.1	49
$Ni_{44}Fe_{20}Cr_{20}Al_{16}$-BCC-B2	6016.8	472.6	144.4	10.2	30

Indentation

Selected samples were subjected to indentation experiments using the depth-sensing indentation technique, as outlined in *Indentation Experiments*. Thereby, synchronously load and depth were recorded and plotted as a load–depth profile. With a known indenter shape, the specimen's hardness and Young's

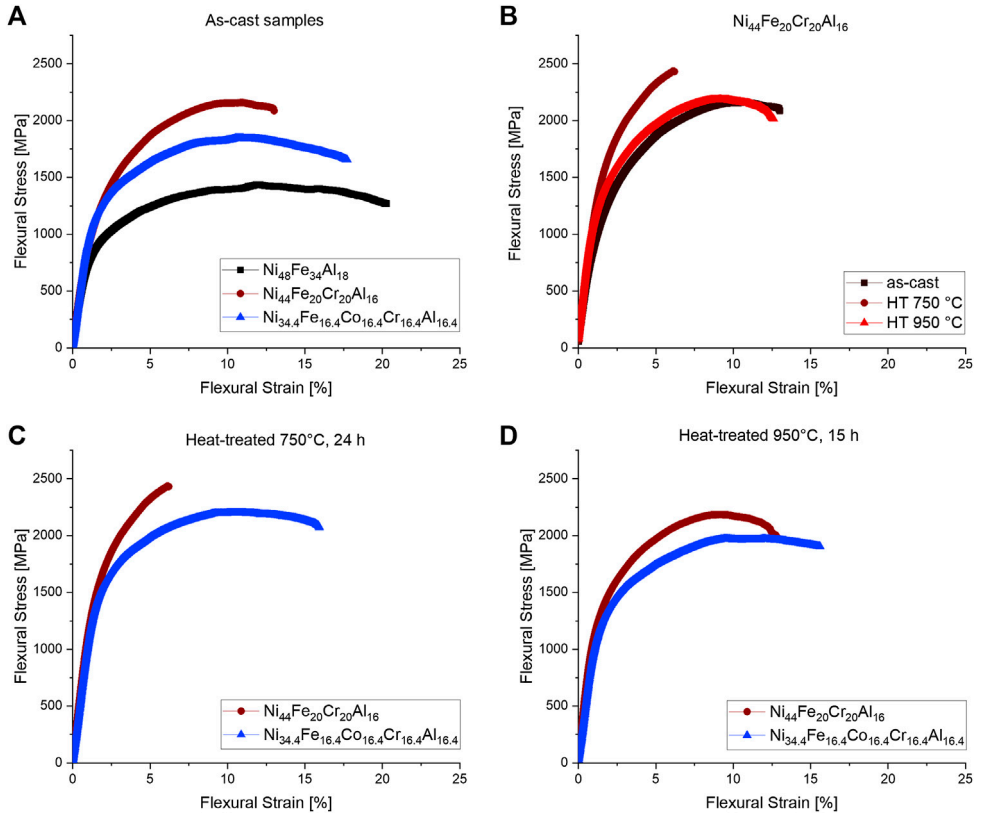

FIGURE 8 | Comparison of results from three point bending experiments of as-cast alloys **(A)**, the $Ni_{44}Fe_{20}Cr_{20}Al_{16}$ alloy after different treatments **(B)**, both the $Ni_{44}Fe_{20}Cr_{20}Al_{16}$ and $Ni_{34.4}Fe_{16.4}Co_{16.4}Cr_{16.4}Al_{16.4}$ alloys after heat treatment at 750 °C for 24 h **(C)**, and after heat treatment at 950 °C for 15 h **(D)**.

modulus were calculated following to the procedure laid out by Oliver and Pharr (1992). The method relies on fitting a power law to the unloading part of the load–depth profile and works well for the comparison of specimens.

Micro-Indentation

The aim of these experiments was the determination of Young's modulus and microhardness for as-cast eutectic samples. The size of the indentation tip always covered several lamellae within a grain. Around 50 individual indents were placed on eutectic grains to ensure sufficient statistics. As can be seen from the data presented in **Table 4** and **Figure 7A**, both the $Ni_{44}Fe_{20}Cr_{20}Al_{16}$ and $Ni_{34.4}Fe_{16.4}Co_{16.4}Cr_{16.4}Al_{16.4}$ alloys showed nearly identical elastic behavior as demonstrated by the instrumented Young modulus. The $Ni_{48}Fe_{34}Al_{18}$ system was found to exhibit a significantly smaller elastic constant. As for the microhardness, all three samples led to similar results, while the $Ni_{44}Fe_{20}Cr_{20}Al_{16}$ alloy was observed to show the highest values, closely followed by the $Ni_{48}Fe_{34}Al_{18}$ within one standard deviation. For the $Ni_{34.4}Fe_{16.4}Co_{16.4}Cr_{16.4}Al_{16.4}$ sample, a statistically significantly smaller hardness was recorded. The local response of the materials did not vary significantly as is demonstrated by the relatively low standard deviations in **Table 4**. In a separate set of experiments, numerous indentations have been placed selectively in different grains. The analysis of that experiment did not give any indication of orientation anisotropy.

The microhardness values for all eutectics in the as-cast state range around 350 H_v, which compares well to the hardness values reported for $Al_xCoCrFeNi$ alloys by Wang et al. (2012), for x ranging from 0.65 to 0.75. This is in agreement with the dual-phase nature of the material which for the given molar ratio x, contains about 60–70% FCC phase.

Nano-Indentation

In contrast to the micro-indentation experiments, the aim of the nano-indentation study was the determination of single-phase properties for the individual FCC and BCC-B2 lamellae. In this part of the study, we focused exclusively on the $Ni_{44}Fe_{20}Cr_{20}Al_{16}$ alloy as a representative system. To ensure a fully single-phase result, we conducted these experiments through cross sections of directionally solidified samples for which lamellar spacings of several micrometers were obtained, much larger than for the as-cast samples. The indentations were positioned so that the actual indent was probing the lamellae in growth direction. Because of the high symmetry of the two phases, we did not expect strong anisotropy of the phase-specific mechanical properties. Further investigation into the anisotropic behavior is beyond the scope of this study, but may be conducted in future research.

The indents were positioned in a quadratic 11 × 11 matrix of equidistant points across the samples, which ensured that five lamellae of each phase were covered within that area. The distance of each point is 3 μm both in the *x* and *y* directions, which is sufficiently large compared to the approximate 0.3–0.5 μm diameter of the indents. This ensures that the mechanical properties determined by the indentation are not influenced by the plastic deformation of neighboring indentations.

The resulting 121 load-controlled single measurements were transformed into load–depth curves and subsequently grouped into two sets of phase-specific measurements according to their position on the microscopic image and the mechanical data. Since the BCC-B2 phase is significantly less deformable than the FCC phase, the phases were identified unambiguously. Only a small number of measurements could not be clearly assigned to one of the two phases, probably due to the proximity to a phase boundary, and they were subsequently removed from the dataset. The number of indentations in the FCC group vs. the BCC-B2 group matches roughly the phase fractions determined by image analysis and EBSD, so the phase assignment during nano-indentation analysis agrees with findings presented in previous chapters (see *Results and Discussion* and *Microstructure*). Each phase specific group of indentation curves was transformed into a mean-curve to visualize and represent the data concisely in **Figure 7B**. As expected, the FCC phase is more ductile, that is, leads to much deeper penetration depths for the same applied maximum load, and also shows an earlier onset of plastic deformation already in the loading curve. Despite the visual appearance, the two unloading curves are not perfectly parallel, which means that the elastic properties for both phases are significantly different. We determined the Young modulus of the ductile FCC phase is significantly larger than the corresponding value for the BCC-B2 phase. The experiments were so far not repeated for the other alloys as the focus of this part of the study was only on the acquisition and comparison of phase-specific data.

It has to be noted that the results for hardness from nano-indentation are not easily comparable to the corresponding results from micro-indentation. As is visible in **Table 4** the apparent hardness as of nano-indentation is significantly higher for both single phases than for the eutectic grains as obtained from micro-indentation. Both values can however not be compared directly, because of the indentation size effect, a phenomenon that is well known and described in the literature (Qian et al., 2005). The magnitude of the indentation size effect is dependent on the maximum load applied and thus most pronounced for nano-indentation experiments. The results from both nano- and micro-indentation are presented in **Figure 7** and summarized in **Table 4**.

Three Point Bending Experiments

In order to investigate the influence of composition and potentially reveal high-entropy effects on the mechanical properties of the alloys, we conducted a set of deformation experiments in three-point bending configuration. The results are shown in **Figure 8** and summarized in **Table 5**.

As is shown in **Figure 8A**, the $Ni_{48}Fe_{34}Al_{18}$ sample was found to be less strong and more ductile than the $Ni_{44}Fe_{20}Cr_{20}Al_{16}$ and $Ni_{34.4}Fe_{16.4}Co_{16.4}Cr_{16.4}Al_{16.4}$ samples in the as-cast state. The coarser lamellar structure of the $Ni_{48}Fe_{34}Al_{18}$ alloy contributes to this behavior. Additionally, we never observed any kind of nanometer-sized precipitation for the $Ni_{48}Fe_{34}Al_{18}$ alloy as opposed to the $Ni_{44}Fe_{20}Cr_{20}Al_{16}$ samples, which also may influence the mechanical response and higher ductility. In fact, during the bending experiments, only the $Ni_{48}Fe_{34}Al_{18}$ samples did not fracture during the measurements, as opposed to the other two samples for which all of the specimens fractured at some earlier point. The maximum flexural strain of 23% for the as-cast $Ni_{48}Fe_{34}Al_{18}$ alloy given in **Table 5** represents the limit of the measurement setup. In agreement with micro-indentation data, the $Ni_{48}Fe_{34}Al_{18}$ system also shows the lowest elastic constant. Remarkably, upon introduction of Cr and Co, the $Ni_{44}Fe_{20}Cr_{20}Al_{16}$ and $Ni_{34.4}Fe_{16.4}Co_{16.4}Cr_{16.4}Al_{16.4}$ eutectic samples showed a higher Young modulus, yield, and ultimate strength, and most importantly a more pronounced work hardening, while all these effects were found to be in a similar range for the $Ni_{44}Fe_{20}Cr_{20}Al_{16}$ and $Ni_{34.4}Fe_{16.4}Co_{16.4}Cr_{16.4}Al_{16.4}$ samples. The work hardening may indeed relate to the high-entropy effect. This finding is even more notable when viewed in the context of the results from quantitative phase analysis in which it was determined that the phase fractions expressed as ratio between FCC and the less ductile BCC-B2 phases went from roughly 60:40 for the $Ni_{48}Fe_{34}Al_{18}$ to roughly 70:30 for the $Ni_{44}Fe_{20}Cr_{20}Al_{16}$ and $Ni_{34.4}Fe_{16.4}Co_{16.4}Cr_{16.4}Al_{16.4}$ samples. The $Ni_{44}Fe_{20}Cr_{20}Al_{16}$

TABLE 5 | Summary of the mechanical data as obtained from three point bending experiments conducted on various bar samples of the three alloys.

	Young's Modulus (GPa)	Yield strength (MPa)	Ultimate strength (MPa)	Flexural strain at fracture (%)
$Ni_{48}Fe_{34}Al_{18}$				
As-cast	76	696	1,394	23.0
$Ni_{44}Fe_{20}Cr_{20}Al_{16}$				
As-cast	96	767	2,157	12.6
Heat-treated 750°C	114	1,181	2,431	6.2
Heat-treated 950°C	123	1,094	2,183	12.5
$Ni_{34.4}Fe_{16.4}Co_{16.4}Cr_{16.4}Al_{16.4}$				
As-cast	94	893	1,842	18.9
Heat-treated 750°C	105	1,291	2,199	16.1
Heat-treated 950°C	104	1,021	1,968	15.6

samples showed higher strength at the expense of ductility than the $Ni_{34.4}Fe_{16.4}Co_{16.4}Cr_{16.4}Al_{16.4}$ samples, which may relate to the presence of the layer of Cr-rich precipitates along the interfacial boundaries.

For the heat-treated samples, we recorded significant changes in the mechanical response as is to be expected considering the microstructural changes discussed in *Indentation*. This was most strongly observed in the $Ni_{44}Fe_{20}Cr_{20}Al_{16}$ alloy (see **Figures 8B,C**), which showed embrittlement after treatment at 750°C, that is, an increase in yield strength and UTS, and a flexural strain at fracture of only 6.2%, the lowest value in the series. We believe the presence of the layer of Cr-rich precipitates along the interfacial boundaries as shown in **Figure 5A** to be responsible for this effect. Upon heat treatment at 950°C, those precipitates were shown do undergo coarsening, leading to fewer but larger precipitates, and most of the phase boundaries were shown to be uncovered (see **Figure 5B**). This finding explains the recovery of the flexural strain while most of the strength is retained (see **Figures 8B,D**). Additionally, for all analyzed samples, a higher elastic constant was determined after heat treatment. The heat-treated samples of the $Ni_{34.4}Fe_{16.4}Co_{16.4}Cr_{16.4}Al_{16.4}$ alloy (see **Figures 8C,D**) behaved similarly in terms of Young's modulus, yield, and UTS points but were shown to be more ductile than the $Ni_{44}Fe_{20}Cr_{20}Al_{16}$ samples. The $Ni_{34.4}Fe_{16.4}Co_{16.4}Cr_{16.4}Al_{16.4}$ sample did not experience a loss of ductility after heat treatment at 750°C, which is consistent with the microstructural analysis (see **Figure 5C**). The increase in yield and ultimate strength for all the heat-treated samples in **Table 5** is related to precipitation hardening due to the formation of small crystallites, as depicted in **Figure 5**.

From these results, we conclude that an annealing heat treatment at 950°C for 6–15 h is a good range for both the $Ni_{44}Fe_{20}Cr_{20}Al_{16}$ and $Ni_{34.4}Fe_{16.4}Co_{16.4}Cr_{16.4}Al_{16.4}$ alloys. Yet, the microstructural findings suggest that care must be taken during thermal treatment in order to avoid detrimental formation of interfacial layers.

CONCLUSIONS

In this study, we investigated three eutectic alloys composed of FCC and BCC-B2 lamellae with ternary ($Ni_{48}Fe_{34}Al_{18}$), ($Ni_{34.4}Fe_{16.4}Co_{16.4}Cr_{16.4}Al_{16.4}$) composition. The main results are as follows:

- All three alloys exhibit a lamellar eutectic microstructure and similar morphology. They consist predominantly of an FCC phase and a smaller but significant fraction of a BCC-B2 phase. The phase fraction of FCC increases when moving $Ni_{34.4}Fe_{16.4}Co_{16.4}Cr_{16.4}Al_{16.4}$ alloy.
- Remarkably, all the elements that make up the three alloys are present in both of the phases, so indeed the $Ni_{44}Fe_{20}Cr_{20}Al_{16}$ and $Ni_{34.4}Fe_{16.4}Co_{16.4}Cr_{16.4}Al_{16.4}$ alloys may be regarded as high-entropy alloys.
- For all three alloys the FCC-phase contains more Fe, Cr, and Co respectively, while the BCC-B2 phase is rich in both Al and Ni, which demonstrates its relationship to the compound NiAl.
- Although it had the highest content of the BCC-B2 phase, the $Ni_{48}Fe_{34}Al_{18}$ alloy showed the least strength and the highest ductility while the effect of work hardening to flexural strength is limited.
- Additions of Cr and Co led to an increase in Young's modulus as measured by three-point bending. Additionally, a higher yield strength and ultimate strength values were recorded for the $Ni_{44}Fe_{20}Cr_{20}Al_{16}$ and $Ni_{34.4}Fe_{16.4}Co_{16.4}Cr_{16.4}Al_{16.4}$ eutectics than for the $Ni_{48}Fe_{34}Al_{18}$. Both alloys show significant work hardening, which may be seen as a high-entropy effect.
- Different heat treatments increase the strength of the $Ni_{44}Fe_{20}Cr_{20}Al_{16}$ and $Ni_{34.4}Fe_{16.4}Co_{16.4}Cr_{16.4}Al_{16.4}$ alloys at the expense of ductility. Embrittlement was recorded for the $Ni_{44}Fe_{20}Cr_{20}Al_{16}$ alloy after heat treatment at 750°C for 24 h, which could be attributed to a covering layer of Cr-rich precipitates along the interfacial boundaries. The annealing treatment at 950°C for 15 h was identified as a feasible option to improve the overall mechanical strength of the two high-entropy alloys.

To summarize, we saw a demonstrable improvement of mechanical properties and, most importantly, the work-hardening behavior when moving from the $Ni_{48}Fe_{34}Al_{18}$ to the $Ni_{44}Fe_{20}Cr_{20}Al_{16}$ and $Ni_{34.4}Fe_{16.4}Co_{16.4}Cr_{16.4}Al_{16.4}$ alloys, that is, upon the introduction of Cr and Co. From todays perspective, the $Ni_{44}Fe_{20}Cr_{20}Al_{16}$ Co-free alloy may constitute further advantages, such as corrosion resistance due to it's high Cr content, or societal and economic considerations that favor Co-free materials (Tkaczyk et al., 2018). When comparing the $Ni_{44}Fe_{20}Cr_{20}Al_{16}$ and $Ni_{34.4}Fe_{16.4}Co_{16.4}Cr_{16.4}Al_{16.4}$ alloys, attention has to be given to the covering layer of Cr-rich precipitates along the interfacial boundaries, which appears in quaternary samples after annealing at 750°C. This effect could be mitigated by applying heat treatment at 950°C. Under these conditions, the flexural yield strength reached 1,094 MPa and 12.5% flexural strain at fracture for the quaternary and 1,021 MPa and 15.6% flexural strain at fracture for the $Ni_{34.4}Fe_{16.4}Co_{16.4}Cr_{16.4}Al_{16.4}$ samples.

This study concludes that both the $Ni_{44}Fe_{20}Cr_{20}Al_{16}$ and $Ni_{34.4}Fe_{16.4}Co_{16.4}Cr_{16.4}Al_{16.4}$ eutectic alloys proposed by Jin and Gao (Gao et al., 2017; Jin et al., 2019) can be understood as a continuation of the earlier work by Misra and Gibala (Misra and Gibala, 1997; Misra and Gibala, 1999; Misra et al., 1998). The eutectic alloys provide good strength, work hardening ability, and the potential to further improve upon those properties by heat treatment. Depending on the targeted use, the room-temperature ductility of the $Ni_{44}Fe_{20}Cr_{20}Al_{16}$ eutectic may be sufficient such that the benefits related to the Co-free composition can be garnered. Further research on the processability of the two alloys are expected to lead to technical applications.

DATA AVAILABILITY STATEMENT

The raw data supporting the conclusions of this article will be made available by the authors, without undue reservation.

AUTHOR CONTRIBUTIONS

DR: writing of the manuscript, analysis of all experimental results, and scientific coordination; NN: arc melting and suction casting of samples; OS: SEM analysis and three-point bending experiments of selected samples; FS, PP, and DM: nano-indentation measurements and analysis; AG: Bridgman solidification and microstructure analysis of samples from the $Ni_{34.4}Fe_{16.4}Co_{16.4}Cr_{16.4}Al_{16.4}$ alloy, work performed as visiting scientist at Access e.V.; UH: design of the study, EBSD analysis of selected samples, scientific supervision, and revision of the manuscript.

FUNDING

This study was conducted within the publicly funded research framework INNO-KOM (Project EVERAM: 49VF180027). Funding by the German Ministry of Economics and Energy (BMWi) is gratefully acknowledged.

ACKNOWLEDGMENTS

The authors would like to thank Klemens Kelm and Frederic Kreps (Institut für Werkstoff-Forschung, DLR, Köln, Germany) for the TEM analysis and interpretation, and Christoph Pickmann for the conduction and technical supervision of directional solidification experiments in the Bridgman furnace.

REFERENCES

Bei, H., and George, E. P. (2005). Microstructures and mechanical properties of a directionally solidified NiAl-Mo eutectic alloy. *Acta Mater.* 53, 69. doi:10.1016/j.actamat.2004.09.003

Bhattacharjee, T., Wani, I. S., Sheikh, S., Clark, I. T., Okawa, T., Guo, S., et al. (2018). Simultaneous strength-ductility enhancement of a nano-lamellar $AlCoCrFeNi_{2.1}$ eutectic high entropy alloy by cryo-rolling and annealing. *Sci. Rep.* 8, 3276. doi:10.1038/s41598-018-21385-y

Cantor, B., Chang, I. T. H., Knight, P., and Vincent, A. J. B. (2004). Microstructural development in equiatomic multicomponent alloys. *Mater. Sci. Eng. A* 375–377, 213–218. doi:10.1016/j.msea.2003.10.257

Chen, T. K., Shun, T. T., Yeh, J. W., and Wong, M. S. (2004). Nanostructured nitride films of multi-element high-entropy alloys by reactive DC sputtering. *Surf. Coating. Technol.* 188–189, 193–200. doi:10.1016/j.surfcoat.2004.08.023

Drevermann, A., Pickmann, C., Sturz, L., and Zimmermann, G. (2004). "Observation and control of solidification processes by ultrasonic pulse-echo technique," in Proceedings of the IEEE ultrasonics symposium, Montreal, Quebec, Canada, September, 2004, Vol. 1, 537–540. (IEEE: New York, NY, USA). Available at: https://www.researchgate.net/publication/4134555 (Accessed September, 2004) [abstract].

Duncan, A. J., Kaufman, M. J., Liu, C. T., and Miller, M. K. (1994). Site occupation of iron in intermetallic NiAl. *Appl. Surf. Sci.* 76–77, 155–159. doi:10.1016/0169-4332(94)90336-0

Gao, X., Lu, Y., Zhang, B., Liang, N., Wu, G., Sha, G., et al. (2017). Microstructural origins of high strength and high ductility in an $AlCoCrFeNi_{2.1}$ eutectic high-entropy alloy. *Acta Mater.* 141, 59–66. doi:10.1016/J.ACTAMAT.2017.07.041

Hu, L., Zhang, G., Hu, W., Gottstein, G., Bogner, S., and Bührig-Polaczek, A. (2013). Tensile creep of directionally solidified NiAl-9Mo in situ composites. *Acta Mater.* 61, 7155–7165. doi:10.1016/j.actamat.2013.08.017

Jin, X., Bi, J., Zhang, L., Zhou, Y., Du, X., Liang, Y., et al. (2019). A new $CrFeNi_2Al$ eutectic high entropy alloy system with excellent mechanical properties. *J. Alloys Compd.* 770, 655. doi:10.1016/j.jallcom.2018.08.176

Jones, I. P. (2003). Determining the locations of chemical species in ordered compounds: ALCHEMI. *Adv. Imag. Electron. Phys.* 125, 63. doi:10.1016/S1076-5670(02)80015-5

Kurdjumow, G., and Sachs, G. (1930). Über den Mechanismus der Stahlhärtung. *Z. Phys.* 64, 325–343. doi:10.1007/BF01397346

Li, H., Cao, Y., Zhou, S., Zhu, P., and Zhu, J. (2016). Site preferences and effects of X (X = Mn, Fe, Co, Cu) on the properties of NiAl: a first-principles study. *Mod. Phys. Lett. B* 30, 1650129–1650133. doi:10.1142/S0217984916501335

Liu, C. T. (1995). Recent advances in ordered intermetallics. *Mater. Chem. Phys.* 42, 77–86. doi:10.1016/0254-0584(95)01546-9

Lu, Y., Dong, Y., Guo, S., Jiang, L., Kang, H., Wang, T., et al. (2014). A promising new class of high-temperature alloys: eutectic high-entropy alloys. *Sci. Rep.* 4, 6200. doi:10.1038/srep06200

Medvedeva, N. I., Gornostyrev, Y. N., Novikov, D. L., Mryasov, O. N., and Freeman, A. J. (1998). Ternary site preference energies, size misfits and solid solution hardening in NiAl and FeAl. *Acta Mater.* 46, 3433–3442. doi:10.1016/S1359-6454(98)00042-1

Miracle, D. B. (1993). Overview No. 104 the physical and mechanical properties of NiAl. *Acta Metall. Mater.* 41, 649–684. doi:10.1016/0956-7151(93)90001-9

Miracle, D. B., and Senkov, O. N. (2017). A critical review of high entropy alloys and related concepts. *Acta Mater.* 122, 448–511. doi:10.1016/J.ACTAMAT.2016.08.081

Misra, A., and Gibala, R. (1997). Room-temperature deformation behavior of directionally solidified multiphase Ni-Fe-Al alloys. *Metall. Mater. Trans.* 28, 795–807. doi:10.1007/s11661-997-0066-x

Misra, A., and Gibala, R. (1999). Slip transfer and dislocation nucleation processes in multiphase ordered Ni-Fe-Al alloys. *Metall. Mater. Trans.A* 30, 991–1001. doi:10.1007/s11661-999-0152-3

Misra, A., Hirth, J. P., and Hoagland, R. G. (2005). Length-scale-dependent deformation mechanisms in incoherent metallic multilayered composites. *Acta Mater.* 53, 4817–4824. doi:10.1016/J.ACTAMAT.2005.06.025

Misra, A., Wu, Z. L., Kush, M. T., and Gibala, R. (1998). Deformation and fracture behaviour of directionally solidified NiAl-Mo and NiAl-Mo(Re) eutectic composites. *Philos. Mag. A* 78, 533–550. doi:10.1080/01418619808241921

Nagase, T., Takemura, M., Matsumuro, M., and Maruyama, T. (2017). Solidification microstructure of $AlCoCrFeNi_{2.1}$ eutectic high entropy alloy ingots. *J. Japan Foundry Eng. Soc.* 89, 119–129. doi:10.11279/jfes.89.119

Newbury, D. E., and Ritchie, N. W. M. (2013). Is scanning electron microscopy/energy dispersive X-ray Spectrometry (SEM/EDS) quantitative? *Scanning* 35, 141–168. doi:10.1002/sca.21041

Noebe, R. D., Bowman, R. R., and Nathal, M. V. (1993). Physical and mechanical properties of the B2 compound NiAl. *Int. Mater. Rev.* 38, 193–232. doi:10.1179/imr.1993.38.4.193

Oliver, W. C., and Pharr, G. M. (1992). An improved technique for determining hardness and elastic modulus using load and displacement sensing indentation experiments. *J. Mater. Res.* 7, 1564–1583. doi:10.1557/JMR.1992.1564

Plapp, M., and Karma, A. (2002). Eutectic colony formation: a phase-field study. *Phys. Rev. E* 66, 61608. doi:10.1103/PhysRevE.66.061608

Qian, L., Li, M., Zhou, Z., Yang, H., and Shi, X. (2005). Comparison of nano-indentation hardness to microhardness. *Surf. Coating. Technol.* 195, 264–271. doi:10.1016/j.surfcoat.2004.07.108

Raheem, Z. (2019). Standard test methods for flexural properties of unreinforced and reinforced plastics and electrical insulating materials. *J. Test. Eval.* 1. doi:10.1520/D0790-02

Schneider, C. A., Rasband, W. S., and Eliceiri, K. W. (2012). NIH Image to ImageJ: 25 years of image analysis. *Nat. Methods* 9, 671–675. doi:10.1038/nmeth.2089

Shang, Z., Shen, J., Zhang, J., Wang, L., and Fu, H. (2012). Effect of withdrawal rate on the microstructure of directionally solidified NiAl-Cr(Mo) hypereutectic alloy. *Intermetallics* 22, 99–105. doi:10.1016/j.intermet.2011.10.018

Shen, Z., Wagoner, R. H., and Clark, W. A. T. (1988). Dislocation and grain boundary interactions in metals. *Acta Metall.* 36, 3231–3242. doi:10.1016/0001-6160(88)90058-2

Tkaczyk, A. H., Bartl, A., Amato, A., Lapkovskis, V., and Petranikova, M. (2018). Sustainability evaluation of essential critical raw materials: Cobalt, Niobium, Tungsten and rare earth elements. *J. Phys. D. Appl. Phys.* 51, 203001. doi:10.1088/1361-6463/aaba99

Wang, L., Shen, J., Shang, Z., and Fu, H. (2014). Microstructure evolution and enhancement of fracture toughness of NiAl-Cr(Mo)-(Hf,Dy) alloy with a small addition of Fe during heat treatment. *Scr. Mater.* 89, 1–4. doi:10.1016/j.scriptamat.2014.07.002

Wang, L., Shen, J., Zhang, Y., Guo, L., Xu, H., and Fu, H. (2017). Microstructure evolution and room temperature fracture toughness of as-cast and directionally solidified novel NiAl-Cr(Fe) alloy. *Intermetallics* 84, 11–19. doi:10.1016/j.intermet.2016.12.021

Wang, L., Yao, C., Shen, J., Zhang, Y., Wang, T., Ge, Y., et al. (2020). Microstructures and room temperature tensile properties of as-cast and directionally solidified $AlCoCrFeNi_{2.1}$ eutectic high-entropy alloy. *Intermetallics* 118, 106681. doi:10.1016/j.intermet.2019.106681

Wang, L., Yao, C., Shen, J., Zhang, Y., Wang, T., Xu, H., et al. (2019). Microstructures and compressive properties of NiAl-Cr(Mo) and NiAl-Cr eutectic alloys with different Fe contents. *Mater. Sci. Eng. A* 744, 593–603. doi:10.1016/j.msea.2018.12.085

Wang, W.-R., Wang, W.-L., Wang, S.-C., Tsai, Y.-C., Lai, C.-H., and Yeh, J.-W. (2012). Effects of Al addition on the microstructure and mechanical property of AlxCoCrFeNi high-entropy alloys. *Intermetallics* 26, 44–51. doi:10.1016/j.intermet.2012.03.005

Wani, I. S., Bhattacharjee, T., Sheikh, S., Bhattacharjee, P. P., Guo, S., and Tsuji, N. (2016). Tailoring nanostructures and mechanical properties of $AlCoCrFeNi_{2.1}$ eutectic high entropy alloy using thermo-mechanical processing. *Mater. Sci. Eng. A* 675, 99–109. doi:10.1016/j.msea.2016.08.048

Conflict of Interest: FS, PP, and DM were employed by the company Anton Paar Germany GmbH.

The remaining authors declare that the research was conducted in the absence of any commercial or financial relationships that could be construed as a potential conflict of interest.

frontiers in Materials

ORIGINAL RESEARCH
published: 22 October 2020
doi: 10.3389/fmats.2020.566336

Corrosion of Al(Co)CrFeNi High-Entropy Alloys

Elżbieta M. Godlewska[1], Marzena Mitoraj-Królikowska[1], Jakub Czerski[1], Monika Jawańska[1], Sergej Gein[2] and Ulrike Hecht[2]*

[1]AGH University of Science and Technology, Faculty of Materials Science and Ceramics, Kraków, Poland, [2]Access V., Aachen, Germany

High-entropy alloys, $AlCrFe_2Ni_2Mo_x$ (x = 0.00, 0.05, 0.10, and 0.15), AlCoCrFeNi, and two quinary alloys with compositions close to its face-centered cubic and body-centered cubic component phases, are tested for corrosion resistance in 3.5 wt% NaCl. The materials with different microstructure produced by arc melting or ingot metallurgy are evaluated by several electrochemical techniques: measurements of open circuit voltage, cyclic potentiodynamic polarization, and electrochemical impedance spectroscopy. Microstructure, surface topography, and composition are systematically characterized by scanning electron microscopy and energy-dispersive x-ray spectroscopy. The results indicate that minor additions of Mo positively affect corrosion resistance of the $AlCrFe_2Ni_2$ alloy by hampering pit formation. The face-centered cubic phase in the equimolar alloy, AlCoCrFeNi, is proved to exhibit more noble corrosion potential and pitting potential, lower corrosion current density and corrosion rate than the body-centered cubic phase. Overall behavior of the investigated alloys is influenced by the manufacturing conditions, exact chemical composition, distribution of phases, and occurrence of physical defects on the surface.

Keywords: high-entropy alloys, microstructure, corrosion resistance, sodium chloride, electrochemical measurements

OPEN ACCESS

Edited by:
Antonio Caggiano, Darmstadt University of Technology, Germany

Reviewed by:
Wislei Riuper Osório, Campinas State University, Brazil
Solomon M. Moses, King Fahd University of Petroleum and Minerals, Saudi Arabia

****Correspondence:***
Elżbieta Godlewska
godlewsk@agh.edu.pl

Specialty section:
This article was submitted to Structural Materials, a section of the journal Frontiers in Materials

Received: *27 May 2020*
Accepted: *02 September 2020*
Published: *22 October 2020*

Citation:
Godlewska EM, Mitoraj-Królikowska M, Czerski J, Jawańska M, Gein S and Hecht U (2020) Corrosion of Al(Co)CrFeNi High-Entropy Alloys. Front. Mater. 7:566336. doi: 10.3389/fmats.2020.566336

INTRODUCTION

The notion of high-entropy alloys (HEAs) or more generally high-entropy materials was coined quite recently and immediately awoke enormous interest by providing pathways for the development of new materials or improvement of the existing ones. In the group of high-entropy alloys, initial efforts were directed on combinations of Al with 3d transition metals, namely, Cr, Fe, Co, Ni, and to a lesser extent Cu and Mn (Miracle and Senkov, 2016). At present, the multi-principal element alloys are referred to as HEAs or compositionally complex alloys even when their configurational entropy is not high enough to secure stability of a single solid solution. Commonly, second phases are formed, including either solid solutions or intermetallics or both, which are accompanied by strong segregation of alloying elements (Pickering and Jones, 2016). AlCoCrFeNi alloys are known to have different phase composition depending on the concentration of Al. As the concentration of Al increases, their structure transforms from face-centered cubic (FCC) through mixed FCC + body-centered cubic (BCC) to BCC (Zhang et al., 2014). Since mechanical properties, that is, ductility and strength, of a number of single-phase HEAs did not meet basic requirements for structural applications, major developments were switched toward the design and fabrication of dual phase FCC + BCC alloys. One of the promising results of this work was $AlCoCrFeNi_{2.1}$, a castable eutectic high-entropy alloy with very good combination of high fracture strength and ductility (Lu et al.,

2015). This composition was further modified to Co-free $AlCrFe_2Ni_2$, which not only had mechanical properties outperforming as-cast HEAs and many titanium alloys at room temperature but also was less expensive. The structure of this alloy, consisting of FCC(A1), disordered BCC(A2), and ordered BBC(B2), results from spinodal decomposition of the original BCC phase upon cooling. The very attractive combination of fracture strength and ductility, characteristic of this alloy, is attributed to the coexistence of harder BCC phases and softer FCC (Dong et al., 2016). In addition to mechanical testing, many HEAs were tested for corrosion resistance in different aqueous environments, mostly in 3.5 wt.% NaCl and 0.1 M H_2SO_4 (Hsu et al., 2005; Lee et al., 2008b; Chou et al., 2010; Kao et al., 2010; Lin and Tsai, 2011; Qiu et al., 2017). The results looked very promising. It was indicated, however, that some alloying additions, such as Al, Cu, or Mo, could induce elemental segregation in HEAs, leading to galvanic coupling or local breakdown of passive films formed on alloy surface in salt or acid solutions. One way to overcome this drawback is seen in microstructure refining by an adequate design of manufacturing processes (Shi et al., 2017). Among the alloying additions, Mo deserves special attention since it is known to reduce the susceptibility of stainless steels to pitting corrosion. It is also known that Mo concentration in steels should be possibly low to avoid precipitation of brittle sigma and alpha phases. Simultaneous depletion in Mo and Cr of the neighboring grains would make them more vulnerable to corrosion attacks (Park and Lee, 2014; Shang et al., 2018; Valeriano et al., 2019). Although the pitting corrosion equivalent used for stainless steels cannot be simply transferred to HEAs, it was reported that small additions of Mo increased pitting corrosion resistance of some HEAs in chloride-containing environments (Chou et al., 2010; Rodriguez et al., 2018).

In this work, corrosion of selected HEAs was investigated in aqueous solutions of sodium chloride. The principal objectives were 1) to verify a hypothesis about different corrosion behavior of alloys with the same nominal composition and different microstructure on the basis of an $AlCrFe_2Ni_2$ alloy produced by different manufacturing routes, 2) to assess whether or not minor additions of Mo can positively affect the corrosion resistance of the baseline alloy, $AlCrFe_2Ni_2$, and 3) to evaluate the susceptibility to corrosion of the FCC and BCC phases in the equimolar alloy, AlCoCrFeNi. A duplex stainless steel EN 1.4517 with excellent corrosion resistance was used as a reference material.

MATERIALS AND METHODS

Experimental alloys, $AlCrFe_2Ni_2$ (with and without Mo) and AlCoCrFeNi (equimolar and with compositions close to its FCC and BCC constituent phases), were obtained from elemental powders (alloys with Co) or granules by arc melting under an argon atmosphere. Purity of the components was: Al 4N; Co 3N; Cr 3N5; Fe 3N; Ni 3N7; Mo 2N8. The reference materials, EN 1.4519 stainless steel, and two Co-free baseline alloys (purity of components: Al 2N5; Cr 2N8; Fe 3N; Ni 2N85) were produced by ingot metallurgy (Otto Junker GmbH). Alloy marked $AlCrFe_2Ni_2$ (1) was cast in air and $AlCrFe_2Ni_2$ (2) in argon. Chemical compositions of all investigated alloys are collected in **Table 1**. The EN 1.4517 duplex stainless steel (STS) had the following composition in wt.%: Fe 61.77; Cr 25.18; Ni 5.70; Cu 3.00; Mo 2.74; Si 0.85; Mn 0.53; N 0.156; V 0.032; C 0.021; P 0.002; S 0.001. Samples in the form of flat plates were ground with abrasive papers up to ISO/FEPA 1200 grit and cleaned with isopropanol. For electrochemical measurements, copper wire connections were attached to each sample using conductive silver lacquer (Leitsilber 200N, Hans Wolbring GmbH). Next, the samples were mounted in epoxy resin (Crystalline 940). Potentiodynamic and electrochemical impedance spectroscopy measurements were done in a three-electrode cell: sample as working electrode (exposed area mostly about 1 cm^2), saturated calomel electrode (SCE) as reference, and graphite as auxiliary electrode (area about 50 cm^2), using SP-150 potentiostat controlled by Bio-Logic EC-lab V11.25 or Nova 2.1.4 Metrohm Autolab B.V. (electrochemical impedance spectroscopy) software. Liquid medium used in this work was 3.5 wt.% NaCl (at 25°C). Long-term (72 h) or short-term (2 h) open circuit voltage measurements in 3.5 wt.% NaCl were conducted for all samples. Potentiodynamic measurements were done in a regular range between −300 and +300 mV vs. open circuit voltage (OCV) (polarization resistance) and in an extended potential range between −300 and +1,500 mV vs. OCV (cyclic potentiodynamic polarization test according to ASTM G61-86). Polarization resistance measurements were done at a potential scan rate of 30 mV/min and consisted of 20 cycles. Each cycle was preceded by monitoring the variations of OCV for 2 h (before the first cycle) and for 30 min (before cycles 2–20). Cyclic potentiodynamic polarization tests were conducted at a scan rate of 10 mV/min until potential reached +1,500 mV vs. OCV or until current density reached 5 mA/cm^2. Then, the reverse scan was activated and continued to the initial OCV value. As previously reported (Zhang et al., 2009), potential scan rate plays an important role in minimizing the effects of distortion of the potentiodynamic polarization curves in the analyses of Tafel slopes and corrosion current density. It is noteworthy that at the selected scan rate of 10 mV/min, no significant distortions were produced. Electrochemical impedance spectroscopy measurements were carried out in the frequency range of 10 mHz–100 kHz in a single-sine excitation mode. The

TABLE 1 | Composition of samples.

Materials	Nominal composition in at.%					
	Al	Cr	Fe	Ni	Mo	Co
$AlCrFe_2Ni_2$	16.7	16.7	33.3	33.3	–	–
$AlCrFe_2Ni_2$ (1)	16.7	16.7	33.3	33.3	–	–
$AlCrFe_2Ni_2$ (2)	16.7	16.7	33.3	33.3	–	–
$AlCrFe_2Ni_2Mo_{0.05}$	16.5	16.5	33.1	33.1	0.8	–
$AlCrFe_2Ni_2Mo_{0.10}$	16.4	16.4	32.8	32.8	1.6	–
$AlCrFe_2Ni_2Mo_{0.15}$	16.3	16.3	32.5	32.5	2.4	–
AlCoCrFeNi	20.0	20.0	20.0	20.0	–	20.0
FCC	3.1	38.8	27.7	7.8	–	22.6
BCC	33.9	5.0	13.4	28.5	–	19.2

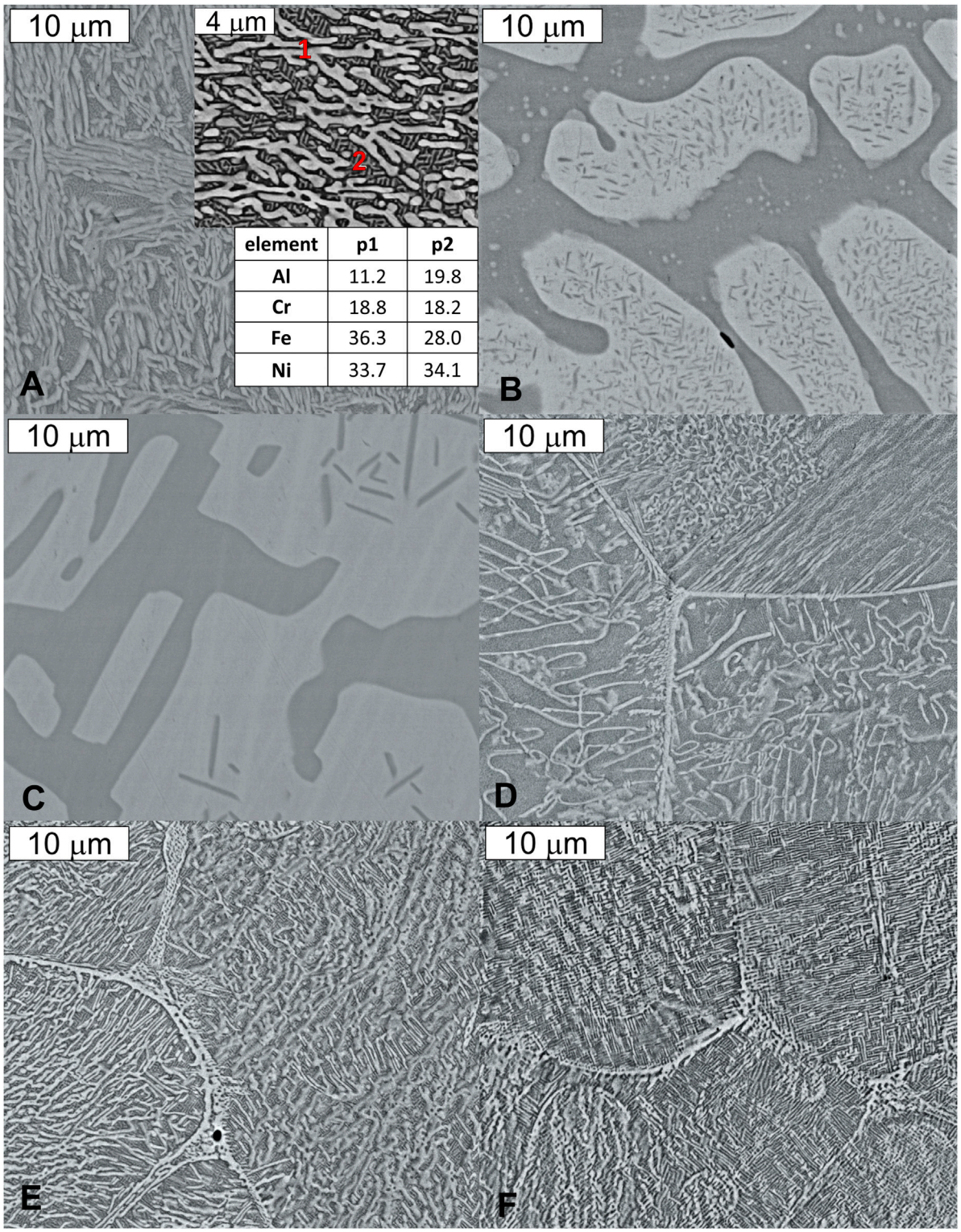

FIGURE 1 | Microstructures of $AlCrFe_2Ni_2$ **(A)**, $AlCrFe_2Ni_2$ (1) **(B)**, $AlCrFe_2Ni_2$ (2) **(C)**, $AlCrFe_2Ni_2Mo_{0.05}$ **(D)**, $AlCrFe_2Ni_2Mo_{0.10}$ **(E)**, and $AlCrFe_2Ni_2Mo_{0.15}$ **(F)**.

potential start point was the last value recorded in the 2-h OCV measurement. Three points for each frequency were recorded, and the number of points per decade was 10 in logarithmic spacing. Each sample and each type of experiment were repeated several times to assess reproducibility of the corrosion parameters. For clarity, the averaged values are presented on

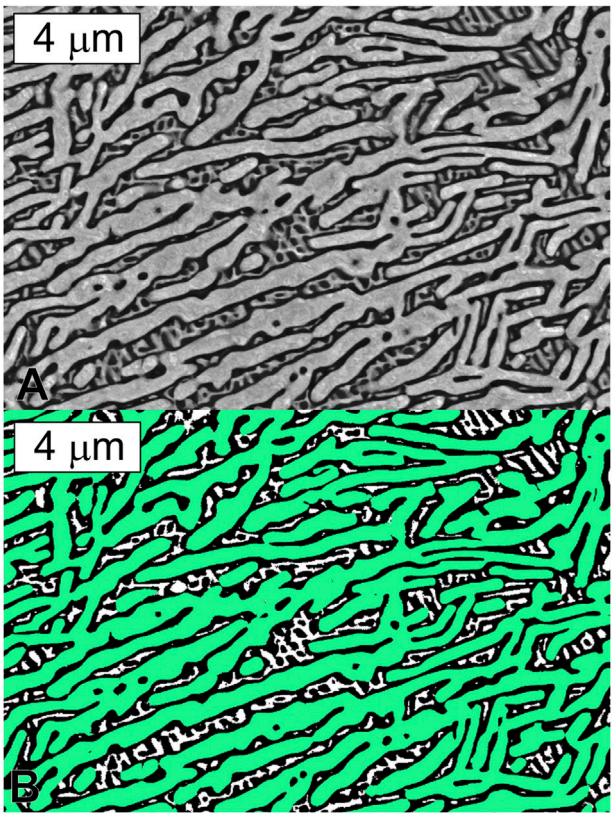

FIGURE 2 | SEM micrograph [backscattered electrons mode (BSE)] **(A)** and image segmentation **(B)** for phase analysis using the software ImageJ; segmented image colors: green—face-centered cubic (FCC), white—body-centered cubic (BCC)(A2), and black—BCC(B2).

diagrams. Sample surfaces or cross-sections before and after the tests were examined by means of a Nova NanoSEM 200 FEI scanning electron microscope (SEM) equipped with an energy-dispersive X-ray spectroscope for chemical analysis. Selected samples were analyzed by transmission electron microscopy (TEM) using a FEI Tecnai TF20 X-TWIN (FEG) microscope, equipped with an EDAX energy dispersive X-ray detector, at an accelerating voltage of 200 kV. Thin foils were prepared by a focused ion beam (FIB) technique, using a FEI Quanta 200 3D Dual Beam FIB/SEM system equipped with an Omniprobe micromanipulator.

RESULTS

Microstructure and Phase Composition

Microstructures of the $AlCrFe_2Ni_2Mo_x$ (x = 0.00, 0.05, 0.10, and 0.15) alloys are shown in **Figure 1**. The SEM image in **Figure 1A** reveals distribution of phases in the baseline alloy, $AlCrFe_2Ni_2$, obtained by arc melting. Phase separation within the grains is distinctly visible with a disordered vermicular FCC phase and a characteristic geometric pattern of very finely dispersed BCC/B2 phases resulting from spinodal decomposition (inset). Based on the results of energy-dispersive X-ray spectroscopy (EDS) analysis, the vermicular phase—marked 1 in the inset—is enriched in Fe and Cr. The two-phase region marked 2 in the inset is enriched in Al and Ni. Minor additions of Mo did not affect the phase composition of the alloy but slightly refined its microstructure, as shown in **Figures 1D,E,F**. Phase fractions in the as-cast alloy $AlCrFe_2Ni_2$ + 1.9 at.% Mo determined by image analysis (**Figures 2A,B**) on several SEM-BSE images were the following in area %: FCC(A1) 55.9 ± 1.3, BCC(B2) 35.5 ± 2.1, and BCC(A2) 8.5 ± 2.0. Micrographs in **Figures 1B,C** present samples produced by ingot metallurgy in air $AlCrFe_2Ni_2$ (1) and in argon $AlCrFe_2Ni_2$ (2). The microstructures are similar with distinctly separated grains composed of FCC and BCC phases. Some second-phase dispersions within the grains do not resemble the intricate patterns originating from spinodal decomposition.

The equimolar alloy, AlCoCrFeNi, consists of FCC and BCC phases in a layout typical of spinodal decomposition (**Figure 3A**). According to EDS analyses, Al and Ni favor the formation of BCC structures (dark gray) while Fe, Cr, and Co favor the formation of FCC structures (light gray). The images in **Figures 3B,C** present microstructures of the two alloys with average compositions corresponding roughly to the BCC and FCC components of the equimolar alloy. In both alloys, there is some amount of the second phase. Alloy denoted as FCC is composed of two Cr-rich phases, as illustrated by transmission electron microscopy images and EDS analysis in **Figure 3D**. X-ray and electron diffraction patterns confirming the structure of predominant phases in the investigated alloys are shown in **Figure 4**.

Open Circuit Voltage

The results of OCV measurements of the Co-free alloys in 3.5 wt% NaCl solution are presented in **Figure 5A**. The most noble (highest) values were recorded for the arc-melted samples $AlCrFe_2Ni_2$ and $AlCrFe_2Ni_2Mo_{0.05}$; however, in both cases, local fluctuations of potential took place. For STS, $AlCrFe_2Ni_2Mo_{0.15}$, and $AlCrFe_2Ni_2Mo_{0.10}$, the fluctuations were less pronounced. $AlCrFe_2Ni_2$ (1), cast in air, had the lowest OCV values. $AlCrFe_2Ni_2$ (2), cast in argon, behaved similarly during first 36 h, and then its potential increased to reach the final value close to those of the best arc-melted alloys containing Mo and STS. All Co-free alloys under investigation exhibited a low spread of OCV values and quick stabilization.

The OCV variations over time for the equimolar alloy, AlCoCrFeNi, and two quinary alloys denoted as BCC and FCC are presented in **Figure 5B** on the background of the STS reference. The values of potential are more negative for all three alloys compared with STS, and all curves are relatively smooth. The lowest OCV values were recorded for the BCC sample, i.e., one rich in Al and Ni. The Cr-rich FCC sample showed OCV values closest to those of STS.

Cyclic Potentiodynamic Polarization

Variations of polarization resistance (Rp) over 20 consecutive cycles of potentiodynamic measurements for all the Co-free alloys and STS reference are presented in **Figure 6A**. Generally, the fluctuating Rp values revealed an increasing trend: the highest on average (up to about 4 MΩ cm^2) being recorded

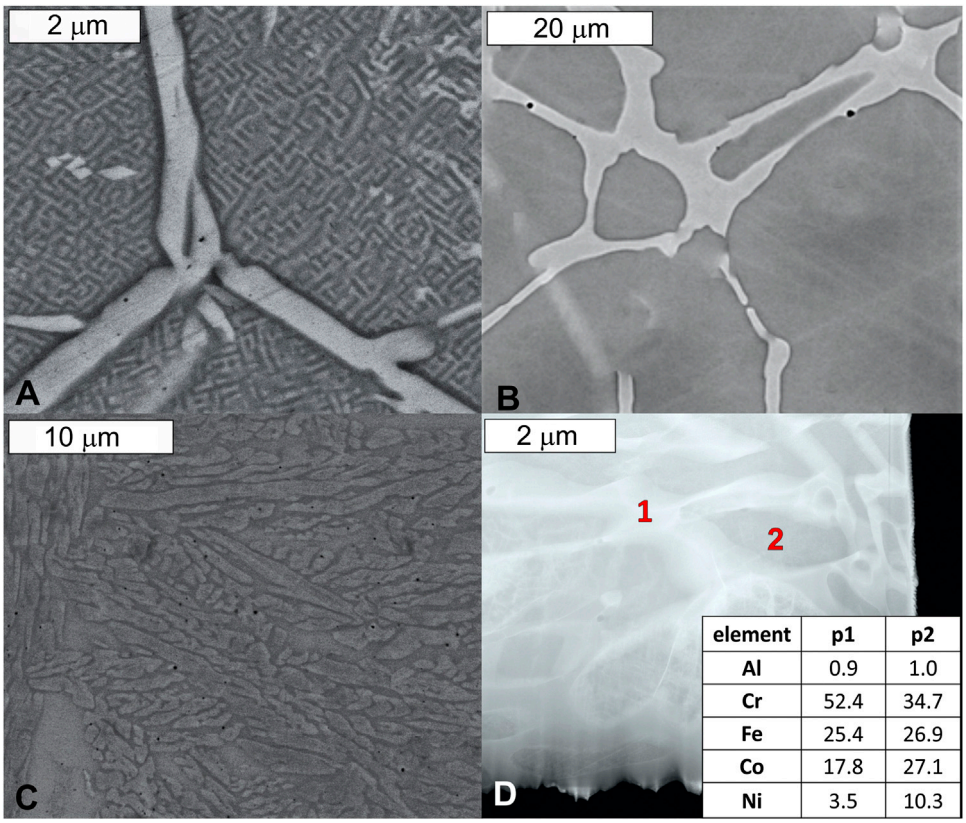

element	p1	p2
Al	0.9	1.0
Cr	52.4	34.7
Fe	25.4	26.9
Co	17.8	27.1
Ni	3.5	10.3

FIGURE 3 | Microstructures of AlCoCrFeNi **(A)** and two quinary alloys with compositions close to its major component BCC **(B)** and FCC **(C,D)**; SEM **(A–C)**, STEM **(D)**, EDS analysis (at.%) in marked points.

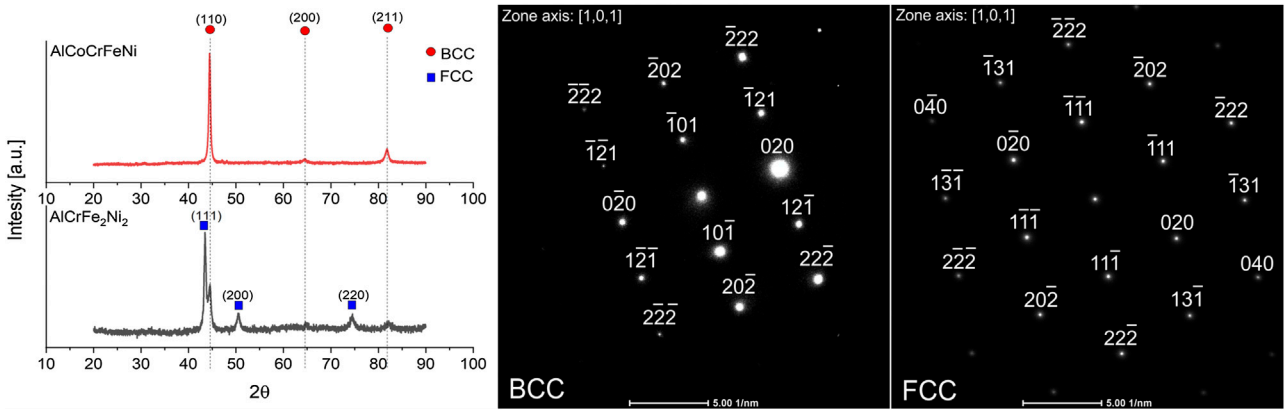

FIGURE 4 | X-ray **(A)** and electron **(B)** diffraction patterns confirming the occurrence of predominant phases in the investigated alloys.

for $AlCrFe_2Ni_2$ and the lowest (up to about 800 kΩ cm^2) for $AlCrFe_2Ni_2Mo_{0.05}$. STS behaved in a more regular manner, but the recorded R*p* values were lower, reaching about 1.5 MΩ cm^2 at the most.

The results of similar measurements for the three alloys containing Co and the STS reference are presented in **Figure 6B**. Compared with STS, the quinary alloy, FCC, rich in Cr and Fe, had higher polarization resistance over 20 cycles of potentiodynamic measurements, approaching 4 MΩ cm^2 at the end of the experiment. The AlCoCrFeNi and BCC samples showed irregular variations of polarization resistance in consecutive cycles, with fluctuations around the values

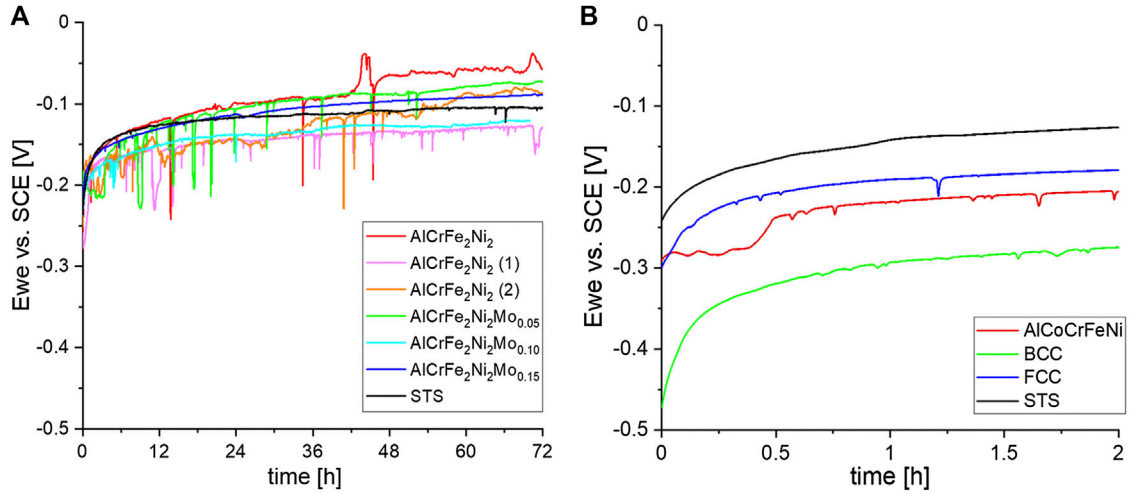

FIGURE 5 | Open circuit voltage evolution over time in 3.5 wt.% NaCl for the Co-free alloys and stainless steel (STS) **(A)**, and for three quinary alloys and STS **(B)**.

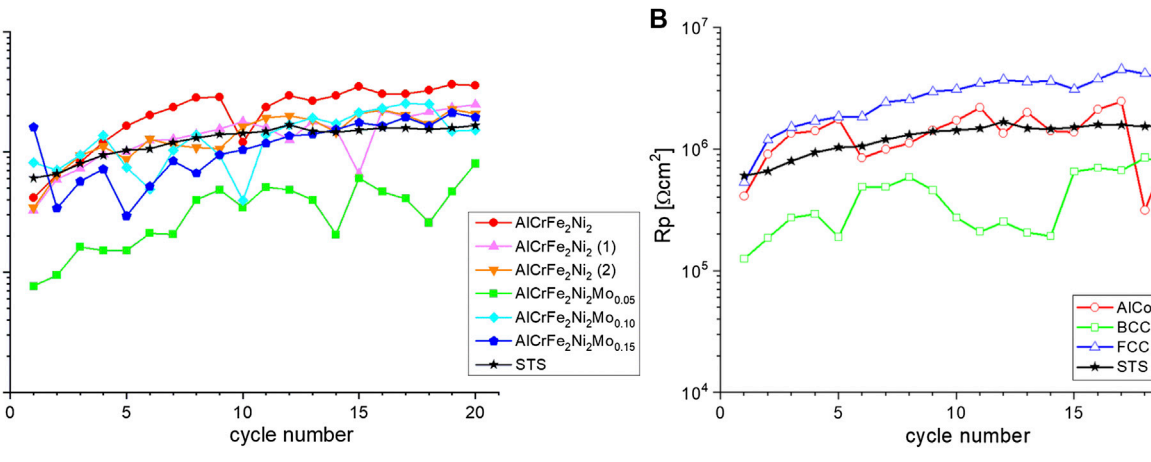

FIGURE 6 | Variations of polarization resistance over 20 consecutive cycles in 3.5 wt.% NaCl for Co-free alloys and STS **(A)**, and for three quinary alloys and STS **(B)**.

recorded for STS in the former case and the lowest values, not exceeding 900 kΩ cm^2, in the latter case.

Tafel polarization curves of the $AlCrFe_2Ni_2Mo_x$ alloys are collected in **Figure 7A**. Compared with the baseline alloy, all other HEAs showed worse corrosion properties, reflected in higher corrosion currents (i_{corr}) and corrosion rates, as illustrated in **Table 2**. Pitting potential was clearly visible only in the case of arc-melted $AlCrFe_2Ni_2$, $AlCrFe_2Ni_2Mo_{0.15}$, and STS. Unlike other alloys, STS exhibited a very wide passivation range and repassivated during the reverse scan. All alloys in this series, except $AlCrFe_2Ni_2Mo_{0.05}$, had corrosion currents lower than 0.1 μA/cm^2.

Tafel plots for AlCoCrFeNi, BCC, FCC, and STS are shown in **Figure 7B**. The polarization curves of FCC and STS are very similar, with a pitting potential (E_{pit}) close to 1.0 V (**Table 2**). However, the repassivation potentials (E_{pass}) were significantly different: −0.13 V for FCC and +0.83 V for STS (**Figure 7B**). According to the data in **Table 2**, the most negative value of E_{pit} was recorded for the BCC sample. Corrosion potentials (E_{corr}) of the investigated alloys ranged between −0.20 and −0.28 V. The least negative E_{corr} (−0.14 V) was recorded for STS and the most negative (equal or lower than −0.30 V) for AlCoCrFeNi and BCC. Current density of 5 mA/cm^2 was reached, and reverse scan was started at potentials (E_{rev}) 0.12–0.15 V ($AlCrFe_2Ni_2Mo_x$ and BCC), 0.16–0.19 V ($AlCrFe_2Ni_2$ and AlCoCrFeNi), and 1.0 V (STS and FCC). The highest corrosion current (i_{corr}) as well as corrosion rate was measured for BCC, $AlCrFe_2Ni_2Mo_{0.05}$, and AlCoCrFeNi.

Electrochemical Impedance Spectroscopy

The results of electrochemical impedance spectroscopy measurements are presented in a form of a Nyquist plot for

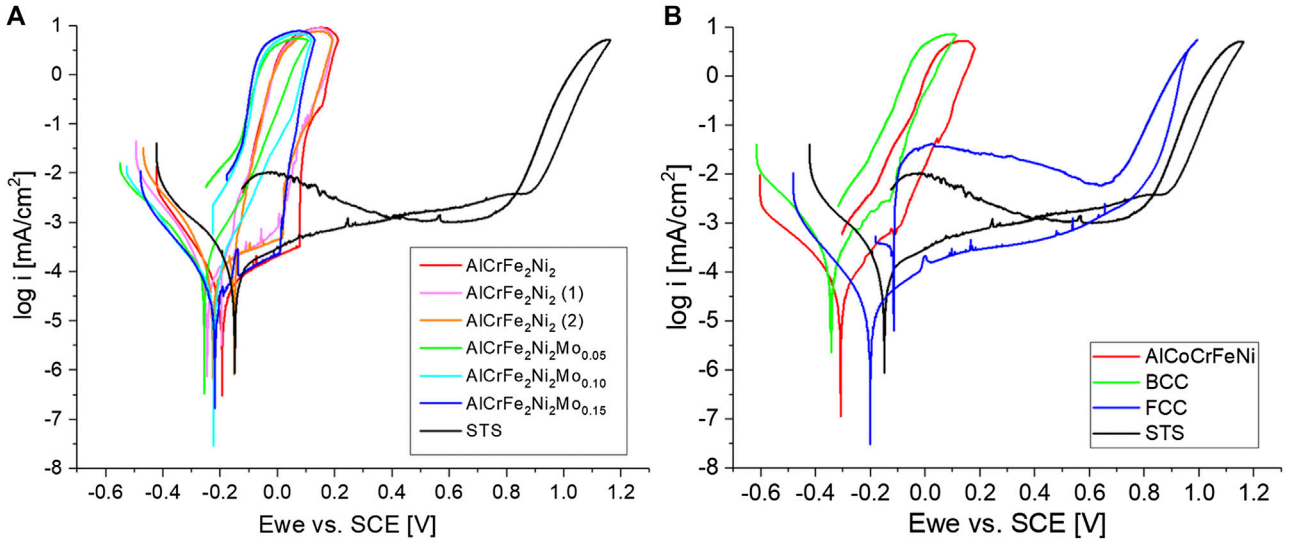

FIGURE 7 | Potentiodynamic polarization curves (Tafel) in 3.5 wt% NaCl for the Co-free alloys and STS **(A)**, and for three quinary alloys and STS **(B)**.

TABLE 2 | Parameters obtained from Tafel plots in **Figures 7A,B**.

Materials	E_{corr} (V)	E_{pit} (V)	E_{rev} (V)	i_{corr} (μA/cm^2)	Corrosion rate (mmpy)
AlCrFe$_2$Ni$_2$	−0.25 ± 0.01	0.07 ± 0.01	0.19 ± 0.02	0.049 ± 0.022	(4.2 ± 0.8) × 10^{-4}
AlCrFe$_2$Ni$_2$ (1)	−0.25 ± 0.01	−0.03 ± 0.01	0.18 ± 0.02	0.052 ± 0.004	(4.9 ± 0.4) × 10^{-4}
AlCrFe$_2$Ni$_2$ (2)	−0.28 ± 0.00	0.00 ± 0.02	0.16 ± 0.00	0.074 ± 0.001	(7.1 ± 0.0) × 10^{-4}
AlCrFe$_2$Ni$_2$Mo$_{0.05}$	−0.27 ± 0.01	–	0.13 ± 0.03	0.166 ± 0.041	(15.8 ± 3.9) × 10^{-4}
AlCrFe$_2$Ni$_2$Mo$_{0.10}$	−0.28 ± 0.00	–	0.14 ± 0.04	0.099 ± 0.003	(8.0 ± 2.1) × 10^{-4}
AlCrFe$_2$Ni$_2$Mo$_{0.15}$	−0.26 ± 0.00	0.02 ± 0.02	0.15 ± 0.03	0.059 ± 0.017	(5.5 ± 1.6) × 10^{-4}
AlCoCrFeNi	−0.30 ± 0.03	–	0.16 ± 0.02	0.116 ± 0.066	(10.2 ± 6.0) × 10^{-4}
BCC	−0.34 ± 0.01	−0.07 ± 0.08	0.12 ± 0.01	0.141 ± 0.046	(13.6 ± 6.3) × 10^{-4}
FCC	−0.20 ± 0.05	0.83 ± 0.05	1.00 ± 0.02	0.022 ± 0.002	(1.9 ± 0.2) × 10^{-4}
STS	−0.14 ± 0.01	0.89 ± 0.01	1.16 ± 0.01	0.040 ± 0.028	(3.9 ± 2.7) × 10^{-4}

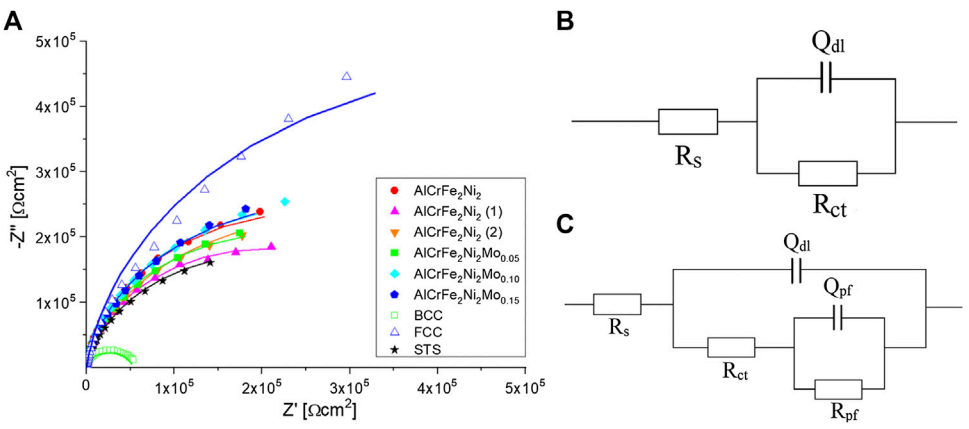

FIGURE 8 | Nyquist plot **(A)** and fitted equivalent electrochemical circuits for all high entropy alloys **(B)**, and STS **(C)**.

TABLE 3 | Fitted parameters for the elements of equivalent circuits.

Sample	R_s (Ω cm^2)	Q_{dl} (μF/cm^2)	n (–)	R_{ct} (kΩ cm^2)	Q_{pf} (μF/cm^2)	n (–)	R_{pf} (kΩ cm^2)	χ^2
$AlCrFe_2Ni_2$	7 ± 0	40 ± 1	0.95 ± 0.01	520 ± 14	–	–	–	0.0410 ± 0.0088
$AlCrFe_2Ni_2$ (1)	9 ± 1	39 ± 8	0.92 ± 0.01	413 ± 24	–	–	–	0.0414 ± 0.0252
$AlCrFe_2Ni_2$ (2)	7 ± 1	44 ± 3	0.89 ± 0.03	537 ± 24	–	–	–	0.0480 ± 0.0330
$AlCrFe_2Ni_2Mo_{0.05}$	6 ± 0	40 ± 1	0.94 ± 0.01	459 ± 34	–	–	–	0.0306 ± 0.0093
$AlCrFe_2Ni_2Mo_{0.10}$	6 ± 0	35 ± 1	0.93 ± 0.01	550 ± 60	–	–	–	0.0215 ± 0.0056
$AlCrFe_2Ni_2Mo_{0.15}$	5 ± 0	32 ± 0	0.92 ± 0.01	573 ± 17	–	–	–	0.0428 ± 0.0134
BCC	6 ± 0	6 ± 0	0.91 ± 0.00	53 ± 0.00	–	–	–	0.0827 ± 0.0004
FCC	9 ± 1	18 ± 0	0.92 ± 0.03	1,039 ± 80	–	–	–	0.1423 ± 0.0327
STS	8 ± 1	41 ± 1	0.91 ± 0.00	275 ± 21	20 ± 1	0.72 ± 0.03	125 ± 7	0.0164 ± 0.0030

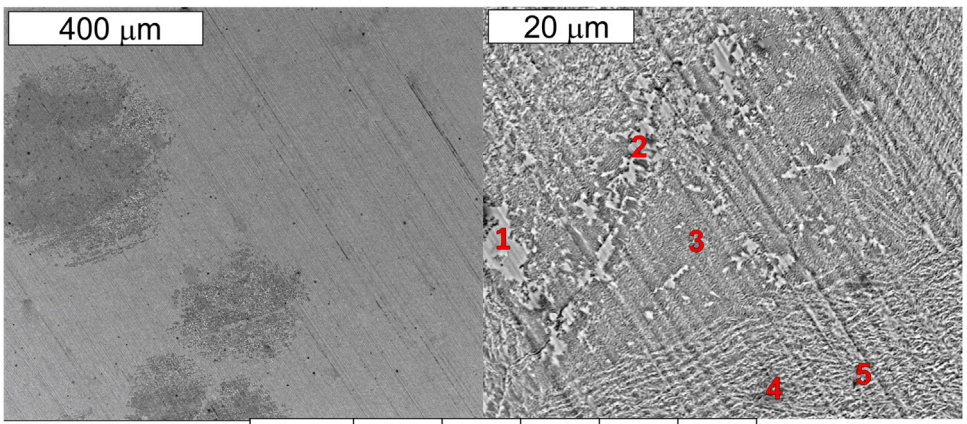

element	p1	p2	p3	p4	p5
Al	10.6	11.0	1.8	4.5	4.4
Cr	16.3	17.3	28.3	21.5	25.1
Fe	33.5	35.0	52.3	46.4	45.0
Ni	38.3	35.2	14.6	25.3	23.6
Mo	1.3	1.5	3.1	2.3	1.9

FIGURE 9 | Surface of an $AlCrFe_2Ni_2Mo_{0.10}$ sample after potentiodynamic polarization test (Tafel) in 3.5 wt% NaCl and EDS analysis (at.%) in marked points.

all the investigated alloys and the STS reference in **Figure 8A**. The related equivalent electrical circuits are shown in **Figures 8B,C**, and the fitted parameters are listed in **Table 3**. The behavior of all samples except STS was described by a simple Randles circuit. A more complex equivalent circuit was proposed for STS, based on the study by Pan et al. (1998) and Mahato and Singh (2011) and the best fitting parameters. In all cases, a constant phase element was selected representing a non-ideal capacitor in order to take account of surface roughness and inhomogeneities, that is, varying surface energy, which affect the reaction rates. Thus, Q_{dl} and Q_{pf} indicate impedances described as constant phase element, CPE = $[Q(i\,\omega)^n]^{-1}$, where Q is the capacitance, $i = (-1)^{0.5}$, ω is the angular frequency, and $-1 \leq n \leq 1$, as previously reported (Osório et al., 2013; Kumar et al., 2017; Rodrigues et al., 2020). The values of solution resistance (R_s) were in the range of 5.0–9.0 Ωcm^2. The values of charge transfer resistance (R_{ct}) for the Co-free samples were between 413 and 573 kΩ cm^2, the highest one being recorded for $AlCrFe_2Ni_2Mo_{0.15}$. For STS, the R_{ct} value was much lower, equal to 275 kΩ cm^2. The relatively low R_{ct} value for STS was probably connected with the occurrence of a protective film characterized by an additional resistance R_{pf} = 125 kΩ cm^2. The electrical double layer capacitance (Q_{dl}) ranged from 32 to 44 μF/cm^2. In the series of quinary alloys, some of the fitted parameters did not fall in the same range, e.g., charge transfer resistance of FCC exceeded 1 MΩ cm^2 but that of BCC was merely 64 kΩ cm^2. The electrical double layer capacitance for FCC and BCC was 18 and 6 μF/cm^2, respectively. The values for AlCoCrFeNi were not quoted in **Table 3** because of poor reproducibility. Although the goodness of fit (χ^2) evaluated by the NOVA 2.1.4. Metrohm Autolab B.V. software for the selected equivalent circuits was not sufficient, some differences in corrosion behavior and tendencies could be deduced from the obtained data.

Typical surface damages of the investigated alloys in 3.5 wt% NaCl solutions after potentiodynamic polarization test are shown in **Figure 9**. In this environment, the dominant corrosion type is pitting corrosion, as evidenced by darker round-shaped areas. The EDS analyses in selected spots on the surface (**Figure 9**)

indicated depletion in Al and Ni (points 3, 4, and 5) compared with the neighboring areas which preserved chemical composition of the FCC phase (points 1 and 2).

DISCUSSION

It has been evidenced by many studies that mechanical properties of HEAs depend on the microstructure (Tang et al., 2013, Tang et al., 2015; Wang et al., 2018). Rapidly solidifying alloys produced by arc melting or additive manufacturing are generally nanostructured, and their nano-sized components are responsible for the dispersion strengthening effect. Subsequent processing, for example, heat treatments, may, however, lead to grain coarsening and loss of superb properties.

Very impressive differences in microstructure were visible in $AlCrFe_2Ni_2$ alloys produced by arc melting and ingot metallurgy. The distribution of phases in the baseline alloy, $AlCrFe_2Ni_2$, obtained by arc melting (**Figure 1A**) was practically the same as that earlier described by Dong et al. (2016), with characteristic vermicular FCC and nanostructured BCC phases, while in cast alloys with the same chemical composition, the nanostructures were absent, and grains were much coarser.

The results of several electrochemical tests carried out in this work indicate that there is a noticeable influence of grain size and distribution of phases on the exposed surface on the corrosion behavior. In the OCV measurements, the trends were similar for the three $AlCrFe_2Ni_2$ samples, that is, the potential increased with time, but the values recorded for the arc-melted material were less negative than those recorded for both cast ones. Numerous spikes on the OCV curves generally reflect local phenomena (pitting), such as damage of a protective layer by ions in the solution (Kabir and Mahmud, 2011). Polarization resistance describes the ability to resist the electron transfer from one phase to another. Values increasing over time suggest improvement of the corrosion resistance. The average values of polarization resistance over 20 consecutive cycles were higher for the arc-melted alloy than those for the cast ones. Significant scatter of the experimental points in consecutive cycles indicates that protective layers formed on alloy surfaces were not stable enough. Tafel polarization curves were very similar in shape, and again some of the derived characteristic parameters, such as corrosion current, pitting potential, and corrosion rate, listed in **Table 2**, were more advantageous for the arc-melted sample. The differences in corrosion behavior can be attributed to different relative areas of individual phases and density of grain/phase boundaries on the surface exposed to the solution, especially when some phases are more reactive than others, as is evidenced by depletion of the BCC phase in aluminum and nickel.

Chloride ions are known to interact with the native oxide films, leading to their breakdown, particularly in the areas where these films are thinner, for example, over intermetallic precipitates in Al-based alloys (Shao et al., 2003; Yasakau et al., 2006; Shi et al., 2017). Failure of the oxide barrier triggers chemical reactions of active metals, such as aluminum, with water, accompanied by the evolution of hydrogen:

$$2Al + 6H_2O = 2Al^{3+} + 6OH^- + 3H_2\uparrow.$$

Susceptibility of the exposed grains to pitting corrosion is also dependent on their crystallographic orientation - crystallographic planes with higher atomic density, higher coordination number, and lower surface energy are expected to be naturally more resistant (Shahryari et al., 2009). As it has been illustrated by numerous examples (Ralston et al., 2010), the reduced grain size has positive effects on corrosion rate only in cases when an oxide/passive film can form on the surface of metallic materials. Otherwise, dense grain boundaries are likely to increase surface reactivity and the corrosion rate. Also, segregation of impurities may contribute to the role of grain refinement in corrosion behavior (Miyamoto et al., 2008). Intergranular corrosion is, namely, often induced by impurity segregation and precipitation at grain boundaries. It has been reported that dilution of the segregated impurities at grain boundaries accounts for the beneficial effect of grain size reduction on corrosion resistance (Palumbo et al., 1990; Wang et al., 1993; Palumbo and Erb, 1999).

In the alloys investigated in this work, major impurities due to processing in air or argon were Al oxide or nitride particles. These might contribute to abrupt fluctuations of potential or current in electrochemical tests. There was no evidence, however, that the alloy processed in air was much more susceptible to pitting than the one processed in argon [$AlCrFe_2Ni_2$ (1) and $AlCrFe_2Ni_2$ (2), respectively]. Another issue is that all metals used for arc melting had better purity than those used for casting, and thus increased concentration of impurities in the intercrystalline regions of the coarse-grained microstructure might lead to worse corrosion resistance.

As mentioned earlier, the Mo additions contributed to some refinement of alloy microstructure. In sodium chloride solution, for the three Mo-containing alloys, the values of measured electrochemical parameters were less advantageous or comparable with the baseline arc-melted alloy. In the OCV measurements, the most striking difference was disappearance of potential spikes at the higher contents of Mo in the alloy, which suggested that local phenomena became less pronounced. In the Tafel plots, the curves shifted toward higher potentials with increasing content of Mo, and fluctuations of current were practically absent for $AlCrFe_2Ni_2Mo_{0.15}$. The values of charge transfer resistance (R_{ct}) derived from the Nyquist plot increased with the Mo content and were in a range typical of alloys with a similar composition and microstructure (Lu et al., 2015). The values of solution resistance (R_s) were similar for all the alloys and consistent with the earlier reported data (Kumar et al., 2017). The double layer capacitance (Q_{dl}) was approximately the same as reported by other researchers (Pan et al., 1998; Kumar et al., 2017). In comparison with other HEAs, such as $Al_xCrFe_{1.5}MnNi_{0.5}$ (Lee et al., 2008b),

$FeCoNiCrCu_x$ (Hsu et al., 2005) or $Co_{1.5}CrFeNi_{1.5}Ti_{0.5}Mo_x$ (Lee et al., 2008a), tested in NaCl solutions, all Co-free alloys investigated in this work had much better corrosion resistance.

Mo together with Cr in steels is very effective in preventing pitting corrosion in chloride-containing media. The exact mechanisms involved are not fully understood. It is believed that Cr and Mo oxides form barriers for the penetration of chloride ions. A number of researchers claimed that Mo in the passive layer on steels was present mostly in a form of adsorbed anions (MoO_4^{2-}), constituting a barrier against the electrochemical attack (Pourbaix, 1974; Kodama and Ambrose, 1977; Ogura and Ohama, 1984; Lu and Clayton, 1985; Brooks et al., 1986; Clayton and Lu, 1986). Mo was reported to lower the chloride ion content in the passive film on steel due to its ability to form soluble stable Mo–oxo–chloro complexes as well as insoluble chlorides and oxide chlorides on the surface (Wegrelius et al., 1999). In the case of HEAs containing aluminum in high proportions, the effect of Mo is by far less strong.

The increasing concentration of aluminum in HEAs generally leads to increased volume fraction of a BCC phase and enhancement of pitting corrosion, as illustrated by the behavior of a series of alloys, $Al_xCrFe_{1.5}MnNi_{0.5}$ (Lee et al., 2008a; Shi et al., 2017). The BCC phase with a low concentration of Cr and high concentration of Al produced porous nonprotective oxide layers in contact with a sodium chloride solution.

The detrimental role of the Al-rich component of the investigated alloys was clearly visible in electrochemical measurements conducted in 3.5 wt.% NaCl. The relative amount of the BCC phase in the equimolar quinary alloy was about 75 vol.%, while only about 40 vol.% in the Co-free baseline alloy and consequently the values of corrosion parameters were significantly worse: corrosion potential was much lower (−0.30 vs. −0.25 V), and corrosion current density was higher (0.116 vs. 0.049 $\mu A/cm^2$). The alloys denoted as BCC and FCC with compositions close to the major phases in the equimolar alloy presented very different chemical properties. The BCC alloy with the Al/Cr atomic ratio of about 7/1 had the lowest OCV, corrosion potential, and pitting potential values among all alloys investigated in this work. Compared with $AlCrFe_2Ni_2$, its corrosion current density and corrosion rate were roughly three times higher (0.141 $\mu A/cm^2$ and 13.6 × 10^{-4} mmpy, respectively). On the contrary, the alloy denoted as FCC with the reversed proportions of Al and Cr, Al/Cr atomic ratio of about 1/10, had very good corrosion resistance, comparable with the STS reference in terms of corrosion and pitting potential, corrosion current density, passivation range, and corrosion rate. It also showed exceptionally high polarization resistance and charge transfer resistance. These observations are consistent with the results previously published by other authors regarding the effects of Al, Mo, and Cr on corrosion resistance of some HEAs in aqueous environments containing chloride or sulfate species (Shi et al., 2017).

CONCLUSIONS

Electrochemical measurements in 3.5 wt% NaCl allowed formulation of the following conclusions regarding corrosion behavior of the investigated high-entropy alloys:

(1) Microstructure of the $AlCrFe_2Ni_2$ alloys determined by the manufacturing and processing conditions influenced their chemical behavior to some extent. Major role was attributed to the grain size, distribution of phases on the surface as well as amount and distribution of impurities. Nanostructures formed by spinodal decomposition contributed to the enhancement of corrosion resistance.
(2) The effect of Mo on pitting corrosion resistance was noticeable, especially at the highest concentration of this additive in the arc-melted alloys, that is, $AlCrFe_2Ni_2Mo_{0.15}$.
(3) The Al/Cr atomic ratio appeared crucial for the corrosion resistance of the investigated Al(Co)CrFeNi alloys because it conditioned formation of the Al-rich BCC phase and its susceptibility to spinodal decomposition.
(4) All experimental alloys investigated in this work, except the Cr-deficient quinary BCC, showed corrosion behavior better than many other HEAs described in the literature.
(5) The nanostructured Co-free alloy, $AlCrFe_2Ni_2$, which has been reported to have excellent combination of strength and ductility, outperformed the equimolar quinary alloy, AlCoCrFeNi, in terms of corrosion resistance owing to the higher volume fraction of the Al-deficient FCC phase.
(6) The $AlCrFe_2Ni_2$ alloy with minor addition of Mo and improved resistance to pit formation has good prospects for application.
(7) Systematic studies are underway to assess further possible improvements in corrosion resistance brought about by Mo in higher proportions also in the environments other than NaCl, and to clarify the mechanisms involved.

DATA AVAILABILITY STATEMENT

The raw data supporting the conclusions of this article will be made available by the authors, without undue reservation.

AUTHOR CONTRIBUTIONS

EG and UH provided general concept of this study, support, and supervision of experiments. MM-K, JC, and MJ were involved in planning and execution of corrosion tests, establishing the system of data collection and archiving. SG was involved in planning and execution of the arc-melting procedure, and characterization of the Co-free alloys. All authors contributed to characterization of samples at different stages of manufacturing and testing. JC wrote the first draft of the manuscript devoted to corrosion testing of the Co-free alloys. MM-K wrote the first draft on quinary alloys with Co. MM-K, JC, MJ, and EG were involved in the discussion and interpretation of experimental results as well as editing of the final version of the paper.

FUNDING

Investigations were conducted within a NADEA project (M-ERA.NET 2017) with a financial support from the National Science Centre Poland (UMO-2017/26/Z/ST8/01238). The measurements of quinary alloys were financed by the Polish Ministry of Science and Education—Subsidy No. 16.16.160.557.

ACKNOWLEDGMENTS

The authors acknowledge the contribution of M. Gajewska from the Academic Centre for Materials and Nanotechnologies, AGH UST, in Kraków PL, who performed TEM/EDS analyses of the quinary alloys, and Krzysztof Mars from the Faculty of Materials Science and Ceramics, AGH UST, who was involved in the manufacturing of these alloys.

REFERENCES

Brooks, A. R., Clayton, C. R., Doss, K., and Lu, Y. C. (1986). On the role of Cr in the passivity of stainless steel. *J. Electrochem. Soc.* 133, 2459–2464. doi:10.1149/1.2108450

Chou, Y. L., Yeh, J. W., and Shih, H. C. (2010). The effect of molybdenum on the corrosion behaviour of the high-entropy alloys Co1.5CrFeNi1.5Ti0.5Mox in aqueous environments. *Corros. Sci.* 52, 2571–2581. doi:10.1016/j.corsci.2010.04.004

Clayton, C. R., and Lu, Y. C. (1986). A bipolar model of the passivity of stainless steel: the role of Mo addition. *J. Electrochem. Soc.* 133, 2465–2473. doi:10.1149/1.2108451

Dong, Y., Gao, X., Lu, Y., Wang, T., and Li, T. (2016). A multi-component $AlCrFe_2Ni_2$ alloy with excellent mechanical properties. *Mater. Lett.* 169, 62–64. doi:10.1016/j.matlet.2016.01.096

Hsu, Y. J., Chiang, W. C., and Wu, J. K. (2005). Corrosion behavior of $FeCoNiCrCu_x$ high-entropy alloys in 3.5% sodium chloride solution. *Mater. Chem. Phys.* 92, 112–117. doi:10.1016/j.matchemphys.2005.01.001

Kabir, K. B., and Mahmud, I. (2011). Study of erosion–corrosion of stainless steel, brass and aluminum by open circuit potential measurements. *J. Chem. Eng.* 25, 13–17. doi:10.3329/jce.v25i0.7234

Kao, Y.-F., Lee, T.-D., Chen, S.-K., and Chang, Y.-S. (2010). Electrochemical passive properties of $Al_xCoCrFeNi$ (x = 0, 0.25, 0.50, 1.00) alloys in sulfuric acids. *Corros. Sci.* 52, 1026–1034. doi:10.1016/j.corsci.2009.11.028

Kodama, T., and Ambrose, J. R. (1977). Effect of molybdate ion on the repassivation kinetics of iron in solutions containing chloride ions. *Corrosion* 33, 155–161. doi:10.5006/0010-9312-33.5.155

Kumar, N., Fusco, M., Komarasamy, M., Mishra, R. S., Bourham, M., and Murty, K. L. (2017). Understanding effect of 3.5 wt.% NaCl on the corrosion of $Al_{0.1}CoCrFeNi$ high-entropy alloy. *J. Nucl. Mater.* 495, 154–163. doi:10.1016/j.jnucmat.2017.08.015

Lee, C. P., Chang, C. C., Chen, Y. Y., Yeh, J. W., and Shih, H. C. (2008a). Effect of the aluminium content of $Al_xCrFe_{1.5}MnNi_{0.5}$ high-entropy alloys on the corrosion behaviour in aqueous environments. *Corros. Sci.* 50, 2053–2060. doi:10.1016/j.corsci.2008.04.011

Lee, C. P., Chen, Y. Y., Hsu, C. Y., Yeh, J. W., and Shih, H. C. (2008b). Enhancing pitting corrosion resistance of $Al_xCrFe_{1.5}MnNi_{0.5}$ high-entropy alloys by anodic treatment in sulfuric acid. *Thin Solid Films.* 517, 1301–1305. doi:10.1016/j.tsf.2008.06.014

Lin, C.-M., and Tsai, H.-L. (2011). Evolution of microstructure, hardness, and corrosion properties of high-entropy $Al_{0.5}CoCrFeNi$ alloy. *Intermetallics* 19, 288–294. doi:10.1016/j.intermet.2010.10.008

Lu, Y. C., and Clayton, C. R. (1985). Evidence for a bipolar mechanism of passivity in Mo bearing stainless steels. *J. Electrochem. Soc.* 132, 2517–2518. doi:10.1149/1.2113614

Lu, Y., Dong, Y., Guo, S., Jiang, L., Kang, H., Wang, T., et al. (2015). A promising new class of high-temperature alloys: eutectic high-entropy alloys. *Sci. Rep.* 4, 6200. doi:10.1038/srep06200.

Mahato, N., and Singh, M. M. (2011). Investigation of passive film properties and pitting resistance of AISI 316 in aqueous ethanoic acid containing chloride ions using electrochemical impedance spectroscopy (EIS). *Port. Electrochim. Acta.* 29, 233–251. doi:10.4152/pea.201104233

Miracle, D., and Senkov, O. (2016). A critical review of high entropy alloys and related concepts. *Acta Mater.* 122, 448–511. doi:10.1016/j.actamat.2016.08.081

Miyamoto, H., Harada, K., Mimaki, T., Vinogradov, A., and Hashimoto, S. (2008). Corrosion of ultra-fine grained copper fabricated by equal-channel angular pressing. *Corros. Sci.* 50, 1215–1220. doi:10.1016/j.corsci.2008.01.024

Ogura, K., and Ohama, T. (1984). Pit formation in the cathodic polarization of passive iron IV. Repair mechanism by molybdate, chromate and tungstate. *Corrosion* 40, 47–51. doi:10.5006/1.3593909

Osório, W. R., Freitas, E. S., and Garcia, A. (2013). EIS and potentiodynamic polarization studies on immiscible monotectic Al–In alloys. *Electrochim. Acta.* 102, 436–445. doi:10.1016/j.electacta.2013.04.047

Palumbo, G., and Erb, U. (1999). Enhancing the operating life and performance of lead-acid batteries via grain-boundary engineering. *MRS Bull.* 24, 27–32. doi:10.1557/s0883769400053422

Palumbo, G., Thorpe, S. J., and Aust, K. T. (1990). On the contribution of triple junctions to the structure and properties of nanocrystalline materials. *Scr. Metall. Mater.* 24, 1347–1350. doi:10.1016/0956-716x(90)90354-j

Pan, J., Leygraf, C., Jargelius-Pettersson, R. F. A., and Linden, J. (1998). Characterization of high-temperature oxide films on stainless steels by electrochemical-impedance spectroscopy. *Oxid. Met.* 50, 431–455. doi:10.1023/A:1018856808917

Park, H.-J., and Lee, H.-W. (2014). Effect of alloyed Mo and W on the corrosion characteristics of super duplex stainless steel weld. *Int. J. Electrochem. Sci.* 9, 6687–6698.

Pickering, E. J., and Jones, N. G. (2016). High-entropy alloys: a critical assessment of their founding principles and future prospects. *Int. Mater. Rev.* 61, 183–202. doi:10.1080/09506608.2016.1180020.

Pourbaix, M. (1974). *Atlas of electrochemical equilibria in aqueous solutions*. Houston, TX: NACE.

Qiu, Y., Thomas, S., Gibson, M. A., Fraser, H. L., and Birbilis, N. (2017). Corrosion of high entropy alloys. *NPJ Mater. Degrad.* 1, 1–18. doi:10.1038/s41529-017-0009-y

Ralston, K. D., Birbilis, N., and Davies, C. H. J. (2010). Revealing the relationship between grain size and corrosion rate of metals. *Scr. Mater.* 63, 1201–1204. doi:10.1016/j.scriptamat.2010.08.035

Rodrigues, J. F. Q., Padilha, G. S., Bortolozo, A. D., and Osório, W. R. (2020). Effect of sintering time on corrosion behavior of an Ag/Al/Nb/Ti/Zn alloy system. *J. Alloys Comp.* 834, 155039. doi:10.1016/j.jallcom.2020.155039

Rodriguez, A. A., Tylczak, J. H., Gao, M. C., Jablonski, P. D., Detrois, M., Ziomek-Moroz, M., et al. (2018). Effect of molybdenum on the corrosion behavior of high-entropy alloys $CoCrFeNi_2$ and $CoCrFeNi_2Mo_{0.25}$ under sodium chloride aqueous conditions. *Adv. Mater. Sci. Eng.* 2018, 1–11. doi:10.1155/2018/3016304

Shahryari, A., Szpunar, J. A., and Omanovic, S. (2009). The influence of crystallographic orientation distribution on 316LVM stainless steel pitting behavior. *Corros. Sci.* 51, 677–682. doi:10.1016/j.corsci.2008.12.019

Shang, X.-L., Wang, Z.-J., Wu, Q.-F., Wang, J.-C., Li, J.-J., and Yu, J.-K. (2018). Effect of Mo addition on corrosion behavior of high-entropy alloys CoCrFeNiMox in aqueous environments. *Acta Metall. Sin. (Engl. Lett.)* 32, 41. doi:10.1007/s40195-018-0812-7

Shao, M., Fu, Y., Hu, R., and Lin, C. (2003). A study on pitting corrosion of aluminum alloy 2024-T3 by scanning microreference electrode technique. *Mater. Sci. Eng. A* 344, 323–327. doi:10.1016/S0921-5093(02)00445-8

Shi, Y., Yang, B., and Liaw, P. (2017). Corrosion-resistant high-entropy alloys: a review. *Metals* 7, 43. doi:10.3390/met7020043.

Tang, Z., Gao, M. C., Diao, H., Yang, T., Liu, J., Zuo, T., et al. (2013). Aluminum alloying effects on lattice types, microstructures, and mechanical behavior of high-entropy alloys systems. *JOM* 65, 1848–1858. doi:10.1007/s11837-013-0776-z

Thang, Z., Senkov, O. N., Parish, C. M., Zhang, C., Zhang, F., Santodonato, L. J., et al. (2015). Tensile ductility of an AlCoCrFeNi multi-phase high-entropy alloy through hot isostatic pressing (HIP) and homogenization. *Mater. Sci. Eng. A* 647, 229–240. doi:10.1016/j.msea.2015.08.078

Valeriano, L., Correa, E. O., Mariano, N. A., Robin, A. L. M., Machado, C., Tommaselli, M., et al. (2019). Influence of the solution-treatment temperature and short aging times on the electrochemical corrosion behaviour of Uns S32520 super duplex stainless steel. *Mat. Res.* 22, 1–7. doi:10.1590/1980-5373-2018-0774

Wang, N., Palumbo, G., Wang, Z., Erb, U., and Aust, K. T. (1993). On the persistence of four-fold triple line nodes in nanostructured materials. *Scr. Metall. Mater.* 28, 253–256. doi:10.1016/0956-716x(93)90572-a

Wang, Q., Lu, Y., Yu, Q., and Zhang, Z. (2018). The exceptional strong face-centered cubic phase and semi-coherent phase boundary in a eutectic dual-phase high entropy alloy AlCoCrFeNi. *Sci. Rep.* 8, 1–7. doi:10.1038/s41598-018-33330-0.

Wegrelius, L., Falkenberg, F., and Olefjord, I. (1999). Passivation of stainless steels in hydrochloric acid. *J. Electrochem. Soc.* 146, 1397–1406. doi:10.1149/1.1391777

Yasakau, K. A., Zheludkevich, M. L., Lamaka, S. V., and Ferreira, M. G. S. (2006). Mechanism of corrosion inhibition of AA2024 by rare-earth compounds. *J. Phys. Chem. B* 110, 5515–5528. doi:10.1021/jp0560664

Zhang, X. L., Jiang, Z. H., Yao, Z. P., Song, Y., and Wu, Z. D. (2009). Effects of scan rate on the potentiodynamic polarization curve obtained to determine the Tafel slopes and corrosion current density. *Corros. Sci.* 51, 581–587. doi:10.1016/j.corsci.2008.12.005

Zhang, Y., Zuo, T. T., Tang, Z., Gao, M. C., Dahmen, K. A., Liaw, P. K., et al. (2014). Microstructures and properties of high-entropy alloys. *Prog. Mater. Sci.* 61, 1–93. doi:10.3390/ma1203037010.1016/j.pmatsci.2013.10.001

Conflict of Interest: The authors declare that the research was conducted in the absence of any commercial or financial relationships that could be construed as a potential conflict of interest.

frontiers in Materials

ORIGINAL RESEARCH
published: 22 April 2021
doi: 10.3389/fmats.2020.533843

Corrosion Behavior of Al0.1CoCrFeNi High Entropy Alloy in Various Chloride-Containing Solutions

K. Wang, A. D. Lan and J. W. Qiao**

College of Materials Science and Engineering, Taiyuan University of Technology, Taiyuan, China

The present work investigates the corrosion behavior of $Al_{0.1}$CoCrFeNi high entropy alloy (HEA) in various concentrations of chloride-containing solutions. Electrochemical tests exhibit overall excellent corrosion resistance of this alloy against the attack of Cl^--containing solutions. The main type of corrosion topography presents an intergranular feature. In addition, electrochemical impedance spectroscopy (EIS) investigation of the HEA samples under immersion test suggests chloride anion–containing environment leads to the decline of passivation film quality. Further analysis of XPS results reveals that significant amounts of elements exist with atomic states in the passive films.

OPEN ACCESS

Keywords: SEM, XPS, passive film analysis, pitting, EIS, corrosion

Edited by:
Mark L. Weaver,
University of Alabama, United States

Reviewed by:
Liang-Yu Chen,
Jiangsu University of Science and Technology, China
Gregory Kubacki,
University of Alabama, United States

****Correspondence:***
A. D. Lan
lanaidong@tyut.edu.cn
J. W. Qiao
qiaojunwei@gmail.com

Specialty section:
This article was submitted to Structural Materials, a section of the journal Frontiers in Materials

Received: *10 February 2020*
Accepted: *29 December 2020*
Published: *22 April 2021*

Citation:
Wang K, Lan AD and Qiao J W (2021) Corrosion Behavior of Al0.1CoCrFeNi High Entropy Alloy in Various Chloride-Containing Solutions. Front. Mater. 7:533843. doi: 10.3389/fmats.2020.533843

INTRODUCTION

Recently high-entropy alloys (HEAs), usually containing five or more alloying elements in approximately equal molar concentrations, have been the focal point of intensive research and investigations due to its tremendous application prospects and scientific significance (Yeh et al., 2004; Green et al., 2013; Gludovatz et al., 2014; Miracle et al., 2014; Senkov et al., 2016). Compared with conventional alloys, HEAs possess excellent microstructural stability and mechanical properties (Chen et al., 2005; Tong et al., 2005; Kao et al., 2009; Hou et al., 2017; Hou et al., 2019; Song et al., 2019).

In addition, HEAs are also considered as promising candidates for practical corrosion-resistant applications because most HEAs consist of corrosion-resistant and passivating elements and are generally free of common corrosion initiate sites such as impurities and inclusions. For instance, there are many studies on the corrosion resistance of Al_xCoCrFeNi alloy system, which has been extensively studied due to its multiple excellent properties (Zhou et al., 2007; Kao et al., 2010; Lin and Tsai, 2011; Wang et al., 2012; Kumar et al., 2017; Shi et al., 2017; Shi et al., 2018). Among them, the Al0.1CoCrFeNi of single-phase face centered cubic (FCC) exhibited extremely high pitting potential and strong corrosion resistance characteristics (Kao et al., 2010; Lin and Tsai, 2011; Kumar et al., 2017; Shi et al., 2017; Shi et al., 2018). Note that the constituent elements of this HEAs system, such as Al, Co, and Fe, are not the corrosion-resistant elements in the traditional sense. From the standpoint of its application and longtime service in real conditions, it is fairly necessary for further research on the corrosion behavior and mechanism of this HEAs alloy.

Therefore, in this work, the corrosion behavior of as-cast $Al_{0.1}$CoCrFeNi (at%) (a single-phase solid solution with FCC structure and almost no component segregation) with a typical dendritic structure in various concentrations of NaCl and Na_2SO_4+NaCl was studied, and the research mainly focuses on potentiodynamic polarization tests, corrosion morphology, passive films, and pitting process.

EXPERIMENTAL PROCEDURE

The $Al_{0.1}CoCrFeNi$ alloy ingots were prepared by vacuum arc melting in a water-cooled copper crucible under a Ti-gettered argon atmosphere. A mixture of the ultrasonically cleansed Al, Co, Cr, Fe, and Ni elements with purity higher than 99.5 wt% was carefully weighted. Compositional homogeneity of the alloy ingots was ensured by flipping over and remelting at least 5 times. Each as-cast rod sample (diameter of 3 mm) was further cut into smaller cylindrical pieces with a length of 3 mm by wire Electrical Discharge Machining (EDM). The surfaces in subsequent tests are all referring to the cross section faces which have an approximate area of $0.07cm^2$. Then, each sample was polished into a mirror-like surface using SiC grit papers (up to grit No. 2000) and alumina polishing agent with a granularity of 2.5 μm. Before the electrochemical and surface analytical tests, all polished specimens were ultrasonically cleaned with distilled water and ethanol and dried up in air. Each electrochemical experiment was carried out at least three times to ensure reproducibility.

In this work, NaCl solutions with concentrations spanning three orders of magnitude were chosen as experimental media (1.5, 1.0, 0.8, 0.6, 0.5, 0.1, 0.05, and 0.01 M). Another corrosion media was chloride-containing Na_2SO_4 solutions with various concentrations. The choice of NaCl solution is certainly for the purpose of investigation of pitting corrosion resistance which usually occurs in chloride-containing solutions. The addition of Na_2SO_4 in the second solution is just a buffer for the pure scientific purpose. All electrochemical experiments were performed using a CHI600 electrochemical measurement system. A three-electrode setup was employed to conduct all the electrochemical tests, which contains a Pt mesh counter electrode and a saturated calomel electrode (SCE); the values of potentials reported in this article are all referred to as V_{SCE} which is equivalent to +0.244 V_{SHE}.

Potentiodynamic polarization and electrochemical impedance spectroscopy (EIS) have been utilized to demonstrate the corrosion resistance behaviors of HEA samples in a variety of test solutions. After 1800s open circuit potential measurement, the equilibrium potential was chosen to be the initial potential for AC impedance test, and the amplitude potential is set to be 5 mV. EIS spectra were acquired with a frequency scan range from 100,000 to 0.01 Hz. Potentiodynamic polarization tests were performed through a range of −0.8–1.3 V with a scanning rate of 1 mV/s. After polarization tests, scanning electron microscope (SEM) was used to characterize the surface morphology of samples, and electron dispersion spectroscopy (EDS) was employed to obtain the corresponding elemental distribution information. A TESCAN LYRA 3 XMH SEM was utilized in this investigation.

For further composition information of the passive film formed under chloride-containing solution, X-ray photoelectron spectroscopy (XPS) has been conducted by using an ESCALAB 250Xi X-photoelectron spectrometer with monochromatized Al K α excitation (hν = 1,486.6 eV). XPS analysis was performed on two samples (denoted as sample 1 and 2). Sample 1 underwent 1800s potentiostatic passivation at 0.5 V potential in 0.5 M NaCl and sample 2 went through a full potentiodynamic polarization test in 0.5 M NaCl. Before XPS tests, both specimens were pretreated at a polarization voltage of −1 V for 5 min to remove the oxide on their surface.

In order to get further understanding of corrosion process of material under chloride-containing solutions, a prepassivation sample (half-hour potentiostatic passivation) at 0.5 M H_2SO_4 solution was chosen to conduct immersion test at 3.5wt% NaCl solution. EIS test was conduct on the immersed sample at the time points of 1 h, 5 h, 100 h and 200 h, respectively.

RESULTS AND DISCUSSION

The Analysis of Electrochemical Test

Potentiodynamic polarization tests have been carried out on $Al_{0.1}CoCrFeNi$ HEA samples in a variety of chloride ion–containing solutions. **Figures 1A,B** present the polarization curves obtained in NaCl and Na_2SO_4+NaCl solutions, respectively. As shown in **Figure 1A**, regardless of the variation of NaCl concentrations, the $Al_{0.1}CoCrFeNi$ exhibits a considerable range of passivation. The passivation current densities increase with the increase of the NaCl concentrations, but not in a monotonic manner. When a certain polarization potential is reached, the pitting or transpassivation occurs as shown in each curve. Close inspection of **Figure 1A** shows that the variation of chloride concentration has an impact on initial passivation stage which takes place around −0.2–0.0 V. To illustrate, for samples in low solution concentrations self-passivation tends to occur without an obvious active-passive peak while for samples in higher solution concentrations one can see a distinct active-passive conversion peak. **Figure 1B** presents the variation of polarization curves with the addition of Na_2SO_4. Apparently, presence of another anion in solution has a marked effect on the active-passive process of the $Al_{0.1}CoCrFeNi$ sample; i.e., the active-passivation peak moves toward negative direction with the increase of chloride concentration.

To appraise the corrosion resistance of $Al_{0.1}CoCrFeNi$ HEAs, parameters such as corrosion current density (I_{corr}) and corrosion potential E_{corr} were derived from polarization curves by the Tafel extrapolation method. The data obtained from **Figure 1A** are plotted out in **Figure 2**. Evidently shown in **Figure 2A**, all the I_{corr} values are in the range of 0–5 ($\mu A/cm^2$), which are very low corrosion rate, suggesting a rather excellent corrosion resistance of $Al_{0.1}CoCrFeNi$ HEAs in NaCl solution. It is also noteworthy that the values of E_{corr} generally decrease with the increase of NaCl concentration, indicating the higher corrosion tendency in higher concentration of NaCl.

It is well established that the corrosion of $Al_{0.1}CoCrFeNi$ HEA in salt solution is mainly oxygen-consuming corrosion. The correlation of corrosion rate I_{corr} vs. salt concentrations should concern two factors: anion concentration and dissolved oxygen content. On one hand, increase of salt concentration generally leads to higher conductivity of the solution, which might provide a beneficial effect on the ongoing corrosion process. On the other hand, the increase of ionic concentration tends to reduce the

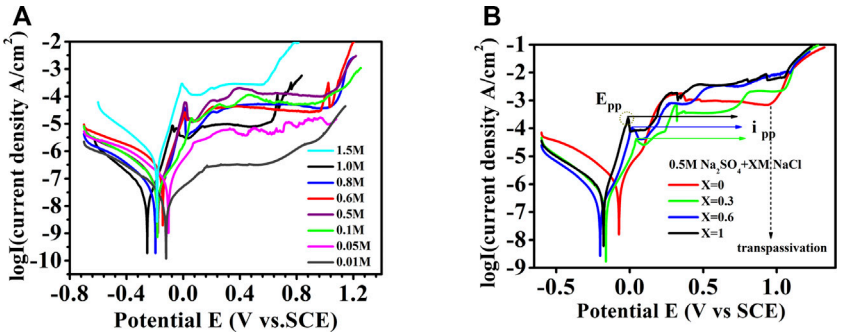

FIGURE 1 | Potentiodynamic polarization test results for $Al_{0.1}CoCrFeNi$ in different concentrations of Cl^- containing solution, **(A)** NaCl and **(B)** Na_2SO_4+NaCl.

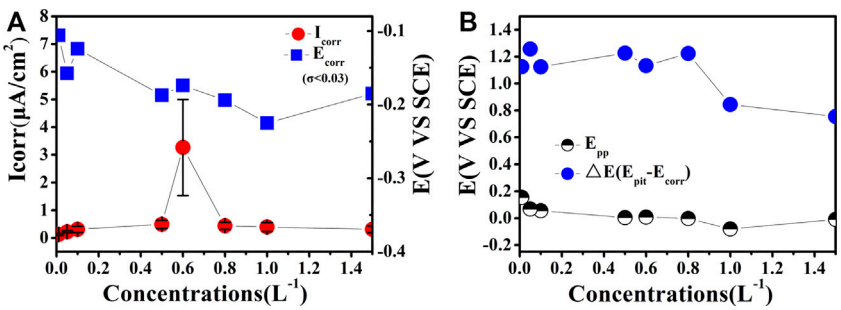

FIGURE 2 | Schematic illustrations of the main corrosion parameters derived from electrochemical tests for Al0.1CoCrFeNi in different concentrations of NaCl solution; all the standard deviation σ of the potential indicators are below 0.03 and there is no error bar identification for them.

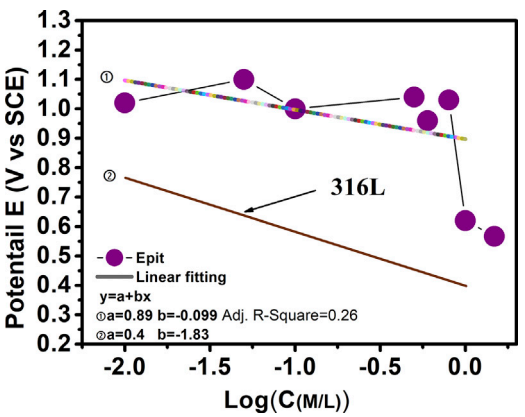

FIGURE 3 | Linear relationship between pitting potential and logarithm of chloride ion concentration.

content of dissolved oxygen and hence leads to the suppression of the cathodic reaction and results in an ultimate weakened corrosion process (Tian et al., 2015). This oxygen supply shortage induced corrosion current densities decrease might offset the increase induced by increased chloride concentration, resulting in a peak current (i_{corr}) at 0.6 M NaCl as shown in **Figure 2A**.

Several parameters for evaluation of passivation properties derived from **Figure 1A** are illustrated in **Figure 2B**. The passivation potential (E_{pp}) generally marks the beginning of passivation. As shown in **Figure 2B**, the E_{pp} values exhibit no clear variation tendency with the increase of Cl^- concentration.

In addition, **Figure 2B** also presents the variation of another metric for evaluating the corrosion behavior, the pitting resistance ($\Delta E = E_{pit}-E_{corr}$) (Ayyagari et al., 2018). One can see in **Figure 2B** that, for the $Al_{0.1}CoCrFeNi$ HEA, the ΔE values lie within the range of 0.8 V ~ 1.2 V with a span of Cl^- concentration up to three orders of magnitude. These values are better than most of the reported HEA alloy systems except that of Ti-containing HEAs (Ayyagari et al., 2018), demonstrating excellent pitting resistance of the $Al_{0.1}CoCrFeNi$ HEA samples.

Point defect model (PDM) proposed that the pitting potential (E_{pit}) has a linear relationship with the logarithm of chloride concentration (Laycock and Newman, 1997). **Figure 3** illustrates the variation of E_{pit} values vs. logarithmical Cl^- concentration. As shown in **Figure 3**, the colorful fitting line suggests that the E_{pit} decreases roughly in a linear way with the increase of the $logC_{Cl^-}$, except two high concentration points. For the sake of comparison, the published results for 316 L stainless steel is also plotted in the graph. It can be clearly seen that the slope for 316 L is slightly higher than that of the $Al_{0.1}CoCrFeNi$ HEA, suggesting this HEA is less susceptible to the point corrosion induced by the detrimental Cl^-. Note that the E_{pit} of

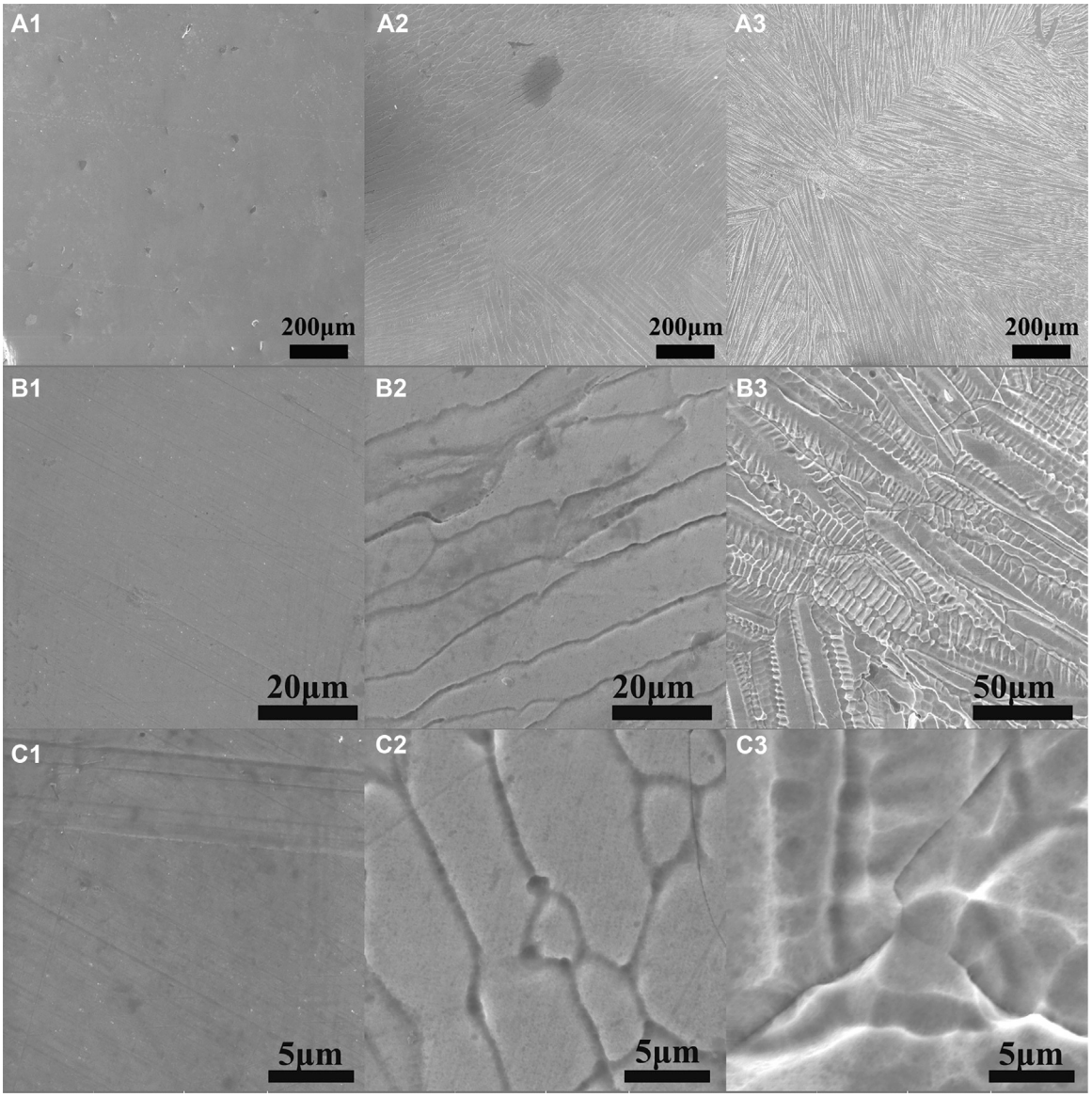

FIGURE 4 | SEM images of Al0.1CoCrFeNi samples after polarization tests. a, b, and c are respectively for the samples in NaCl solutions with concentrations of 0.1, 0.5, and 1.0 M.

$Al_{0.1}$CoCrFeNi HEA is averagely 0.4 V higher than that of 316 L, indicating a rather superior pitting resistance. The reason why this particular HEA is "better" than others is not clear at this moment. However, the answer is likely associated with the synergism of two passivating elements of Al and Cr. It is also worth noting that the plots of 1.0 and 1.5 M have a severe deviation from the fitted line, which is not clear at this moment.

Microstructure and Chemical Analysis

In order to acquire detailed information about the corrosion morphology of $Al_{0.1}$CoCrFeNi HEA in chloride containing solution, SEM investigation was carried out on the specimens after potentiodynamic polarization tests, and major results are shown in **Figure 4**. Careful inspection of the SEM images in **Figure 4** reveals that there is a distinctive morphology difference with the increase of NaCl concentration. To be brief, there is no recognized feature on the surface morphology for samples in low concentration of NaCl solution (0.1 M), and clear evidence of initiation of corrosion can be probed for samples in the salt solution of higher concentration of (0.5 M). For the samples in 1.0 M NaCl solution, typical interdendrite corrosion patterns are present. It is likely that the corrosion of $Al_{0.1}$CoCrFeNi HEA was initiated in intergranular region and propagated in interdendrite region with the increase of chloride concentration.

Three types of pitting topography were probed in the images obtained from Al0.1CoCrFeNi samples after electrochemical tests in chloride solution. **Figure 5** shows some images about these three pitting topographies found in various samples. **Figures 5E,F** presents

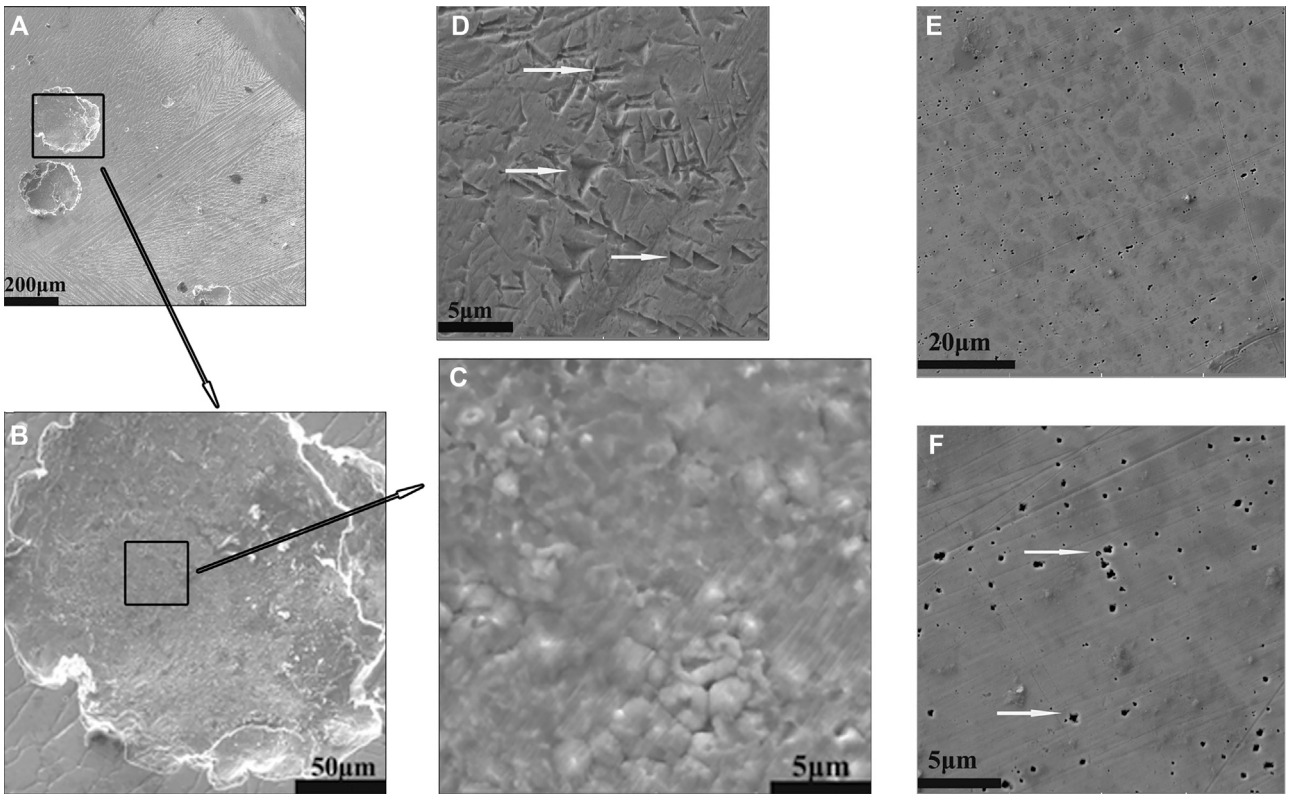

FIGURE 5 | Three types of pitting topography for Al0.1CoCrFeNi samples: **(A–C)** are for 0.4 M NaCl; **(D)** is for 1 M NaCl; and **(E, F)** are for 0.1 M NaCl.

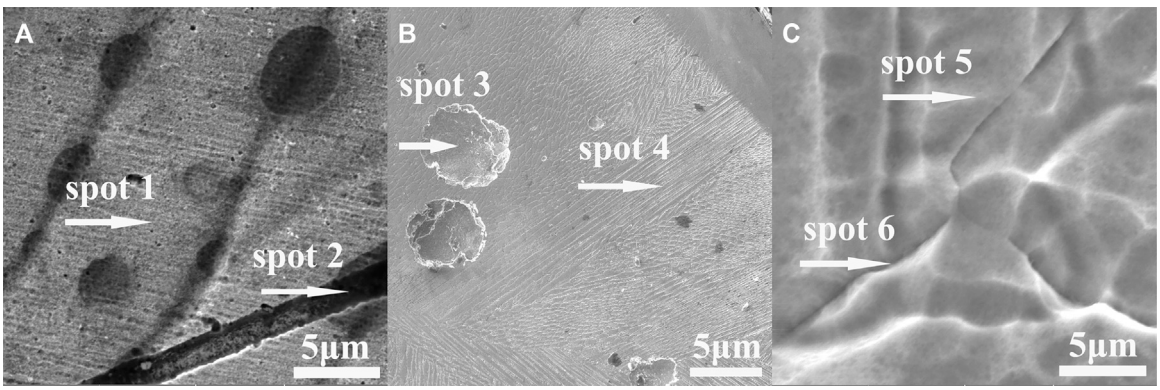

FIGURE 6 | EDS analysis of selected SEM images: **(A–C)** are respectively for the concentrations of 0.1, 0.4, and 1.0 M in NaCl solutions. The test locations are dendrite, pits, and grain boundary.

the tiny pitting pits usually found in low chloride concentration (0.1 M). **Figures 5A,B** shows the big round pit normally found in higher concentration of 0.4 M NaCl solution. **Figure 5D** exhibits the pits of irregular shape which are frequently observed in Cl^- concentrations greater than 1.0 M. The correlation between the pitting topography and chloride concentration reveals the complexity of the nucleation and development of chloride-induced pitting process, which is not clear yet.

For further elemental composition evidence, EDS tests were conducted in selected locations in some SEM images of Al0.1CoCrFeNi samples. The selected spots such as dendrite, pits, and grain boundary are shown in **Figure 6** and corresponding elemental distribution results are listed in **Table 1**.

As manifestly shown in **Table 1**, the elemental distribution of each element between dendrite and interdendrite is essentially the same, indicating the absence of obvious elemental segregation.

TABLE 1 | EDS analysis on the surface of samples after corrosion in NaCl.

NaCl (M/L)	Selected point		Al (%)	Co (%)	Cr (%)	Fe (%)	Ni (%)
0.05	Spot 1	Dendrite	2.1	25.2	23.9	25.8	23.0
	Spot 2	Grain boundary	3.2	25.0	29.2	26.4	16.1
0.4	Spot 3	Pit	2.7	24.2	24.4	25.3	23.4
	Spot 4	Outside the pit	1.3	24.6	29.6	24.4	20.1
0.8	Spot 5	Dendrite	1.9	24.8	24.5	24.5	24.3
	Spot 6	Interdendrite	2.3	24.6	24.6	24.7	23.8

Comparison of elemental distribution between dendrites and the grain boundary suggests that there is slight Cr enrichment and Ni depletion in grain boundary. It can be understandable considering that with the presence of Cl^-, element Ni is more susceptible to dissolution among the alloying metallic elements in this HEAs alloy. Conversely, element Cr is the most stable one according to the literature (Keller and Strehblow, 2004).

XPS Investigation

For $Al_{0.1}$CoCrFeNi HEA, the presence of multiple passive elements demands further chemical evidence of the sample surface to get better understanding of the passivation mechanism. XPS analyses were undertaken to attain information with respect to surface compositions and elemental chemical status vs. anodic polarization. Two samples were selected (denoted as sample 1 and 2), and 400s cathodic polarization at −1.0 V was conducted for each sample in order to remove the outside oxides. Sample 1 was conducted by 1800s potentiostatic polarization in 0.5 M NaCl in order to make the newly formed oxide film stable and integral; sample 2 was the specimen after potentiodynamic polarization test in 0.5 M NaCl.

Major XPS analysis results are presented in **Figure 7**. Before analysis, the positions of binding energy were calibrated by comparing the binding energy of the C 1s peak to its standard binding energy, 284.8 eV. **Figure 7** presented the adjusted core level XPS spectra of Fe2p, Cr 2p, Ni 2p, Co 2p, and O1s.

The deconvolution fittings take into account the fact that there are spin-orbit splittings inducing doublet separation for Cr 2p, Ni 2p, Fe 2p, and Co 2p spectra, with 9.2 eV splitting between the Cr $2p_{1/2}$ and Cr $2p_{3/2}$, 17.3 eV splitting between the Ni $2p_{1/2}$ and Ni $2p_{3/2}$, 13.2 eV splitting between the Fe $2p_{3/2}$ and Fe $2p_{1/2}$, and 15.4 eV splitting between the Co $2p_{3/2}$ and Co $2p_{1/2}$, respectively.

The deconvolution fittings of Cr, Co, Fe, and Ni reveal the appearance of two distinct chemical states of all these metallic elements: elemental and oxidized. Therefore, these spectra are all fitted by two photoelectron doublets. For example, two peaks located around 574.3 and 583.5 eV (representing Cr $2p_{3/2}$ and Cr $2p_{1/2,}$ respectively) are designated by the photoelectron doublet of Cr and the two peaks located at 576.6 and 585.5 eV are designated

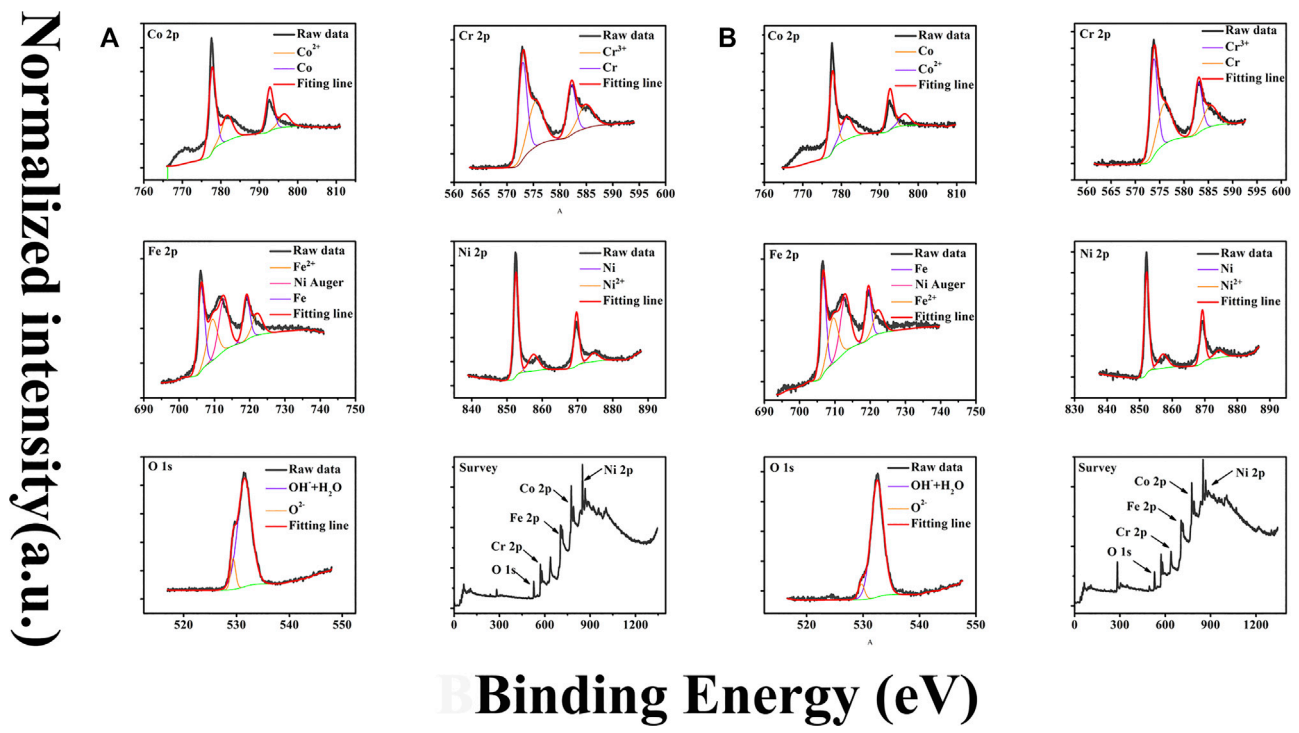

FIGURE 7 | (A) and **(B)** are XPS spectra for sample 1 and 2, respectively. Data for each sample include Fe2p, Ni2p, Cr2p, Co2p, O1s, and the survey spectrum. The black lines are measurements data and the ones with color are their fitting results.

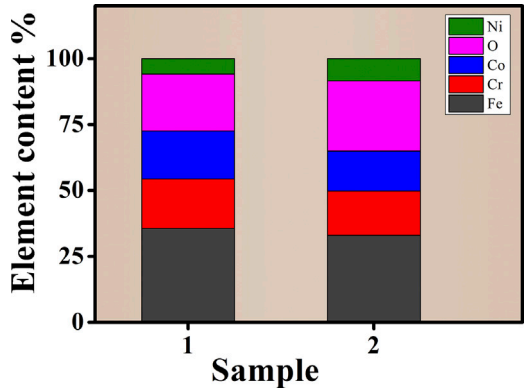

FIGURE 8 | The element contents (at%) in passivation films of sample 1 and 2.

by the photoelectron doublet of Cr^{2+}. The peaks of Ni $2p_{3/2}$ at 852.6 and 854.3 eV are designated to Ni and Ni^{2+}, respectively, and the ones of Co $2p_{3/2}$ at 778.3 and 780.9 eV are designated to Co and Co^{2+}, respectively.

The absence of photoelectron peaks of Al in both survey spectra shown in **Figure 7** indicates that the amount of elemental Al in the surface film is virtually beyond the detection limit of the instrument, suggesting Al element in passive films is not stable with the presence of Cl^-. The elemental distributions of two samples are illustrated in **Figure 8**. Examination of **Figure 8** suggests that the difference of element content between sample 1 and 2 is nearly neglectable. Among all elements in films, Fe element is with the largest amount and its content reaches 35 and 33% for sample 1 and 2; Cr and Co have similar contents around 15%; Ni element has a minimum content of 5 and 8% for sample 1 and 2, respectively. Surprisingly, the O element is 25 and 31% for the two samples which is far below the values attained in films formed in H_2SO_4 according to our unpublished work and other research. The relatively less oxygen content suggests a significant number of elements exist with atomic state in the passive film. Detailed chemical state distributions of various elements derived from XPS data fitting are listed in **Table 2**. Careful inspection of **Table 2** reveals that the percentage of atomic state is indeed higher than that of oxidation state of each element and even reaches around 70% for Ni and Co. The observed oxygen deficiency in the passive film of $Al_{0.1}$CoCrFeNi HEA might be due to the competitive adsorption of oxygen and chloride.

It is noteworthy that the history of the passive film formation in sample 1 and 2 is quite different. In particular, the high potential exerted on sample 2 at the end of potentiodynamic polarization test might lead to the following situations independently or simultaneously: transpassivation of passive films, and micropitting formation. Therefore, it is of a little surprise to observe the striking similarity of the elemental and valence distribution between the two samples.

Electrochemical Impedance Spectroscopy Investigation of Immersion Test

To further explore the mechanism of pitting process for $Al_{0.1}$CoCrFeNi HEA, the immersion test was conducted. The chosen sample was passivated in 0.5 M H_2SO_4 at 0.4 V (referring to Mercury sulfate reference electrode) for 1800s, then immersion media is 3.5wt% NaCl solution. During immersion, interval acquisition data of EIS continued till the end of immersion test. Before every data collection for EIS, open circuit potential measurement was conducted to set an initial potential for AC impedance test. **Figure 9** presents the EIS data attained at various immersion duration such as 1 h, 5 h, 100 h, and 200 h. A common model for electrode with passive film was chosen as the equivalent circuit for EIS fitting, which was shown in **Figure 9D**. As shown in **Figure 9D**, the equivalent circuit consists of a constant phase element (CPE), capacitance of passive film (CPE_f), film resistance (R_f), a Warburg diffusional impedance parameter (W_f), CPE capacitance of film electrolyte interface (CPE_{fle}), film electrolyte interface resistance (R_{fle}), and solution resistance (R_s). The value of Z_{CPE} and Z_W can be given by the following equation (Jeyaprabha et al., 2006; Bentiss et al., 2009):

$$Z_{CPE} = Y0^{-1}(j\omega)^{-n}, \quad (1)$$

$$Z_W = Y0^{-1}(2\omega)^{-\frac{1}{2}}(1-j), \quad (2)$$

where Y0 is the proportionality factor (Y0>0), j is the imaginary unit, ω is the angular frequency, and n is a dimensionless index. For example, it represents a pure capacitor, when n = 1; a pure resistance for n = 0; a Warburg impedance for n = 0.5; and an inductance for n = −1. And the EIS data have been fitted by software Z-sim.

As shown in **Figure 9A**, the Nyquist graphs underwent significant change with the variation of immersion duration. Namely, with immersion time varying from 1 to 5 h, the big semicircle arc dramatically changes to a much smaller arc with a straight-line tail. With further increase of immersion time, the shape alteration is becoming smaller and only the size of arc keeps shrinking with a much slower rate. Generally speaking, there is a positive correlation between the size of the arc and the corrosion resistance, the bigger the size, the higher the corrosion resistance. The sharp drop of the arc size in the first 5 h of immersion

TABLE 2 | Valence states distribution of each element derived from the XPS data for sample 1 and 2.

Sample	Composition of valence states for each element (at%)						Fe (valence)	
	Cr (valence)		Ni (valence)		Co (valence)			
1	55 (0)	45 (+3)	76 (0)	24 (+2)	68 (0)	32 (+2)	57 (0)	43 (+3)
2	56 (0)	44 (+3)	78 (0)	22 (+2)	67 (0)	33 (+2)	55 (0)	45 (+3)

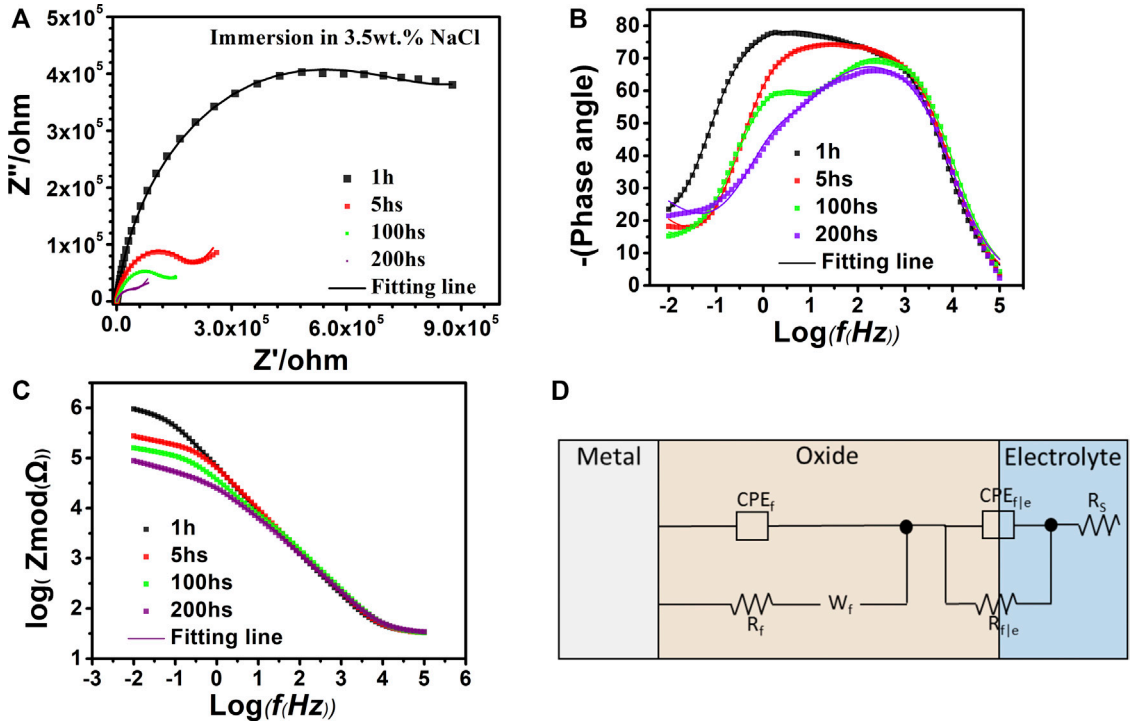

FIGURE 9 | Electrochemical impedance spectra of passivated Al0.1CoCrFeNi after different immersion times. **(A)** Nyquist. **(B)** and **(C)** Bode and phase-angle plots. **(D)** Equivalent circuit (Li et al., 2019).

strongly suggests occurrence of the considerable decline of the passivation film quality. Furthermore, it can be clearly seen from **Figure 9C** that the overall resistance clearly decreases with the increase of immersion time. In addition, with the immersion time increasing, a Warburg impedance appears in Nyquist, which is often an oblique line immediately following the capacitance arc. The presence of Warburg impedance tail usually indicates that the diffusion of species begins to take a more prominent role in electrode process.

In early immersion of **Figure 9B**, phase-angle plots of samples with 1 h and 5 h immersion exhibit a rather broad frequency span at near 90°, indicating the whole film acts like a pure capacitor. Then, as the immersion time increases, phase angles at low frequency decline and two peaks appear suggesting the existence of more than one time constant. The time constants corresponding to low frequency eventually disappear with the further increase of the immersion time.

The fitting results with the equivalent circuits are listed in **Table 3**. Close examination of **Table 3** suggests that with immersion time reaching 200 h, film resistance (R_f) and film electrolyte interface resistance ($R_{f|e}$) exhibit considerable drop, indicating the prolonged immersion finally induces the possible tiny corrosion pits on electrode surface and resulting in the decline of passivation film quality. It is worth noting that the index of n for CPE_F has decreased as immersion time increases, suggesting the increase of surface roughness of the film which is likely due to the impact of surrounding chloride ions (Zhang et al., 2018).

TABLE 3 | Impedance parameters of equivalent circuit (**Figure 9D**).

Time (H)	Rs(Ω)	CPEI		RetI(Ω)	CPEF		RetF(Ω)	W
		Y0 (μF)	n		Y0 (μF)	n		Y0 (μF)
1	32.6	3.5	0.73	4.4×10^5	2.8	0.90	8.3×10^5	13.0
5	32.3	3.2	0.90	1.7×10^5	9.4	0.83	1.1×10^5	31.2
100	31.7	6.4	0.84	2.8×10^5	5.5	0.81	1.0×10^5	81.0
200	32.7	1.1	0.81	3183	7.8	0.80	4.7×10^4	76.0

CONCLUSION

In this work, a comprehensive investigation on corrosion behavior of the $Al_{0.1}CoCrFeNi$ HEA in various concentrations of chloride-containing solutions is carried out, and major conclusions are as follows.

(1) Electrochemical tests demonstrate the excellent overall corrosion resistance of $Al_{0.1}CoCrFeNi$ HEAs against the attack of chloride-containing solutions.
(2) XPS measurements reveal that the passive film of $Al_{0.1}CoCrFeNi$ HEA is of multielemental nature, which is beneficial for its superior corrosion resistance to the pitting. Further analysis of XPS results also reveals evident oxygen deficiencies in the passive films.
(3) Investigation on corrosion topography by SEM suggests that the corrosion of Al0.1CoCrFeNi HEA is likely initiated in

intergranular region and propagated in interdendrite region with the increase of chloride concentration. Three types of pitting topography were probed on Al0.1CoCrFeNi samples.
(4) EIS investigation of immersion tests of the HEA samples suggests that the decline of passivation film quality might be attributable to the chloride anion–containing environment.

DATA AVAILABILITY STATEMENT

All datasets generated for this study are included in the article/ Supplementary Material.

AUTHOR CONTRIBUTIONS

KW carried out experiments and wrote this article. AL and JQ discussed and modified the article.

FUNDING

The authors would like to acknowledge the financial support of the Natural Science Foundation of Shanxi Province, China (Nos. 201901D111105 and 201901D111114) and Transformation of Scientific and Technological Achievements Programs of Higher Education Institutions in Shanxi (2019).

REFERENCES

Ayyagari, A., Hasannaeimi, V., Grewal, H. S., Arora, H., and Mukherjee, S. (2018). Corrosion, erosion and wear behavior of complex concentrated alloys: a review. *J. Metals*, 8, 16–20. doi:10.3390/met8080603

Bentiss, F., Jama, C., Mernari, B., Attari, H. E., Kadi, L. E., Lebrini, M., et al. (2009). Corrosion control of mild steel using 3,5-bis(4-methoxyphenyl)-4-amino-1,2,4-triazole in normal hydrochloric acid medium. *Corros. Sci.* 51, 1628–1635. doi:10.1016/j.corsci.2009.04.009

Chen, Y. Y., Duval, T., Hung, U. D., Yeh, J. W., and Shih, H. C. (2005). Microstructure and electrochemical properties of high entropy alloys-a comparison with type-304 stainless steel. *Corros. Sci.* 47, 2257–2279. doi:10.1016/j.corsci.2004.11.008

Gludovatz, B., Hohenwarter, A., Catoor, D., Chang, E. H., George, E. P., Ritchie, R. O., et al. (2014). A fracture-resistant high-entropy alloy for cryogenic applications. *Science* 345, 1153. doi:10.1126/science.1254581

Green, M. L., Takeuchi, I., and Hattrick-Simpers, J. R. (2013). Applications of high throughput (combinatorial) methodologies to electronic, magnetic, optical, and energy-related materials. *J. Appl. Phys.* 231, 101–113. doi:10.1063/1.4803530

Hou, J., Shi, X., Qiao, J., Zhang, Y., Liaw, P. K., Wu, Y., et al. (2019). Ultrafine-grained dual phase Al0.45CoCrFeNi high-entropy alloys. *Mater. Des.* 180, 897–910. doi:10.1016/j.matdes.2019.107910

Hou, J., Zhang, M., Ma, S., Liaw, P. K., Zhang, Y., Qiao, J., et al. (2017). Strengthening in Al0.25CoCrFeNi high-entropy alloys by cold rolling. *Mater. Sci. Eng. A* 707, 593–601. doi:10.1016/j.msea.2017.09.089

Jeyaprabha, C., Sathiyanarayanan, S., and Venkatachari, G. (2006). Effect of cerium ions on corrosion inhibition of PANI for iron in 0.5 M H 2 SO 4. *Appl. Surf. Sci.* 253, 432–438. doi:10.1016/j.apsusc.2005.12.081

Kao, Y.-F., Chen, T.-J., Chen, S.-K., and Yeh, J.-W. (2009). Microstructure and mechanical property of as-cast, -homogenized, and -deformed AlxCoCrFeNi (0≤x≤2) high-entropy alloys. *J. Alloys Compd.* 488, 57–64. doi:10.1016/j.jallcom.2009.08.090

Kao, Y.-F., Lee, T.-D., Chen, S.-K., and Chang, Y.-S. (2010). Electrochemical passive properties of AlxCoCrFeNi (x=0, 0.25, 0.50, 1.00) alloys in sulfuric acids. *Corros. Sci.* 52, 1026–1034. doi:10.1016/j.corsci.2009.11.028

Keller, P., and Strehblow, H.-H. (2004). XPS investigations of electrochemically formed passive layers on Fe/Cr-alloys in 0.5 M H2SO4. *Corros. Sci.* 46, 1939–1952. doi:10.1016/j.corsci.2004.01.007

Kumar, N., Fusco, M., Komarasamy, M., Mishra, R. S., Bourham, M., Murty, K. L., et al. (2017). Understanding effect of 3.5 wt.% NaCl on the corrosion of Al0.1CoCrFeNi high-entropy alloy. *J. Nucl. Mater.* 495, 154–163. doi:10.1016/j.jnucmat.2017.08.015

Laycock, N. J., and Newman, R. C. (1997). Localised dissolution kinetics, salt films and pitting potentials. *Corros. Sci.* 39, 1771–1790. doi:10.1016/s0010-938x(97)00049-8

Li, T., Swanson, O. J., Frankel, G. S., Gerard, A. Y., Lu, P., Saal, J. E., et al. (2019). Localized corrosion behavior of a single-phase non-equimolar high entropy alloy. *Electrochimica Acta* 306, 71–84. doi:10.1016/j.electacta.2019.03.104

Lin, C.-M., and Tsai, H.-L. (2011). Evolution of microstructure, hardness, and corrosion properties of high-entropy Al0.5CoCrFeNi alloy. *Intermetallics* 19, 288–294. doi:10.1016/j.intermet.2010.10.008

Miracle, B. D., Miller, D. J., Senkov, N. O., Woodward, C., Uchic, D. M., Tiley, J., et al. (2014). Exploration and development of high entropy alloys for structural applications. *Entropy* 16. doi:10.3390/e16010494

Senkov, N. O., Isheim, D., Seidman, N. D., and Pilchak, L. A. (2016). Development of a refractory high entropy superalloy. *Entropy* 18, 102. doi:10.3390/e18030102

Shi, Y., Collins, L., Balke, N., Liaw, P. K., and Yang, B. (2018). *In-situ* electrochemical-AFM study of localized corrosion of Al CoCrFeNi high-entropy alloys in chloride solution. *Appl. Surf. Sci.* 439, 533–544. doi:10.1016/j.apsusc.2018.01.047

Shi, Y., Yang, B., Xie, X., Brechtl, J., Dahmen, K. A., Liaw, P. K., et al. (2017). Corrosion of Al CoCrFeNi high-entropy alloys: Al-content and potential scan-rate dependent pitting behavior. *Corros. Sci.* 119, 33–45. doi:10.1016/j.corsci.2017.02.019

Song, X. T., Shi, X. H., Xia, Z. H., Yang, H. J., Wu, Y. C., Liaw, P. K., et al. (2019). Effects of Ni P coating on mechanical properties of Al0.3CoCrFeNi high-entropy alloys. *Mater. Sci. Eng. A* 752, 152–159. doi:10.1016/j.msea.2019.03.010

Tian, H., Lan, A., Wang, Y., Pan, H. S., and Qiao, J. (2015). Corrosion behavior of *in situ* dendrite-reinforced Zr-based metallic glass matrix composites in NaCl solutions of varied concentrations. *Mater. Chem. Phys.* 162, 326–331. doi:10.1016/j.matchemphys.2015.05.074

Tong, C.-J., Chen, Y.-L., Yeh, J.-W., Lin, S.-J., Chen, S.-K., Shun, T.-T., et al. (2005). Microstructure characterization of Al x CoCrCuFeNi high-entropy alloy system with multiprincipal elements. *Metall. Mat Trans. A.* 36, 881–893. doi:10.1007/s11661-005-0283-0

Wang, W.-R., Wang, W.-L., Wang, S.-C., Tsai, Y.-C., Lai, C.-H., Yeh, J.-W., et al. (2012). Effects of Al addition on the microstructure and mechanical property of AlxCoCrFeNi high-entropy alloys. *Intermetallics* 26, 44–51. doi:10.1016/j.intermet.2012.03.005

Yeh, J.-W., Chen, S.-K., Lin, S.-J., Gan, J.-Y., Chin, T.-S., Shun, T.-T., et al. (2004). Nanostructured high-entropy alloys with multiple principal elements: novel alloy design concepts and outcomes. *Adv. Eng. Mater.* 6, 299–303. doi:10.1002/adem.200300567

Zhang, B., Wang, J., Wu, B., Guo, X. W., Wang, Y. J., Chen, D., et al. (2018). Unmasking chloride attack on the passive film of metals. *Nat. Commun.* 9, 2559. doi:10.1038/s41467-018-04942-x

Zhou, Y. J., Zhang, Y., Wang, Y. L., and Chen, G. L. (2007). Solid solution alloys of AlCoCrFeNiTix with excellent room-temperature mechanical properties. *Appl. Phys. Lett.* 90, 181–904. doi:10.1063/1.2734517

Conflict of Interest: The authors declare that the research was conducted in the absence of any commercial or financial relationships that could be construed as a potential conflict of interest.

Advantages of publishing in Frontiers

OPEN ACCESS
Articles are free to read for greatest visibility and readership

FAST PUBLICATION
Around 90 days from submission to decision

HIGH QUALITY PEER-REVIEW
Rigorous, collaborative, and constructive peer-review

TRANSPARENT PEER-REVIEW
Editors and reviewers acknowledged by name on published articles

Frontiers
Avenue du Tribunal-Fédéral 34
1005 Lausanne | Switzerland

Visit us: www.frontiersin.org
Contact us: frontiersin.org/about/contact

REPRODUCIBILITY OF RESEARCH
Support open data and methods to enhance research reproducibility

DIGITAL PUBLISHING
Articles designed for optimal readership across devices

FOLLOW US
@frontiersin

IMPACT METRICS
Advanced article metrics track visibility across digital media

EXTENSIVE PROMOTION
Marketing and promotion of impactful research

LOOP RESEARCH NETWORK
Our network increases your article's readership